Incorporating Inter-Sample Variability into Cardiac Electrophysiology Simulations

John Walmsley
Balliol College



Computational Biology Research Group
Department of Computer Science
University of Oxford

Trinity Term 2013

Dissertation submitted for the degree of Doctor of Philosophy

Incorporating Inter-Sample Variability into Cardiac Electrophysiology Simulations

John Walmsley

Balliol College

Submitted for the degree of Doctor of Philosophy

Trinity Term 2013

Sudden cardiac death kills 5–10 people per 10,000 population in Europe and the US each year. Individual propensity to arrhythmia and sudden cardiac death is typically assessed through clinical biomarkers. Variability in these biomarkers is a major challenge for risk stratification. Variability is observed at a wide range of spatio-temporal scales within the heart, from temporal fluctuations in ion channel behaviour, to inter-cell and inter-regional differences in ion channel expression, to structural differences between hearts. The extent to which variability manifests between spatial and temporal scales remains unclear but has a potentially crucial role in determining susceptibility to arrhythmia.

In this dissertation we present a multi-scale study of the causes and consequences of variability in electrophysiology. At a sub-cellular level we demonstrate that, taking into account inter-individual variability in ion channel conductance, mRNA expression levels in failing human hearts predict the electrophysiological remodelling observed experimentally.

On a tissue scale, we advocate the use of phenomenological models where information on subcellular processes is unavailable. We introduce a modification to a phenomenological model to capture beat-to-beat variability in action potential repolarisation recorded from four individual guinea pig myocytes. We demonstrate that, whilst temporal variability is dramatically reduced by inter-cell coupling, differences in their mean action potential duration may become apparent at a tissue level.

The ventricular myocardium has a heterogeneous structure not captured by the simplified representation of conduction used above. In our final case study, we challenge a model of conduction by directly comparing simulations to optical mapping recordings of ventricular activation from failing and non-failing human hearts. We observe that good fits to experimental data are obtained only when endocardially bound structures are not in view, suggesting a role in conduction for these structures that are often ignored in cardiac simulations.

Finally, we present future directions for the work presented. We make the case for reporting of inter-sample variability in experimental results and conclude that whilst variability may not always manifest across scales, its impact should be considered in both theoretical and experimental studies.

Acknowledgements

It's easy to know where to begin with the acknowledgements to all those who have helped and supported me through the DPhil process: my supervisors. To Kevin, Blanca and Gary I want to say an enormous and heartfelt thank you for all the work you've put into my projects and my development as a scientist over the last four years. Thank you for all the ideas, the guidance, the patience, and the support when I couldn't make Chaste work and it was all a bit much. Thank you for all the opportunities I've had through travel, conferences and visits to academic institutions the world over. Not to mention the Blue Mountains, Fraser Island, Iguazu Falls, the Pyrennees, ...

None of the work presented here would have been possible without the generosity, patience and enthusiasm of our experimental collaborators. In particular, I am indebted to Igor Efimov of Washington University in St. Louis for his generosity with human left ventricular optical mapping recordings and mRNA expression data. It was a real privilege to spend a month working in his lab and I learned a lot from it. I'd also like to thank the members of the lab for their help and patience with me whilst I was there. I am grateful to Christina Ambrosi and Qing Lou, who were primarily responsible for recording the data used in this thesis. I would also like to acknowledge Christian Bollensdorff, who supplied me with the guinea pig isolated left ventricular myocyte recordings used in this dissertation, and for his help with their analysis.

I also owe a huge debt of gratitude to members of the Chaste team, whose excellent and powerful software has enabled so much of the research I present in this dissertation. In particular, I'd like to thank Gary Mirams, Joe Pitt-Francis and Jonathan Cooper for their help and patient support. I'd also like to thank Mihai Duta from the Oxford Supercomputing Centre for his help with getting the population of models running. From the computational biology group, I'd additionally like to thank Alex Quinn, Alfonso Bueno-Orovio, Ciara Dangerfield, Chris Arthurs, Mikael Wallman, Rafel Bordas and Sara Dutta for all their helpful input over the past few years.

Finally, I'd like to take the opportunity to dedicate this work to my parents, without whom it could never have happened at all.

Contents

List of Figures **7**

List of Tables **13**

List of Abbreviations **15**

1 Introduction **17**

1.1 Motivation 17

1.2 Aims 20

1.3 Thesis 21

1.4 Thesis Structure 22

2 Evidence for Variability in Cardiac Electrophysiology **25**

2.1 Introduction 25

2.2 Cardiac Physiology 26

2.3 An Introduction to Cardiac Cellular Electrophysiology 29

2.4 Propagation of the Action Potential 32

2.5 Experimental Techniques 33

2.6 Heterogeneity and Variability 39

2.7 Experimental Data Summary 47

2.8 Conclusion 48

3 Modelling Variability in Cardiac Electrophysiology **51**

3.1 Introduction . . . 51
3.2 The Role of Modelling in Cardiac Electrophysiology . . . 52
3.3 Biophysically Detailed Models . . . 53
3.4 The O'Hara (2011) Human Ventricular Model . . . 61
3.5 Parameterisation of Cardiac Cell Models . . . 63
3.6 Modelling the Propagation of the Action Potential . . . 77
3.7 Phenomenological and Reduced Models . . . 81
3.8 Relating conductivity, diffusion coefficient and gap junctional resistance . . . 83
3.9 Simulating Heterogeneity and Variability . . . 85
3.10 Conclusions . . . 97

4 Simulation Methods **99**
4.1 Introduction . . . 99
4.2 CVODE . . . 100
4.3 Stochastic Differential Equations and the Euler-Maruyama method . . . 101
4.4 The Finite Element Method . . . 103
4.5 Chaste . . . 108
4.6 Convergence Analysis . . . 109
4.7 Discussion . . . 113

5 Prediction of Electrophysiological Changes in Heart Failure Based on mRNA Expression Data **115**
5.1 Introduction . . . 115
5.2 Methods . . . 117
5.3 Results . . . 122
5.4 Discussion . . . 138

6 Fitting and Extending A Phenomenological Model To Capture Variability **145**
6.1 Introduction . . . 145

6.2 The Bueno-Orovio (2008) Phenomenological Model 146
6.3 Discussion 164

7 Consequences of Sample-Specific Beat-to-Beat Variability in Repolarisation in Tissue 167

7.1 Introduction 167
7.2 Methods 168
7.3 Results 172
7.4 Discussion 184

8 Sample-Specific Fitting of Conductivity Tensors from Human Optical Mapping Recordings 187

8.1 Introduction 187
8.2 Methods 189
8.3 Results 197
8.4 Discussion 217

9 Conclusions and Future Directions 223

9.1 Conclusions 223
9.2 Future Directions 225
9.3 Final Thought 231

A Experimental Data Tables for Human Heart Failure 233

B Regression Coefficients and R^2 Values 239

List of Figures

1.1 **Variability in QTc between patients and over time.** 19

2.1 **The basic anatomy of the heart with the major veins, arteries and valves labelled.** 27

2.2 **The Electrocardiogram.** 28

2.3 **Major currents making up the ventricular action potential.** 30

2.4 **Experimentally recorded action potentials from isolated guinea pig ventricular myocytes isolated from the apex of the heart using whole-cell patch clamp.** 35

2.5 **Experimentally recorded voltage clamps of the sodium current in guinea pig ventricular myocytes.** 36

2.6 **Optical mapping data from raw data published by Lou et al. (2011).** . . . 38

2.7 **Histology slice of a rat heart.** 40

2.8 **Heterogeneity in distribution and structure of collagen through the wall of the myocardium of two rats.** 41

2.9 **Enhancement of beat-to-beat variability of repolarisation in response to pharmaceutical intervention.** 47

3.1 **The development of action potential models over the last 60 years.** . . . 56

3.2 **Structure of different ionic channel formulations, taken from Fink and Noble (2009).** 61

3.3 **Schematic of the O'Hara et al. (2011) human ventricular electrophysiology model.** . . . 62
3.4 **Fitting the inactivation parameters of the sodium current in the Hodgkin-Huxley model.** . . . 67
3.5 **Fitting the conductance and activation parameters for the sodium current in the Hodgkin-Huxley model.** . . . 68

4.1 **Different timescales in an ODE model of the AP.** . . . 100
4.2 **Construction of linear basis functions for the finite element method.** . . . 106
4.3 **Conserved Brownian path.** . . . 112

5.1 **Parameter ranges for the failing and non-failing cell model populations.** 119
5.2 **Biomarkers calculated from simulated AP and CaT traces using the baseline ORd model.** . . . 120
5.3 **Sample AP and CaT traces obtained from the non-failing (blue) and failing (red) populations.** . . . 123
5.4 **Histograms showing biomarker values obtained for the non-failing (blue) and failing (red) cell model populations.** . . . 124
5.5 **Correlation plots of one biomarker against another at 600ms CL.** . . . 130
5.6 **Linear regression fits for individual parameters.** . . . 132
5.7 **Regression coefficients obtained in the non-failing and failing populations.** . . . 133
5.8 **Parameter surfaces for $CaTD_{3080}$ as a function of G_{CaL} and J_{up}.** . . . 136
5.9 **Occurrence of voltage and calcium alternans in the non-failing and failing populations.** . . . 137
5.10 **Alternans traces in the non-failing population (blue) and the failing population (red).** . . . 138

6.1 **Variables and currents in the BO08 phenomenological model simulated using the published human endocardial cell parameter set.** . . . 149

6.2 **Effect of varying v_0 and τ_{fi} on upstroke velocity in the BO08 model.** . . 151
6.3 **Effect of varying τ_{fi} and D on conduction velocity in the BO08 model.** . 152
6.4 **Effect of varying τ_{v^-} on conduction velocity restitution in the BO08 model.** 153
6.5 **Effect of varying θ_v on the excitability of the BO08 model.** 154
6.6 **S1-S2 restitution in the BO08 model.** 155
6.7 **Determining a point of maximum difference from the original restitution curve.** 158
6.8 **Example of S1-S2 restitution fitting in the BO08 model.** 159
6.9 **Effect of time constant rescaling on the action potential duration of the BO08 model.** 160
6.10 **The BO08 model can reproduce a range of experimentally derived action potential morphologies.** 161
6.11 **Simulated and experimental temporal variability in repolarisation.** . . . 164

7.1 **Onset of alternans in a stochastic phenomenological model of an isolated guinea pig ventricular myocyte.** 169
7.2 **Convergence analysis for the deterministic model investigating the effects of PDE time step and spatial discretisation for each value of D.** . 171
7.3 **Convergence analysis for the stochastic model.** 171
7.4 **Mean APD_{90} from tissue simulations using homogeneous cell models.** 173
7.5 **Difference between stochastic and deterministic simulations using homogeneous cell models.** 174
7.6 **Variance in the difference between stochastic and deterministic APD_{90} values for the homogeneous tissue simulations.** 175
7.7 **Heat maps of spatial dispersion in APD_{90} for apex cell 1.** 176
7.8 **Mean and variance in APD_{90} from tissue simulations using a random cell model distribution.** 177

7.9 **Heat maps of spatial dispersion in APD_{90} using a randomly generated cell distribution.** . . . 178
7.10 **Mean APD in the fast pacing protocol.** . . . 179
7.11 **Maximum absolute difference between stochastic and deterministic APD in the fast pacing protocol.** . . . 180
7.12 **Variance in APD_{90} for the fast pacing protocol.** . . . 181
7.13 **Mean APD_{90} over the last ten beats at each cycle length in the fast pacing protocol.** . . . 181
7.14 **Variance in APD_{90} over the last ten beats at each cycle length.** . . . 182
7.15 **Spatially discordant alternans-like behaviour recorded in the action potential duration at 228ms pacing cycle length in the stochastic model.** . . 183

8.1 **Generation of simulation meshes from wedge photographs.** . . . 192
8.2 **Definition of the fibre parameters under investigation.** . . . 193
8.3 **Selecting an elliptical region for activation from experimental data.** . . . 195
8.4 **Non-Failing Wedge 1: Experimental data.** . . . 197
8.5 **Non-Failing Wedge 1: Assessment of effect of conduction parameter variability on difference between simulation and experiment.** . . . 198
8.6 **Non-Failing Wedge 1: Difference between simulation and experiment in the optimal case.** . . . 199
8.7 **Non-Failing Wedge 2: Experimental data.** . . . 200
8.8 **Non-Failing Wedge 2: Assessment of effect of conduction parameter variability on difference between simulation and experiment.** . . . 201
8.9 **Non-Failing Wedge 2: Difference between simulation and experiment in the optimal cases.** . . . 202
8.10 **Non-Failing Wedge 3: Experimental data.** . . . 204
8.11 **Non-Failing Wedge 3: Assessment of effect of conduction parameter variability on difference between simulation and experiment.** . . . 205

8.12 **Non-Failing Wedge 3: Difference between simulation and experiment in the optimal cases.** 206
8.13 **Failing Wedge 1: Experimental data.** 207
8.14 **Failing Wedge 1: Assessment of effect of conduction parameter variability on difference between simulation and experiment.** 208
8.15 **Failing Wedge 1: Difference between simulation and experiment in the optimal cases.** 209
8.16 **Failing Wedge 2: Experimental data.** 210
8.17 **Failing Wedge 2: Normalised objective function values.** 211
8.18 **Failing Wedge 2: Difference between simulation and experiment in the optimal cases.** 212
8.19 **Failing Wedge 3: Experimental data.** 213
8.20 **Failing Wedge 3: Normalised objective function values.** 214
8.21 **Failing Wedge 3: Difference between simulation and experiment in the optimal cases.** 215

9.1 **A conceptual framework for the production of sample-specific models of human ventricular electrophysiology.** 229

List of Tables

5.1 **Parameters under investigation** 117

5.2 **Experimental data summary** 125

6.1 **Parameter sets for the modified BO08 model** 150

6.2 **Experimental and simulated variability in APD_{90}** 163

7.1 **Summary of homogeneous simulations** 172

8.1 **Simulation Comparison Summary** 216

A.1 **Experimental Data: Population Details** 234

A.2 **Experimental Data: Action potential biomarkers** 235

A.3 **Experimental Data: Calcium transient durations** 236

A.4 **Experimental Data: Calcium transient decay time constants** 236

A.5 **Experimental Data: Calcium transient magnitude** 236

A.6 **Experimental Data: Calcium transient triangulation** 237

A.7 **Experimental Data: Calcium transient upstroke** 237

B.1 **Regression coefficients: nonfailing, APD80** 239

B.2 **Regression coefficients: nonfailing, APD3080** 239

B.3 **Regression coefficients: nonfailing, CaTD80** 240

B.4 **Regression coefficients: nonfailing, CaTD3080** 240

B.5 **Regression coefficients: nonfailing, CaTmax** 240

B.6 **Regression coefficients: nonfailing, AP-CaT delay** 240

B.7 **Regression coefficients: failing, APD80** 241
B.8 **Regression coefficients: failing, APD3080** 241
B.9 **Regression coefficients: failing, CaTD80** 241
B.10 **Regression coefficients: failing, CaTD3080** 241
B.11 **Regression coefficients: failing, CaTmax** 242
B.12 **Regression coefficients: failing, AP-CaT delay** 242
B.13 **Non-failing R^2 values** 243
B.14 **Failing R^2 values** 243

List of Abbreviations

Abbreviations used are defined at the start of each chapter in which they appear. Abbreviations used only in Appendix A are omitted here for brevity.

AP Action Potential

APD Action Potential Duration

APD_X Action Potential Duration, defined as the time from the time of maximum upstroke velocity to X% repolarisation

APD_{3080} AP triangulation, defined as the ratio of APD_{30} to APD_{80}

BO08 The Bueno-Orovio et al. (2008) phenomenological model

BO12 The Bueno-Orovio et al. (2012) phenomenological model

BVR Beat-to-beat Variability in Repolarisation

CaT Cytosolic Calcium Transient

CaTD Cytosolic Calcium Transient Duration

$CaTD_X$ Cytosolic Calcium Transient Duration, defined as the time from the time of maximum calcium transient velocity to X% return to diastolic levels

$CaTD_{3080}$ CaT triangulation, defined as the ratio of $CaTD_{30}$ to $CaTD_{80}$

CL Cycle Length

CV Conduction Velocity

DAPCaT Delay between AP and CaT, defined as time from maximum upstroke velocity of AP to time of maximum upstroke velocity of CaT

dtMRI Diffusion Tensor Magnetic Resonance Imaging

EAD Early after-depolarisation

ECG ElectroCardioGram

mRNA messenger RiboNucleic Acid

ORd The O'Hara et al. (2011) human ventricular electrophysiology model

QTc QT-interval corrected for heart rate, defined as $QT/\sqrt{RR}$ (Bazett, 1920)

Chapter 1

Introduction

1.1 Motivation

1.1.1 Ventricular Arrhythmia and Sudden Cardiac Death

Sudden cardiac death is a major cause of mortality, killing 5–10 people per 10,000 population every year in North America and Europe. About half of these deaths are directly attributable to ventricular arrhythmia (John et al., 2012). A particularly dangerous form of arrhythmia is ventricular fibrillation, whereby electrical waves break up completely into small, highly disorganised wavelets propagating throughout the myocardium. The heart's ability to contract synchronously is lost, and pumping of blood almost ceases. Such episodes are often preceded by episodes of ventricular tachycardia and are hypothesised to result from the breakup of a spiral or scroll wave. In particular, ventricular fibrillation is almost inevitably fatal without the rapid application of a defibrillatory electric shock.

Atrial arrhythmias are more common, but not as dangerous. However, atrial fibrillation is still a serious concern due to impaired ventricular filling, and increased formation of blood clots that can cause strokes. Prolonged episodes of atrial fibrillation can cause restructuring of the atria, making atrial fibrillation increasingly likely to occur in future.

The last one hundred years have seen a vast amount of progress in understanding the electrophysiological mechanisms underlying cardiac excitation, their remodelling in

pathological conditions such as heart failure, and their role in the genesis of arrhythmias. However, clinical treatments remain limited. In particular, pharmaceutical interventions to prevent arrhythmia have proved disappointing given their frequent toxic and even pro-arrhythmogenic effects. Even when they do work, results are relatively modest (Grace and Roden, 2012). Therefore, patients deemed susceptible to ventricular arrhythmias often have cardioverter defibrillators implanted; an effective but expensive and invasive intervention. Patients exhibiting a recurrent non-fatal arrhythmia in either the atria or the ventricles may also be treated using catheter ablation to destroy regions of excitable tissue from which arrhythmias originate. These techniques have their own costs and complications too.

1.1.2 The Problem of Variability

A major problem in identifying those at risk of arrhythmia is the substantial and often poorly understood inter-individual variability that occurs in cardiac biomarkers. This phenomenon has been particularly damaging in anti-arrhythmic drug development, where many apparently promising treatments have had to be abandoned after inducing arrhythmia in a subset of the population (Camm, 2012). Factors predisposing particular individuals to arrhythmia in response to pharmaceutical intervention remain unclear, which may explain the disappointing outcomes. Improved understanding of the causes and consequences of inter-patient variability should lead to improved targeting of pharmaceutical interventions and electrical therapy, and therefore improved clinical outcomes for patients.

Major difficulties are encountered when attempting the risk stratification of patients. This is in part due to variability in widely-used arrhythmic risk biomarkers such as QTc (QT-interval corrected for heart rate). An example occurring frequently in the literature is arrhythmic risk in individuals diagnosed with long QT-syndrome, either as a result of ion channel mutations or in response to drug treatment. Whilst a QTc $\geq$ 500ms has been shown to be associated with increased risk of cardiac events (such as loss of consciousness or cardiac arrest), this biomarker shows a dramatic degree of variation both between patients with the same mutation, and when recorded from the same patient over time (Fig. 1.1).

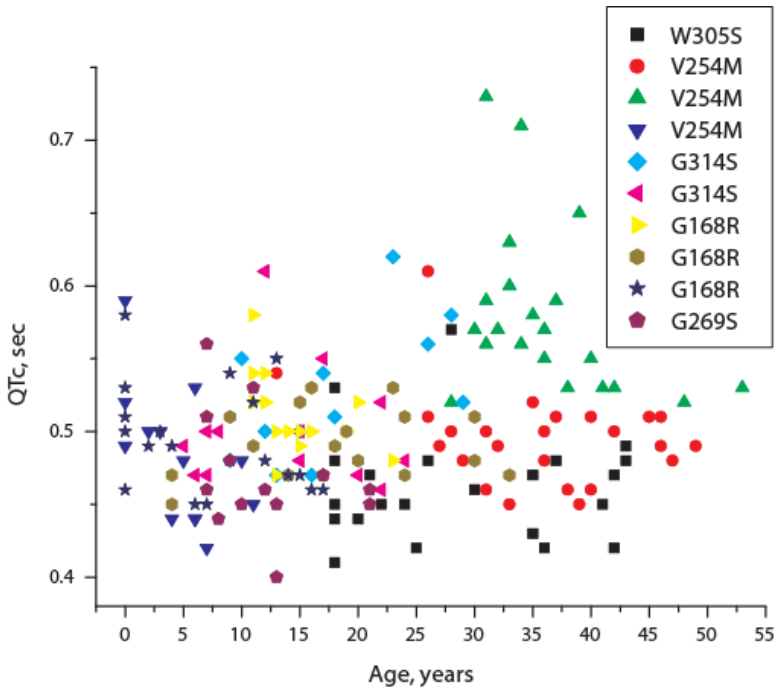

Figure 1.1: **Variability in QTc between patients and over time.** A demonstration of the degree of variability in QTc both between patients and over time from Hoefen et al. (2012). All mutations shown lead to a long QT 1 syndrome phenotype. Note that some patients share the same mutation underlying long QT 1 syndrome. Reprinted from Journal of the American College of Cardiology, Vol 60, Issue 21, R. Hoefen, M. Reumann, I. Goldenberg, A.J. Moss, J. O-Uchi, Y. Gu, S. McNitt, W. Zareba, C. Jons, J.K. Kanters, P.G. Platonov, W. Shimizu, A.A.M. Wilde, J.J. Rice and C.M. Lopes, *In silico* cardiac risk assessment in patients with long QT syndrome : type 1: clinical predictability of cardiac models, Pages 2182–2191, Copyright (2012), online data supplement, with permission from Elsevier.

Some of the causes of electrophysiological variability are well known, even if the mechanisms by which they act are still being elucidated. However, electrophysiological studies ranging from isolated cell experiments, to tissue samples, to *in vivo* experiments performed during coronary bypass operations, reveal a large degree of variability in electrophysiological properties of human ventricles. Furthermore, isolated cells demonstrate a beat-to-beat variability in their action potential duration (APD) which may also contribute to tissue and ECG level beat-to-beat variability.

Determining the mechanistic consequences of experimentally recorded variability is challenging, as by its very nature variability may not be reproducible between samples. Computational modelling offers a way to obtain a sample-specific or patient-specific under-

standing of potential arrhythmogenic consequences of variability.

1.2 Aims

Computational cardiac electrophysiology models have recently begun to incorporate inter-sample variability both between cells (Sarkar et al., 2012) and in structure (Bordas et al., 2011). Comparing the output of models exhibiting variability with experimentally recorded variability, however, is not generally practiced (Carusi et al., 2012). This validation step is important to build confidence in the model, as well as to allow consideration and comparison of sample specific effects. The methods appropriate for both modelling variability in experimental data and for comparison of model output and experimental data depends upon: the modelling question at hand; the experimental data used for model construction; and the experimental data available for model validation.

In this thesis, we shall consider the problem of appropriate model construction, and validation against experimental data, incorporating variability at multiple spatial and temporal scales within the heart. We examine three case studies from a sub-cellular to a structural level:

1. A recent study of mRNA expression levels in human ventricular myocytes (Ambrosi et al., 2013) revealed altered expression in heart failure. Determining the consequences of these changes on electrophysiology is difficult since the changes are averaged over the population under investigation and are compounded by the many difficulties in extrapolating from mRNA expression levels to functional effect at a cellular scale. Can computational modelling be used to predict the potential consequences of these changes in expression, taking into account uncertainty in the degree of the effect?

2. Isolated cardiac ventricular myocytes display inter-cell variability in action potential duration despite coming from ostensibly the same region of the heart. Furthermore,

these isolated ventricular myocytes display a beat-to-beat variability in repolarisation times. Can a model of the action potential be developed that is capable of making predictions about this behaviour in tissue?

3. Transmural optical mapping recordings in failing and non-failing human left ventricles demonstrate variability in activation time between preparations. Can we assign a sample-specific conductivity tensor to the preparation by varying both the conductivity and the fibre orientation on a sample-specific mesh? By considering the difference between the best fit to the data and the experimentally recorded activation time, we can detect which regions of the tissue display irregular conduction, and through image registration determine whether this coincides with structural heterogeneities in tissue.

1.3 Thesis

Given an appropriate underlying model of electrophysiological behaviour in cardiac tissue, it is possible to construct sample-specific models of cardiac electrophysiology at both a cell and tissue level. These models provide insight into the consequences of variability in activation and repolarisation of the cardiac action potential. Where only information on activation or action potential morphology is available, then a phenomenological model that reproduces these properties without reconstructing membrane currents suffices. If sub-cellular phenomena are being investigated then a biophysically detailed model of the cardiac action potential is required. Whether or not direct comparison to experimental data is possible depends on both the simulation results generated and the experimental data available.

1.4 Thesis Structure

- **Chapter 2: Evidence for Variability in Cardiac Electrophysiology.** A brief introduction to the structure and function of the human heart, followed by a more detailed description of the electrophysiology of mammalian cardiac ventricular cells. After briefly discussing the strengths and weaknesses of experimental techniques used to record the electrophysiological data used in this thesis, we critically review the extant literature on heterogeneities and variability in cardiac electrophysiology, focussing where possible on controversies within the field. We then provide a brief summary of the experimental data used within this thesis for model construction and validation.

- **Chapter 3: Modelling Variability in Cardiac Electrophysiology.** A review of the history of the development of cardiac cell electrophysiology models and their parameterisation, as well as alternative methodologies such as phenomenological models and Eikonal models of activation. We then briefly discuss the derivation of the monodomain and bidomain equations for coupled tissue. Finally, we critically review the literature existing in the field on the simulation of heterogeneities in cardiac tissue, inter-sample variability in action potential behaviour, and temporal variability.

- **Chapter 4: Simulation Methods.** In this chapter, we describe the numerical methods and software packages used for numerical solution of model equations within this dissertation. Specifically, we cover CVODE, the finite element method, Chaste, and the Euler-Maruyama method. We then describe techniques for checking convergence of stochastic schemes and tissue electrophysiology simulations.

- **Chapter 5: Prediction of Electrophysiological Changes in Heart Failure Based on mRNA Expression Data.** After discussing the problems in extrapolating from mRNA expression levels to the functional effect of the proteins under investigation, we generate two populations of human electrophysiological cell models representing failing and non-failing ventricular myocytes based on the O'Hara et al. (2011) ven-

tricular model. By calculating six potential biomarkers of arrhythmic risk for each cell in the population, we can predict how cells in heart failure are remodelled. Furthermore, using linear regression analysis we can demonstrate which changes in ionic currents and fluxes have had the largest effect on each biomarker under investigation. Finally, we compare the results of our simulation study to published values from multiple experimental studies on electrophysiological remodelling between failing and non-failing human ventricles.

- **Chapter 6: Properties of Phenomenological Cell Models.** We demonstrate the ability of phenomenological models of the action potential to fit a variety of action potential morphologies from a number of different species. Furthermore, we develop a modification to the restitution properties of a popular phenomenological model allowing easier fitting of restitution properties. Finally, we modify the Bueno-Orovio et al. (2008) phenomenological model using stochastic differential equations to allow the simulation of temporal variability in the action potential ('intrinsic noise').

- **Chapter 7: Consequences of Sample-Specific Beat-to-Beat Variability in Repolarisation in Tissue.** We generate four action potential models using experimental data from isolated guinea pig ventricular myocytes and the stochastic differential equation model in Chapter 6. We then simulate each model at four levels of coupling in a two-dimensional tissue sample in order to investigate how this temporal variability might manifest in tissue. Simulations are performed with and without extrinsic noise in the form of inter-cell variability. Simulations are performed at both a 1Hz pacing rate and a series of fast pacing rates to investigate the effect of restitution properties on dispersion of repolarisation.

- **Chapter 8: Sample-Specific Fitting of Conductivity Tensors from Human Optical Mapping Recordings.** We use a data set consisting of optical mapping recordings of membrane voltage from three failing and three non-failing human left ventricular wedges, previously published by Lou et al. (2011). We register the optical

camera field of view for each experiment onto a photograph of the wedge in that experiment. We then construct a simulation mesh from the wedge photograph to give a map between the optical mapping camera field of view and the simulation mesh. A fibre orientation is assigned to each wedge to give a conductivity tensor, whose parameters are allowed to vary. By direct comparison of simulation results and experimentally recorded activation time, we select an optimal conductivity tensor for each wedge preparation. By directly mapping structural heterogeneities onto the difference between simulated and experimental activation times, we attempt to determine which structural features are affecting conduction.

- **Chapter 9: Conclusions and Future Directions.** We critically appraise the successes and shortcomings of the methods described in the dissertation, and discuss future avenues of investigation to build on the work presented.

- **Appendix A: Comparative Data on Failing and Non-Failing Human Ventricular Electrophysiology.** Experimental data from studies comparing the electrophysiology of failing and non-failing human ventricular tissue referred to in Chapter 5.

- **Appendix B: Regression Coefficients and R^2 Values** Regression coefficients and R^2 values generated in Chapter 5.

Chapter 2

Evidence for Variability in Cardiac Electrophysiology

2.1 Introduction

Having motivated our study in Chapter 1, we now review the experimental evidence for variability in cardiac electrophysiology. In Section 2.2, we describe the basic anatomy of the heart and the basic mechanism of its electrical excitation. Section 2.3 and Section 2.4 introduce fundamental concepts of cardiac cellular electrophysiology and inter-cell coupling which are critical for the studies making up this thesis. We then briefly describe patch clamping and optical mapping, which are used in recording the electrophysiological data used in subsequent studies in Section 2.5. In Section 2.6, we review experimentally reported structural, inter-cell and beat-to-beat variability. We focus on areas of controversy where computational modelling is beginning to play a role in understanding causes and consequences of variability. Finally, we provide a summary of the raw experimental data from a wide range of spatial and temporal scales used within this thesis to construct and validate models of variability in electrophysiology.

2.2 Cardiac Physiology

2.2.1 Cardiac Anatomy

The mammalian heart is a pump whose purpose is to drive blood around the body. Its basic anatomy is shown in Fig. 2.1. The heart consists of four chambers in total — the left and right atria and the left and right ventricles. The atria and ventricles have contractile walls consisting mainly of muscular tissue known as the myocardium. The ventricles are divided by the muscular wall of the septum. Blood is held in the atria before being pushed into the appropriate ventricle, which then ejects the blood out into the body. The larger left side of the heart pumps oxygenated blood returned from the lungs via the pulmonary vein around the body through the aorta, and the smaller right side pumps de-oxygenated blood returned from the body via the vena cava to the lungs through the pulmonary artery. The ejection of blood is achieved via a contraction of the muscular walls of the chamber causing an increase in blood pressure. The walls of the left ventricle are significantly thicker than those of the right ventricle due to the greater pressures required to pump blood around the whole body as opposed to the lungs alone.

2.2.2 Electrical excitation of the heart

The contractions that drive the heart's action are caused by a release of calcium into the heart's muscle cells, known as cardiomyocytes. This release is itself triggered by electrical activation, as well as stretch activation leading to a mechano-electric feedback loop (Kohl and Sachs, 2001). The process of excitation of the heart begins with the pacemaker cells of the sino-atrial node, located between the base of the vena cava and the right atrium (Katz, 2006). These cells have a self-exciting transmembrane potential that causes the depolarisation of the atrial myocytes surrounding them. This leads to a propagation of electrical activity through the right and then left atria, causing the P wave on the electrocardiogram (ECG) shown in Fig. 2.2.

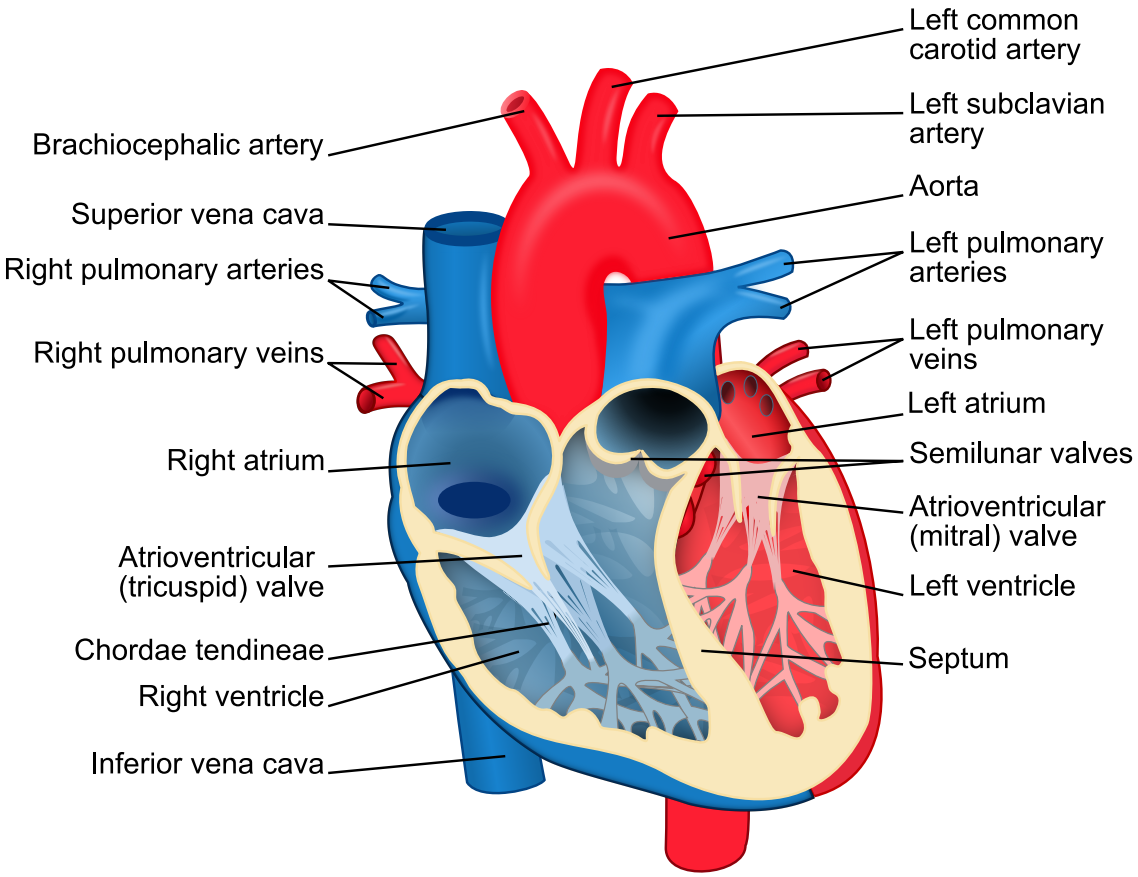

Figure 2.1: **The basic anatomy of the heart with the major veins, arteries and valves labelled.** The left side of the heart and its related arteries and veins are coloured red, and the right hand side is coloured blue. This image is from Wikimedia Commons and is re-used under the Creative Commons Attribution-Share Alike 3.0 Unported license. The original image was created by Wikimedia Commons user 'ZooFari'.

Upon reaching the atrioventricular (AV) node at the junction between the right atrium and the septum, the AV node causes a slight delay in propagation of the electrical signal of approximately 100ms before activating the bundle of His. This bundle of fast conducting fibres breaks into a left and right branch before propagating an excitation down the septum and into the left and right ventricles. The His-Purkinje network is then activated. The Purkinje network travels through the subendocardium (inside wall) of the ventricles as well as in free-running fibres across the ventricles.

The excited Purkinje fibres pass stimulation on to nearby ventricular myocytes, causing propagation through the entire ventricle transmitted from myocyte to myocyte. Propagation occurs primarily through gap junctions formed from a pair of channel proteins directly

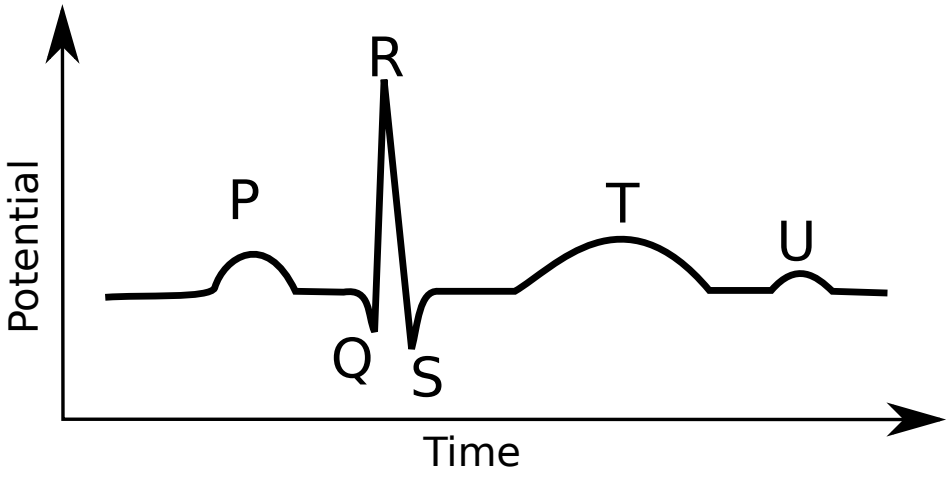

Figure 2.2: **The Electrocardiogram.** The electrocardiogram (ECG) is a plot of the electrical potential across the heart during the cardiac cycle, typically recorded from multiple electrodes placed on the thorax. The common features of the ECG are labelled. The P wave is caused by atrial excitation. The distinctive spike of the QRS complex results from the depolarisation of the ventricles. The T wave arises from the repolarisation of the ventricles. The causation of the U wave remains highly controversial (Goernig et al., 2010). It is often not shown on ECG diagrams.

connecting the cytoplasm of neighbouring cells. The myocytes themselves form fibre-like strands throughout the myocardium, commonly referred to as 'fibres'. These fibres are then themselves loosely arranged into sheet-like structures. Propagation is fastest in the fibre direction as gap junctions are primarily localised to the intercalated discs at either end of the cell in this fibrous arrangement.

The activation of cardiac ventricular myocytes in the ventricles is responsible for the characteristic QRS complex in the ECG. Once activated, or depolarised, the cardiac cells contract in response to an internal release of calcium into the cytoplasm. This cytosolic calcium then causes a contraction of the myocyte, which generates the pressure required to force blood out of the chambers of the heart. As the cell repolarises, calcium is re-absorbed into the sarcoplasmic reticulum, and the myocytes relax. This process of repolarisation causes a repolarising wave to spread across the ventricles, responsible for the T-wave in the ECG. The process of the electrical excitation (depolarisation) and relaxation (repolarisation) of a cardiac myocyte is known as the action potential (AP) and is discussed in detail in the following section.

2.3 An Introduction to Cardiac Cellular Electrophysiology

The formation of the AP is a highly complex process and there exist thorough descriptions in the literature such as Carmeliet and Vereecke (2002). We base our brief description of the formation of the ventricular AP upon their account. It should be noted that the AP has different properties and morphologies depending on species and cell location, as discussed in Section 2.6.1. An outward rectifier current increases the repolarising current when depolarisation occurs, and inward rectifier current increases as hyperpolarisation occurs. A channel which passes an outward current more easily than an inward current is said to display outward rectification, and a channel which passes an inward current more easily than an outward current is said to display inward rectification as determined by the gradient of its current-voltage relation.

The AP generated by the Ten Tusscher and Panfilov (2006) computational model of a human cardiac ventricular myocyte is shown in Fig. 2.3. A balance of the effects of diffusion across the membrane and electrical repulsion between charged ions is fundamental to the generation of the AP. For a given ion, the point at which its diffusion across the cell membrane is balanced by the electrically repulsive effects of equivalently charged ions on the other side of the membrane is known as the Nernst potential.

Prior to initiation of the AP the membrane will be at a negative rest potential, generally between -85mV and -95mV dependent upon species, cell type, and pathology. This negative potential is due to the concentration of positively charged ions such as calcium, potassium and sodium being greater outside the cell than inside. Stimulation of the cell through either a propagating electrical wave from an adjacent cell at the gap junctions or an externally applied stimulus through an electrode leads to opening of ion channels responsible for the voltage sensitive fast sodium current, I_{Na}. The fast opening of sodium channels leads to a rapid and large influx of positively charged sodium ions across the cell membrane. This pushes the cell's membrane potential up to approximately $+40$mV, again dependent on the cell in question. This rapid influx is known as the upstroke. In response

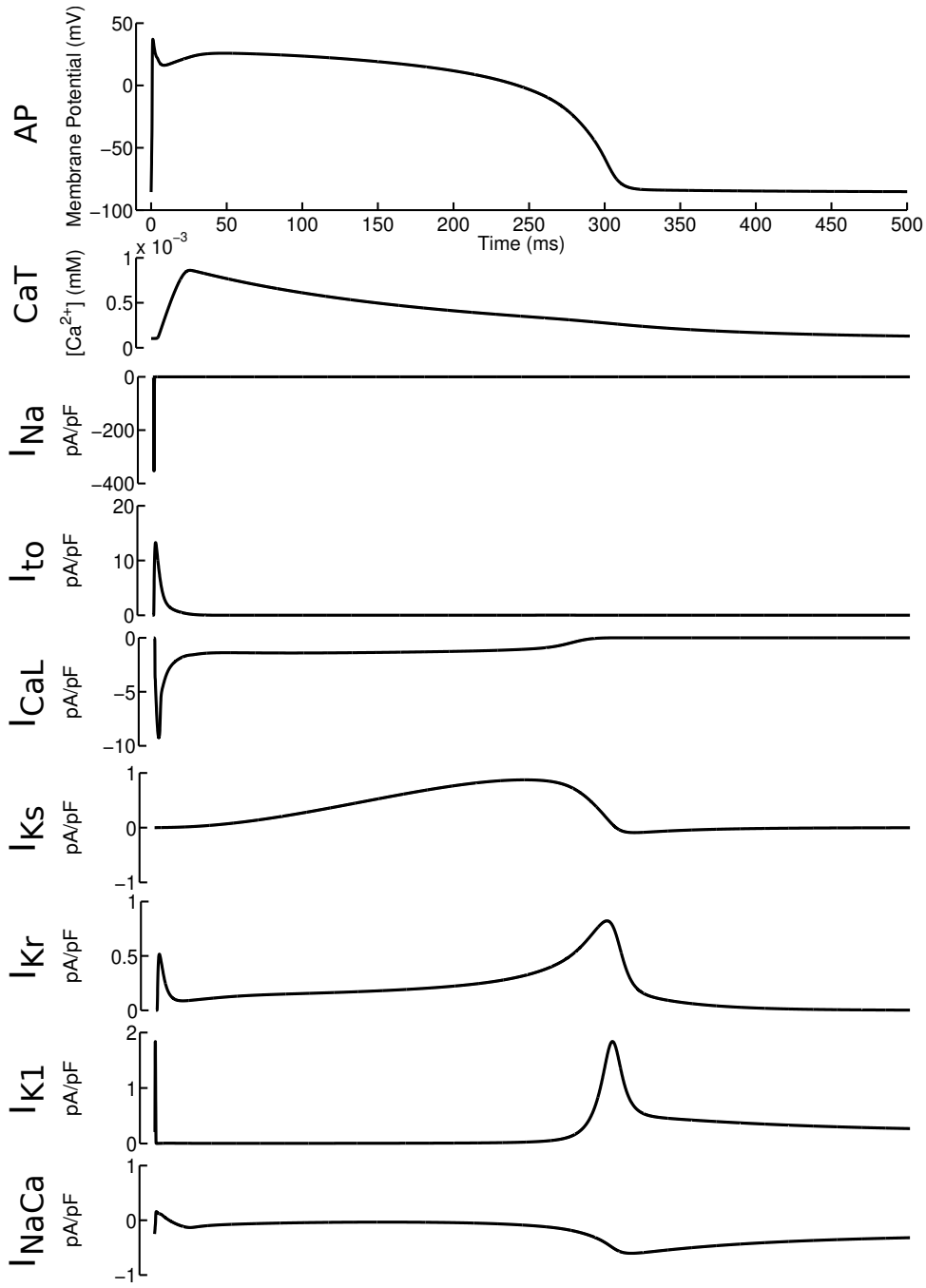

Figure 2.3: **Major currents making up the ventricular action potential.** Major currents making up the human ventricular action potential (AP) are reproduced from the Ten Tusscher and Panfilov (2006) human ventricular model. The AP, cytosolic calcium transient (CaT), fast sodium current (I_{Na}), transient outward potassium current (I_{to}), L-type calcium current (I_{CaL}), slow delayed rectifier potassium current (I_{Ks}), fast delayed rectifier potassium current (I_{Kr}), inward rectifier potassium current (I_{K1} and the sodium calcium exchange current (I_{NaCa})) are shown.

to this rapid increase in transmembrane potential, a fast activating transient outward potassium current known as I_{to} is activated, causing a brief current of potassium ions out of the cell, causing a distinctive notch as the flow of positively charged potassium out of the cell reduces the positive charge inside the cell.

The plateau is initiated by I_{to}, which triggers an initial small repolarisation. During the plateau, the gradient of the AP is relatively low, suggesting a small net outward current. We see the increasing influence of the L-type calcium current, I_{CaL}, providing a flow of positively charged ions into the cell, creating the extra depolarisation of the cell leading to a domed morphology. The influx of calcium into the cell during the AP is critical to cardiac function as this activates calcium-induced calcium release from the sarcoplasmic reticulum, in response to which the calcium concentration in the cytosol is raised. Cytosolic calcium binds to troponin-C, causing a conformational change in troponin-I. This then exposes a site on the actin fibres, to which myosin can bind, thus causing contraction of the cell.

I_{CaL}, together with an inward contribution from the late sodium current I_{NaL}, counteracts the two major outward potassium currents active in the plateau phase, leading to the prolonged AP that distinguishes cardiac ventricular APs in larger mammals from the sharply spiked neuronal AP. The main two potassium currents active during this phase are the rapid delayed outward rectifier potassium current, I_{Kr}, and the slow delayed outward rectifier potassium current, I_{Ks}. The sodium/calcium exchanger, I_{NaCa}, is also active during the plateau phase, and extrudes calcium from the cytoplasm towards the end of the plateau, causing an inward current that slows the repolarisation. This is an inward current as the exchanger moves a greater charge carried by sodium into the cell than it moves charge carried by calcium out of the cell.

Repolarisation of the cell is carried predominantly by the outward flow of potassium by I_{Kr} and I_{Ks} and occurs in response to the repolarisation of the cell causing deactivation of the L-type calcium current in response to the increasing magnitude of this delayed rectifying current. The inward rectifier potassium current I_{K1} is also activated during repolarisation as the transmembrane potential becomes sufficiently negative, causing a steep final gradient

of the AP.

During diastole the sodium/potassium pump removes sodium from the cell in exchange for potassium, which is removed from the cell by the large conductance of the I_{K1} current. Thus, the resting membrane potential is conserved, with sodium and calcium predominantly exterior to the cell, although it should be noted that concentrations of calcium remain buffered in the cytoplasm and also in the sarcoplasmic reticulum. The time the cell spends in the diastolic phase before its next activation is known as the diastolic interval.

An important property of the AP is that its duration depends on the frequency at which the cell is stimulated. An acceleration in the pacing of the cell results in reduced APD, and an increased diastolic interval results in an increased APD. In response to a change in pacing cycle length the APD adapts to a new value over a number of beats, often recorded as an APD-rate dependence curve. Alternatively, the relationship can be recorded as an S1-S2 restitution curve, by pacing at a constant fixed pacing rate (S1). A stimulus is then applied at a range of different diastolic intervals (S2), giving a measure of the transient response of the AP to a premature or late stimulus.

2.4 Propagation of the Action Potential

Propagation of membrane activation between cells may occur in a variety of mechanisms throughout the heart, such as through the Purkinje-myocardial junctions and possibly myofibroblasts. Our discussion here deals with the most commonly studied method of electrical conduction within the ventricular myocardium — diffusion of charged ions through gap junctions. Gap junctions are channels that link the cytosol of two cells, formed of two protein complexes — one in each cell membrane. The hemi-channels are known as connexons and are formed of connexin proteins. In the case of the mammalian ventricular myocardium this is predominantly connexin43. When the cell is excited, changes in ionic concentrations in one cell will then lead to diffusion of ions across the gap junctions, producing a current between the cells, which may activate a neighbouring cell due to a rise in its transmem-

brane potential leading to the opening of sodium channels. During repolarisation, inter-cell currents may modulate the repolarisation of neighbouring cells by acting as either a source or sink depending on the stage of repolarisation. Gap junctions are primarily localised to the intercalated discs at either end of the cell, which form the fibre orientation. To a lesser extent, gap junctions also form laterally to the cell orientation, producing cross-fibre connections. In conditions of normal and uniform coupling, these lateral gap junctions appear to contribute to the uniform propagation of activation in tissue, as strands that lag behind the main activation front are activated by neighbouring fibres (Rohr, 2004).

The conduction velocity (CV) is the speed at which the AP propagates through tissue. The CV depends upon the number of gap junctions in the direction of propagation, hence giving a larger CV in the direction of cardiac fibres. The velocity of the upstroke of the AP also determines the CV as a fast upstroke increases the potential difference and hence diffusive current between cells. At fast pacing rates, the dependence of CV on upstroke velocity leads to a reduction in CV due to incomplete recovery of sodium channels from the previous stimulation. This property is known as CV restitution.

2.5 Experimental Techniques

In this section we briefly describe two methods for recording cardiac electrophysiological measurements that are frequently referred to in this thesis — namely patch clamp and optical mapping recordings. There are, of course, a wide variety of other methods used for the recording of changes in membrane potential in both isolated cells and tissue, such as the recording of monophasic APs using extracellular electrodes or microelectrode recordings; in the interests of space we do not describe these in detail here.

2.5.1 Patch clamp

In patch clamp experiments, a polished glass pipette containing an electrode is used to form a seal of high resistance (ideally GΩ) on the cell membrane (Hamill et al., 1981).

Leaving the pipette attached to the cell, the membrane may be either broken or unbroken. By breaking the cell membrane, access is provided to the intracellular space of the cell. This allows the injection of current, and measurement of a macroscopic cell membrane potential (Plonsey and Barr, 2000). By applying channel blocking drugs, it is then possible to attempt to isolate the effects of particular ionic currents.

With the membrane unbroken, the kinetics of a single ion channel *in situ* may be explored. Pulling the pipette away from the membrane results in an 'inside-out' patch: a thin strip of membrane containing the channel is left inside the pipette aperture, with the exterior cell membrane inside the pipette. This configuration enables recordings of individual opening and closing events. An important feature of such recordings is that they reveal the stochastic nature of channel opening. Single channel recordings from a particular ion channel offer the greatest insights into channel kinetics and single channel conductivity but contain no information on the whole cell conductance of a particular current.

By breaking the cell membrance but leaving the pipette in place, the intracellular ionic concentration equilibrates with that contained within the pipette. Stimulating the cell with an electrode causes depolarisation of the membrane and generates an AP which is recorded through the pipette, as shown in Fig. 2.4. Measurement of the effects of certain currents (or more realistically, groups of currents) are taken using either pharmacological blockers to inhibit certain currents, or by using a voltage pulse to activate and deactivate certain channels before measuring the effects of the remaining active currents.

One of the most important protocols for studying the currents that make up the AP is the voltage clamp protocol. Under a voltage clamp protocol a current is injected into the cell to hold the transmembrane potential constant. Typical protocols used are 'step' and 'ramp' protocols. Under a step protocol, the membrane potential is stepped from one base potential to a new potential, allowing determination of the opening kinetics and maximal conductance of the current, and similarly by stepping from a set of potentials to a fixed potential the closing kinetics of the current may be determined. Both protocols and resulting currents are shown in Fig. 2.5. Under a ramp protocol, the transmembrane potential is

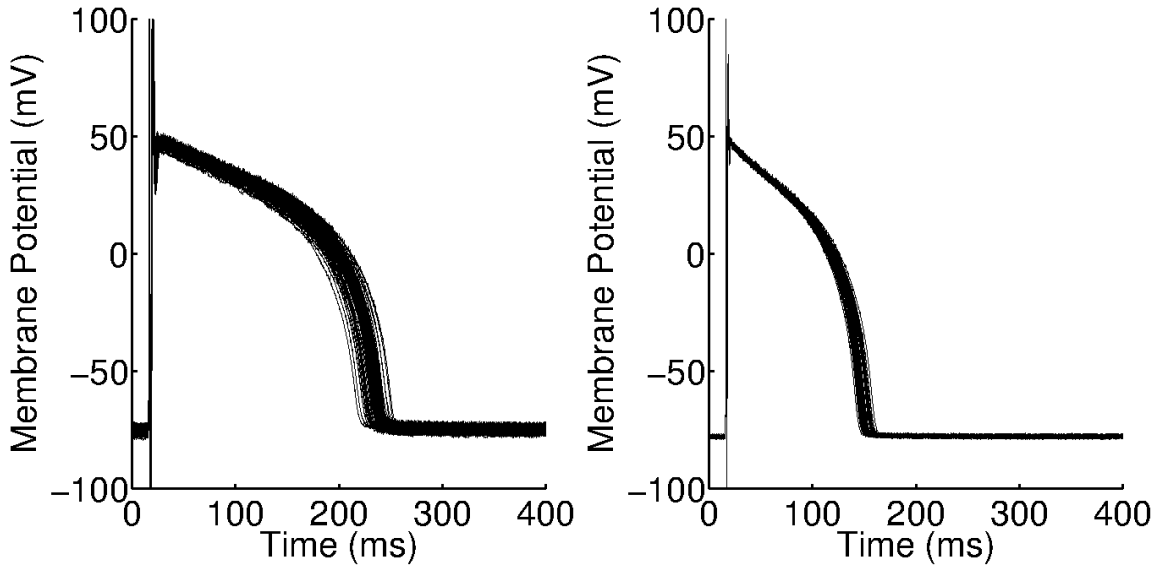

Figure 2.4: **Experimentally recorded APs from isolated guinea pig ventricular myocytes isolated from the apex of the heart using whole-cell patch clamp.** The cells were paced at a cycle length of 1000ms. Both cells are from the same heart but have different mean AP durations (APDs). Note also the beat-to-beat variability in APD, discussed in section 2.6.4. Data supplied by Dr. Christian Bollensdorff and Maya Bahoshy, Department of Physiology, Anatomy and Genetics, University of Oxford, Oxford, UK.

increased from one fixed potential to another at a fixed rate.

2.5.2 Optical mapping

Optically-excitable dyes can be used to measure electrophysiological properties such as membrane potential and cytosolic calcium concentration in cardiac cells and tissue in a wide range of preparations, including isolated cells, muscle strips, myocardial slices, wedge preparations and Langendorff perfused hearts. A recent review is provided by Herron et al. (2012). The method has also recently been demonstrated *in vivo* in a rat model (Lee et al., 2012a). The principle behind the optical recording of membrane potential is that fluorescent dyes can be designed to insert themselves into the lipid bilayer that forms the cell membrane of an electrically active cell. When excited by light at a certain wavelength, the dye fluoresces at a different wavelength. Crucially, the emission spectrum of the dye changes with the membrane potential of the cell due to a change in the conformation of the dye molecule, resulting in a deflection in the intensity of light when passed through

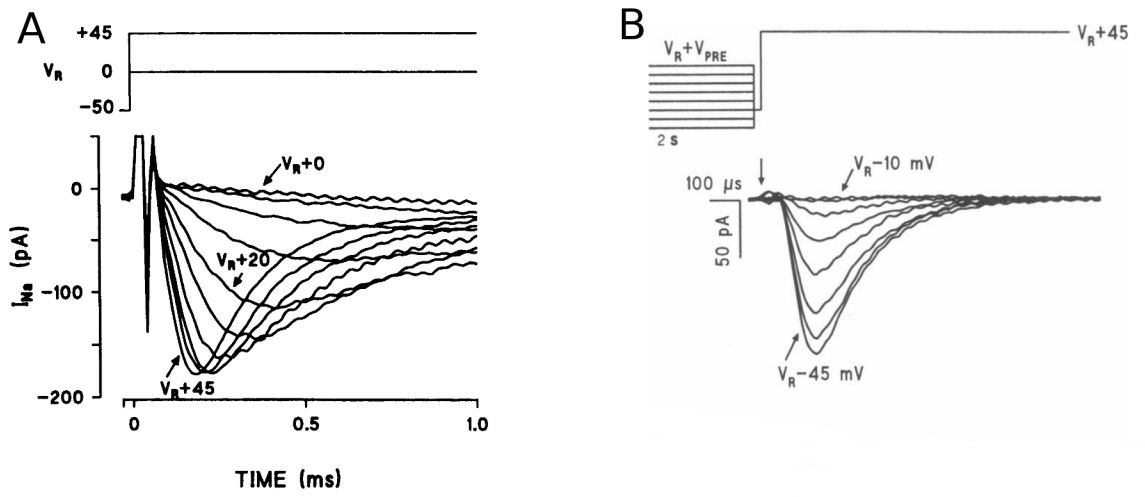

Figure 2.5: **Experimentally recorded voltage clamps of the sodium current in guinea pig ventricular myocytes.** The figure is modified from Murray et al. (1990). A) shows an activation step protocol, and B) shows a deactivation step protocol. Reprinted from Biophysical Journal, Vol 57(3), K.T. Murray, T. Anno, P.B. Bennett and L.M. Hondeghem, Voltage clamp of the cardiac sodium current at 37°C in physiologic solutions, Pages 607–613, Copyright (1990), with permission from Elsevier.

a filter admitting this emission spectrum. The signal is then recorded using a camera. A similar principle is used to record calcium transients, except that the change in the emission spectrum of the dye results from the binding of the dye molecule to calcium ions, localised in the cytosol.

A range of dyes is available for the imaging of voltage and calcium transients, such as di-4-ANEPPS for membrane voltage mapping and Rhod-2 AM for calcium mapping. Each has differing properties in terms of absorption and emission spectra. Careful selection of dyes enables the simultaneous mapping of membrane voltage and cytosolic calcium concentration, provided the emission spectra of the two dyes is separated. By using two different filters and two different cameras, the signals from both voltage and calcium transients may be recorded simultaneously (Choi and Salama, 2000). It is possible, though more technically challenging, to use only one camera for the recording as demonstrated by Lee et al. (2011), by using dyes with different absorption and emission spectra and a rapidly switching LED array for excitation, together with a dual pass filter for the two different emission spectra of the dyes. This is a promising technology as it may dramatically reduce the cost of performing optical mapping experiments. Presumably, dual mapping systems

could be extended to three or more dyes, although eventually temporal resolution of the signal may render the recordings of questionable use.

When recording optical signals a decoupling agent such as 2,3 butanedione monoxime (BDM), cytochalasin D or blebbistatin is generally used to decouple mechanical and electrical effects in the heart. This prevents contraction during the plateau and repolarisation phases of the AP, which creates a difficult image registration problem. Blebbistatin is currently the preferred choice for optical experiments, as Fedorov et al. (2007) demonstrated that blebbistatin had relatively little effect on electrophysiological activity, as it works by inhibiting binding between actin and myosin. Blebbistatin and BDM have recently been shown to have different arrhythmogenic properties in the rabbit ventricles (Lou et al., 2012). Mechanical restraints on the tissue and image registration techniques are also sometimes used instead of de-coupling.

Optical mapping experiments in tissue provide a significantly higher spatial resolution than can be achieved with electrode methods. Consequently, optical mapping is a good choice for the recording of arrhythmia maintenance and genesis (Nanthakumar et al., 2007). However, care must be taken when analysing the resulting images as the temporal and spatial filtering methods used can affect results, particularly around the AP upstroke, which is particularly vulnerable to both Gibbs phenomena as a result of an inappropriate choice of temporal filter, and artificial prolongation as a result of excessive spatial filtering (Laughner et al., 2012). A further source of distortion of the AP morphology is photon scattering effects (Hyatt et al., 2005; Bishop et al., 2006), where subsurface electrophysiological activity is recorded by the camera due to light penetrating into the tissue, and scattering on its emission from deep tissue. This can result in a distortion of the recorded AP upstroke in particular. Additionally, the angle at which the wave is incident to the surface can affect the recorded two-dimensional upstroke dynamics (Hyatt et al., 2005).

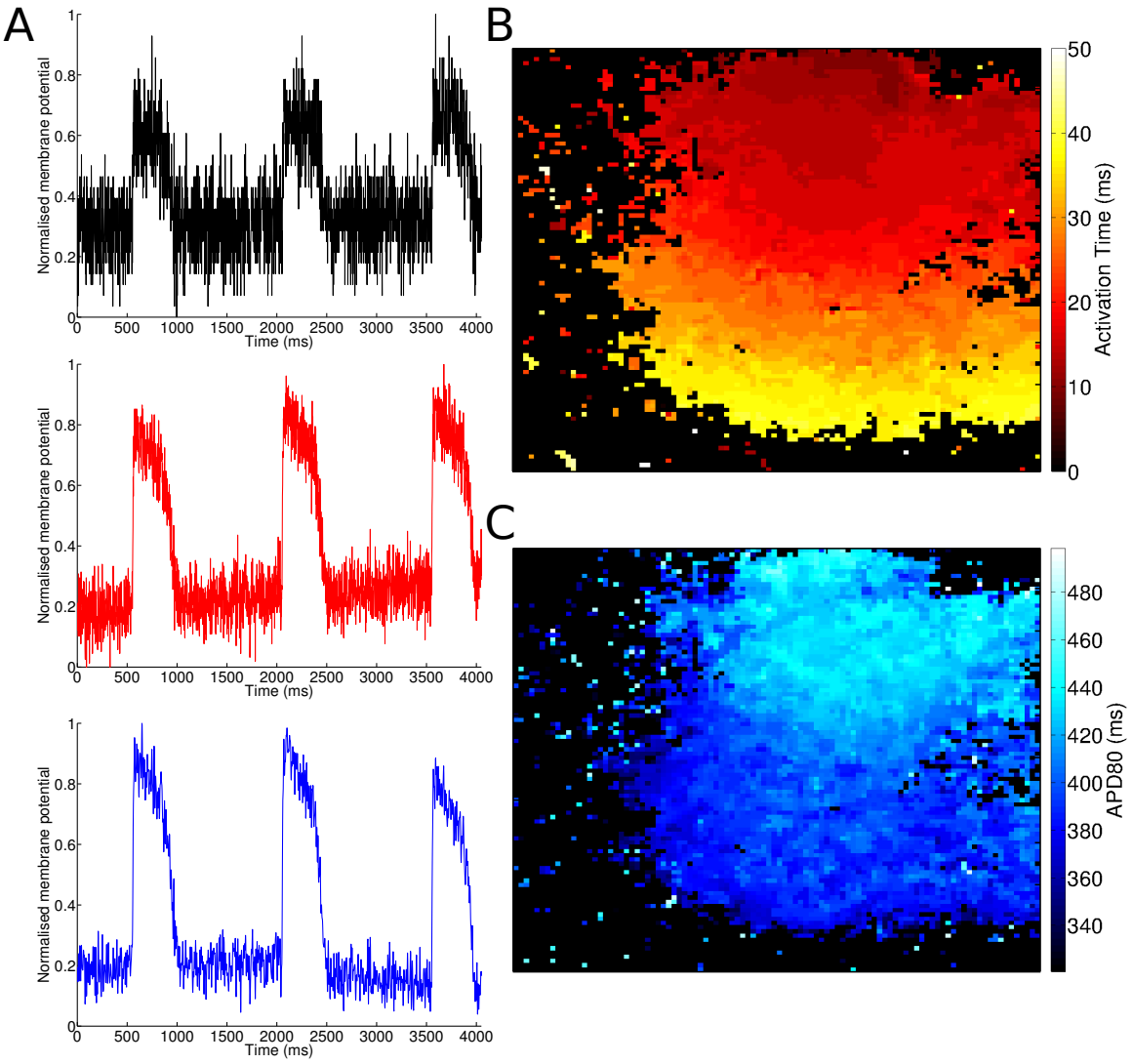

Figure 2.6: **Optical mapping data from raw data published by Lou et al. (2011).** A) shows membrane voltage raw data before filtering (black), after spatial filtering (red), and after spatial and temporal filtering, and drift removal (blue), according to the guidelines provided by Laughner et al. (2012). All traces have been normalised for comparison. B) A map of activation time, as determined by the time of maximum velocity of upstroke after the filtering in Fig. A). C) A map of APD80 from the same sample.

2.6 Heterogeneity and Variability

2.6.1 Structural Heterogeneity and Variability

The heterogeneity of cardiac tissue is well known. Ventricular tissue is constructed of a myriad of different cell and tissue types including myocytes, collagen sheets, blood vessels, neurons, fat, fibroblasts and Purkinje fibres. Orientation of cardiac myocytes varies through the wall of the heart (Streeter et al., 1969), commonly referred to as fibre orientation. A large degree of variability is observed in this orientation in humans (Greenbaum et al., 1981). Fibre orientation is generally reported as varying throughout the myocardium, from a helix angle of approximately 60° at the epicardium to -60° in the subendocardium. A rapid change in fibre orientation is often reported close to the epicardium that may affect conduction there (Vetter et al., 2005). The fibres themselves are then arranged loosely into sheets (Hooks et al., 2007). Furthermore, expression of connexin 43 has been shown to be spatially heterogeneous across the myocardium, providing a further source of heterogeneity in electrotonic load in the form of heterogeneous distribution of gap junctions (Poelzing et al., 2004).

As the histology slice in Fig. 2.7 reveals, the tissue itself contains gaps known as interlaminal spaces. All of these different tissue types may affect conduction and electrotonic load within the ventricles and atria. Furthermore, there exists a spatial distribution of tissue types. As shown by Pope et al. (2008), collagen is not constantly distributed throughout the heart but instead is ordered into both sheetlike structures and cords (Fig. 2.8). In rat hearts the sheets were in the endocardium and epicardium, whereas only cords were observed through the midmyocardium. A significant degree of variability was also noted between different preparations. Such transmural heterogeneities in collagen matrix organisation have been shown to provide a substrate upon which re-entry of propagating waves may occur (Engelman et al., 2010) and also contribute to bulk activation of the myocardium during defibrillation (Hooks et al., 2002). Recent developments in imaging technology have allowed the capture of some of these structural heterogeneities within a highly detailed rabbit mesh

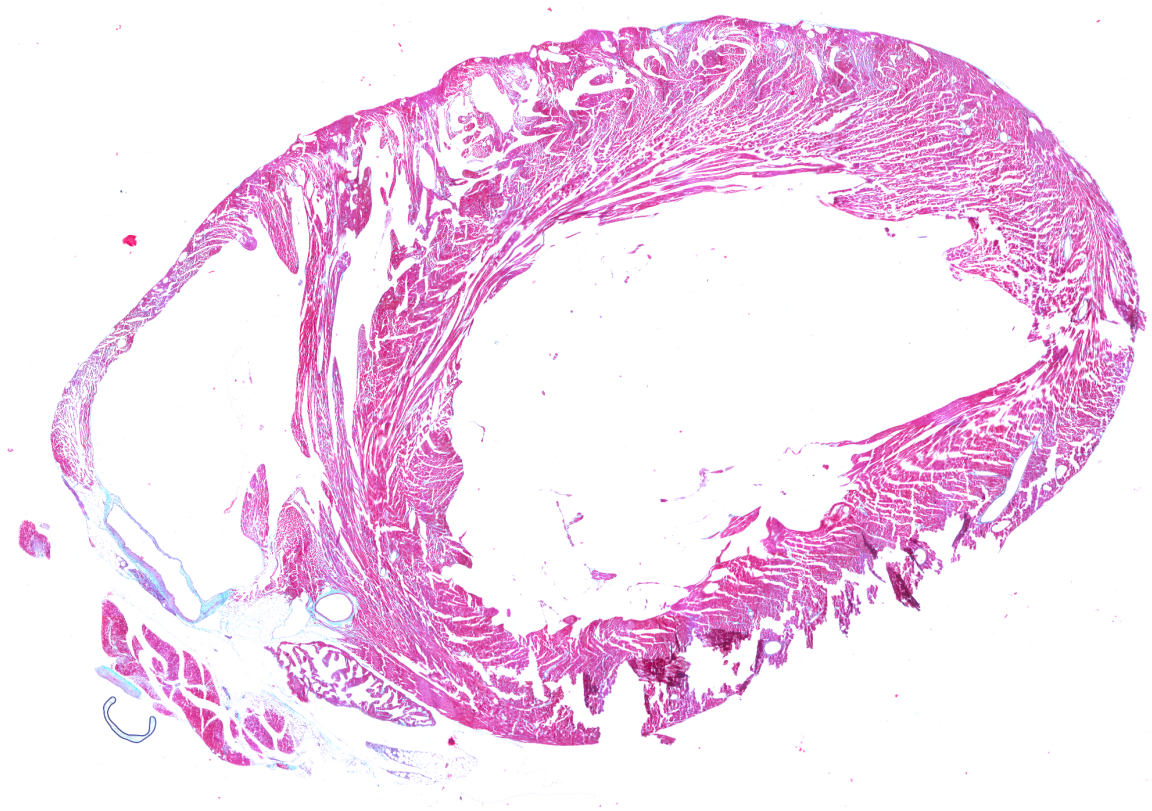

Figure 2.7: **Histology slice of a rat heart.** Interluminal spaces, blood vessels and a variety of tissue types are all shown. The size of the interluminal spaces is exaggerated due to drying out during the creation of the histology slice. The original image (down-sampled to fit this page) reaches a cellular level resolution. See Burton et al. (2006) for details of the experimental technique. Image courtesy of Dr. Rebecca Burton, Department of Physiology, Anatomy and Genetics, University of Oxford, Oxford, UK.

suitable for cardiac simulation (Bishop et al., 2010).

Not only is the structure of the heart heterogeneous, it is variable between individuals too. For example, Bordas et al. (2011) describe a large degree of variability in the structure of the free running Purkinje system between different rats, while Burton et al. (2011) note that the structure of the healthy human heart can be so variable that some individuals have a third coronary artery. Thus whilst every heart is heterogeneous, we cannot assume that each heart displays the same degree of heterogeneity. In many ways it is tribute to the remarkable plasticity and stability of development processes that, despite such variability, a functional heart can still emerge. This is before we begin to consider the range of congenital defects and pathological conditions that may negatively alter the structure of the heart.

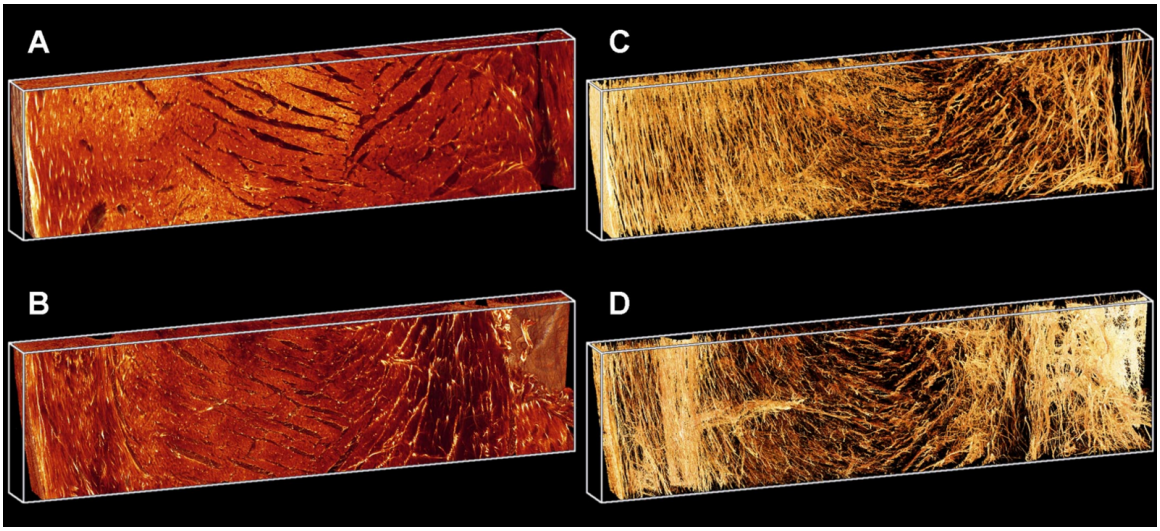

Figure 2.8: **Heterogeneity in distribution and structure of collagen through the wall of the myocardium of two rats.** Figure is from Pope et al. (2008). A) and B) show the original images from a Wistar-Kyoto and Wistar rat respectively, whereas C) and D) have low intensity tissue made transparent, revealing the structure of the collagen. The American Physiological Society does not require copyright permission for reproduction of this figure in a thesis or dissertation.

2.6.2 Electrophysiological Heterogeneity

The behaviour of cardiac myocytes through the wall of the heart both in isolation and tissue samples has been shown to be heterogeneous, producing a variety of AP morphologies often classified as endocardial, midmyocardial and epicardial in both isolated cell and tissue studies (Antzelevitch et al., 1991; Drouin et al., 1995). Most studies report a prolongation in the AP at the endocaridum as compared to the epicardium. Furthermore, there exists a difference in APD between myocytes at the apex of the heart and at the base (Rosenbaum et al., 1991; Kanai and Salama, 1995; Cheng et al., 1999; Szentandrássy et al., 2005), with apex cells typically having a prolonged action potential as compared to basal cells. The existence of a mid-myocardial cell type with a significantly prolonged APD ('M cell') has frequently been reported in the literature across a variety of species (Sicouri and Antzelevitch, 1991; Li et al., 1998), although the significance of this in the intact human heart remains a subject of fierce debate in the literature to this day (Nattel et al., 2011). Some authors report no transmural heterogeneities in intact human hearts (Taggart et al., 2001) and canine hearts (Voss et al., 2009), whilst others have demonstrated a significant

degree of heterogeneity in the transmural APD profile of non-failing human hearts using a wedge preparation (Glukhov et al., 2010). These spatial heterogeneities are not limited to just APD, with Nash et al. (2006) reporting a heterogeneous dispersion of restitution properties in the human heart *in vivo*.

Pathological conditions such as heart failure and ischæmia have also been shown to influence spatial heterogeneities in the heart. Experimental results on the subject are again frequently contradictory. Taggart et al. (2001) report a homogeneous activation recovery interval across an intact *in vivo* non-failing human heart, whereas Glukhov et al. (2010) report highly heterogeneous transmural APD in non-failing hearts, with an increase in homogeneity in explanted failing human hearts.

There is certainly a difference in methods between these sets of results, with authors reporting a lack of transmural heterogeneity using low resolution recording methods such as plunge electrodes on intact hearts, whereas those reporting large degrees of heterogeneity have preferred higher resolution methods such as patch clamps and optical mapping on tissue sections and isolated cells. These samples are under very different electrotonic and mechanical loads compared to the intact heart. A potential explanation for the discrepancy may be offered by the optical mapping experiments performed by Glukhov et al. (2010), Lou et al. (2011), and Glukhov et al. (2012) in human left-ventricular wedge preparations. They report the existence of 'islands' of dramatically prolonged APD in the midmyocardium in some (but not all) non-failing left ventricular wedges. This phenomenon has also been reported in the canine left ventricle (Akar et al., 2002). Thus it may be that either the plunge electrode experiments missed these islands, or that they are only present in a subset of the population. Equally well, it has not been conclusively demonstrated that these 'islands' share the properties of the mid-myocardial cells reported by Sicouri and Antzelevitch (1991), or that the origin of the prolongation results from heterogeneity in ionic currents in the myocytes.

The above notwithstanding, it is clear that whatever their significance there exist differences in behaviour of ventricular myocytes that have been isolated from the coupled

environment that depends on their transmural location. One cause appears to be the heterogeneous distribution of currents within the ventricles. In particular, the outward transient current I_{to} is frequently reported as being larger at the epicardium than the endocardium, resulting in a more pronounced notch in the AP morphology at the epicardium. Transmural gradients in I_{Ks} are also often reported with a reduced current towards the endocardium, consistent with the longer action potentials reported there. The expression of mRNA transcripts encoding subunits associated with these ion channels has also been shown to be spatially heterogeneous (Li et al., 1998; Soltysinska et al., 2009). These phenomena may therefore be responsible for a substantial degree of variability between electrophysiological recordings at a variety of scales, depending on the location at which they are taken from in the heart.

So, why do these heterogeneities matter? Enhanced dispersion of repolarisation across the surface of the heart is thought to coincide with a vulnerability to ventricular arrhythmias in human (Chauhan et al., 2006) and rabbit (Brunner et al., 2008). Akar and Rosenbaum (2003) report that a high degree of transmural heterogeneity in canine wedge preparations provides a substrate for arrhythmogenesis in a model of heart failure. This is in contrast to the findings of Glukhov et al. (2010) that suggest increased transmural homogeneity in human hearts resulting from prolongation of the AP at the epicardium only. Thus, the *in vivo* significance of the heterogeneities reported could be profound in terms of vulnerability to arrhythmia. It has also been suggested by Katz and Katz (1989) that the heterogeneity in electrophysiological properties of the heart may be required for its synchronous contraction. In light of this theory, it is not the heterogeneities themselves that are dangerous; rather, either their response to pathological conditions or their exaggeration in response to pharmaceutical intervention renders them dangerous.

2.6.3 Inter-Sample Variability

As mentioned above the experiments of Glukhov et al. (2010), Lou et al. (2011) and Glukhov et al. (2012) demonstrate a considerable degree of variability between different

samples from the same population. These studies each report that some, but not all, non-failing human left ventricular wedges exhibited the island behaviour. In any case, they reported a large range in the APD within the failing samples and within the non-failing samples. Indeed, individual samples within the two populations are in general far more different than the two populations considered as a whole. Thus, it seems that we may reasonably talk about variability in heterogeneity between different hearts within a population, which may affect an individual's propensity to arrhythmia in response to pharmaceuticals or pathological remodelling.

It is worth noting that variability is reported between isolated cells, even from what is ostensibly the same location of the same heart, as shown in the two guinea pig ventricular myocytes in Fig. 2.4, isolated from the endocardium at the apex of the heart. These cells display very different APDs despite the similarity in their original locations. A potential source of this difference is damage caused to the cells during the isolation procedure, which has been shown to affect the number of functional ion channels present (Yue et al., 1996). However, it is also possible that the cells were simply different before isolation. This leads to the concept of 'repolarisation reserve', first introduced by Roden (1998). This is the concept that, under normal conditions, a number of currents contribute to the repolarisation of the cell, including I_{Kr}, I_{Ks}, I_{CaL}, I_{NaL} and I_{NaCa}. Thus, in normal circumstances damage or blockade of a strong repolarisation current such as I_{Kr} should not lead to dramatic prolongation of the action potential as repolarisation is achieved through alternative mechanisms. However, in cells where this repolarisation reserve is compromised through pathology, mutation, or pharmaceutical action, or simply through inter-individual variability, the response of the cell to the reduction or loss of one repolarisation may be pronounced (Roden and Abraham, 2011).

In the intact heart, we would expect coupling between cells to reduce this inter-cell dispersion dramatically as shown by the isolated cell coupling experiments of Zaniboni et al. (2000), who demonstrated that when two cells with different APs were coupled together, their APDs became similar, and furthermore the longer AP was preferentially shortened.

Hence, the coupling of the myocardium may smooth out local differences in elecrophysiological properties between cells, which still allows for a spatial variation in response to differing mean behaviour throughout the ventricles. Pathological conditions such as ischæmia, which reduce inter-cellular coupling, could then cause the re-emergence of such phenomena.

There are other potential causes of electrophysiological variability between samples. We have already seen that heart failure may affect the heterogeneities reported across the ventricular wall in humans, further reviewed by Holzem and Efimov (2012). A wide range of genetic mutations, such as those in KCNQ1 (a subunit of channels making up I_{Ks} that is associated with Long QT syndrome type 1), can contribute to changes in AP behaviour and therefore will increase variability between samples at a population level if they are not screened and separated into a control group. Similarly, a growing body of evidence from animal models suggests that gender differences in calcium handling and the density of I_{Kr} and I_{K1} may underlie the gender differences reported in gender-related susceptibility to arrhythmia and sudden cardiac death (James et al., 2007). In particular, testosterone has been shown to increase the density of I_{Kr} and I_{K1}, suggesting a hormonal basis for this difference. Recently, mRNA expression studies have investigated whether such ionic differences extend to humans, with mixed results. Gaborit et al. (2010) report changed expression in a number of transcripts encoding subunits of repolarising currents, whereas Ambrosi et al. (2013) report no differences in the ventricles, but a large difference between atrial transcripts. Circadian rhythm has also been repeatedly reported as a source of variability in parameters such as heart rate and recent mRNA studies have begun to suggest a potential cellular or ionic basis for this (Bray et al., 2008; Jeyaraj et al., 2012).

2.6.4 Beat-to-Beat Temporal Variability

Beat-to-beat variability of repolarisation (BVR) in the heart manifests itself at various levels. Single cell beat-to-beat variability in APD (Zaniboni et al., 2000), beat-to-beat dispersion of repolarisation in tissue (Hondeghem et al., 2001), and variability in the QT interval at

the ECG level (Thomsen et al., 2004) have all been reported. This beat-to-beat temporal variability is distinct in concept from variability that may arise over longer time scales due to phenomena such as hormonal action, circadian rhythms and aging. It is a distinct difference between the APD or QT interval resulting from subsequent activations of the cell or tissue. However, unlike the short-long APD characteristic of alternans, this temporal variability is apparently random (Johnson et al., 2010).

BVR is typically characterised through the use of Poincaré plots (Brennan et al., 2001), where the quantity of interest in this context (APD, monophasic activation-recovery interval or QT interval) at one beat is plotted against the value at the subsequent beat for all recorded beats in the series, resulting in a cloud of points. The area of this cloud of points is then used as a measure for the degree of BVR. Fig. 2.9 shows Poincaré plots from isolated canine ventricular myocytes under conditions of pharmaceutical blockade and β-adrenergic stimulation (Johnson et al., 2010).

At each scale, a variety of hypotheses exist to explain such phenomena, including chaotic (but deterministic) dynamics existing within the propagation of waves around the heart, spontaneous calcium release from the sarcoplasmic reticulum, and stochastic ion channel gating. It is at present unclear to what extent the beat-to-beat phenomena described here are multi-scale. It has been established for some time that an increased beat-to-beat variability in the QT interval in response to a particular pharmaceutical intervention is associated with an increased risk of Torsades de Pointes and sudden cardiac death (Kääb et al., 2003; Hinterseer et al., 2010). More recently, an increased BVR in isolated myocytes has been demonstrated to be an effective biomarker for Torsadogenic risk in response to pharmaceutical intervention (Johnson et al., 2010). It remains unclear as to whether the same cellular mechanisms underlie these two biomarkers of pharmaceutical arrhythmogenic risk, or whether they work through different mechanisms. Both may be surrogate markers for a different mechanism, or enhanced cellular BVR may directly cause QT-level BVR. At present, it is unknown why either phenomena is correlated with arrhythmic risk, although a potential explanation would be an increase in dispersion of repolarisation

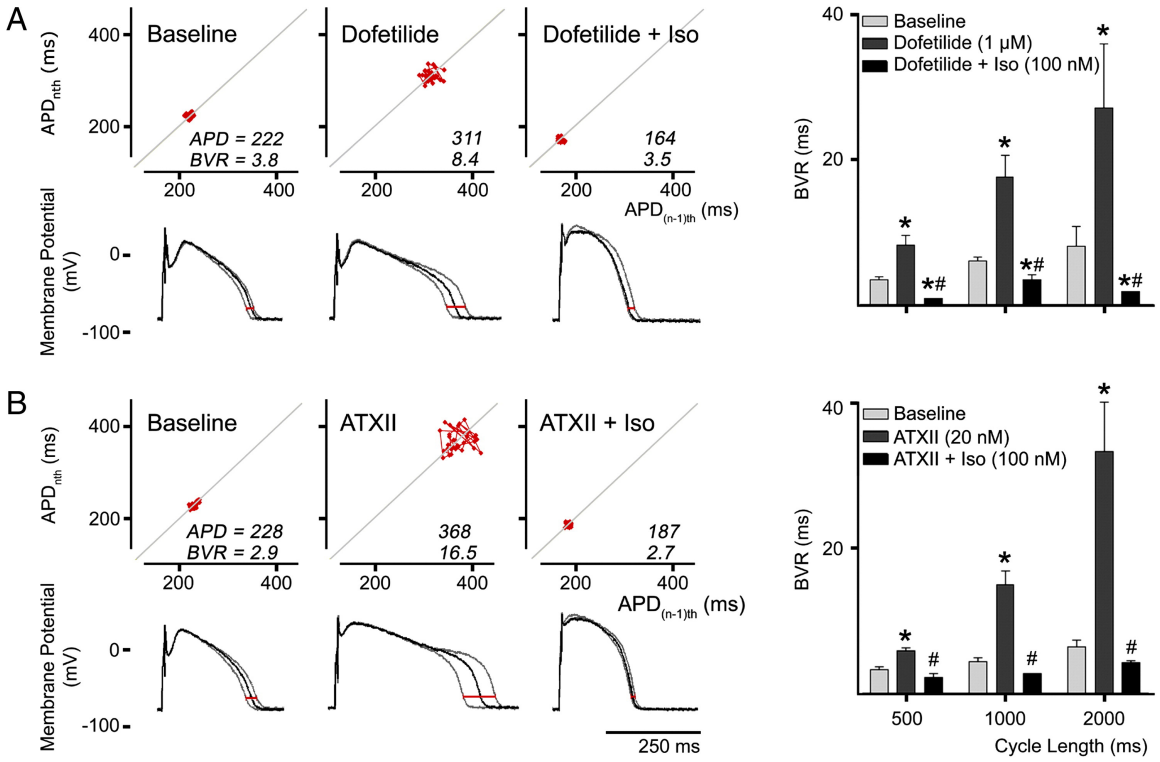

Figure 2.9: **Enhancement of beat-to-beat variability of repolarisation in response to pharmaceutical intervention.** A) shows increased BVR in response to blockade of I_{Kr} with Dofetilide, and subsequent reduction when treated with Isopreternol. B) shows the same effects when I_{NaL} is enhanced with ATXII. Reprinted from Journal of Molecular and Cellular Cardiology, Vol 48(1), D.M. Johnson, J. Heijman, C.E. Pollard, J-P. Valentin, H.J.G.M. Crijns, N. Abi-Gerges and P.G.A. Volders, I_{Ks} restricts excessive beat-to-beat variability of repolarization during beta-adrenergic receptor stimulation, Pages 122–130, Copyright (2010), with permission from Elsevier.

creating an arrhythmogenic substrate.

2.7 Experimental Data Summary

Having presented a review of experimental evidence for variability in cardiac electrophysiology we now quickly summarise the multi-scale nature of the experimental data used throughout this thesis for both model construction and model assessment.

- **Chapter 5: Prediction of Electrophysiological Changes in Heart Failure Based on mRNA Expression Data.** We use mRNA expression data gathered from failing and non-failing human hearts (Ambrosi et al., 2013) for model construction. We then conduct a literature review on comparative studies of electrophysiological remodelling

in failing and non-failing human ventricular electrophysiology. The findings of this review are presented in Appendix A. The findings of the literature review are compared to model predictions.

Chapter 6: Properties of Phenomenological Cell Models. We use patch clamp AP data from four guinea pig left ventricular myocytes for fitting model morphology. Two of the guinea pig myocytes are from the apex of one heart, and two are from the base of a different heart. We then use a sequence of 50–100 APs from each cell in order to produce four cell specific models of BVR.

Chapter 8: Sample-Specific Fitting of Conductivity Tensors from Human Optical Mapping Recordings. We use optical mapping recordings from three non-failing and three failing human left ventricular wedges, published by Lou et al. (2011). We use experimentally recorded activation times to construct sample specific models of human wedges. We then compare the quality of fit to structural information from wedge photographs.

2.8 Conclusion

In this chapter, we have reviewed evidence for variability in the behaviour in the AP from ventricular myocytes. It is worth noting that the review presented above has focussed predominantly on ionic mechanisms. There are a number of other important mechanisms worth mentioning which may also contribute to variability observed between different recordings. In particular, sympathetic and parasympathetic activation of cardiac tissue will modulate cardiac excitation and electrophysiology. Understanding the variability apparent in experimental data is crucial both for the development of mathematical models of cardiac electrophysiology, and the interpretation of their findings. More broadly, understanding variability will impact physiological and clinical understanding of propensity to arrhythmia. As we shall see in Chapter 3, research on systematic computational modelling taking variability into account has only just begun. Furthermore, the high degree of variability between

electrophysiological recordings raises major questions as to how, or indeed whether, computational models can be used in ways other than the basic testing of mechanisms.

Chapter 3

Modelling Variability in Cardiac Electrophysiology

3.1 Introduction

In Chapter 2, we have seen experimental evidence for inter-cell and beat-to-beat variability in the AP. Variability is difficult to explore within an experimental framework due to its multi-scale nature. Computational models offer a way to integrate information between scales and probe the consequences of this variability. This chapter begins with a summary of the important role of computational modelling in cardiac electrophysiology (Section 3.2). We then describe biophysically detailed computational models of the AP in Section 3.3. We include a more detailed description of a recent human ventricular model used later in this thesis in section 3.4 (O'Hara et al., 2011). We also discuss methods for parameterising biophysically detailed models in Section 3.5. Models of this kind are electrotonically coupled in tissue in order to allow investigation of multi-scale effects. We describe the monodomain and bidomain models for the propagation of the AP in Section 3.6. We then discuss phenomenological models also used to study the propagation of the AP in Section 3.7.

Having comprehensively introduced techniques used for cardiac electrophysiology mod-

elling, we are now in a position to discuss how computer simulation has helped to address the issue of variability in cardiac electrophysiology to date in Section 3.9. In sub-section 3.9.2, we discuss how the consequences of spatial heterogeneities in cell distribution have been addressed by a successful combination of simulation and experiment. In sub-section 3.9.3 we explore how the concept of a population of models has been used to investigate the consequences of inter-cell variability. Finally, we discuss modelling efforts to date in addressing the issue of BVR in sub-section 3.9.4.

3.2 The Role of Modelling in Cardiac Electrophysiology

Simulation has been combined with experimentation in the study of electrophysiology since the 1950s (Hodgkin and Huxley, 1952d; Noble, 1960). In its early years, computational modelling served both as a tool for integrating experimental findings, and understanding the generation of the AP. The value of computational models has often proved to be when they failed to predict an experimental phenomenon, thereby pointing the way to deficiencies in contemporary knowledge of ionic currents (Noble, 2011).

Models of cardiac electrophysiology initially took the form of single-cell membrane potential models but have now expanded to a plethora of different scales, from simulations of electrical activity in the whole heart within the whole body (Zemzemi et al., 2012), down to the molecular dynamics of ion channels (Silva et al., 2009). Many of these models may legitimately claim to be multi-scale, incorporating sub-cellular processes and complex ion channel gating within a model of membrane electrophysiology, together with structural information at the whole heart level, such as fibre orientation and spatial distributions of myocyte properties (Potse et al., 2006).

Several important discoveries in cardiac electrophysiology have been due in large part to the combination of computational modelling and experiment (Noble, 2011), such as the stochiometry of the Na^{+}/Ca^{2+} exchanger, explanation of the impact of heterogeneities in cell behaviour on the morphology of the T-wave (Gima and Rudy, 2002) and the role of

virtual electrodes in the failure of arrhythmia termination during defibrillation (Efimov et al., 2000). Whole-heart models have allowed investigation of the dynamic maintenance and break-up of cardiac arrhythmias, both in homogeneous and heterogeneous tissue, providing insight into the effects of cardiac memory and restitution that cannot currently be gained through experiment (Trayanova, 2011).

Computational cardiac electrophysiology is an increasingly mature field, to the extent that studies have recently shown predictive properties useful in, for example, stratifying arrhythmic risk as a result of channel mutation in type 1 long-QT syndrome (Hoefen et al., 2012), or for predicting the arrhythmogenic potential of drugs (Mirams et al., 2011). Thus, computational simulations are beginning to translate from the field of basic physiology into clinical and drug development pipelines.

3.3 Biophysically Detailed Models

The mathematical modelling of cardiac cells is based upon the theory of excitable membranes with its mathematical foundations in the epoch making work of Alan Hodgkin and Andrew Huxley. In their work, Hodgkin and Huxley used the newly developed voltage clamp technique to ascertain the magnitudes and gating kinetics of the transmembrane currents present during the AP of the squid giant axon (Hodgkin and Huxley, 1952a,b,c; Hodgkin et al., 1952). This stage of the work utilised new techniques (the voltage clamp) to develop a theory of membrane voltage gated channels allowing ions to flow across the cell membrane. Furthermore, the authors were able to develop a mathematical framework that we know today as the Hodgkin-Huxley equations for this voltage dependent gating, and use these in conjunction with their experimental data to reconstruct the APs they originally observed, as well as their propagation along the axon (Hodgkin and Huxley, 1952d). Thus, not only had they proposed a theory for the generation of the AP, they had demonstrated its plausibility through a mathematical model based upon their own experimental data. That modern authors have been able to demonstrate only slightly better fits to the original data

through improvements to the equations and parameter fitting technique (Clay et al., 2008) emphasises just how well the original model was conceived.

The Hodgkin-Huxley model for the flow of charged ions across an electrically excitable cell membrane is described below. The original model is based on cable theory, and so also contains a spatial diffusion term to describe propagation of the electrical signal along the neuron. This is not a property seen in cardiac isolated cell models but it does have an analogue in the bidomain and monodomain equations in Section 3.6. We do not discuss this here. The model treats the neuron as a cable whose membrane acts as a capacitor. Specifically, the total current across the membrane (in the absence of flow along the cable) is described as

$$I_{tot} = C_m \frac{dV}{dt} + I_{ion}, \tag{3.1}$$

where V is the membrane potential[1], C_m the membrane capacitance, $C_m \frac{dV}{dt}$ is the capacitative current and I_{ion} is the current due to flow of charged ions across the membrane. The Hodgkin-Huxley model considers three ionic currents, sodium, potassium, and a 'leakage' current consisting of chloride and other ions. Each ionic current reverses either side of its Nernst potential (V_{Na}, V_K, V_l), and is proportional to a conductance G across the cell membrane as follows

$$I_{ion} = I_{Na} + I_K + I_l, \tag{3.2}$$

$$I_{Na} = G_{Na}(V)(V - V_{Na}), \tag{3.3}$$

$$I_K = G_K(V)(V - V_K), \tag{3.4}$$

$$I_l = \bar{G}(V - V_l). \tag{3.5}$$

Crucially, whilst the conductance of the leakage current is constant, the conductances of I_{Na} and I_{K} are functions of the membrane potential. Non-dimensional variables m,h and

[1]Note that Hodgkin and Huxley defined V as the difference between the membrane potential and the rest potential, unlike many of the later models in this chapter

n taking values between 0 and 1 were introduced, themselves functions of membrane voltage, in order to scale the conductances. Since the activation of these channels were voltage dependent, so are the 'rate constants' given in the model,

$$G_{Na} = \bar{G}_{Na} m^3 h \tag{3.6}$$

$$\frac{dm}{dt} = \alpha_m(V)(1-m) + \beta_m(V)m \tag{3.7}$$

$$\frac{dh}{dt} = \alpha_h(V)(1-h) + \beta_h(V)h \tag{3.8}$$

$$G_K = \bar{G}_K n^4 \tag{3.9}$$

$$\frac{dn}{dt} = \alpha_n(V)(1-n) + \beta_n(V)n \tag{3.10}$$

The activation and inactivation parameters α and β are given functional forms as follows following parameterisation based on voltage clamp experiments,

$$\alpha_m = \frac{0.1(V+25)}{\exp\left(\frac{V+25}{10}\right) - 1}, \tag{3.11}$$

$$\beta_m = 4\exp\left(\frac{V}{18}\right), \tag{3.12}$$

$$\alpha_h = 0.07\exp\left(\frac{V}{20}\right), \tag{3.13}$$

$$\beta_h = \frac{1}{\exp\left(\frac{V+30}{10}\right) + 1}, \tag{3.14}$$

$$\alpha_n = \frac{0.01(V+10)}{\exp\left(\frac{V+10}{10}\right) - 1}, \tag{3.15}$$

$$\beta_n = 0.125\exp\left(\frac{V}{80}\right). \tag{3.16}$$

The response of this model to depolarisation of the cell membrane is shown in Fig. 3.1 A.

A common interpretation of the physical meaning of the parameters m,h and n is to view them as representing the probability of open state occupancy of independent voltage activated components of an ion channel. The probability of the channel being open is then the product of the values for each independent subunit in that channel, m^3h for I_{Na} and n^4

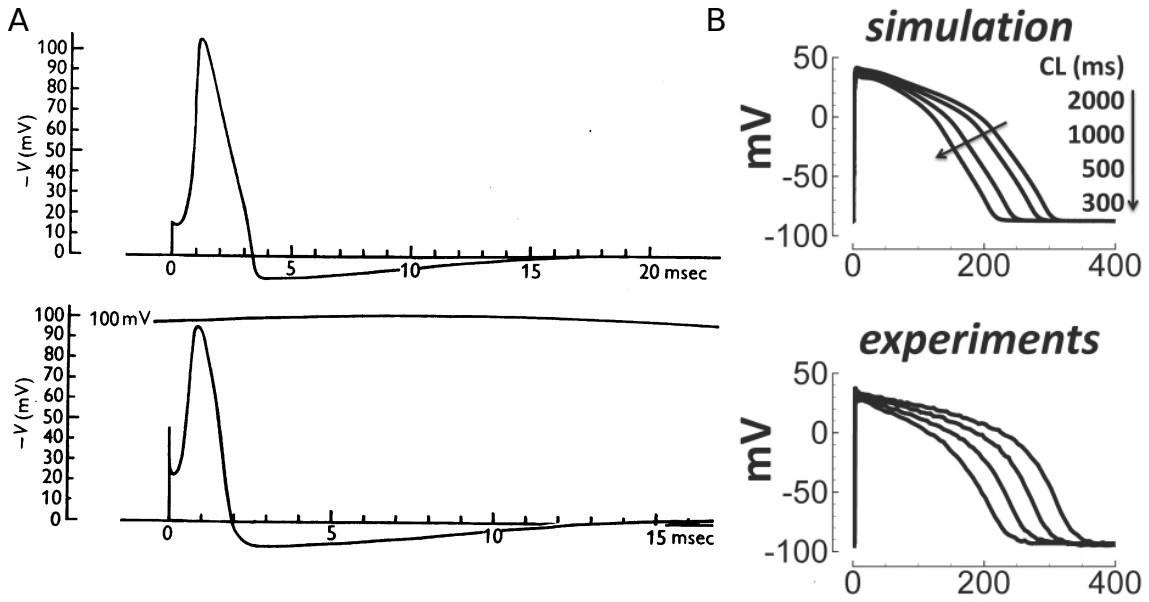

Figure 3.1: **The development of AP models over the last 60 years.** A) Neuronal APs from Hodgkin and Huxley (1952d). The top trace shows the simulated AP and the bottom trace shows an experimentally recorded AP, both with a 15mV depolarisation. Reprinted from Journal of Physiology, Vol 117, A.L. Hodgkin and A.H. Huxley, A quantitative description of membrane current and its application to conduction and excitation in nerve, Pages 500–544, Copyright (1952), with permission from John Wiley & Sons Ltd. B) Human ventricular APs taken from O'Hara et al. (2011). The top traces show simulated APs and the bottom traces show experimentally recorded APs, both at multiple pacing cycle lengths. This figure is reproduced from PLoS Computational Biology, Vol. 7, T. O'Hara, L. Virág, A. Varró and Y. Rudy, Simulation of the undiseased human cardiac ventricular action potential: Model formulation and experimental validation, Page e1002061, Copyright (2011), under the Creative Commons Attribution License.

for I_K. Under this interpretation, the above equations are equivalent to a potassium channel with four components that is open only when all four n gates are in the open position. The sodium channel has three m gates functioning to open the channel when all three are opened, as well as one h gate that, when activated, closes the channel. The offering of this interpretation by Hodgkin and Huxley is remarkable given that voltage gated ion channel proteins had not been discovered at that time.

The Hodgkin and Huxley (1952d) model forms a basis in terms of key concepts for nearly all later work done in the field of cardiac modelling, comprehensively reviewed for the years 1960 to 2001 in Noble and Rudy (2001). This review stresses the important point that often the failures of cardiac cellular models to reproduce observed experimental data have been more useful to our understanding of electrophysiology than their successful

predictions, as does Noble (2011). More up to date reviews can be found in the work of Rudy and Silva (2006), Fink et al. (2011), and Noble et al. (2012).

Following the development of a mathematical theory of excitable membranes for nerve cells, Noble (1960) demonstrated that the same mechanisms could be used to reconstruct the AP morphology of the cardiac pacemaker cell that possesses a prolonged 'plateau' phase. The Noble (1962) model took this approach a step further by showing that introducing two recently determined potassium currents could explain this phenomenon using biophysically realistic current magnitudes. From these papers it was concluded that the theory presented by Hodgkin and Huxley (1952d) was capable of explaining the AP observed in cardiac pacemaker and Purkinje cells, the cell types for which experimental data were available at the time. McAllister et al. (1975) published an extended model incorporating new experimental information on the voltage dependent components of the potassium current. This model successfully reconciled several apparently paradoxical experimental results but contained a major flaw in that it had both the voltage activation and direction of what is now known as the 'funny' or pacemaker current totally wrong (Noble and Rudy, 2001). The effects of this inward potassium and calcium current, activated by hyperpolarisation of the cell membrane, were instead attributed to a depolarisation activated outward potassium channel I_{K2}. Analysis of this problem revealed inconsistencies between current behaviour and the known accumulation of ions in the extracellular space, prompting the development of later models containing dynamic ion concentrations (DiFrancsesco and Noble, 1985). Modelling efforts in Purkinje fibres continue, with new models of human and rabbit Purkinje (Sampson et al., 2010; Corrias et al., 2011).

The first model of a ventricular myocyte was produced by Beeler and Reuter (1977) based upon the Hodgkin and Huxley (1952d) and McAllister et al. (1975) models. This model successfully reproduced many of the properties of the ventricular action potential but lacked many important details, most notably ionic exchangers and intracellular calcium handling. In light of new experimental data from single channels and patch clamps, the Luo-Rudy model was developed (Luo and Rudy, 1991, 1994a,b). The model was devel-

oped in two phases, known as the Luo-Rudy I (or passive) model (Luo and Rudy, 1991) and the Luo-Rudy dynamic model (Luo and Rudy, 1994a,b). In the passive model, the intracellular ionic concentrations of K^+ and Na^+ are clamped, with intracellular Ca^{2+} able to vary. The included inward currents were the fast sodium current I_{Na}, a slow inward current I_{si} and a background current I_b. Outward currents are the delayed rectifier potassium current I_K, the inward rectifier potassium current I_{K1} and a plateau potassium current I_{Kp}. The conductances of I_K and I_{K1} depended upon the square root of the (clamped) concentration of K^+. The dynamic model extended this framework by unclamping K^+ and Na^+ concentrations. This required the addition of ionic pumps and exchangers, and the buffering of Ca^{2+} in both the myoplasm and sarcoplasmic reticulum. The slow inward current I_{si} was also identified with the L-type calcium current I_{CaL} and reformulated, building on channel kinetics from the Rasmusson et al. (1990) bullfrog atrial cell model. Additionally, processes handling the intracellular calcium concentration were incorporated into the model, including uptake of calcium into the network sarcoplasmic reticulum, buffering of calcium ions in both the cytoplasm and the sarcoplasmic reticulum, and release of calcium from the junctional sarcoplasmic reticulum. Zeng et al. (1995) extended the dynamic model to include formulations of the rapid and slow components of the repolarising potassium current, I_{Kr} and I_{Ks}. Further development of the model incorporating features such as spatial co-localisation of I_{CaL} and ryanodine receptors followed (Jafri et al., 1998). This was not the first model to represent subcellular calcium handling (Hilgemann and Noble, 1987; Earm and Noble, 1990) but it was the most detailed at the time and many of its features have been inherited into the 'modern' models used today.

The Luo and Rudy (1994a) model has formed the foundation of almost all subsequent biophysically detailed models of ventricular myocytes. The development of many previous modelling frameworks continued however, with Noble et al. (1991) producing a guinea pig ventricular model roughly concurrently with the original Luo-Rudy model. Development continued with the Noble et al. (1998) and Noble and Noble (2001) models. It is instructive that a major reason that Luo-Rudy type models have been so widely used over the last

twenty years is that the source code has always been freely available to download and use. This was not the case with the Noble models when they were released, although they are now freely available in the CellML repository (Lloyd et al., 2008). Ventricular models are now available for a wide variety of mammalian species, including guinea pig (Zeng et al., 1995; Jafri et al., 1998; Noble et al., 1998; Noble and Noble, 2001; Faber et al., 2007), mouse (Bondarenko et al., 2004; Li et al., 2010; Land et al., 2012), rat (Pandit et al., 2001; Wang and Sobie, 2008), human (Priebe and Beuckelmann, 1998; Iyer et al., 2004; Ten Tusscher et al., 2004; Ten Tusscher and Panfilov, 2006; Grandi et al., 2010; Carro et al., 2011; O'Hara et al., 2011), dog (Winslow et al., 1999; Fox et al., 2002; Cabo and Boyden, 2003; Hund and Rudy, 2004; Decker et al., 2009) and rabbit (Puglisi and Bers, 2001; Shannon et al., 2004; Mahajan et al., 2008). A simulated AP from the O'Hara et al. (2011) model is shown in Fig. 3.1 B. There are now over 100 different models of cardiac cellular electrophysiology, briefly reviewed in Noble et al. (2012). Subcellular phenomena such as β-adrenergic signalling (Saucerman et al., 2003) and mitochondrial energetics (Cortassa et al., 2006) are sometimes also incorporated into models. It is becoming increasingly clear that with so many models available comparison between models will become important. This has been shown by the comparative studies for ventricular models of dog (Cherry and Fenton, 2007), human (Bueno-Orovio et al., 2008) and rabbit (Romero et al., 2011), which reveal sometimes large differences in behaviour between models of the same species.

A criticism of the Luo-Rudy dynamic model formulation discussed above is that at fast pacing rates it exhibits a drift in ionic concentration and transmembrane potential over long pacing times, suggesting that the model is biophysically inconsistent (Varghese and Sell, 1997). These concerns have been largely answered by Hund et al. (2001), who suggest that the reason for the discrepancy is that the charged ions carried in the stimulus current were not accounted for. Including these as potassium ions appears to remove the problem. The stimulus current applied to the cell has also been investigated, with Livshitz and Rudy (2009) proposing an alternative to the standard square wave pulse to more accurately reflect the flow of currents in an electrotonically coupled cell. Livshitz and Rudy (2009) also

proposed a method to remove discontinuities in some of the original Luo-Rudy equations that can cause issues in adaptive numerical solvers and when performing numerical analysis for tissue models, which tends to require continuous functions and derivatives.

There have been several technical innovations in modelling the behaviour of heart cells since the publication of the Luo-Rudy model. Perhaps the most prominent is the inclusion of a pseudo-Markov model of ion channel gating in response to the failure of the Hodgkin-Huxley formalism to fit the activation and deactivation processes of ionic currents. A thorough review of the gating properties of pseudo-Markov gating models is given in Rudy and Silva (2006). Under this formalism, an ion channel may inhabit a number of conformational states and the transitions between them rely upon only the current state occupancy *i.e.,* not the previous states occupied as well (the Markov property). These may then be simulated either as a stochastic discrete state Markov model or as a continuous ODE giving a pseudo-Markov model of state occupancy. These models differ crucially from the Hodgkin and Huxley (1952d) model in that the activation and inactivation processes are no longer independent of one another. Whilst such models better represent the conformational changes present in the ion channel proteins they can suffer from poor parameter identifiability and also increased computational overheads (Fink and Noble, 2009). Generally, most recent cardiac cell models will use Hodgkin-Huxley kinetics for most currents, resorting only to Markov models where either the specific gating of the channel is of relevance (such as mutation or drug block), or the kinetics simply cannot be captured through a Hodgkin-Huxley formulation. A notable exception is the Iyer et al. (2004) model of the human ventricular AP, with a Markov formulation for almost every current. A schematic illustration of the difference in structure between a Markov model and a Hodgkin-Huxley formulation can be seen in Fig. 3.2.

It is also possible to simulate the effects of drug block through either including drug binding states to a pseudo-Markov model (Clancy et al., 2007) or, more simply, through reduction in channel conductance in accordance with the drug concentration as in Mirams et al. (2011). A review of methods to incorporate drug block of ion channels in cardiac

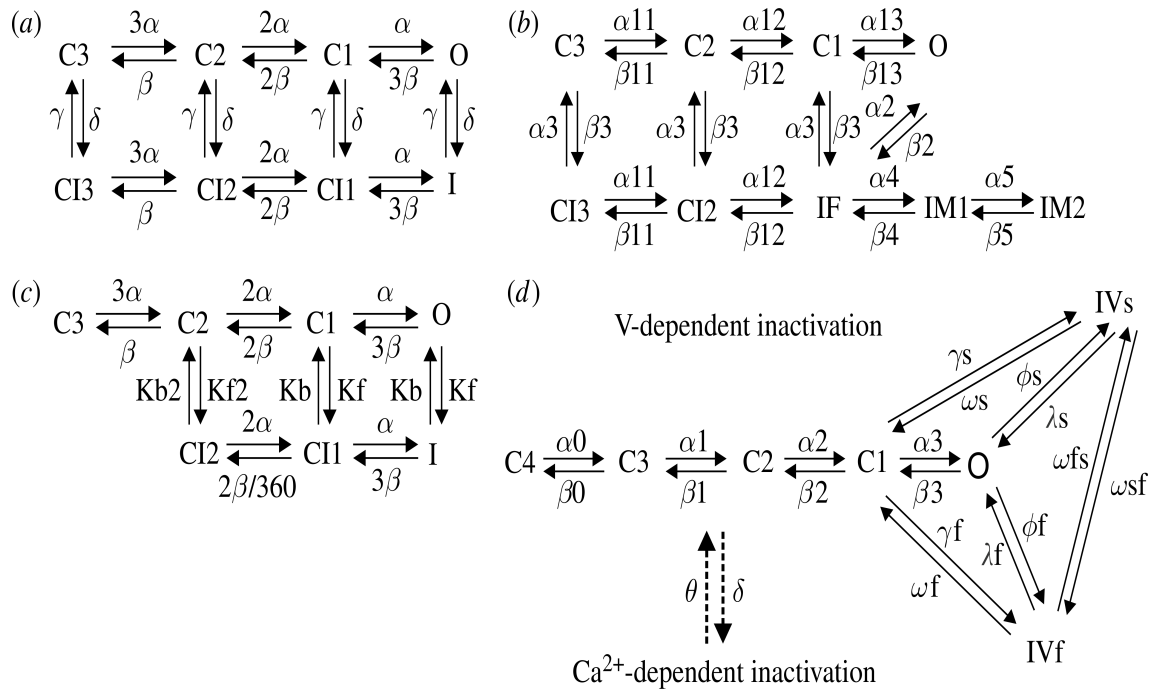

Figure 3.2: **Structure of different ionic channel formulations, taken from Fink and Noble (2009).** A) The original Hodgkin-Huxley formulation for I_{Na} (Hodgkin and Huxley, 1952d). B) A Markov model of I_{Na} (Clancy et al., 2007). C) A Markov model of I_{to} (Campbell et al., 1993). D) A Markov model of I_{CaL} (Faber et al., 2007). Reprinted from Philosophical Transactions of the Royal Society A: Mathematical, Physical & Engineering Sciences, Vol. 367, M. Fink and D. Noble, Markov models for ion channels: versatility versus identifiability and speed, Pages 2161–279, Copyright (2009), with permission from The Royal Society.

electrophysiology is provided by Brennan et al. (2009).

3.4 The O'Hara (2011) Human Ventricular Model

Having reviewed the history of biophysically detailed ventricular electrophysiology models, we now present the model of choice used in this thesis, the O'Hara et al. (2011) (ORd) human ventricular model. The ORd model was parameterised using one of the most consistent data sets on undiseased human ventricular electrophysiology to date, recorded from over 100 human hearts by the laboratory of Prof. Andras Varró at the University of Szeged, Hungary. This motivates our usage of the model later in this thesis (Chapter 5).

A schematic of the ORd model is shown in Fig. 3.3. The overall structure of the ORd model is retained from the Decker et al. (2009) canine ventricular model, which was then

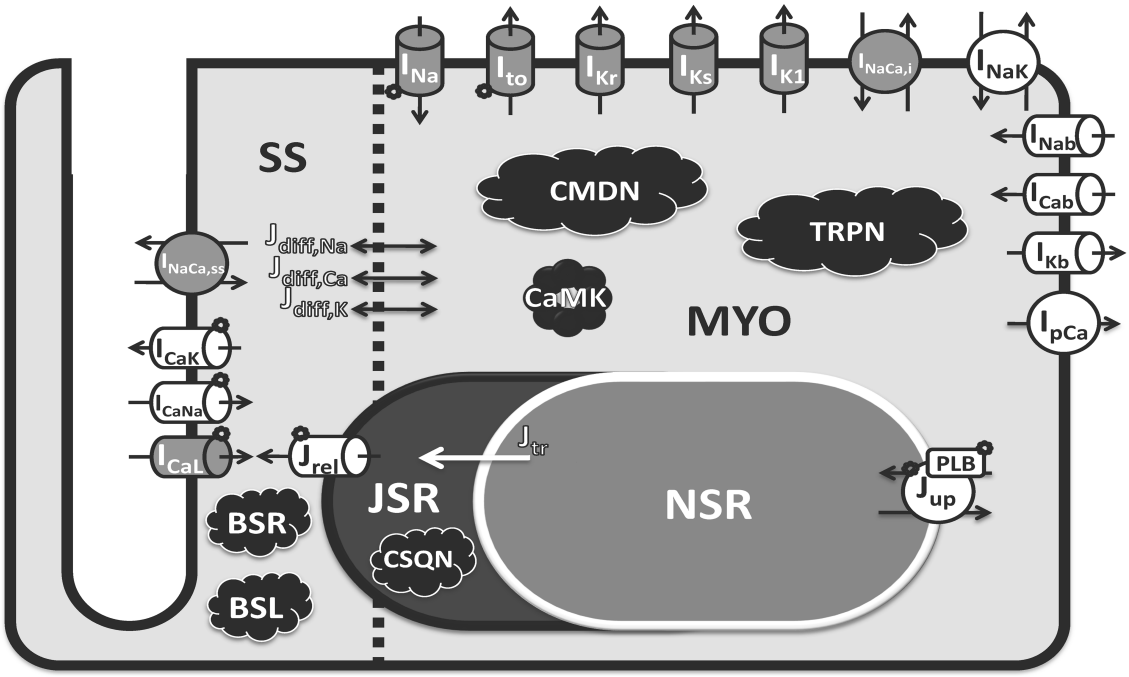

Figure 3.3: **Schematic of the O'Hara et al. (2011) human ventricular electrophysiology model.** The subspaces, currents, fluxes and calcium buffers are labelled as in the text. Currents labelled in gray were developed directly from human experimental data. This figure is reproduced from PLoS Computational Biology, Vol. 7, T. O'Hara, L. Virág, A. Varró and Y. Rudy, Simulation of the undiseased human cardiac ventricular action potential: Model formulation and experimental validation, Page e1002061, Copyright (2011), under the Creative Commons Attribution License.

modified and parameterised based on both new experimental data and values taken from the literature. Specifically, the model presents reformulations of I_{CaL}, I_{Kr}, I_{to}, I_{K1} and I_{NaCa} in response to new experimental data produced for model construction. I_{Ks}, I_{Na}, and I_{NaK} were also reformulated based on human experimental data from the existing experimental literature.

The ORd model features a detailed description of sub-cellular calcium handling. There are four compartments within the model, the myoplasm (myo), the junctional sarcoplasmic reticulum (JSR), the network sarcoplasmic reticulum (NSR) and the T-tubular subspace (SS). Calcium is released from the JSR in response to I_{CaL} through the ryanodine receptor release flux (J_{rel}). Uptake of calcium into the NSR through SERCA (J_{up}) is inhibited by unphosphorylated phospholamban (PLB). Phosphorylation of PLB and J_{up}, as well as several other currents and fluxes is controlled by calmodulin-dependent protein kinase II (CaMK)

is also included in the model.

The formulation of the model is too long to describe in full here, and can be found in the supplementary material provided by O'Hara et al. (2011). The model is parameterised and primarily validated using data from endocardial cells. Epicardial and midmyocardial versions of the model are then derived by rescaling the conductances of I_{to}, the late component of I_{Na}, I_{Kr}, I_{Ks}, I_{k1}, I_{NaCa}, I_{NaK} and the background potassium current I_{Kb}, the permissivity of I_{CaL} to calcium, sodium and potassium, and maximum fluxes of J_{rel} and J_{up}. Ratios of transmural mRNA expression are used to determine the scaling of the currents. The time constant of inactivation of I_{to} is also reformulated in the epicardial cell model.

3.5 Parameterisation of Cardiac Cell Models

A key factor in the construction of the cardiac cell models in section 3.3 is the determination of the parameters used within the model. Ideally, these parameters are determined from experimental traces, but they may also be either inherited from earlier models, or set through trial and error to produce a desired behaviour in the model output. Parameter estimation for cardiac cell models is a topic of considerable debate in the scientific literature. In this review methods in use for fitting the currents to models of the single cell will be discussed. Proposed methods will be reviewed for both cardiac cells and the related problem of the excitable membrane of the neuron. Finally alternate methods for parameter fitting to such models will be considered. Due to the inherent complexity of the ionic currents that form the AP across the cell membrane, state of the art models consist of large numbers of ordinary differential equations, and consequently a huge number of parameters to be estimated, often with incomplete experimental data. By way of example, the Iyer et al. (2004) model of a human ventricular myocyte contains sixty-seven different variables.

Given a lack of species-specific kinetic data it is often necessary to re-use model components when developing new models. This process can lead to inconsistencies between models where the same components from different models do not produce identical results

when interchanged between different models of what is ostensibly the same cell type as discussed above (Cherry and Fenton, 2007; Bueno-Orovio et al., 2008; Niederer et al., 2009; Romero et al., 2011). Niederer et al. (2009) examined the data sources for parameters used in two state of the art models of a human ventricular myocyte (Ten Tusscher et al., 2004; Iyer et al., 2004) and found that the parameters used were estimated from data for human, guinea pig, sheep, bullfrog, rabbit and mouse cells across a wide range of temperatures and experimental conditions. An encouraging development on this front is the recent publication of the O'Hara et al. (2011) model of the undiseased human ventricular myocyte (see Section 3.4). This represents a major step forward as the authors used what is probably the most consistent dataset to date: human data produced at the University of Szeged in Hungary over a period of about twenty years. It is worth noting that another potential source in the differences between models describing the same cell type may lie in the variability that occurs between individuals within a species as described in Chapter 2. In this sense, models displaying different properties need not be wrong, or even mutually exclusive. They may instead represent different aspects of the considerable variation observed within the experimental literature. Understanding how we model such variation will form an important theme throughout this thesis.

Population level variability notwithstanding, it is clear that our usage of the available experimental data must extract as much of the available information as possible. Efforts to fit data to models may then be further compounded by problems with parameter identifiability. This may take two forms — *a priori* unidentifiability whereby multiple parameters may give the same solution to an equation and numerical unidentifiability that can depend upon both the quality of the experimental data and the ability of the parameter identification technique to converge through the parameter space (Fink and Noble, 2009).

The original methods for fitting cardiac models begin in the neuron with the seminal paper of Hodgkin and Huxley (1952d). In this paper the authors attempted to demonstrate that the experimental results recorded in earlier papers could explain the observed propagating wave of transmembrane voltage perturbation following stimulation of the giant axon

of the squid. We briefly describe Hodgkin and Huxley's original method to fit parameters to the sodium channel equations Eqs. (3.6)–(3.8).

Solving Eqs. (3.7) and (3.8) for fixed V gives

$$m = m_\infty - (m_\infty - m_0)\exp\Big(\frac{-t}{\tau_m}\Big), \tag{3.17}$$

$$h = h_\infty - (h_\infty - h_0)\exp\Big(\frac{-t}{\tau_h}\Big), \tag{3.18}$$

$$\tag{3.19}$$

where

$$m_\infty = \frac{\alpha_m}{\alpha_m + \beta_m}, \tag{3.20}$$

$$\tau_m = \frac{1}{\alpha_m + \beta_m}, \tag{3.21}$$

$$m(0) = m_0, \tag{3.22}$$

$$h_\infty = \frac{\alpha_h}{\alpha_h + \beta_h}, \tag{3.23}$$

$$\tau_h = \frac{1}{\alpha_h + \beta_h}, \tag{3.24}$$

$$h(0) = h_0. \tag{3.25}$$

Hodgkin and Huxley then made the assumption that the timescales of activation and repolarisation are separated, and so this conductance is the maximum conductance achieved during any depolarising step. Voltage clamp experiments are then used to parameterise the model.

The parameters h_∞ and τ_h are fitted from time traces of inactivation as shown in Fig. 3.4 according to the method in Hodgkin and Huxley (1952c). The inactivation time constant $\tau_h(V)$ was determined by clamping the voltage for a variable time t and recording the ratio of the sodium current to the current at resting potential. The time constants of decay were recorded for each voltage step V and were assigned value $\tau_h(V)$, as shown in Fig. 3.4 A,B. After applying a 40ms voltage clamp, the inactivation of the sodium channel was assumed

to reach steady state. By plotting the value of the ratio of the current at rest to the current following depolarised conditioning steps, the value of the steady state curve $h_\infty(V)$ was fitted, as shown in Fig. 3.4 C,D. Typically, the parameter estimation method used was one of comparison to graphs at various conductances. Having fitted these parameters, they then set at each potential

$$\alpha_h = \frac{h_\infty}{\tau_h}, \tag{3.26}$$

$$\beta_h = \frac{1 - h_\infty}{\tau_h}. \tag{3.27}$$

Having obtained values for α_h and β_h at a range of membrane potentials, the parameters are fitted as functions of the membrane potential of the form

$$\alpha_h(V) = A_\alpha \exp\left(\frac{V}{V_\alpha}\right), \tag{3.28}$$

$$\beta_h(V) = \frac{1}{\exp\left(\frac{V+V_{\beta 1}}{V_{\beta 2}}\right) + B_\beta}, \tag{3.29}$$

$$\tag{3.30}$$

where A_α, V_α, $V_{\beta 1}$, $V_{\beta 2}$ and B_β are allowed to vary.

To fit the activation parameter m, Eqns. (3.3), (3.6), (3.17) and (3.18) give

$$G_{Na} = \bar{G}_N a m_\infty^3 h_0 \left(1 - \exp\left(\frac{-t}{\tau_m}\right)\right)^3 \exp\left(\frac{-t}{\tau_h}\right). \tag{3.31}$$

Experimental current traces recorded in response to the step protocol are shown in Fig. 3.5 A. After dividing through by a factor of $V - V_R$, traces of sodium channel conductance as a function of time in response to membrane depolarisations are obtained, shown in Fig. 3.5B. The parameters $\tau_m(V)$ and $G'_{Na}(V) = \bar{G}_{Na} m_\infty^3 h_0$ are then fitted to the traces for each depolarising step V. Since the initial step is to a known voltage, h_0 can be calculated (in fact $h_0 \approx 1$). At peak, h_0 is assumed to remain unchanged due to the slower timescale of inactivation. Thus, with the assumption that $m_\infty \approx 1$ at high depolarisations Hodgkin and

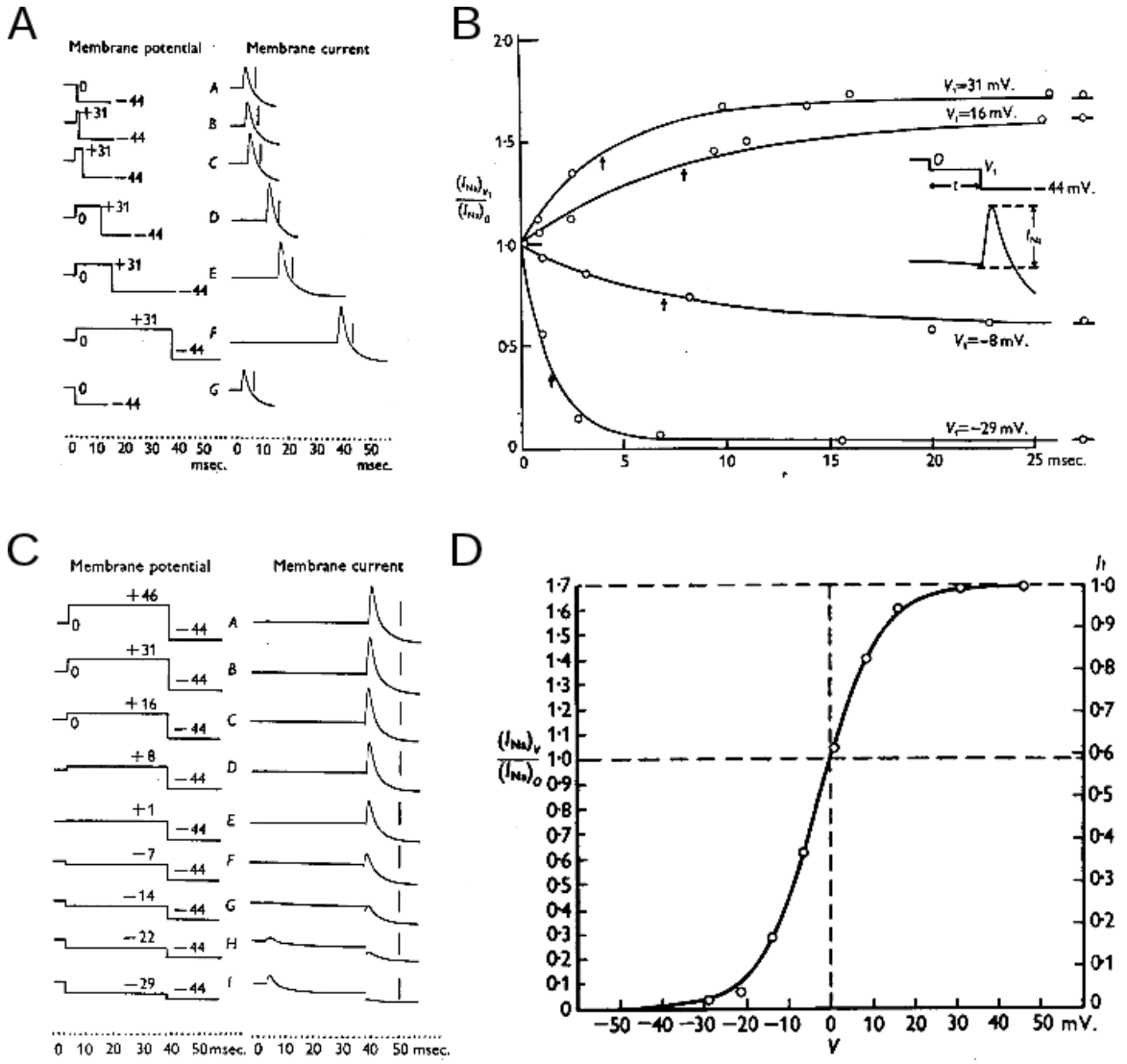

Figure 3.4: **Fitting the inactivation parameters of the sodium current in the Hodgkin-Huxley model.** A) shows the response of the sodium current to a series of voltage clamp experiments for different step times. B) The current magnitude is plotted as a ratio of the current at the step potential to the current at the rest potential step for different times. The time constant of inactivation τ_h is calculated from this curve. C) Response of a squid axon to a voltage steps of 40ms duration, reaching steady state. D) The resulting steady state $h_\infty(V)$ curve. Adapted from Journal of Physiology, Vol 116, A.L. Hodgkin and A.H. Huxley, The dual effect of membrane potential on sodium conductance in the giant axon of *Loligo*, Pages 497–506, Copyright (1952), with permission from John Wiley & Sons Ltd.

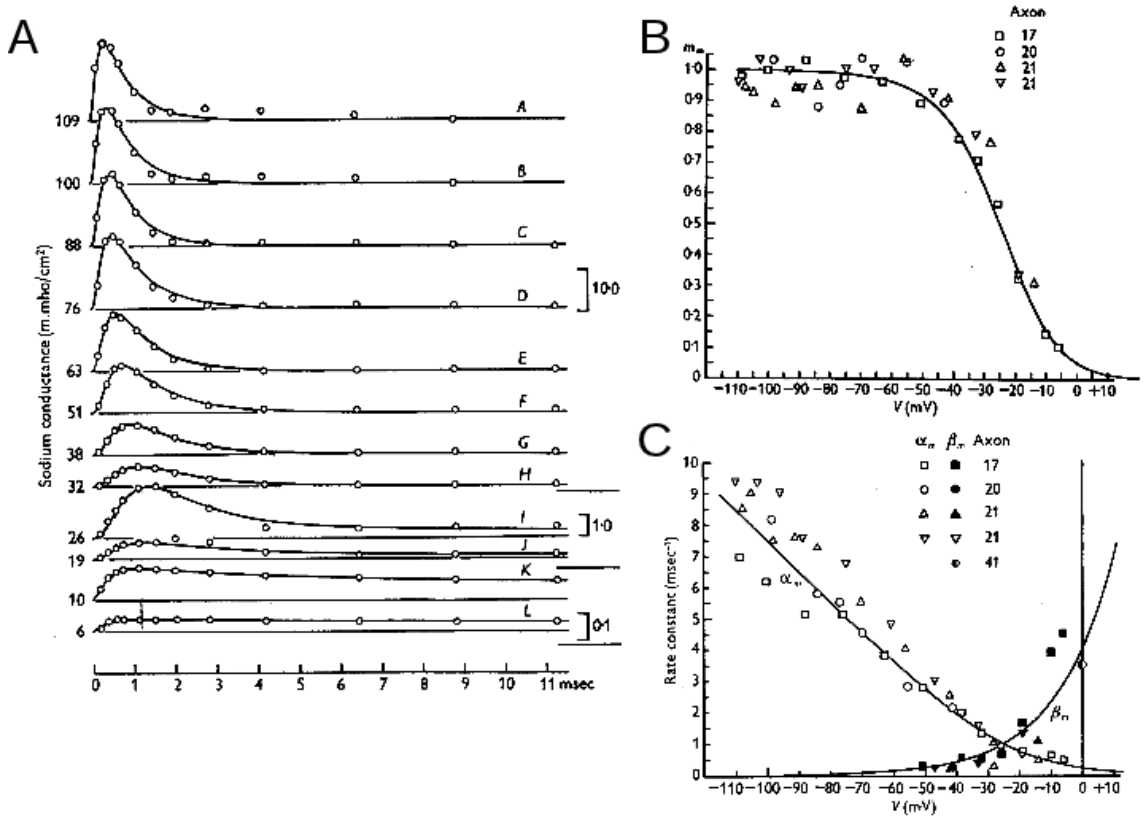

Figure 3.5: **Fitting the conductance and activation parameters for the sodium current in the Hodgkin-Huxley model.** A) Conductance traces in response to a series of voltage step protocols. B) Calculated kinetic parameters α_m and β_m. C) Calculated steady state constant $m_\infty(V)$. Adapted from Journal of Physiology, Vol 117, A.L. Hodgkin and A.H. Huxley, A quantitative description of membrane current and its application to conduction and excitation in nerve, Pages 500–544, Copyright (1952), with permission from John Wiley & Sons Ltd.

Huxley then derive $\bar{G}_{Na}$ and hence $m_\infty(V)$ from $G'_{Na}(V)$. α_m and β_m are then fitted as for α_h and β_h, although with the functional forms reversed.

Methods similar to this remain in place to this day. Given the additional complexity of the currents involved in the cardiac ventricular myocyte and the difficulties in recording patch clamp data for the individual currents present, models are often 'hand tuned' to reproduce an AP of the desired shape, as in Beeler and Reuter (1977), once the available experimental data has been gathered. This process involves the varying of one parameter at a time by the model developer to bring the model closer to the desired AP morphology. Sensitivity analysis can be a useful tool in such a situation to guide the choice of parameter variation (Hafner et al., 1981; Sobie, 2009).

Perhaps inevitably given the number of assumptions made throughout the above parameterisation scheme and the lack of computational power available at the time, the parameters derived using the above methods leave something to be desired. As we shall see in the next section, models of the cardiac cell based on conductances derived using the above method are likely to significantly underestimate the conductance of many currents. This has major consequences for their use in simulation studies on subjects such as pharmaceutical blockade.

3.5.1 Refining the Hodgkin-Huxley method: Improved estimation from voltage clamp data

Voltage clamp data are available for most currents in the cardiac cell, containing information on the activation and inactivation properties of these currents. As such, it is important that these data should be exploited as far as is possible. Most published techniques make the assumption of a Hodgkin-Huxley formalism for the behaviour of the current. Several different approaches to the problem of fitting kinetic parameters are shown in the literature, and many papers have highlighted the weaknesses of the technique originally proposed (Beaumont et al., 1993b; Willms et al., 1999; Lee et al., 2006). One of the major problems comes from Hodgkin and Huxley's assumption that the timescales of activation and inactivation are widely separated. Willms et al. (1999) and Lee et al. (2006) have shown that this assumption will lead to failure to predict both the kinetic properties of the current and the maximal conductance of the current effectively, in particular leading to underestimation of the maximal conductance where the two timescales are not widely separated.

In Beaumont et al. (1993b) this problem is addressed *via* an analytic procedure for the estimation of the ratio between the time constants and finding a range for the maximal conductance given that the steady state curves are known. The authors also claim that the existence of such a range confirms the applicability of the Hodgkin-Huxley model to the data. This method relies on a large separation between the timescales of activation

and inactivation. In the companion paper (Beaumont et al., 1993a), the authors construct a more generalised method for parameterisation not reliant on either a large separation of timescales or knowing steady-state curves, although the powers of the gating variables as shown in equations (3.6) and (3.9) are assumed. Approximations to an analytic formulation for the peak current and time to peak are then used to parameterise the steady state curves via a least-squares minimisation approach. These are then used to find the time constants and ranges in which the maximal conductances can lie. Wang and Beaumont (2004) take this work to its logical conclusion with a full inversion procedure to find values of the steady-state curves for m_∞, h_∞ and n_∞, time constants and maximal conductances. This method requires experiments that are not currently standard practice, and the authors do not demonstrate the usage of their technique even on simulated data. Nonetheless it does illustrate additional requirements that may be needed to fully determine parameters in a Hodgkin-Huxley-type model.

Lee et al. (2006) adopt an approach similar to that demonstrated by Beaumont et al. (1993b) in that they aim to use properties of the voltage clamp current trace to fit the model, namely the peak current, time to peak current and the steady state current. Their technique requires an additional constant, taken to be the current at twice the time to peak current. One variable may then be factored out, giving three objective functions to minimize using the Nelder-Mead simplex method (Nelder and Mead, 1965). The authors also propose a modification to allow calculation of the maximal conductance by estimating $\bar{g}x_\infty$ and then assuming that the depolarising step is sufficiently large that $x_\infty = 1$, where x is the activation gating variable in question. Simulation studies demonstrate a significant improvement over the standard method, both with and without estimating the maximal conductance. Tóth and Crunelli (1995) also use the time to peak current as a part of their method for finding kinetic parameters in a Hodgkin-Huxley model. In their method analytic forms for kinetic parameters are taken in terms of properties such as time to peak potential. They do however make several major assumptions, for example that for an inactivation voltage clamp protocol the steady state of activation is small and can therefore be ignored. Their method

is unable to distinguish between different powers of the gating variables however, and so must be repeated with 1–4 gates.

In contrast to the above method, Willms et al. (1999) offer the more computationally intensive approach of taking a set of voltage clamp experiments, expressing the corresponding current traces in analytic form and then minimising the least squares residuals over all the traces simultaneously, with a factorisation for the noise levels present in each experiment. Software to perform this technique on experimental data has been published by Willms (2002). Interval analysis, whereby hypercubes within parameter space are subdivided and analysed for the potential presence of a global minimum using a twice differentiable objective function has been used by Madden et al. (2000) to fit a Hodgkin-Huxley model to voltage clamp traces, but the results are disappointing in terms of the final fit to voltage clamp experimental data.

3.5.2 Parameter fitting for Markov models

In general, as pointed out in Fink and Noble (2009), the parameters of a Markov model may theoretically be fitted using single ion channel data, provided the model is constructed well enough to avoid any *a priori* unidentifiable parameters (Bauer et al., 1987). Sensitivity analyses such as that published by Sher et al. (2013) may help remove such unidentifiable parameters in the development of future models. The problem comes when experimental noise shields more subtle effects in the gating properties of the channel. Given this, most methods used in practice rely either on 'hand tuning' the model, or minimisations such as those described below.

An early attempt at fitting parameters to such models was proposed by Balser et al. (1990), who fitted a three state model using multiple membrane potentials simultaneously, noting that the problem was undetermined for any one voltage. A Boltzmann curve was used for the steady state activations and both a Levenberg-Marquardt algorithm and a Nelder-Mead simplex approach were used. The authors also investigated their results in the context of stochastic ion channel gating (Colquhoun and Hawkes, 1981) *via* a Monte-

Carlo simulation study. It was found that the greatest inaccuracies in parameter estimation for the activation constants occurred at negative membrane potentials where few channels were open, and correspondingly the worst fits for the inactivation constants were at positive membrane potentials where few channels were closed.

Gurkiewicz and Korngreen (2007) proposed a combined genetic algorithm and hill climbing algorithm wherein the parameters are initially defined upon a wide but physiologically realistic range, and then the genetic algorithm is run until the best parameter value does not change significantly. The hill climbing algorithm then takes over and attempts to converge more accurately to a solution. Neither the genetic algorithm nor the hill climbing algorithm reached an acceptable solution on their own. When combined they were able to estimate parameters accurately using several different Markov models with both simulated and experimental data from voltage clamp protocols. This represents a valuable contribution due to successfully navigating the requirement of a gradient-type algorithm to start relatively near to the required parameters by using a genetic algorithm to provide a sensible initial guess. However, this does not address the recurring problem of local minima.

3.5.3 Fitting to the action potential

It is worth noting that there are two main philosophies available for model fit: fitting directly to the AP morphology and gaining more accurate estimates of parameters from voltage clamp experiments. For the first approach, an early method proposed was that of Hafner et al. (1981). They demonstrated the use of parameter sensitivity equations to fit both the Hodgkin and Huxley (1952d) and Beeler and Reuter (1977) models to an AP morphology by minimising the least squares distance between the model and the data. In this case the parameter sensitivity equations are used for gradient descent to a minimum of the optimisation function.

Fitting to the AP has also been demonstrated by Dokos and Lovell (2004) who, rather than fit directly to the AP morphology, use a 'data clamp' approach wherein the model is forced to follow the target AP morphology by the insertion of an additional compensatory

current. This compensatory current is then the target for minimisation. A major drawback of such minimisation schemes is their tendency to get trapped in local minima away from the global minimum of the objective function that Dokos and Lovell (2004) attempted to avoid through a re-weighting scheme. Whilst an excellent fit to the morphology of the Beeler and Reuter (1977) model is demonstrated, the authors show that the method fails to adequately reconstruct the individual transmembrane currents. They additionally proposed the use of pseudo-random injection current protocols enabling a significantly improved reconstruction of the component currents of the AP. This method has been made available as software able to interface with CellML models (Hui et al., 2007).

An extension of the results of Dokos and Lovell (2004) showing their significance in a physiological context has been presented by Zaniboni et al. (2010), who reparameterised the Luo and Rudy (1991) model to produce a second AP with an almost identical morphology to the original model but with different underlying parameters, notably a reduced slow inward current maximal conductance, a shift in the activation curve of the plateau potassium current by 27mV towards depolarisation, and modifying the time constant of activation of the slow inward current. They observed that whilst the two single cell models appeared identical in single cell simulations, the refitted model was a much weaker current source, and therefore was affected far more by electrotonic interactions than the original model when coupled either as a pair of cells or into a one-dimensional cable. Furthermore, the models exhibited radically different reactions to simulated drug block, with 30% reduction of I_K causing a modest prolongation in the original model, but inducing early after-depolarisation-like behaviour in the modified parameter set. These findings show that simply fitting to the AP morphology can have consequences for physiological conclusions drawn from models constructed in this way, and so it must be done with caution, and due consideration given to the possibility of multiple parameter sets capable of generating the same result.

Genetic algorithms have also been successfully used to fit to AP morphology. Syed et al. (2005) used a genetic algorithm to demonstrate the fitting of conductances of two

different human atrial cell models, as well as to experimental data from canine atrial cells. Significantly, the authors demonstrated that it was possible to refit the conductances of a model exhibiting a 'spike and dome' (Courtemanche et al., 1998) morphology to one exhibiting a 'triangular' morphology (Nygren et al., 1998). Due to the model channel kinetics remaining unchanged this result lends support to the hypothesis that the differences in observed APs throughout the myocardium may be caused by differences in expression levels of ion channel proteins. This effect was also observed by Nygren et al. (2001), although they tuned parameters by hand rather than algorithmically.

Learning algorithms such as that proposed by Doya and Selverston (1993) have been used to fit the Hodgkin-Huxley model directly to an AP morphology. This methodology was later modified to refit the Luo and Rudy (1991) model by Iwasa et al. (2003) and later the more complex Luo and Rudy (1994a,b) (dynamic) model by Takahashi et al. (2006). The algorithm as proposed by Takahashi et al. (2006) is based around a gradient descent method, with the error used to select the parameter (learned one at a time) that changes every 200 stimuli. The parameters for which the learning algorithm was performed were the maximal conductances. By setting certain parameters in the model to be abnormal the authors were able to successfully reconstruct the resulting AP trace using their algorithm, although some parameters were unphysiological.

One major criticism of all the above schemes is that they tend to estimate the maximal conductances of the model only, taking the original kinetic parameters of the model as given. In the absence of this information most of these methods are untested if we wanted to fit kinetic parameters to the model. Thus, whilst these methods may be suitable for re-parameterising existing models, for example when modelling transmural ion channel distribution, they are unlikely to be effective in the construction of an entirely new model. This need not be a problem provided that ion channel kinetics are conserved between species, and have not been modulated by phosphorylation or other subcellular phenomena.

3.5.4 Parameter space exploration

Parameter space exploration is another possibility for parameter fitting to cellular models that can avoid one of the major pitfalls of minimization methods, namely that of getting trapped in local minima. Bhalla and Bower (1993) used both brute-force and conjugate gradient methods to explore a 36-dimensional parameter space for spatially structured neuron models: they remark that neither method is independently likely to be effective as the models do not contain a unique minimum for conjugate gradients, but brute force exploration becomes rapidly computationally intractable. The brute-force method's efficiency was improved using experimental data to constrain the parameter space, lumping of groups of parameters, and examining plane sections through the parameter space by varying pairs of parameters. The authors remark that the method finally used for model development was a combination of the two — using brute-force methods to locate a likely region of parameter space, and then a conjugate gradient method within this region. Plane sections may then be used to estimate both the smoothness of parameter space in the region of the solution and the robustness of the model within this region. Foster et al. (1993) used a stochastic search method to produce Hodgkin-Huxley type models that reproduce desired characteristics by exploring the conductances of the model. The method does however assume that the kinetic variables are known. This method is extended by Reid et al. (2007) to include a cost function based on the firing frequency of the model together with the stochastic search algorithm, and noted an improvement in the efficiency of the algorithm over a random search. Prinz et al. (2003) go about the problem of exploring the parameter space in an entirely different way by creating a searchable database of over 1.7 million different neuronal models. However, Archard and De Schutter (2006) note that the grid search method used by Prinz et al. (2003) could not find good solutions that were uncovered by the evolutionary strategy they employed upon a similar problem. Thus systematic sampling of parameter space may miss 'good' solutions, and also has a vast computational cost.

This approach has recently become a feature of parameter estimation schemes in car-

diac electrophysiology. Sobie (2009) demonstrates the use of linear regression as a parameter estimation technique. In this approach, conductances for multiple channels are drawn from a log-normal distribution, and the resulting set of APD_{90} values are fitted to a linear regression model. The linear model is then used to determine the conductances required to generate a given APD. Whilst the response of the model is not strictly linear in each conductance, the response is close enough to give a good approximation to the correct conductance, which may then be refined. This method has been extended in Sarkar and Sobie (2010), who examined a wider range of biomarkers, and demonstrated that many of these contained redundant information, reducing the number of biomarkers required to fit the AP. It is worth noting that all of these parameter space exploration methods are closely related to the concept of a population of models, discussed in detail in Section 3.9.3 and in further detail in Chapter 5.

3.5.5 Summary

We have now reviewed some of the mathematical methods available for the parameterisation of electrophysiology models. We note that given appropriate data from a single current, be this whole cell or single channel patch clamp data, the parameterisation is often a tractable problem although the determination of parameters may not be unique, especially in larger Markov models. Problems are more likely to occur in the absence of suitable data for the current in question, be this because of a lack of specificity between different currents in the experimental data available or an absence of species-specific current data. In these situations a wide variety of methods exist to parameterise the model but we can no longer be sure that these parameterisations are a solid reflection of the reality of the kinetics present. Such problems may be confounded by the need to fit rate parameters for subcellular phenomena. Nonetheless, the above techniques have allowed the construction of biophysically detailed models that capture known behaviour and allow the testing of hypotheses into cardiac cellular function.

In the absence of detailed information being available on transmembrane current in

cardiac tissue, we suggest that a simpler model of the AP may be a more tractable solution. This is due to the large number of parameters present in a biophysically detailed model and the inapplicability of the above methods described in the absence of ionic currents, not to mention the time required to optimize large models. This necessitates a refocusing of what we intend our model to reproduce. It is clear that we cannot now expect to study the details of calcium dynamics, or the long term effects on ionic concentration in tissue. What we can instead focus on are tissue level properties of the AP such as conduction velocity and restitution. The phenomenological models discussed in section 3.7 fit this purpose perfectly.

3.6 Modelling the Propagation of the Action Potential

3.6.1 Introduction

Mathematical modelling of isolated cardiac cells has provided insight into the mechanisms by which the cardiac AP is generated. In the intact heart, cells are coupled together to create an excitable medium through which a wave of activation of cardiac cells can propagate. It is therefore natural to couple together computational cell models in a similar manner. Modelling inter-cell coupling is crucial to investigate the effect of many features of cardiac tissue, such as cardiac fibre orientation or spatial heterogeneity in cell behaviour. In this section, we discuss commonly used methods for the simulation of wave propagation in cardiac tissue.

3.6.2 The bidomain equations

The bidomain equations remain the state-of-the-art for the modelling of electrical propagation in an excitable biological medium, including cardiac tissue. The bidomain equations consider the tissue as averaged at each point and consider each point in the tissue to exist simultaneously in two domains, intracellular and extracellular (Miller and Geselowitz, 1978;

Tung, 1978). The electrical potential in each domain is considered to be continuous. The justification for this in the intracellular domain is that cells are connected by gap junctions that allow the passage of ions directly from one cell to the next. The cell membrane is considered to be a resistor and barrier between the two domains, thus creating a potential difference (known as the transmembrane potential) between the two domains and allowing the model to be coupled to cellular electrophysiology models (described in Section 3.3). Ions may flow across the membrane in response to changes in transmembrane potential as in the single cell models, creating a current between the two domains.

To derive the bidomain equation a quasi-static assumption is made, *i.e.*, temporal variations in the field are considered insignificant and that at each moment in time the field is static. We also assume that there are no sources or sinks of current aside from the ionic current between the two domains, and that there is no buildup of charge at any point. Given the small width of the cell membrane, it is additionally assumed that any charge on one side of the membrane leads to an instantaneous opposing charge developing on the other side of the membrane. The net current at any point in a domain is taken to be the rate of accumulation of charge at the point combined with the ionic current leaving that domain at the point.

Derivation of the bidomain equations has been covered in detail in Sundnes et al. (2006). From the assumptions above, we arrive at the following set of partial differential equations

$$\nabla \cdot \big(\sigma_i \nabla(\Phi_e + v)\big) = \chi\big(C_m \frac{\partial v}{\partial t} + I_{ion}\big) - I_{intra} \text{ in } \Omega, \tag{3.32}$$

$$\nabla \cdot \big(\sigma_i \nabla v + (\sigma_i + \sigma_e)\nabla \Phi_e\big) = -I_{total} \text{ in } \Omega, \tag{3.33}$$

where σ_i is the conductivity tensor in the intracellular domain, σ_e is the conductivity tensor in the extracellular domain, Φ_e is the extracellular potential, v is the transmembrane potential (as in the cell model), C_m is the membrane capacitance, I_{ion} is the current across the cell membrane as described by the coupled cell model, I_{intra} is the intracellular stimulus

current, I_{intra} is the stimulus current applied to the intracellular space, I_{total} is the total current applied to the intracellular and extracellular spaces, Ω is the region in which the domains lie and $\partial\Omega$ its boundary.

To solve these equations, appropriate boundary conditions are required. Under the assumption that the normal component of both the intracellular and extracellular currents are zero at the boundary, we reach the boundary conditions

$$\mathbf{n} \cdot \big(\sigma_i \nabla(v + u_e)\big) = 0 \text{ on } \partial\Omega, \tag{3.34}$$

$$\mathbf{n} \cdot \big(\sigma_e \nabla u_e\big) = 0 \text{ on } \partial\Omega, \tag{3.35}$$

where $\mathbf{n}$ is the unit normal to the boundary of the domain. In some cases, it is deemed necessary to add a second region to the model, called the extramyocardial region (Lines et al., 2003). This is often the case where the heart is modelled as surrounded by a fluid bath, for example defibrillation studies (Rodríguez et al., 2005). There are also multi-domain models now available for use when multiple different excitable cells are present (Corrias et al., 2012).

The presence of a conductivity tensor in these equations allows the incorporation of cardiac fibre orientation into cardiac simulations. As the conductivity is greater parallel to the fibre than it is perpendicular to it, conductivites are typically assigned as a diagonal matrix of the longitudinal, transverse, and normal conductivities. Through the application of a suitable change of basis tensor field these orientations are then rotated appropriately and placed within a cardiac tissue geometry. Such tensor fields may either be derived from MRI measurements or they can be assigned using a rule-based method where the fibre angle varies as a function of the transmural location of the point in question (Potse et al., 2006).

The bidomain model may be applied to most tissue preparations, including simplified rectangular blocks, wedges, whole ventricles and whole hearts. We also often require a representation of the orientation of cardiac fibres from the endocardial to epicardial surface

(Fenton and Karma, 1998; Potse et al., 2006). It should be noted that most 'whole heart' simulations take place on either one or both ventricles only, and the atria and Purkinje system are often neglected. There exists a large body of work on simulating both of these important cardiac systems, and integrating them into whole heart and torso models (Cherry et al., 2001; Bordas et al., 2011; Zemzemi et al., 2012). We do not review this here.

3.6.3 The monodomain equation

Under certain condition the bidomain model may be simplified to form a single partial differential equation known as the monodomain equation. The assumption required is that the intracellular and extracellular domains have equal anisotropy rates, *i.e.* $\lambda\sigma_i = \sigma_e$ (Sundnes et al., 2006). After suitable rearrangement under this assumption, Equations (3.32) and (3.33) become

$$\frac{\lambda}{1+\lambda}\nabla \cdot \big(\sigma_i \nabla v\big) = \chi\big(C_m \frac{\partial v}{\partial t} + I_{ion}\big) - I_{stim} \text{ in } \Omega. \tag{3.36}$$

and the boundary conditions (3.34) and (3.35) become

$$\mathbf{n} \cdot \big(\sigma_i \nabla v\big) = 0 \text{ on } \partial\Omega. \tag{3.37}$$

The monodomain equation has the advantage that it is significantly easier to solve than the bidomain equations as there is no extracellular potential Φ_e to compute. This reduces computational effort, and also the complexity required for its solution. Potse et al. (2006) conducted a study into the difference between results in a monodomain and bidomain model of human heart electrophysiology. They concluded that, excepting cases where the extracellular potential becomes important such as defibrillation, a monodomain simulation was adequate for capturing electrophysiological behaviour, with results being nearly identical to the bidomain model. It is also possible to include wave front curvature induced by a bath loading effect in bidomain simulations in a monodomain model (Bishop and Plank,

2011).

Other tissue modelling techniques exist, including eikonal equations (Colli Franzone et al., 1990) and graph-based methods (Wallman et al., 2012) for activation, and discrete cell models such as Bub and Shrier (2002).

3.7 Phenomenological and Reduced Models

An alternative methodology to the biophysical models described in Section 3.3 for the modelling of cardiac electophysiology in tissue is the phenomenological modelling approach. The earliest phenomenological model for an electrically exciteable cell is the FitzHugh-Nagumo model (FitzHugh, 1955, 1961; Nagumo et al., 1962). The aim of this model was to isolate the fundamental mathematical properties of the excitable membrane by reducing the Hodgkin-Huxley model to a two dimensional system of equations, allowing its visualisation using a phase plane. The model has been used to explain phenomena such as excitation block (cessation of neuronal excitation when stimulus current increases above a certain level). The model's main attraction is that it is analytically tractable and so can be used for mathematical analysis of traveling wave phenomena in cardiac electrophysiology and neuroscience.

In cardiac electrophysiology, the prevalent framework for a phenomenological model is the Fenton-Karma three variable model (Fenton and Karma, 1998), based on the earlier two-variable Karma (1993) model. These models are typically partially non-dimensionalised to remove membrane potential, surface area to volume ratio and capacitance. They are usually expressed in form

$$\frac{\partial u}{\partial t} = \nabla \cdot \big(D \nabla u\big) - f(u, \mathbf{v}), \tag{3.38}$$

where D is a diffusion coefficient with dimension cm^2 s^{-1}, u is a non-dimensional 'voltage', $\mathbf{v}$ are non-dimensional variables controlling the current amplitude and $f(u, \mathbf{v})$ is a 'current'

with dimension s^{-1}. The three variable model is able to reproduce certain properties of cardiac experimental data and/or models, namely the velocity of upstroke of the AP, the AP duration (APD), its steady state restitution properties, its conduction velocity and its conduction-restitution relation. The approach is that of a reaction-diffusion equation, analogous to the monodomain equations of Section 3.6.3 with two simplified 'currents'. The original model was used to study the effects of fibre orientation on the breakup of spiral wave dynamics. Through modifications of the model, later work has also encompassed investigation of different mechanisms that may cause spiral wave breakup (Fenton et al., 2002) and the effects of pacing history and restitution slope steepness on suppression of alternans and conduction block (Fenton et al., 1999; Cherry and Fenton, 2004). Bueno-Orovio et al. (2008) added a fourth variable to the Fenton and Karma (1998) phenomenological model to accurately reproduce action potential morphology. The model was then fitted to three human ventricular models (Priebe and Beuckelmann, 1998; Iyer et al., 2004; Ten Tusscher and Panfilov, 2006) and compared simulations of ventricular tachycardia to the models' (different) patterns of wave break. By adding a further two variables to this model, the time course of adaption to a change in pacing cycle length can also be simulated (Bueno-Orovio et al., 2012). The Fenton and Karma (1998) model has recently been modified to include a current analogous to the fast potassium transient I_{to} by Cantalapiedra et al. (2010) in order to model the consequences of Brugada syndrome in the context of generation of short APs and re-entry. The current in this model is not a representation of the kinetics of I_{to} as in the biophysically detailed models discussed previously, but is activated during the same phase of the AP in order to reproduce the desired morphology.

Models of the cardiac cell may also be reduced analytically, resulting in a model with fewer variables that is easier to parameterise, although some biophysical detail is lost. One example of this is the Bernus et al. (2002) reduced model. In this work, the human model of Priebe and Beuckelmann (1998) was reduced to a six variable model by clamping all ionic concentrations, including calcium. I_{Kr} and I_{Ks} were merged into a single potassium current and multiple sets of gating kinetics were either removed or reduced. The resulting six

variable model was capable of reproducing human ventricular AP morphologies, restitution curves and conduction velocity restitution. This model serves as an intermediate step between 'full' biophysically detailed models as described in the previous section, and the phenomenological models described above.

An alternative approach that has recently appeared is that of using a generalised Hodgkin-Huxley type equation (Guo et al., 2010). In this approach, three basic Hodgkin-Huxley currents, an inward, outward and leak current are fitted to experimental data for sino-atrial node and atrial cells. Each current has a generalised Hodgkin-Huxley scheme with two independent gating variables representing activation and inactivation. The parameters are then optimised against experimental AP traces to produce the desired waveform. Additional currents may be incorporated to reproduce cell responses to changes in pacing rate or pharmaceutical intervention.

3.8 Relating conductivity, diffusion coefficient and gap junctional resistance

Throughout this thesis, we use the diffusion coefficient (units cm^2 s^{-1}) in our monodomain tissue simulations, as we use a phenomenological framework which has been partially non-dimensionalised. In particular, we refer to a 'standard' diffusion coefficient of 1.171cm^2 s^{-1} for both human and guinea pig. This parameter is related to the bulk conductivity of the tissue by the ratio of the cell membrane surface area to volume ratio (χ), and the cell membrane capacitance (C_m).

Thus, to re-dimensionalise this parameter we can multiply both sides of (3.38) by a factor of χC_m, giving a conductivity tensor $\sigma = \chi C_m D$. For a human cell, O'Hara et al. (2011) use a cylindrical geometry with length 0.01cm (L) and radius 0.0011cm (r) as provided by Forbes and Sperelakis (1989). This gives a surface area of $2\pi r^2 + 2\pi r L$ = 7.67$\times$10^{-5} cm^2,

and a volume of $\pi r^2 L$ = 3.8 $\times 10^{-8}$cm^3. Thus for a human cell using these values,

$$\begin{aligned}\chi &= 7.67 \times 10^{-}5\text{cm}^2/3.8 \times 10^{-8}\text{cm}^3, \\ &= 2.02 \times 10^3\text{cm}^{-1}.\end{aligned}$$

For a human cell, O'Hara et al. (2011) give a total membrane capacitance of 1μF/cm^2. Thus, the diffusion coefficient given above corresponds in human to a conductivity in tissue of approximately 2.36$\times 10^3$ μF s^{-1}cm^{-1}. One Farad is one Coulomb/Volt, so one Farad s^{-1} is one (Coulomb s^{-1}) / Volt, which is one Ampere/Volt, i.e. one Siemen (S). Thus we have a conductivity of σ = 2.36$\times 10^3$ μS cm^{-1}, or 0.24 S m^{-1}.

This value is a bulk conductivity used in a monodomain framework. Hence it arises from the assumption that the anisotropy ratios are equal between the intracellular and extracellular domains in the bidomain model. Hence if λ is the ratio such that $\lambda\sigma_i = \sigma_e$, then we have $\sigma = \frac{\lambda}{1+\lambda}\sigma_i$ as in Section 3.6.3. Potse et al. (2006) give a longitudinal intracellular conductivity of 0.12 S m^{-1} and a longitudinal extracellular conductivity of 0.30 S m^{-1} for human, hence the ratio λ is 0.30/0.12 = 2.5. Thus we arrive at an intracellular conductivity of

$$\begin{aligned}\sigma_i &= \frac{1+\lambda}{\lambda}\sigma, \\ &= 0.34\text{S m}^{-1}.\end{aligned}$$

This is higher than the value above given by Potse et al. (2006), and slightly higher than that given by Roth (1997) of 0.20 S m^{-1}.

Resistivity is the reciprocal of conductance. Shaw and Rudy (1997) give the lumped resistivity across a single cell as R_i = $R_{\text{myo}} + \frac{R_{\text{g}}}{L}$, where R_{myo} is the resistance of the myoplasm in Ω m and R_{g} is the gap-junctional resistance in Ω m^2. In their study, they use

a value of R_{myo} = 150 Ω cm, or 1.5 Ω m. Hence we have

$$\begin{aligned}\sigma_i &= \frac{1}{R_i}, \\ &= \frac{1}{1.5\Omega\text{m} + \frac{R_\text{g}}{1\times10^{-4}\text{m}}}.\end{aligned}$$

Re-arranging gives

$$\begin{aligned}R_g &= 10^{-4}\left(\frac{1}{\sigma_i} - 1.5\right)\Omega\text{m}^2, \\ &= 1.48\times10^{-4}\Omega\text{m}^2, \\ &= 1.48\Omega\text{cm}^2.\end{aligned}$$

This value is very close to the gap junctional resistivity given by Shaw and Rudy (1997) of 1.5Ω cm^2. To convert this value to a conductance, we divide by the area (πr^2), and take the reciprocal, giving a gap junctional conductance of 2.57μS.

In later chapters, we will explore the effects of scaling the diffusion coefficient. We assume that scaling the diffusion coefficient represents a change in the gap-junctional resistivity alone and so R_{myo} remains constant. Applying a scaling to the diffusion coefficient also scales σ_i by the same amount. Applying the same analysis as above, scalings of 0.5$\times$, 0.1$\times$ and 0.05$\times$ the conductivity tensor result in gap-junctional resistivities of 4.5Ω cm^2, 28.3Ω cm^2, and 58.0Ω cm^2, respectively. These resistivities correspond to gap-junctional conductances of 0.9μS, 0.1μS, and 0.07μS,respectively.

3.9 Simulating Heterogeneity and Variability

3.9.1 Introduction

We have summarised the history of cardiac cell models and how they are simulated in a tissue. We can now consider the efforts made to date in the simulation of heterogeneity

and variability in cardiac electrophysiology.

3.9.2 Heterogeneous Tissue Models

An early model of heterogeneous cardiac tissue was published by Lesh et al. (1989), who generated versions of the Beeler and Reuter (1977) model by drawing conductances from a Gaussian distribution at each node in a 1cm $\times$ 1cm tissue. The resulting monodomain model was simulated using a progressively reduced conductivity tensor to provide support for the theory that heterogeneities in APD are masked at physiological conductances, and become progressively revealed as intercellular coupling is reduced. This principle has been returned to a number of times to address physiological questions through computational modelling.

Viswanathan et al. (1999) divided a single strand of cardiac cells into epicardial, endocardial and midmyocardial regions with differing electrophysiological properties based upon the density of I_{Ks}. The properties of each cell region were set by modulating conductances of I_{Kr} and I_{ks}. At high conductances, the observed heterogeneities were negligible, but as in Lesh et al. (1989) the heterogeneities became increasingly apparent as conductivity decreased. This suggests that electrophysiological heterogeneities between cells may become more important in pathologies that disrupt coupling in the myocardium, such as ischæmia and heart failure.

One particular application of such a method was an attempt to resolve the well known M-cell controversy discussed in Chapter 2. To support their experimental findings, Conrath et al. (2004) demonstrated that under conditions of physiological coupling, an M-cell region would not be expected to produce a significant difference in APD in a one-dimensional fibre model of transmural heterogeneity. A combined simulation and experimental study by Myles et al. (2010) also concluded that, in rabbit left ventricular wedge preparations, electrotonic modulation of APD had a more pronounced effect than intrinsic transmural heterogeneities in APD. This was due to the reversal of gradients in repolarisation time between endocardial and epicardial stimulation in both simulation and experiment, despite

the presence of a transmural gradient in cellular APD.

Whilst most studies of heterogeneous cardiac tissue use modified versions of relatively simple models such as Luo and Rudy (1994a) or Bernus et al. (2002), recently published isolated ventricular myocyte models have increasingly tended to come with epicardial, endocardial and midmyocardial versions, such as Ten Tusscher and Panfilov (2006) and O'Hara et al. (2011). In general, the model is constructed primarily using endocardial data and then modified to produce midmyocardial and epicardial variants. In the case of the O'Hara et al. (2011) model, this modification is guided by transmural expression levels of mRNA. These models can then be either considered in isolation or inserted into tissue simulations with cell models assigned based upon their distance from the endocardium, such as the Ten Tusscher et al. (2004) model used by Potse et al. (2006) to produce a human biventricular model.

Another question that has been addressed using heterogeneous models of cardiac tissue is the morphology of the T-wave in the electrocardiogram (ECG). The T-wave is generally interpreted as a measure of the ventricular dispersion in repolarisation in the ventricles. Gima and Rudy (2002) investigated the consequences of I_{Ks} heterogeneity on the morphology of the pseudo-ECG in a one-dimensional fibre, building on the work done by Viswanathan et al. (1999). In their study, they demonstrated that heterogeneous APDs were necessary throughout the wall of the heart to ensure that the T-wave of the ECG was upright, as has been observed in transmural wedge preparations. When the heterogeneity was removed, so that repolarisation followed depolarisation, the polarity of the T-wave became negative. Clayton and Holden (2004) expanded this work into two dimensional and three dimensional tissue preparations. In particular, they showed that whilst the presence of a midmyocardial M-cell region did produce an upright T-wave on the pseudo-ECG, this M-cell region was not necessary and the effect could be achieved with a transmural heterogeneity consisting of a band of epicardial cells and endocardial cells, with a slightly longer endocardial APD. This study also investigated the effects of coupling on simulated tissues featuring epicardial, M-cell and endocardial regions, demonstrating that, despite

decreasing APD heterogeneity, increased coupling also increased the magnitude of the T-wave.

Work on T-wave orientation continued in a biventricular study by Keller et al. (2012), who performed a thorough study of the effect of localisation of the three commonly reported ventricular cell types mentioned previously on the polarity of the T-wave. They considered differing widths of bands of epicardial, M-cell and endocardial variants of the Ten Tusscher and Panfilov (2006) human ventricular cell model. Islands of M-cells, as reported by Glukhov et al. (2010), were also simulated at varying distances from the endocardium. Additionally, the conductance of I_{Ks} was scaled to simulate differences between the left and right ventricles, and to create an apico-basal gradient in repolarisation. Combinations of the above parameters, for example with both transmural heterogeneities and apico-basal gradients, were also considered. In this study, the authors found that the best match to experimentally recorded human ECGs were obtained with either an apex-base gradient in I_{Ks} with raised I_{Ks} density at the apex, or with a combination of transmural and apex-base heterogeneities. Whilst they stimulated their model at the apex only, a more elaborate model featuring the His-Purkinje fast conduction system such as that presented by Bordas et al. (2011) or Sebastian et al. (2013) might produce different results by modulating the activation sequence.

Relatively few authors have addressed ventricular heterogeneities other than the well established transmural changes. The consequences of both apico-basal and transmural heterogeneities in APD properties on the repolarisaton sequence were simulated by Efimov et al. (1996) in a rectangular geometry. This study demonstrated that activation and repolarisation were driven by entirely different parameters. Activation was driven by the fibre orientation, and repolarisation primarily by the linear heterogeneity in APD from apex to base, as well as by the transmural heterogeneities. Furthermore, two whole heart simulation studies have also addressed apex-base heterogeneity. Colli Franzone et al. (2008) used the Luo and Rudy (1991) model together with a continuous variation in the conductance of I_K to introduce both transmural and apico-basal gradients in APD into an idealised

left-ventricular geometry. They found that epicardial APD maps were affected only by the apex-base gradient, and the transmural heterogeneity only became manifest when examining transmural sections of the heart model. As discussed above, Keller et al. (2012) considered the impact of apico-basal heterogeneities in their study. Similarly, whilst differences in electrophysiological properties between left and right ventricles are reported in the experimental literature (Bueno-Orovio et al., 2012), they are not represented within most cardiac cell models.

A further way in which heterogeneities may be induced in cardiac tissue is through spatial heterogeneity in restitution properties. One such study was that of Nash et al. (2006), who used computational modelling to investigate the arrhythmogenic consequences of spatial heterogeneities they observed in AP restitution on human epicardium. Simulations were performed with the Fenton and Karma (1998) phenomenological model and a simplified geometry consisting of a circular region with a steeper S1-S2 restitution curve than the surrounding tissue. This study demonstrated the principle that such a heterogeneity could act as a substrate for re-entrant arrhythmias, and also cause spiral waves to destabilise into fibrillating wavelets, depending on the size of the heterogeneous area.

An important point to make about heterogeneities in cardiac tissue simulation is that they are induced in a homogeneous tissue simulation by both the stimulus current, causing prolongation of the AP, and the propagating wave terminating at an insulating boundary of the tissue, causing a shortening of the AP. These electrotonic effects are explained in detail in Cherry and Fenton (2011). Cain and Schaeffer (2008) have also performed an asymptotic analysis of shortening at an insulating boundary in a two-current ionic model.

It has been suggested that fibre orientation induces heterogeneity in cardiac electrophysiology simulations (Colli Franzone et al., 2005). In light of the analysis presented by Cherry and Fenton (2011) this seems to be incomplete — it is more accurate to say that the heterogeneities induced by boundary and stimulus effects are modulated by the effect of the anisotropic tissue due to modification of the magnitude of the electrotonic current, producing a heterogeneous APD distribution. It remains unclear as to whether these elec-

trotonic stimulus and boundary effects are a physiological effect or an artifact of the modelling methodology used. Such electrotonic effects may also be modulated by bath loading effects resulting from the medium the which surrounds the experimental or simulated tissue (Bishop et al., 2011).

3.9.3 Populations of models

The roots of population-based approaches to computational physiology lie in neuroscience, stemming from the work of Prinz et al. (2003), who constructed a database of over 1.5 million different neuronal models, exhibiting different behaviours. For a recent review of this field of neuroscience, see Marder and Taylor (2011).

The developing role of computational model populations as a tool for understanding variability in patient responses in cardiac electrophysiology has recently been reviewed in Sarkar et al. (2012). The concept of populations of models in cardiac electrophysiology is a relatively new one, and to a large extent has grown out of methods to constrain parameters in neuronal models. One of the first studies to consider this approach applied to a cardiac cell was by Romero et al. (2009), who simulated natural variability in human ventricular electrophysiology using the Ten Tusscher and Panfilov (2006) model. Conductances of I_{Kr}, I_{Ks},I_{K1}, I_{CaL}, Na/Ca exchanger and Na/K pump, as well as some activation and inactivation time constants for these channels were varied by $\pm$15% and $\pm$30% relative to baseline. The effect of these parameter changes on APD_{90}, time constants of adaptation to change in pacing and systolic and diastolic cytosolic calicum concentrations were then recorded and plotted against the change in conductance. This effectively produced a local sensitivity analysis demonstrating which naturally occurring conductances could lead to noticeable changes in biomarker values within a human population. Unlike previous sensitivity analysis studies the aim was to investigate the effect of variability on biomarkers within a patient population, rather than on model parameterisation (Hafner et al., 1981). One disadvantage of this method is that each change is applied in isolation only, and so two currents may not vary simultaneously. The same technique has recently been applied to the Shannon et al.

(2004) and Mahajan et al. (2008) rabbit ventricular models in an attempt to understand differences in behaviour between those two models (Romero et al., 2011).

The concept of parameter space exploration, as mentioned earlier for neuronal studies, has also recently appeared in cardiac models. Gemmell et al. (2010) considered the effect of varying the conductances of I_{CaL} and I_{Ks} simultaneously in the Mahajan et al. (2008) rabbit ventricular model, constructing a parameter space on the outputs using a grid search method. This can be viewed as an extension of the method of Romero et al. (2009) to allow simultaneous variation of parameters. This work has been expanded to include variations in a further four conductances (I_{to}, I_{Kr}, I_{NaK}, I_{K1}) in Gemmell et al. (2012), using dimensional stacking to visualise the six-dimensional space as described previously by Prinz et al. (2003). Rodríguez et al. (2012) introduced a similar method incorporating a quadratic response curve to attempt to visualise nonlinear interactions.

The other major approach currently in the literature began as an approach to parameter estimation in cardiac models. Sobie (2009) allowed the conductance of several currents to vary simultaneously using Monte-Carlo sampling, and then used a linear regression model to fit the APD90 of the Luo and Rudy (1994a) model. This was extended by Sarkar and Sobie (2010) to investigate more biomarkers and exclude biomarkers containing redundant information. The authors realised that the Monte-Carlo sampling of the parameters could be used to model natural variability within a population. This led to a simulation study of heterogeneity in AP prolongation between patients in response to pharmaceutical blockade of I_{Kr} (Sarkar and Sobie, 2011). In this study, the authors investigated how this variability may originate from the repolarisation reserve. A population of 300 models was generated as before by varying parameters related to conductance, activation kinetics, and voltage thresholds of activation and inactivation. Their major findings were that cells with abnormal APD need not have an abnormal response to drug block, and conversely that two cells with similar APDs may demonstrate radically different responses to drug block. They found that across a number of different computational models the parameters predominantly affecting the repolarisation reserve were the conductances of I_{Kr}, I_{K1},I_{Ks} and I_{CaL}, combined with the

voltage dependence of I_{K1} rectification.

As discussed in Sarkar et al. (2012), some of the above results were hinted at by those of Dokos and Lovell (2004) whereby two APs with the same morphology could be generated using totally different conductances, also reported by Zaniboni et al. (2010). The Monte-Carlo method can be viewed as an alternate way to sample a parameter space, as opposed to the grid search method of Gemmell et al. (2012). However the major advantage of Monte-Carlo sampling is that it allows regression analysis to be performed far more effectively than a grid search method. In the work of Sobie (2009) and Sarkar and Sobie (2010, 2011) a log-normal distribution is used. This distribution has the attractive property of having positive support (unlike a normal distribution, that can become negative), and that the probabilities of (for example) halving versus doubling a parameter are equal. The disadvantage of this method is that unphysiologically large conductances may occasionally be obtained, necessitating an algorithm for the removal of non-physiological parameter sets (and a definition of what this might be).

The concept of a population of models has recently been taken further by Britton et al. (2013), who created a distribution of 10,000 versions of the Corrias et al. (2011) rabbit Purkinje model using latin hypercube sampling on twelve parameters. By comparing this distribution to a set of experimentally recorded APs, they then produced a calibrated population containing 213 models lying within the bounds of the experimental data. These models were then shown to predict the effects of the application of Dofetilide (an I_{Kr} blocker) on the set of experimentally recorded APs.

Yang and Clancy (2012) investigated the effects of gender on the O'Hara et al. (2011) model using a population based approach in single cell, and then the mean of the populations in tissue. Population construction was guided by mRNA expression data from Gaborit et al. (2010). They demonstrated a prolonged APD in female cells that caused a prolonged QT-interval in tissue simulations. When coupled with decreased connexin levels reported in female hearts, this APD prolongation allowed sustained re-entry not generated in the male model.

As noted by Yang and Clancy (2012), a challenge is to determine the extent to which the baseline model is 'male'. In this case, 56% of the human data in the model is from male samples, and 44 % is female. Thus, the 'male' model is in fact hermaphroditic. Nevertheless, their results demonstrate that the gender of a model can affect the predictions made. Gender is a clear target for a more personalised medical approach if the required data can be successfully gathered.

Another potential source of ionic variability is circadian rhythm, recently investigated by Fotiadis and Forger (2013). They allowed KChIP2 levels to oscillate sinusoidally based on the results of Jeyaraj et al. (2012). This lead to a 50% change in APD throughout the day in the Pandit et al. (2001) mouse model, and a smaller change (15%) in APD of the Grandi et al. (2010) human model, primarily because I_{to} is critical for repolarisation in mouse myocytes, but has a much smaller effect on repolarisation in humans.

It is clear that the systematic study of population variability is going to form an essential part of the future development of cardiac electrophysiology models. In particular, a quantitative understanding of how drug effects change with population variability will be essential if computational drug safety evaluation is to get beyond preliminary screening studies such as Mirams et al. (2011). Furthermore, to progress to what many hold to be the 'Holy Grail' of cardiac modelling — patient specific cardiac models — we must at least understand the consequences of individual electrophysiological variation in order to determine whether or not its inclusion is required in the final models. If so, this will become an even more challenging aim than is already the case. To date there have been few if any simulation studies in the literature on population level variability in tissue. The closest to population level variability in simulations thus far are Pueyo et al. (2011) and Lemay et al. (2011) who allowed an extrinsic variability in the conductance in I_{Ks} between different tissue simulations (see next section).

3.9.4 Beat-to-Beat Variability in Repolarisation

The above discussion focusses on differences between different cells. Variability between AP recordings may also be temporal in nature as discussed in Chapter 2. Attempts to simulate BVR in the cardiac AP first began with studies on the rabbit sino-atrial node cell, growing from the discovery that single channel gating was a stochastic, rather than deterministic, process (Wilders and Jongsma, 1993; Guevara and Lewis, 1995). In particular, these studies established that stochastic fluctuations in channel gating were a valid explanation for the variability they observed. Their model treated the opening or closing of each gate in each channel as a Markov process through the method of Clay and DeFelice (1983) that calculates probabilities of transition from the model's rate constants. As this method requires tracking each state transition for each ion channel under investigation in the computational cell their method is extremely computationally intensive. This work was extended to investigate phase resetting in sino-atrial node cells to explain apparently unpredictable changes of phase in response to a well-timed stimulus in a spontaneously beating cell culture (Krogh-Madsen et al., 2004). In this work the authors demonstrated that such a resetting was not possible with a deterministic AP model but could be achieved using a stochastic model based on that of Guevara and Lewis (1995).

The effects of coupling on BVR were addressed by Zaniboni et al. (2000). In their study, the authors observed that two isolated cardiac ventricular myocytes exhibited drastically reduced BVR in APD when they were electrically coupled together through simultaneous suction pipette attachments. Furthermore, the cells tended towards the smaller APD exhibited by the pair. The same effect was observed in simulations of two coupled myocytes, wherein one cell had lengthened APD through reduction of the conductance of I_{Kr} and the other had a shorter APD through an increase in the conductance of I_{Ks}. Their coupled cell simulations similarly showed that the APD of the longer cell was reduced to that of the shorter cell. Thus whilst they did address the difference in APD in their simulations, this was effectively over one beat and did not address BVR. This result does however extend that of Lesh et al. (1989) in that it demonstrates that cells with shorter APDs tend to shorten

those around them, rather than being lengthened or averaged.

A more recent approach to the problem of modelling stochastic variability is to use a stochastic differential equation (SDE) to represent ion channel gating dynamics. The concept was introduced in neuroscience, where the effects of stochastic gating on neuronal firing have been investigated computationally (Fox and Lu, 1994). The concept crossed over into cardiac electrophysiology in the simulations of Lerma et al. (2007), who added a stochastic noise current that effectively formed a Weiner process to a deterministic Hodgkin-Huxley model. They demonstrated that this could lead to early afterdepolarisations (EADs) in some but not all APs. This showed the possibilities arising from introducing stochastic noise. However, neither the biophysical detail of the channel opening probabilities nor any consideration to whether the noise may arise from some channels more than others based on channel number were considered. Ponard et al. (2007) used a stochastic model of chick embryo monolayers to demonstrate that stochastic effects could cause both BVR in beating rate and movement of the focus of excitation, continuing the work on monolayers described above. Their work used a fluctuation current similar to that of Lerma et al. (2007), and also incorporated stochastic gating of ryanodine receptors using 5000 individual stochastic channels.

Work has only recently begun on studying the consequences of the observed BVR in the APD of isolated ventricular cells. In particular, two studies have focussed on the consequences of the strong coupling typically exhibited between myocardial cells on BVR. Pueyo et al. (2011) explored the possibility that the low channel numbers of I_{Ks} typically observed in isolated ventricular myocytes may contribute to beat-to-beat variability in both human and guinea pig models. This study used a Langevin formulation of the stochastic gating processes in the ion channels and an estimation method for channel numbers of I_{Ks} from epicardial, midmyocardial and endocardial cells. Using these estimates of channel numbers in their Langevin formulation, the authors produced a cell model whose BVR was consistent with that observed in isolated myoctes. This model was then simulated in a tissue preparation, demonstrating the result that BVR was markedly reduced in tissue but

could increase with a reduction in conductivity. Another finding was that whilst stochasticity could cause EADs in up to 20% of APs in the human model in the presence of a block of I_{Kr}, coupling completely removed this effect even when severely reduced. This extended the findings of Zaniboni et al. (2000) on coupled isolated cells to a tissue setting. One potential disadvantage of this work is that by focussing solely on I_{Ks} the authors did not consider other potential sources of BVR, such as calcium sparking or stochastic gating variability in other ion channels.

The study by Lemay et al. (2011) investigated stochasticity in multiple channels (I_{CaL}, I_{Na}, I_{Kr}, I_{Ks}, I_{K1} and in calcium induced calcium release) but did not use experimental data to establish channel numbers as was done in the work of Pueyo et al. (2011). This study used a fully Markovian version of the Faber et al. (2007) guinea pig model, following the work of Milescu et al. (2005), to give a discrete stochastic model rather than the continuous Langevin formulation of Pueyo et al. (2011). They also observed the development of prolonged APs and EADs in response to I_{Ks} block. Unlike Pueyo et al. (2011), Lemay et al. (2011) used a network model of tissue coupling, and allowed for variability in the number of gap junction channels between cells. Unlike Zaniboni et al. (2000) and Pueyo et al. (2011), they only observed a moderate reduction in BVR. It is an open question as to whether this study underestimates cellular coupling, or Zaniboni et al. (2000) and the bidomain formulation of Pueyo et al. (2011) and others overestimate the effect of cellular coupling on repolarisation.

Whilst most of the models used in these studies tend to use Hodgkin-Huxley gating kinetics for their channels, Milescu et al. (2005) have shown that to preserve the statistics of channel opening and closing events a pseudo-Markov approach should be used. Dangerfield et al. (2012) have demonstrated that if the correct reflective term is incorporated into the model to prevent non-physiological negative channel opening probabilities, then a Langevin SDE formulation of channel gating will accurately reproduce the results of the discrete gating model in considerably less computational time.

An important consideration in all the studies described above is that, as discussed in

Chapter 2, there is also the possibility that damage to ion channels during isolation procedures causes a reduction in channel number and hence increases stochastic effects in isolated myocytes. This may cause an overestimation of the magnitude of an effect in tissue compared with intact hearts. A counter-point to this is that since isolated cardiac myocytes are common experimental models in both basic electrophysiology and pharmaceutical development it remains important to understand the causes and consequences of such stochastic variability even if the effect is exaggerated in simulations.

3.10 Conclusions

We have seen throughout the course of this chapter that computational cardiac electrophysiology is a maturing field that has provided physiological and clinical insight into the workings of cardiac tissue and the genesis of potentially fatal arrhythmias. Recent simulation studies have demonstrated the potential importance of spatial heterogeneities of cell types in determining the repolarisation patterns of the heart. In this way, simulations have added interpretative and predictive value to clinical and experimental recordings such as ECG morphology or optical mapping recordings of transmural repolarisation. Some studies have also begun to investigate population-level variability and temporal variability as described in Chapter 2, but these are very much emerging fields.

Chapter 4

Simulation Methods

4.1 Introduction

We have reviewed both experimental evidence for variability in Chapter 2 and efforts to date in modelling this variability in Chapter 3. As envisioned by Carusi et al. (2012), modelling and experimental data are linked by simulation of model equations. In this chapter, we review the simulation methods and software used in this thesis, and methods for determining the convergence of the numerical schemes where appropriate.

In all but the most simple of cases, the monodomain and bidomain partial differential equations described in Chapter 3 are not analytically tractable. Hence, in order to integrate the equations making up our models of electrophysiological behaviour we must use numerical approximations. Numerical implementations allow the use of computing resources in calculating solutions to these equations.

For the solution of the monodomain and bidomain equations, finite elements, finite differences, finite volumes and spectral methods are all frequently used. Implementation of any of the many numerical schemes used to integrate the monodomain or bidomain equations for any more than the most basic problems is a demanding and time consuming programming task. As a result, several computational research groups and companies from around the world have written simulation software. Some of these codes are available in

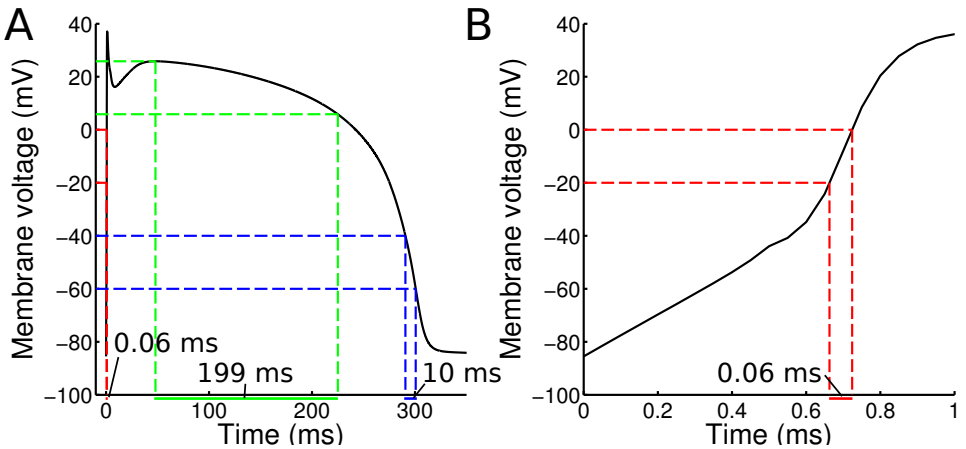

Figure 4.1: **Different timescales in an ODE model of the AP.** A) The stiffness of the Ten Tusscher and Panfilov (2006) human ventricular model is illustrated by showing the time taken for a 20 mV change in the membrane potential during the upstroke (red), plateau (green) and repolarisation (blue) phases of the simulated AP. The time taken for 20 mV change is 0.06ms in the upstroke, 199ms in the plateau and 10ms in the repolarisation phase. B) shows an enlargement of the upstroke, which is obscured in the first figure due to its short time scale.

house only (CMISS), some are commercially available (CARP), and some are freely available (Continuity) or open source (OpenCMISS, Chaste). We now describe the simulation methods and software used to solve the model equations in this thesis in the rest of this chapter.

4.2 CVODE

The CVODE libraries are our solver of choice for single cell deterministic models, which take the form of a set of non-linear differential/algebraic equations (Cohen and Hindmarsh, 1996). CVODE is provided as a part of the SUNDIALS suite (Hindmarsh et al., 2005). CVODE is integrated within Chaste (see Section 4.5), and we use it in Chapter 5 to simulate populations of models.

Whilst CVODE contains implementations of several different solution methods for ODEs, the version we use is a backwards differentiation formula with an adaptive order between 1 and 5, and a variable time step. This method is known to work well for stiff differential equations. Stiffness is a property of differential equations whereby their solution exhibits dif-

ferent time scales. This makes them difficult to solve and requires either fine time stepping throughout the solution, an adaptive scheme, or ideally an implicit highly stable method, in order to get an accurate solution. The backwards differentiation formula method is used since many cardiac cell models are stiff, particularly around the upstroke due to the large change in the derivative of the membrane voltage during the upstroke (Fig. 4.1). Given an ODE system of the form,

$$\dot{y} = f(t, y), \tag{4.1}$$

$$y(0) = y_0, \tag{4.2}$$

the order q backwards differentiation formula for time step h gives

$$y_n = \sum_{i=1}^{q} \alpha_{i,q} y_{n-i} + h\beta_{0,q} f(t, y_n), \tag{4.3}$$

where the coefficients $\alpha_{i,q}$ and $\beta_{0,q}$ depend on the order, q. A Newton method is then used to solve the resulting nonlinear system. As an adaptive ODE solver, CVODE also incorporates control of the estimated relative and absolute error in order to control the order and time step of the method.

4.3 Stochastic Differential Equations and the Euler-Maruyama method

As we have seen in Chapter 3, stochastic differential equations (SDEs) have been used to capture stochastic fluctuations in ion channel opening, leading to beat-to-beat variability in repolarisation in computational cells. We shall use these equations in Chapters 6 and Chapter 7. As described by Kloeden and Platen (2010), an SDE is analogous to an ordinary differential equation (ODE) with an additional stochastic term. For a random variable

$\mathbf{X}(t) \in \mathbb{R}^n$, and continuous functions $f : \mathbb{R}^n \to \mathbb{R}^n$, $g : \mathbb{R}^n \to \mathbb{R}^n \times \mathbb{R}^d$,

$$d\mathbf{X} = f(X)dt + g(X)d\mathbf{W}. \tag{4.4}$$

Here, $d\mathbf{W}$ is the stochastic differential of a random process $\mathbf{W}(t) = (W_1(t) \dots W_d(t))^T$. Under certain conditions on f and g, Eqn. 4.4 admits a unique solution with a deterministic (drift) term and stochastically varying (diffusion) term (Kloeden and Platen, 2010).

In the simplest case, used in this thesis, the random processes $W_1(t) \dots W_d(t)$ are Weiner processes. A Weiner process $W(t)$ is a stochastic process such that;

1. $W(0) = 0$ with probability 1;
2. $W(t+h) - W(t)$ is independent of $W(t)\ \forall\ h \geq 0$;
3. $W(t+h) - W(t) \sim N(0, h)$;
4. $W(t)$ is continuous with probability 1.

Thus the Weiner increment dW_h on the interval $[t\ \ t+h]$ is a normally distributed random variable with mean 0 and variance h.

For the additive noise terms used in this thesis, where g is constant, we need only describe the Itô integral of Eqn. 4.4, as it is equivalent to the alternative Stratonovich formulation in this case (Kloeden and Platen, 2010). Eqn. 4.4 may be written, on integration, as

$$\mathbf{X}(t+h) = \mathbf{X}(t) + \int_t^{t+h} f\left(X(s)\right) ds + \int_t^{t+h} g\left(X(s)\right) d\mathbf{W}(s). \tag{4.5}$$

In the Itô formulation, the stochastic integral is defined by taking the mean square limit of the Riemann sum,

$$\int_t^{t+h} g\left(X(s)\right) d\mathbf{W}(s) = \sum_{i=0}^{n-1} g\left(\mathbf{X}(t_i)\right) \left(\mathbf{X}(t_{i+1}) - \mathbf{X}(t_i)\right), \tag{4.6}$$

where $t = t_0 \leq t_1 \ldots \leq t_n = t + h$ is a partition of the interval $[t\ t + h]$.The limit is taken as the number of points in the partition goes to infinity.

In order to evaluate trajectories of $\mathbf{X}(t)$ in this thesis we use an Euler-Maruyama method (Maruyama, 1955), which we have implemented within Chaste. The Euler-Maruyama method is analogous to the Euler method for the solution of deterministic ODEs. In this method the trajectory is simulated over each time interval $[t\ t + h]$ as

$$\mathbf{X}(t + h) = \mathbf{X}(t) + f\left(\mathbf{X}(t)\right) h + g\left(\mathbf{X}(t)\right) d\mathbf{W}_h, \tag{4.7}$$

where $d\mathbf{W}_h$ is a vector of d Weiner increments. The Euler-Maruyama method has strong order 0.5 and weak order 1. Loosely, this means that the error in the mean difference between the simulated and exact solution is proportional to h, and the mean difference in the absolute error between the simulated and the exact solution is proportional to $\sqrt{h}$.

4.4 The Finite Element Method

A brief summary of the finite element method (FEM) and the use of this method to solve the monodomain equation follows. The FEM has emerged as one of the most popular choices for the numerical solution of the monodomain and bidomain equations. One of the major reasons for this is that the FEM is well suited to complex geometries such as the ventricles. When performing computer simulations on any geometry a discretisation of the tissue is required, known as a mesh. A mesh may consist of either discrete points as in the finite difference method, or consist of multi-dimensional elements as for the FEM. The use of these elements allows the representation of curved surfaces which are more difficult to achieve in schemes such as finite differences.

Numerous reviews have addressed the use of FEMs for the solution of the bidomain equations (Vigmond et al., 2008; Pathmanathan et al., 2010). For brevity, we just describe this in the case of the monodomain equations here (Eqs. (3.36) and (3.37)). We drop the

constant $\frac{\lambda}{1+\lambda}$ from Eq. (3.36) for clarity. We follow the method presented by Pathmanathan et al. (2010). Let v be a function satisfying Eqs. (3.36) and (3.37) on a domain Ω and its boundary $\partial\Omega$ respectively. Then,

$$\nabla \cdot \big(\sigma \nabla v\big) = \chi\big(C_m \frac{\partial v}{\partial t} + I_{ion}\big) - I_{stim} \text{ in } \Omega, \tag{4.8}$$

$$\mathbf{n} \cdot \big(\sigma \nabla v\big) = 0 \text{ on } \partial\Omega. \tag{4.9}$$

To begin, we establish a discretisation in time. As described in Pathmanathan et al. (2010), we use a semi-implicit time discretisation as follows. Given a time step Δt, at time $t = n\Delta t$ we define $v^n(x) = v(x, n\Delta t)$. This then gives the following discrete-time approximation to Eq. (4.8)

$$\nabla \cdot \big(\sigma \nabla v^n\big) = \chi\big(C_m \frac{v^n - v^{n-1}}{\Delta t} + I_{ion}^{n-1}\big) - I_{stim} \text{ in } \Omega, \tag{4.10}$$

$$\mathbf{n} \cdot \big(\sigma \nabla v^n\big) = 0 \text{ on } \partial\Omega. \tag{4.11}$$

where I_{ion}^{n-1} denotes the ionic current calculated at the previous time step.

The FEM is based upon the idea of finding a weak solution to Eqs. (3.32)–(3.35) or Eq. (3.36) and (3.37). This concept is outlined below. For any continuous and once differentiable function u defined on Ω we must have,

$$\nabla \cdot \big(\sigma \nabla v^n\big) u = \Big(\chi\big(C_m \frac{v^n - v^{n-1}}{\Delta t} + I_{ion}^{n-1}\big) - I_{stim}\Big) u, \tag{4.12}$$

and therefore

$$\int_\Omega \nabla \cdot \big(\sigma \nabla v^n\big) u \, d\Omega = \int_\Omega \Big(\chi\big(C_m \frac{v^n - v^{n-1}}{\Delta t} + I_{ion}^{n-1}\big) - I_{stim}.\Big) u \, d\Omega. \tag{4.13}$$

Any such function u is said to be a *test function*. Then, applying the divergence theorem to

the left hand side of Eq. (4.13),

$$\int_\Omega \nabla \cdot \big(\sigma \nabla v^n\big) u \, d\Omega = -\int_\Omega \big(\sigma \nabla v^n\big) \cdot \nabla u \, d\Omega \; + \int_{\partial\Omega} u \sigma \nabla v^n \cdot \mathbf{n}, \tag{4.14}$$

$$= -\int_\Omega \big(\sigma \nabla v^n\big) \cdot \nabla u \, d\Omega, \tag{4.15}$$

since $\mathbf{n} \cdot \big(\sigma \nabla v\big) = 0$ on $\partial\Omega$ from the boundary condition in Eq. (4.11). Thus we have,

$$\int_\Omega \big(\sigma \nabla v^n\big) \cdot \nabla u + \Big(\chi\big(C_m \frac{v^n - v^{n-1}}{\Delta t} + I_{ion}^{n-1}\big) - I_{stim.}\Big) u \, d\Omega = 0, \tag{4.16}$$

from Eqs. (4.13) and (4.15). We then define v^n to be a *weak solution* of Eq. (4.8) if v^n satisfies Eq. (4.16) for all test functions u on Ω.

Having defined a weak solution to these equations, we can now illustrate how a numerical method can be developed to solve for such a solution to Eqs. (4.10) and (4.9). For the finite element method, we must divide our domain into discrete elements. In this thesis, this takes the form of a triangulation, although other schemes do exist such as hexahedral meshes (Triedman et al., 2008). Points in the domain, known as nodes, are selected. The nodes then form a set of intervals on the domain (two nodes) in one dimension. In two dimensions it forms a set of triangles covering the domain (three nodes) and in three dimensions it forms a set of tetrahedrons covering the domain (four nodes). These are the finite elements referred to in the naming of the system, and the nodes and elements together form a *mesh*. There are several relatively simple conditions on how these elements must interlock, but we do not cover these in detail here. Briefly, the elements must cover the entire space, must not overlap, and the nodes of an element may not be a point on an edge of another element which is not a node in that element. There are also conditions on the regularity of the shape of the elements — they must all be similar in shape, though they need not be the same.

On each element, we define linear functions taking value 1 at each node in turn, and zero at the others. As an example, given a triangle with corners (0,0), (1,0), and (0,1),

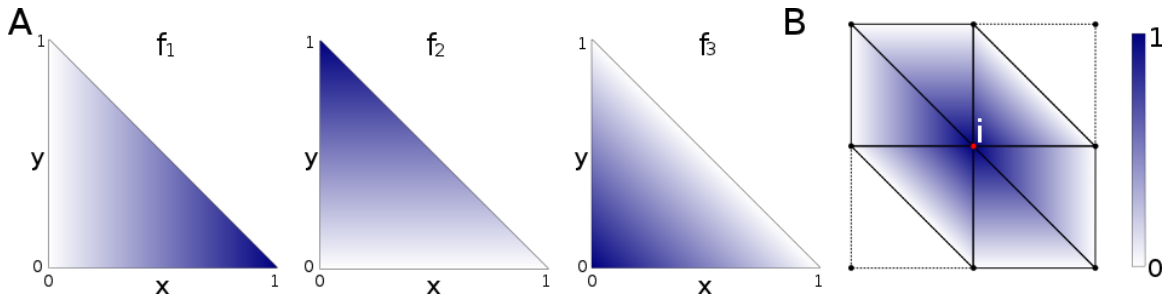

Figure 4.2: **Construction of linear basis functions for the finite element method.** A) Linear functions f_1, f_2 and f_3 as described in the text shown on one triangular element. B) Schematic of the basis function ϕ_i and the corresponding support in a two-dimensional mesh. The node i is indicated in red.

these functions are

$$f_1(x, y) = x, \tag{4.17}$$

$$f_2(x, y) = y, \tag{4.18}$$

$$f_3(x, y) = 1 - x - y, \tag{4.19}$$

as shown in Fig. 4.2 A. Now, for each node i in the mesh we can define a function $\phi_i : \Omega \rightarrow [0\,1]$ that takes value 1 at node i and 0 at all other nodes in the mesh. These functions are constructed by considering each node i in turn. For each element containing node i, the linear function (as above) taking value 1 on i and 0 on all other nodes in the element is taken to be the value of ϕ_i on that element. On all elements not containing i, ϕ_i takes value 0. This is illustrated in Fig. 4.2 B. The elements on which ϕ_i is non-zero are known as the *support* of ϕ_i. These functions are piecewise linear. The set of these functions is then linearly independent and so they form a basis for a subspace of $H^1(\Omega)$, the Sobolev space of square-integrable functions on Ω whose first weak derivative is also square-integrable. This basis shall be referred to as Φ_m for the current mesh m. Note that it is possible to use higher order basis functions for finite element methods and this would enable the use of coarser meshes (Arthurs et al., 2012).

At each timestep we will look for an approximate solution $\tilde{v}^n$ to Eqs. (4.8) and (4.9), that

is a member of the span of Φ_m (a linear combination of elements of Φ_m). Thus

$$\tilde{v}^n = \sum_i \alpha_i^n \phi_i, \tag{4.20}$$

for constants α_i. This has the substantial advantage of changing from the infinite dimensional space $H^1(\Omega)$ for the solution to a finite one. Furthermore, since the functions ϕ_i are a basis of this space, it suffices to check that Eq. (4.16) holds for all ϕ_i in Φ_m. Substituting into this equation, we obtain the condition

$$\int_\Omega \left(\sigma \nabla \tilde{v}^n\right) \cdot \nabla \phi_j + \left(\chi \left(C_m \frac{\tilde{v}^n - \tilde{v}^{n-1}}{\Delta t} + I_{ion}\right) - I_{stim}.\right) \phi_j \, d\Omega = 0, \; \forall \phi_j \in \Phi_m \tag{4.21}$$

and so by linearity,

$$\sum_i \alpha_i^n \int_\Omega \left((\sigma \nabla \phi_i) \cdot \nabla \phi_j\right) + \chi C_m \frac{1}{\Delta t} \left(\sum_i \alpha_i^n \int_\Omega \phi_i \phi_j - \sum_i \alpha_i^{n-1} \int_\Omega \phi_i \phi_j\right) + \ldots$$
$$\int_\Omega \left(\chi I_{ion}^{n-1} - I_{stim}\right) \phi_j = 0, \; \forall \phi_j \in \Phi_m \tag{4.22}$$

where α_i^{n-1} are known for all i. If we define the mass matrix $\mathbf{M} = \left(\int_\Omega \phi_i \phi_j\right)$, the stiffness matrix $\mathbf{S} = \left(\int_\Omega (\sigma \nabla \phi_i) \cdot \nabla \phi_j\right)$, $\mathbf{I}^{n-1} = \left(\int_\Omega \left(\chi I_{ion}^{n-1} - I_{stim}\right) \phi_j\right)$, and $\boldsymbol{\alpha}^n = (\alpha_i^n)$, we arrive at the following matrix-vector equation system,

$$\mathbf{S}\boldsymbol{\alpha}^n + \chi C_m \frac{1}{\Delta t} \mathbf{M}\left(\boldsymbol{\alpha}^n - \boldsymbol{\alpha}^{n-1}\right) + \mathbf{I}^{n-1} = 0, \tag{4.23}$$

and re-arranging gives the linear system

$$\left(\Delta t \mathbf{S} + \chi C_m \mathbf{M}\right) \boldsymbol{\alpha}^n = \chi C_m \mathbf{M} \boldsymbol{\alpha}^{n-1} - \Delta t \mathbf{I}^{n-1}, \tag{4.24}$$

which we must solve for each time step n.

Solving the linear system in Eq. (4.24) is non-trivial as the matrices involved are typically very large. The problem is tractable as they are generally sparse, due to the definition

of ϕ_i meaning that most of the matrix entries are zero. We do not discuss the iterative methods such as GMRES (Saad and Schultz, 1986) and conjugate gradients (Hestenes and Stiefel, 1952) used in Chaste (section 4.5) for solving these linear systems here. See also Pathmanathan et al. (2011) for treatment of ionic model state variables.

4.5 Chaste

Chaste is the Cancer, Heart and Soft Tissue Environment, developed in the Computational Biology group at the University of Oxford (Pitt-Francis et al., 2009; Mirams et al., 2013). Chaste is primarily used for the simulation of monodomain and bidomain models using FEM, and has an increasingly powerful set of tools for ODE simulation through integration with CVODE as described in section 4.2.

A recent study provided an N-version benchmark of 17 such codes (Niederer et al., 2011). This study gave each code a relatively simple problem — a cuboid of dimensions 3mm $\times$ 7mm $\times$ 20mm was provided with a stimulus in one corner. Simulations were performed at three different mesh resolutions, 0.5mm, 0.2mm and 0.1mm, and with three PDE time steps, 0.05ms, 0.01ms and 0.005ms, using the Ten Tusscher and Panfilov (2006) human ventricular cell model (epicardial variant). Activation times across a diagonal plane were then compared and analysed. The study concluded that, whilst all the software did converge to very similar answers by the final mesh resolution, Chaste produced converged results at much higher mesh resolutions than all but one of the other codes (acCELLerate, Seemann et al. 2010). Throughout this thesis, Chaste will be used as the cardiac simulator of choice both for isolated cell simulations through CVODE, and for the monodomain equations. There are six major reasons for this choice,

1. Using state variable interpolation, Chaste converges in conduction velocity at lower mesh resolution than other leading codes (Niederer et al. 2011, see above);

2. Easy import of models from the CellML model repository via PyCML (Cooper, 2009; Cooper et al., 2011a);

3. Parallelised code can be run on supercomputing facilities, with near linear speed-up up to 512 cores, and 70% up to 4000 cores (Bernabeu et al., 2013);

4. Open-source software means that results can be checked by any external reviewer, increasing transparency in the academic process;

5. In-house development team means that bug hunting can be done quickly and interactively in a way that is impossible with closed-source codes;

6. Open source format allows modification of existing subroutines within the source code, for example the fibre generator used in Chapter 8.

4.6 Convergence Analysis

4.6.1 Conduction Velocity Convergence

As the upstroke is the stiffest part of the AP, affecting conduction, convergence in conduction velocity is typically used in order to assess the convergence of a numerical scheme, both in terms of mesh resolution and the PDE time step. Once there is no significant change in the conduction velocity, the simulation is considered to be converged. Since the tissue conductivity will affect conduction velocity a convergence analysis is typically required for the minimum conductivity value as lower conductivities require smaller mesh resolutions.

4.6.2 Stochastic Convergence

In order to investigate convergence properties of stochastic models we use a technique for convergence testing known as a conserved Brownian path (Gaines and Lyons, 1997). A conserved Brownian path is a path sampled such that at multiple temporal resolutions it remains a Brownian path. To construct such a path, we sample a Brownian path at the lowest temporal resolution of interest, in this case 0.01ms. This Brownian path $b(t)$ is

sampled in the usual way, i.e.

$$d_t b = dW_t, \tag{4.25}$$

where $b(t)$ is a Weiner process whose Gaussian increment W_h has mean 0 and variance h on the increment $[t \quad t+h]$. Hence $W_t \sim N(0, \sqrt{h})$. We now construct a new Brownian path from the original Brownian path, which preserves the increments of the old path, but has a resolution of $\frac{h}{2}$. Consider each time increment $[t \quad t+h]$ in the original path in turn. We bisect this interval to get two subintervals $[t \quad t+\frac{h}{2}]$ and $[t+\frac{h}{2} \quad t+h]$. We now wish to construct a random variable for each subincrement, such that both new variables are Weiner increments on the subintervals $[t \quad t+\frac{h}{2}]$ and $[t+\frac{h}{2} \quad t+h]$. Furthermore, their sum must be equal to dW_t, to conserve the original Brownian path.

Let $Z \sim N(0, \frac{\sqrt{h}}{2})$ be independent of W_h. Then consider the increments $\frac{1}{2}W_h - Z$ and $\frac{1}{2}W_h + Z$. We claim that these are Weiner increments on the intervals $[t \quad t+\frac{\Delta t}{2}]$ and $[t+\frac{\Delta t}{2} \quad t+\Delta t]$, respectively.

Proof: To show that each is a Weiner increment, we must show that four conditions hold.

1. $\frac{1}{2}W_h - Z$ and $\frac{1}{2}W_h + Z$ are Gaussian: Note that by definition, W_h and Z are Gaussian. As a linear combination of Gaussian variables is also Gaussian, it therefore follows that the random variables $\frac{1}{2}W_h - Z$ and $\frac{1}{2}W_h + Z$ are also Gaussian.

2. $\mathrm{E}\left(\frac{1}{2}W_h - Z\right) = 0$ and $\mathrm{E}\left(\frac{1}{2}W_h + Z\right) = 0$:

$$\mathrm{E}\left(\frac{1}{2}W_h - Z\right) = \frac{1}{2}\mathrm{E}\left(W_h\right) - \mathrm{E}\left(Z\right), \tag{4.26}$$

$$= 0, \tag{4.27}$$

since by definition $\mathrm{E}(W_h) = 0$ and $\mathrm{E}(Z) = 0$. Similarly, $\mathrm{E}\left(\frac{1}{2}W_h + Z\right) = 0$.

3. $\mathrm{Var}\left(\frac{1}{2}W_h - Z\right) = \frac{h}{2}$ and $\mathrm{Var}\left(\frac{1}{2}W_h + Z\right) = \frac{h}{2}$: Since for two random variables X and Y,

and $a, b \in \mathrm{R}$,

$$\mathrm{Var}(aX + bY) = a^2 Var(X^2) + b^2 Var(Y^2) + 2ab\mathrm{Cov}(X, Y), \tag{4.28}$$

where Cov is the covariance, we have,

$$\mathrm{Var}\left(\frac{1}{2}W_h - Z\right) = \frac{1}{4}\mathrm{E}(W_h^2) + \mathrm{E}(Z^2) - 2.\frac{1}{2}\mathrm{Var}(W_h Z), \tag{4.29}$$

and as W_h and Z are independent, hence $\mathrm{Cov}(X, Y) = 0$, Eqn. (4.29) gives,

$$\mathrm{Var}\left(\frac{1}{2}W_h - Z\right) = \frac{1}{4}\mathrm{E}(W_h^2) + \mathrm{E}(Z^2). \tag{4.30}$$

Now, since for any random variable X we have $\mathrm{Var}(X) = \mathrm{E}(X^2) - \big(\mathrm{E}(X)\big)^2$, and by definition $\mathrm{E}(W_h) = 0$ and $\mathrm{E}(Z) = 0$, we must have $\mathrm{E}(W_h^2) = h$ and $\mathrm{E}(Z^2) = \frac{h}{4}$. Thus,

$$\begin{aligned}
\mathrm{Var}\left(\frac{1}{2}W_h - Z\right) &= \frac{1}{4}\mathrm{E}(W_h^2) + \mathrm{E}(Z^2), && (4.31)\\
&= \frac{1}{4}h + \frac{h}{4}, && (4.32)\\
&= \frac{h}{2}. && (4.33)
\end{aligned}$$

A similar method gives $\mathrm{Var}\left(\frac{1}{2}W_h + Z\right) = \frac{h}{2}$.

4. $\frac{1}{2}W_h - Z$ and $\frac{1}{2}W_h + Z$ are independent: Note that $\frac{1}{2}W_h$ and Z are independent and have the same mean (0) and variance $(\frac{h}{2})$, and that they are normal. For any two independent and identically distributed normal distributions X and Y we have that $X + Y$ and $X - Y$ are also independent and identically distributed. Hence $\frac{1}{2}W_h - Z$ and $\frac{1}{2}W_h + Z$ are independent.

Hence all four conditions hold and the two variables are Weiner increments on the intervals $[t \quad t + \frac{\Delta t}{2}]$ and $[t + \frac{\Delta t}{2} \quad t + \Delta t]$.

Furthermore, $(\frac{1}{2}W_h - Z) + (\frac{1}{2}W_h + Z) = W_h$, and so setting the variables $(\frac{1}{2}W_h - Z)$ and $(\frac{1}{2}W_h + Z)$ as the Weiner increments on the intervals $[t \quad t + \frac{\Delta t}{2}]$ and $[t + \frac{\Delta t}{2} \quad t + \Delta t]$ respectively conserves the original increment W_h over $[t \quad t + \Delta t]$.

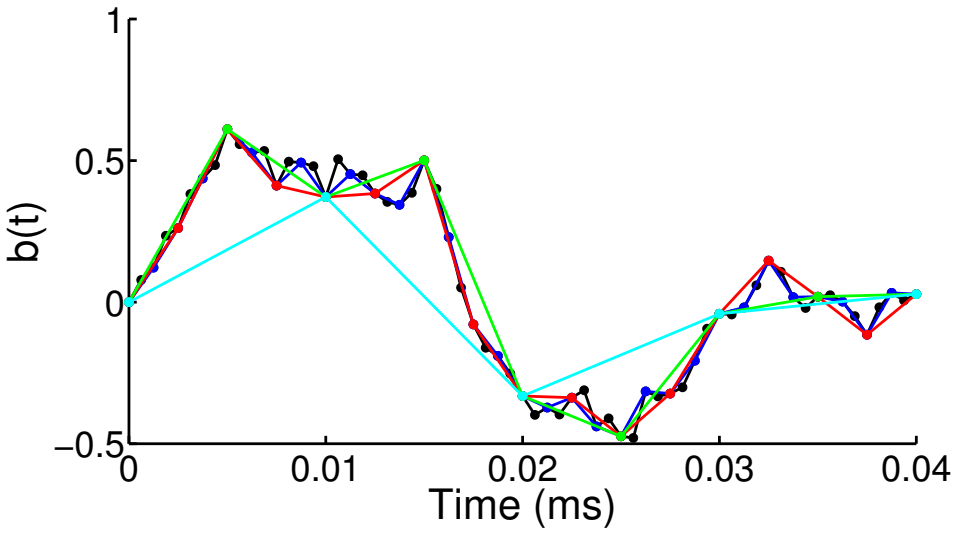

Figure 4.3: **Conserved Brownian path.** Constructing a conserved Brownian path with timesteps 0.01ms (cyan), 0.005ms (green), 0.0025ms (red), 0.00125ms (blue) and 0.000625ms (black).

When constructing the conserved Brownian paths used for convergence testing we use an initial time step of 0.01ms, to which the above construction is applied recursively to construct conserved Brownian paths with timesteps 0.005ms, 0.0025ms, 0.00125ms and 0.000625ms. An example of the construction of a conserved Brownian path can be found in Fig. 4.3, showing five levels of refinement from the coarsest (0.01ms, cyan) to the finest (0.000625ms, black).

In order to test convergence using the conserved path we pre-generate a conserved Brownian path for each of the variables under investigation, and for each node in the mesh under investigation. Simulations are performed for all tissue conductivities under investigation by taking the appropriate Weiner increment by summing over the smaller timesteps in the conserved Brownian path for each variable and each node, instead of randomly generating a Weiner increment at each time step. The result is a set of quasi-stochastic simulations that may be directly compared to one another at decreasing time steps. The resulting APD_{90}s are then compared for stochastic simulations to check convergence.

4.7 Discussion

We have now reviewed the mathematical and numerical techniques used to simulate cardiac electrophysiology in this thesis. It is essential for computational modellers to consider the numerical methods used in solving their tissue electrophysiology equations. (Carusi et al., 2012). There are two major reasons for this. Firstly, an inadequate or nonconverged method for computing numerical solutions to the monodomain or bidomain equations will produce unreliable answers. For example, if the mesh used for simulation has elements that are too large then the method will not converge to the correct conduction velocity (as in the Niederer et al. (2011) benchmark above). Thus, activation times will not be correct.

The other major impact of numerical and computational methods for the modeller lies in the tractability of their proposed theoretical studies. By speeding up cardiac simulation with improved numerical or software engineering methods there is the possibility of opening up new cardiac modelling studies. This will also come about through improved computational hardware: running a whole heart simulation on a highly detailed human mesh using a desktop PC is currently impossible, but can be done in tractable timescales on supercomputers. We can also use our computational resources more effectively by improving numerical schemes, thereby speeding up simulations. This requires a concerted effort between numerical analysts, software engineers, and computational modellers.

Chapter 5

Prediction of Electrophysiological Changes in Heart Failure Based on mRNA Expression Data

5.1 Introduction

We have seen in Chapter 2 that a potential source of variability in the electrophysiology of cardiac cells lies at the level of ion channel expression. In this chapter, we expand upon the previous studies presented in Chapter 3 by investigating a particular disease state: human heart failure. We aim to investigate how inter-individual variability may impact electrophysiological remodelling in failing human ventricles.

A growing number of studies examine mRNA expression levels in human cardiac tissue in order to characterize electrophysiological remodelling associated with disease conditions such as heart failure and atrial fibrillation (Gaborit et al., 2010; Soltysinska et al., 2009; Ambrosi et al., 2013). Recent studies have shown alterations in expression of mRNA transcripts in human failing hearts compared to non-failing hearts (Soltysinska et al., 2009; Ambrosi et al., 2013). Furthermore, recent optical mapping measurements have also demonstrated differences in AP and calcium transients (CaT) between failing and non-

failing human hearts (Glukhov et al., 2010; Lou et al., 2011; Glukhov et al., 2012), with potentially pro-arrhythmic implications (Tomaselli and Márban, 1999; Tomaselli and Zipes, 2004; Nattel et al., 2007; Cutler et al., 2011).

Linking mRNA changes to AP and CaT alterations has several complications (Nattel et al., 2010). Firstly, mRNA expression is only one of the factors determining ion channel expression at the cell membrane. Translation rate, binding with channel subunits, methylation, membrane localization, trafficking and phosphorylation all affect the activity of ion channels. Furthermore, variability resulting from, for example, age, gender, spatial location within the heart and circadian rhythm will all affect mRNA expression levels in cardiac tissue.

Nonetheless, several recent model studies have attempted to use mRNA expression data as a proxy for changes in electrophysiological data (O'Hara et al., 2011; Yang and Clancy, 2012). mRNA expression data provide information on heterogeneity and variability in the heart, in both healthy and diseased states. In this chapter, we aim to show how computational modelling can be used to understand the electrophysiological consequences of differences in mRNA expression levels between failing and non-failing human hearts. The methodology proposed is flexible and can be applied to any set of mRNA measurements and models. Our method is tailored to a particular series of experiments, recently published by Ambrosi et al. (2013). We will seek to establish whether information contained in mRNA transcription data can predict the functional differences in AP and CaT reported between failing and non-failing human hearts. We develop an approach that takes into account potential sources of variability in the change in conductance due to mRNA expression.

We construct a failing and a non-failing cell model population based on a biophysically detailed human ventricular model (O'Hara et al., 2011), as the question under investigation requires the incorporation of channel level phenomena not captured by phenomenological models. Each population consists of an ensemble of cell models sharing the same equations representing ionic current kinetics, but having different conductance values. As in the studies by Romero et al. (2009), Sarkar and Sobie (2011), Pueyo et al. (2011), Rodríguez

Table 5.1: **Parameters under investigation**

Gene	Current	Parameter	Regulation in heart failure (Ambrosi et al., 2013)
KChIP2	I_{to}, I_{CaL} (a)	G_{to}, G_{CaL}	$\downarrow$
NCX1	I_{NaCa}	G_{NaCa}	$\uparrow$ (b)
Serca2A	SERCA	J_{up}	$\downarrow$
Kv4.3	I_{to}	G_{to}	$\downarrow$
Kv11.1 / *HERG*	I_{Kr}	G_{Kr}	$\downarrow$
Kv7.1	I_{Ks}	G_{Ks}	$-$
Kir2.1	I_{K1}	G_{K1}	$-$

a) *KChIP2* has recently been shown to form an accessory subunit of I_{CaL} (Thomsen et al., 2009).
b) *NCX1* was downregulated in non-ischæmic cardiac myopathy patients but showed no difference from the non-failing group in ischæmic cardiac myopathy.

et al. (2012), Sarkar et al. (2012) and Yang and Clancy (2012), we incorporate variability, which may arise from a variety of sources, by using a range of values for ion channel conductances rather than a single parameter value. The failing population is then constructed by additionally incorporating the upregulation or downregulation of conductances corresponding to mRNA expression changes reported in heart failure (Ambrosi et al., 2013).

AP and CaT properties are quantified across both populations and compared to experimental measurements obtained in failing and non-failing human ventricles. We then predict the electrophysiological response of human ventricular myocytes at different stimulation rates and quantify the relative importance of each ionic current in determining AP and CaT differences in the human non-failing and failing cell populations.

5.2 Methods

5.2.1 mRNA expression data

We use mRNA expression data (Ambrosi et al., 2013) to determine directions of changes in ionic conductances in failing human cardiomyocytes compared with non-failing human

cardiomyocytes, as summarized in Table 5.1. Three gene transcripts show a trend towards downregulation in heart failure, contributing to the conductances of L-type Ca^{2+} current I_{CaL} (G_{CaL}), transient outward current I_{to} (G_{to}), and the SERCA pump (J_{up}). Gene transcripts for the rapid component of the delayed rectifier K^+ current I_{Kr} (HERG) also show a trend towards downregulation and are included in the simulations by altering the conductance of I_{Kr} (G_{Kr}). One gene transcript shows a trend towards upregulation in the heart failure cases, contributing to the conductance of the Na^+/Ca^{2+} exchange current I_{NaCa} (G_{NaCa}). Two further currents are included in the analysis as they are active during the repolarisation phase of the AP, namely the inward rectifier current I_{K1} and the slow component of the delayed rectifier K^+ current I_{Ks}. As gene transcripts associated with these channels show no trend in the data published by Ambrosi et al. (2013) they are considered to have natural variability only in both populations.

5.2.2 Populations of human failing and non-failing cell models

The O'Hara-Rudy (ORd) human ventricular endocardial model (O'Hara et al., 2011) is used to generate populations of non-failing and failing cell models. Each population contained 16,384 models sharing the same equations as the ORd model but different parameter sets. This is equivalent to the number of simulations required for a grid search with four points in each dimension. The failing and non-failing populations are constructed by Monte-Carlo sampling of the parameters under investigation (G_{Kr}, G_{Ks}, G_{K1}, G_{CaL}, J_{up}, G_{NaCa}, G_{to}) from uniform distributions over the ranges shown in Fig. 5.1.

5.2.3 Stimulation protocol

The stimulation protocol mimics the one used by Lou et al. (2011) to obtain optical mapping measurements in failing versus non-failing left ventricular wedges. Cell models are stimulated 100 times at each of the following pacing cycle lengths (CLs) in a step protocol; 1500ms, 1000ms, 900ms, 800ms, 700ms, 600ms, 500ms, 450ms, 400ms, 350ms and

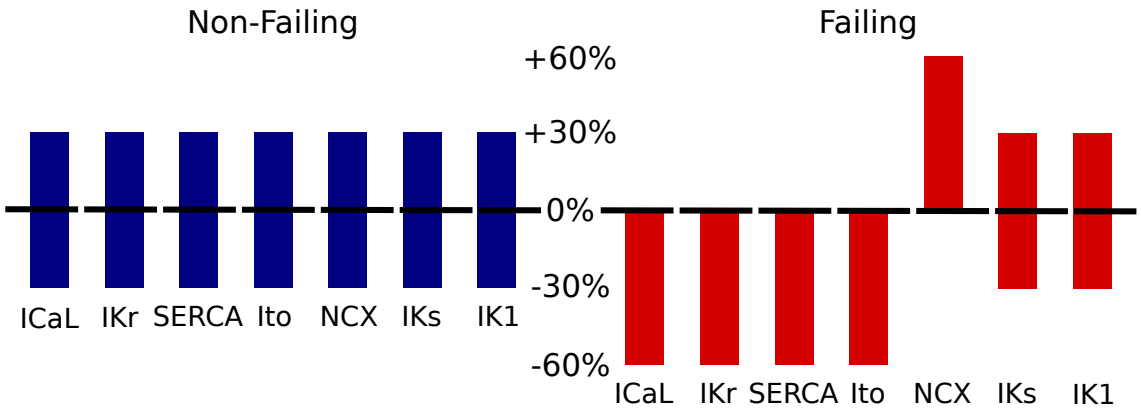

Figure 5.1: **Parameter ranges for the failing and non-failing cell model populations.** The non-failing parameter ranges are shown in blue, and the failing parameter ranges are shown in red. In the non-failing population, all parameters vary uniformly by between -30% and +30% of their original value (from the ORd model). In the failing population, the downregulated parameters G_{Kr}, G_{CaL}, J_{up} and G_{to} vary by between 0 % and -60% from their original value, and the upregulated parameter G_{NaCa} varies by between 0% and +60% from its original value. The non-regulated parameters G_{Ks} and G_{K1} vary between -30% and +30% from their original value as in the non-failing population.

300ms. A stimulus current of magnitude -80μA/cm^2 and duration 0.5ms is applied at each pace.

5.2.4 Biomarkers

As illustrated in Fig. 5.2, the following biomarkers are calculated from the two last APs simulated for each CL: AP duration to 80% repolarisation (APD_{80}), AP triangulation (APD_{3080}) defined as the ratio between APD to 30% repolarisation (APD_{30}) and APD_{80}, CaT duration to 80% of repolarisation ($CaTD_{80}$), CaT triangulation ($CaTD_{3080}$) defined as the ratio between CaT duration to 30% repolarisation ($CaTD_{30}$) and $CaTD_{80}$, maximum cytosolic calcium concentration (CaTMax) and the delay between the AP and CaT upstrokes (DAP-CaT). The occurrence of voltage and calcium alternans is defined as a difference of $\geq$5ms between the APD_{80} or $CaTD_{80}$, respectively, in the penultimate and final APs.

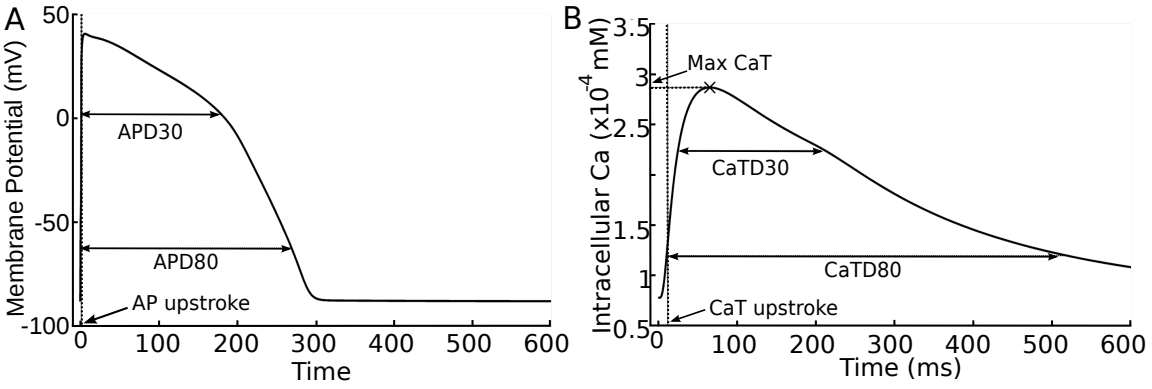

Figure 5.2: **Biomarkers calculated from simulated AP and CaT traces using the baseline ORd model.** A) shows the calculation of APD_{80}, APD_{30} and APD_{3080}, and B) shows $CaTD_{30}$, $CaTD_{80}$, $CaTD_{3080}$ and CaTMax. AP-CaT delay is the difference between the AP and CaT upstroke times.

5.2.5 Regression analysis

To quantify the relative importance of ionic conductances in determining changes in the biomarkers, linear regression (Sobie, 2009; Sarkar and Sobie, 2010) is performed on the failing and non-failing populations, leaving out the cases showing alternans in APD_{80} or $CaTD_{80}$. For each population, the following procedure is applied for each biomarker. Biomarker outputs are mean centred and normalised with respect to their standard deviation at each CL, as in Sobie (2009). We seek linear regression coefficients β_i for each of the $i = 1, \ldots, n$ parameters under investigation such that for each of the $j = 1, \ldots, m$ cells their predicted biomarker output y_j^p is given by

$$y_j^p = \sum_{i=1}^{n} \beta_i x_{ij}, \quad j = 1, \ldots, m.$$

Here j denotes the current cell, and x_{ij} denotes the scaling of the ith conductance for the jth cell. This may be re-written as the matrix system

$$\mathbf{Y^p} = \mathbf{Xb},$$

where the coefficients of $\mathbf{Y^p}$ are (y_j^p), the coefficients of $\mathbf{X}$ are (x_{ij}) and the coefficients of $\mathbf{b}$ are (β_i). Let $\mathbf{Y}$ have coefficients (y_j), the computed biomarker values for each cell.

We want to find a solution $\mathbf{b}$ such that the least squares difference between y_j and y_j^p is minimised over all cells j. This solution is given by $\mathbf{b} = (\mathbf{X}^T\mathbf{X})^{-1}\mathbf{X}^T\mathbf{Y}$. The vector $\mathbf{b}$ then contains the linear regression coefficients. This is repeated for each biomarker at each CL.

To determine the effectiveness of this fit, the correlation coefficient R^2 (R-squared) is computed for each linear regression fit. This coefficient is computed as

$$R^2 = 1 - \frac{\sum_{j=1}^{m} \left(y_j^p - y_j\right)^2}{(m-1)\,\mathrm{Var}(\mathbf{Y})}.$$

The closer R^2 is to one, the more of the variance in the data is accounted for by the linear fit.

5.2.6 Numerical methods

All numerical simulations are performed using Chaste. A CellML (Lloyd et al., 2008) implementation of the ORd model is used from the functional curation database available within Chaste (Cooper et al., 2011b). The ordinary differential equations are integrated using CVODE as described in Chapter 4. We use absolute and relative error tolerances of 10^{-5} and 10^{-7}, respectively. The output time step for biomarker calculation was 1ms. All postprocessing of traces to calculate biomarker values was performed within the Chaste environment. Analysis of biomarkers was performed using Matlab. A Chaste user project containing the simulation codes used in this study is available to download from the Chaste website. Matlab data analysis scripts are also included. All simulations are performed on a 512 core cluster utilising 2.8GHz Intel processors at the Oxford Supercomputing Centre (OSC).

5.3 Results

5.3.1 Voltage and calcium transients

Fig. 5.3 shows sample AP and Ca transients from the non-failing and failing populations at CLs of 1500ms and 300ms. Histograms based on these traces, shown in Fig. 5.4, illustrate the variability encountered across populations for each biomarker. Simulation results show major differences in biomarker values between the failing and non-failing populations at all CLs, but an overlap between the two populations also exists. The circle in each panel indicates the biomarker value obtained using the standard ORd model. The cross in each panel indicates the biomarker value obtained by including specific values of 60% down-regulation of G_{CaL}, G_{to}, G_{Kr} and J_{up} and 60% upregulation of G_{NaCa} as indicated by the mean change in mRNA expression in Ambrosi et al. (2013) (therefore without considering electrophysological variability in ionic currents and electrophysiological measurements). As expected, biomarker values in the non-failing population are centered around results marked by the circle. In contrast, the cross is often located at the higher end of biomarker values for APD_{80}, $CaTD_{80}$, $CaTD_{80}$ and DAPCaT and at the lower end for APD_{3080}, which could lead to an overestimation of remodelling-related changes. Results corresponding to each biomarker are discussed in detail below, and compared to previously published experimental studies, summarized in Table 5.2. A summary of the experimental data may be found in Tables 1–7 in Appendix A.

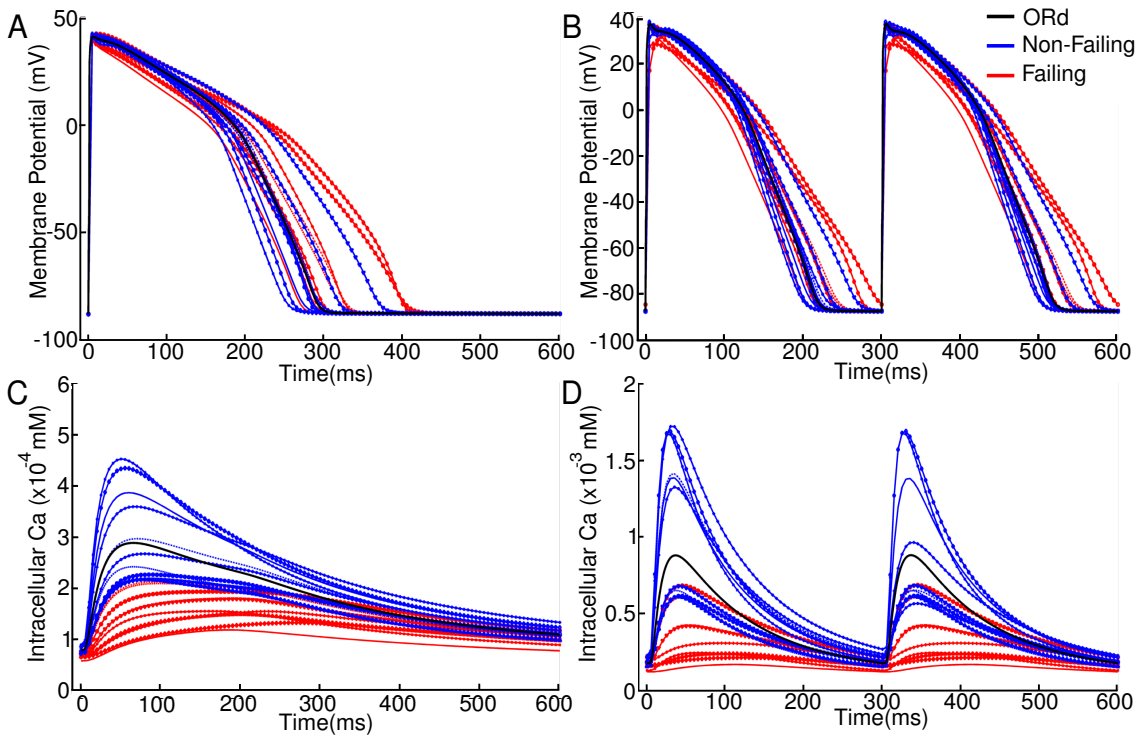

Figure 5.3: **Sample AP and CaT traces obtained from the non-failing (blue) and failing (red) populations.** Traces are shown for CL=1500ms (A,C) and 300ms (B,D). The AP for the standard ORd endocardial model is shown in black.

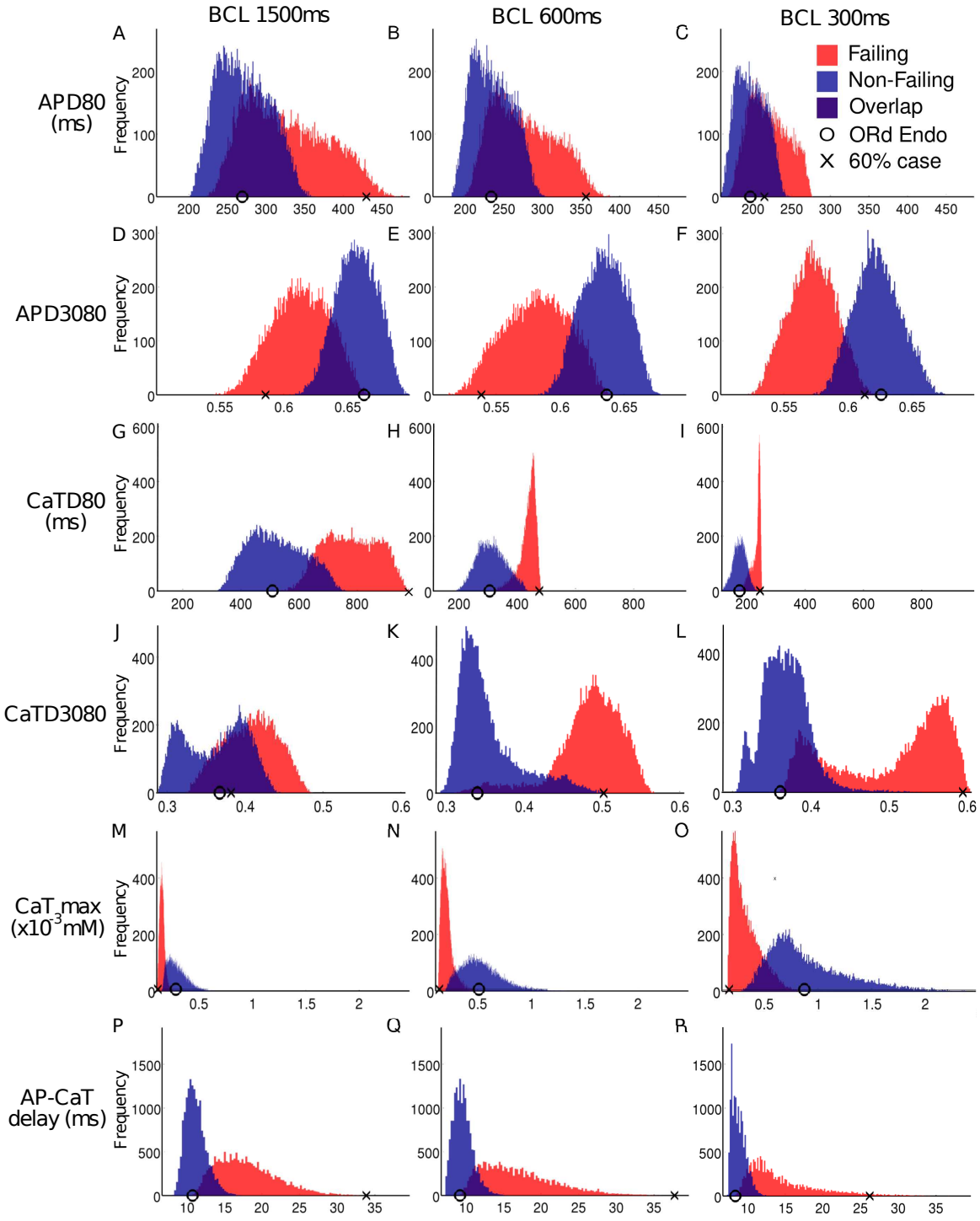

Figure 5.4: **Histograms showing biomarker values obtained for the non-failing (blue) and failing (red) cell model populations.** Histograms shown are recorded at CL = 1500ms, 600ms and 300ms for A–C) APD_{80}, D–F) APD_{3080}, G–I) $CaTD_{80}$, J–L) $CaTD_{3080}$, M–O) CaTmax and P–R) AP-CaT delay. In each panel, the circle indicates biomarker values obtained with the standard ORd model whereas the cross indicates the value obtained with the ORd model including 60% downregulation of G_{to}, G_{CaL}, J_{up} and G_{Kr} and 60% upregulation of G_{NaCa}.

Table 5.2: **Experimental data summary**

Biomarker	Increase in HF	Decrease in HF	No change	Simulation △median (1500ms CL)
AP duration	Beuckelmann et al. (1992) Beuckelmann et al. (1993) Piacentino III et al. (2003) Li et al. (2004) Glukhov et al. (2010)(a) Glukhov et al. (2012)(a)	–	Lou et al. (2011)	↑ 19.7%
AP triangulation	Beuckelmann et al. (1992)(b) Priebe and Beuckelmann (1998)(b)	– –	– –	↑ 6.6%
CaT duration	Gwathmey et al. (1987) Beuckelmann et al. (1992) Kubo et al. (2001) Piacentino III et al. (2003)	–	Lou et al. (2011)	↑ 51.7%
CaT triangulation	–	Lou et al. (2011)	–	↓ 11.6%
CaT max	–	Beuckelmann et al. (1992) Kubo et al. (2001) Piacentino III et al. (2003)	Vahl et al. (1994)	↓ 44.4%
AP-CaT delay	Gwathmey et al. (1987) Lou et al. (2011)	–	–	↑ 59.6%

a) Glukhov et al. (2010) and Glukhov et al. (2012) report a transmural flattening of APD in heart failure caused by prolongation of AP at the epicardium, but not in the midmyocardium or endocardium.
b) Not computed, see figures in those papers.

Action potential duration

As shown in Fig. 5.4 A–C, APD_{80} values in the non-failing population range between 201ms and 362ms for CL=1500ms and between 158ms and 248ms for CL=300ms. Introducing mRNA expression changes associated with heart failure results in prolonged APD_{80} values in the failing population with a 19.6% median increase at all CLs. APD_{80} values in the failing population range between 223ms and 486ms for CL=1500ms and between 167ms and 277ms for CL=300ms. An overlap in APD_{80} values between the non-failing and failing populations exists for all CLs.

Experimental recordings obtained in failing and non-failing cardiac preparations show a wide range of APD_{80} values (shown in Table 2 in Appendix A), possibly explained by inter-subject and intra-subject variability as well as differences in experimental conditions and preparations between studies. Overall, experimentally-reported APD values are longer in failing hearts than in non-failing hearts, as our simulation results show in Fig. 5.4 A–C. In particular, our results for APD_{80} are comparable to those of Li et al. (2004) which had a mean value of 305ms in the failing population, and 450ms in the non-failing population at 1000ms CL. The failing population also gives similar values to the results of Sipido et al. (1998) for ischæmic and dilated cardiomyopathy at 1000ms, with means of 451ms and 417ms, respectively. Both populations have significantly smaller absolute values than those published by Beuckelmann et al. (1992, 1993), however these values are considerably longer than those reported in the other experimental studies we reviewed. Beuckelmann et al. (1992, 1993) found a mean APD_{90} of approximately 650ms in non-failing human myocytes and over 1000ms in the non-failing myocytes. Optical mapping measurements in the left-ventricular transmural wedge report AP prolongation at the epicardium and shortening at the endocardium in failing versus non-failing hearts, indicating potential location specific remodelling effects caused by heart failure (Lou et al., 2011).

Action potential triangulation

As shown in Fig. 5.4 D–F, AP triangulation increases (*i.e.* APD_{3080} decreases) by a median value of between 7 and 10% at all CLs in the failing population as compared to the non-failing population, due to a decrease in APD_{30} relative to APD_{80}. The range in APD_{3080} values observed in the failing population is larger than that observed in the non-failing population. AP triangulation was not generally quantified in the reviewed literature. However, visual inspection of APs given in the experimental studies by Beuckelmann et al. (1992) and Priebe and Beuckelmann (1998) does reveal a marked increase in AP triangulation in failing myocytes, in agreement with our simulation results.

Calcium transient duration

$CaTD_{80}$ is increased at all CLs compared with the non-failing population (Fig. 5.4 G–I). At 1500ms cycle length, the median value of $CaTD_{80}$ in the failing population is 777ms, a 51.7% increase in the median value recorded for the non-failing population of 512ms. The percentage increase in the median value of the failing population decreases with cycle length to a 36% increase compared to the non-failing median value of 176ms at a 300ms cycle length. Either no change (Lou et al., 2011) or a prolongation of the CaT (Gwathmey et al., 1987; Beuckelmann et al., 1992; Kubo et al., 2001) was reported in the reviewed literature, as summarized in Table 5.2. Numerical values from experimental studies are shown in full in Table 3 in Appendix A.

Calcium transient triangulation

As shown in Fig. 5.4 J–L, $CaTD_{3080}$ values tend to increase in the failing population relative to the non-failing population, corresponding to a decrease in the CaT triangulation. This is in agreement with the only experimental study to explicitly report CaT triangulation values by Lou et al. (2011) (see Table 6 in Appendix A).

Our simulations show that $CaTD_{3080}$ values display a complex behaviour that is depen-

dent upon the CL in both the non-failing and failing populations. At 1500ms CL, $CaTD_{3080}$ values for the non-failing population display a bimodality in their distribution corresponding to two subpopulations of cells, the larger one close to the value shown by the original ORd model, and the other one with markedly reduced $CaTD_{3080}$ values. The latter disappears with decreasing CLs below 1000ms in the non-failing population. In the failing population however, the bimodality appears for CLs $\leq$ 600ms, with one sub-population appearing close to the original ORd model value and one significantly greater, corresponding to significantly decreased triangulation. At a CL of 300ms, the subpopulation with lower $CaTD_{3080}$ values is a larger proportion of the failing population.

Maximum cytosolic calcium concentration

Fig. 5.4 M–O show that at all CLs, both magnitude and range of CaTmax values decrease in the failing population as compared to the non-failing population. As CL decreases, the range in values increases in each population. At 1500ms the non-failing population has a median value of 2.82×10^{-4} mM, increasing to 9.0×10^{-4} mM at 300ms cycle length. The failing population has a median value of 1.58×10^{-4} mM at 1500ms, increasing to 2.96×10^{-4} mM at 300ms cycle length. In both populations, the dispersion increases as CL decreases. The experimental values for maximum cytosolic calcium vary widely in the literature, but a reduction in failing hearts is reported by Beuckelmann et al. (1992), Kubo et al. (2001), and Piacentino III et al. (2003) in line with our simulations (see Table 5 in Appendix A). Vahl et al. (1994) reported no significant difference between failing and non-failing calcium transients. In the experimental studies, the mean non-failing maximum systolic calcium concentrations range between 5.06 $\times10^{-4}$ mM (Kubo et al. (2001), 500ms CL) to 14.4 $\times10^{-4}$ mM (Vahl et al. (1994), no CL given). The mean failing systolic calcium concentrations range between 3.67 $\times10^{-4}$ mM (Beuckelmann et al. (1992), 2000ms CL) and 15.6 $\times10^{-4}$ mM (Vahl et al. (1994), no CL given).

A potential disagreement with the experimental data is that systolic Ca^{2+} may decrease with CL (Table 5 in Appendix A), contradicting what we see in our simulations. As this trend

for decreasing systolic Ca^{2+} with decreasing CL spans multiple papers (Vahl et al., 1994; Kubo et al., 2001; Piacentino III et al., 2003) it is possible that differences in the preparation of myocytes and recording techniques are responsible for this apparent effect.

Action potential-calcium transient delay

As illustrated in Fig. 5.4 P–R, at all CLs, DAPCaT values tend to be larger and more variable in the failing population than in the non-failing population, in agreement with the only experimental study to measure the AP-CaT delay (Lou et al., 2011). They report mean DAPCaT values of 8.8ms at the endocardium, 8.3ms in the midmyocardium and 8.1ms at the epicardium in the non-failing wedges, as compared to 9.7ms, 9ms and 8.0ms respectively for the failing population. Increased rise time to peak, as observed by Gwathmey et al. (1987) and Lou et al. (2011) is also consistent with slowed rise of the CaT, as shown in our simulations (Table 7 in Appendix A).

At 1500ms the median value for DAPCaT in the failing population is 17.4ms, as opposed to 10.9ms in the non-failing population. At a cycle length of 300ms, the median value for the failing population is 13.1ms and the median value for the non-failing population is 8.6ms.

5.3.2 Correlation between biomarkers

In order to determine the potential correlation between the different biomarkers values shown above, Fig. 5.5 plots values for each biomarker against each of the other biomarker values for each model in the non-failing and failing populations. As shown in Fig. 5.5 (first column, first row), APD_{80} and APD_{3080} are correlated as expected from the formulation of APD_{3080} and increasing APD_{80} is associated with increased triangulation (decreased APD_{3080}) in both populations. The correlation is found for all CLs, except for CL=300ms, where the failing population shows no such correlation (not shown). In general, AP biomarkers are only weakly correlated with CaT biomarkers suggesting the underlying ionic mechanisms driving changes in these biomarkers are different. The exception is

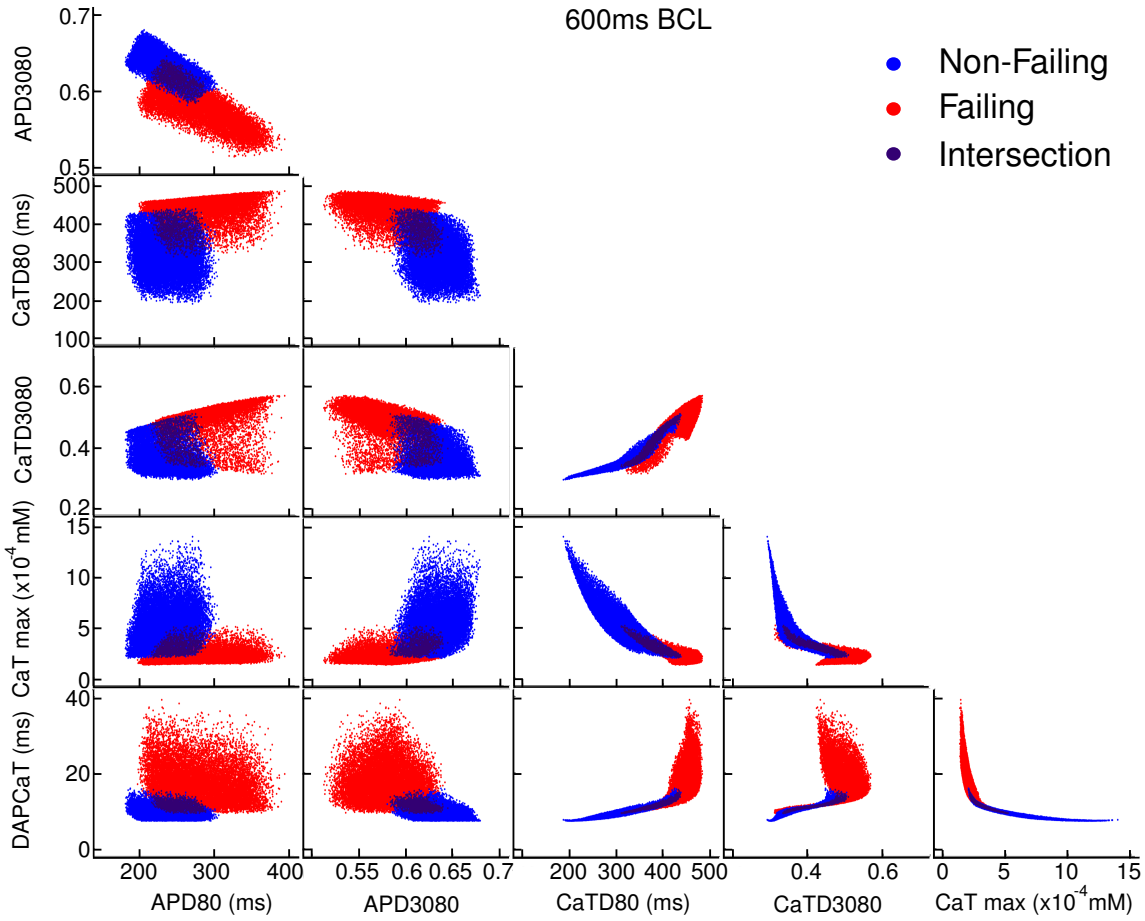

Figure 5.5: **Correlation plots of one biomarker against another at 600ms CL.** Red denotes the failing population, blue denotes the non-failing population, and the darker shade represents cells lying in the intersection between the two populations. Points which develop alternans are removed from these plots. Each biomarker is plotted against each other.

APD_{80} at 1500ms CL in the failing population, which shows a correlation with $CaTD_{3080}$.

Fig. 5.5 indicates that calcium biomarkers ($CaTD_{80}$, $CaTD_{3080}$, CaTMax and DAPCaT) show strong correlation with one another. In general, increased $CaTD_{80}$ is correlated with decreased CaT triangulation (increased $CaTD_{3080}$), decreased CaTmax and increased DAPCaT. Increased triangulation (decreased $CaTD_{3080}$) is also correlated with decreased CaTmax, and increased DAPCaT in the non-failing population only. Finally increased CaTmax is correlated with decreased DAPCaT. The correlation shown between certain biomarkers may be explained by common ionic mechanisms, as explored below using regression analysis.

5.3.3 Regression Analysis

We further exploit the potential of a population-based computational approach to investigate the relative importance of ionic properties in determining changes in each biomarker in failing versus non-failing human cardiomyoctes. The correlation found in the previous section with respect to AP and Ca biomarkers suggests that different ionic properties determine AP and Ca biomarkers values, respectively, within each population. We use regression analysis to establish which ionic currents determine biomarker values in the failing versus non-failing population. Examples of regression fits are shown in Fig. 5.6. Fig. 5.7 shows regression coefficients for each of the biomarkers under investigation at all CLs in the non-failing (left) and failing (right) populations. For clarity, only coefficients reaching an absolute value greater than 0.2 are given (those that come outside of the grey band in the plots). Regression coefficients are shown for both failing and non-failing populations. Regression coefficients for all biomarkers at all CLs are shown in Tables 1–12 in Appendix B. The regression method produces good fits as measured by the R^2 values that lay in a range between 0.75 and 0.98, with the exception of $CaTD_{80}$ in the failing case. R^2 values for all regression fits are shown in Tables 13 and 14 in Appendix B.

Action potential duration

In both the failing and non-failing populations, long APD_{80} values are correlated with low G_{Kr}, as shown by the large negative correlation coefficient of around -0.9 (Fig. 5.7 A,B). Regression analysis also gives a small positive correlation of APD_{80} with G_{CaL} in the failing population that increases as CL is decreased. In the non-failing population the effect of G_{CaL} shows no significant change with CL.

Action potential triangulation

As expected from the strong correlation between APD_{80} and AP triangulation shown in Fig. 5.5, large AP triangulation (*i.e.* small APD_{3080} value) is correlated with low G_{Kr}, but

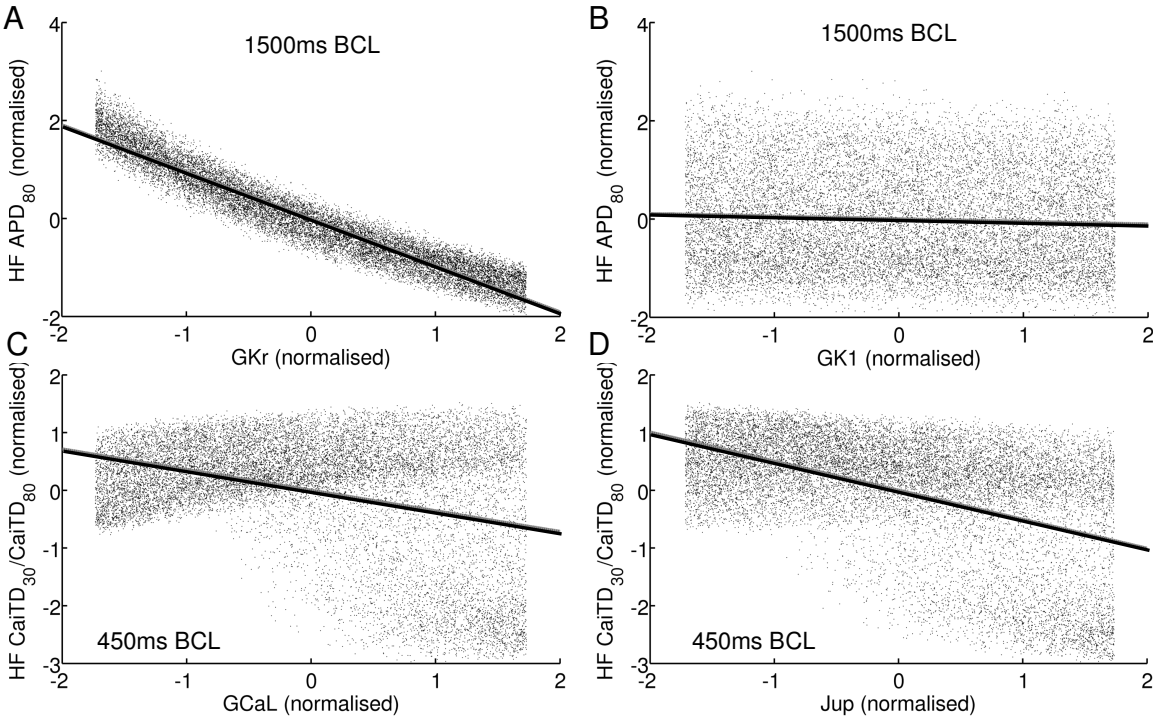

Figure 5.6: **Linear regression fits for individual parameters.** We show one dimensional cross sections through the seven dimensional parameter space. R^2 values shown are for the seven-dimensional fit. Regression lines are plotted over the data set for A) G_{Kr} and B) G_{K1} in the HF population at CL 1500ms, and for C) G_{CaL} and D) J_{up} in the failing population at CL 450ms to illustrate low R^2 in this case.

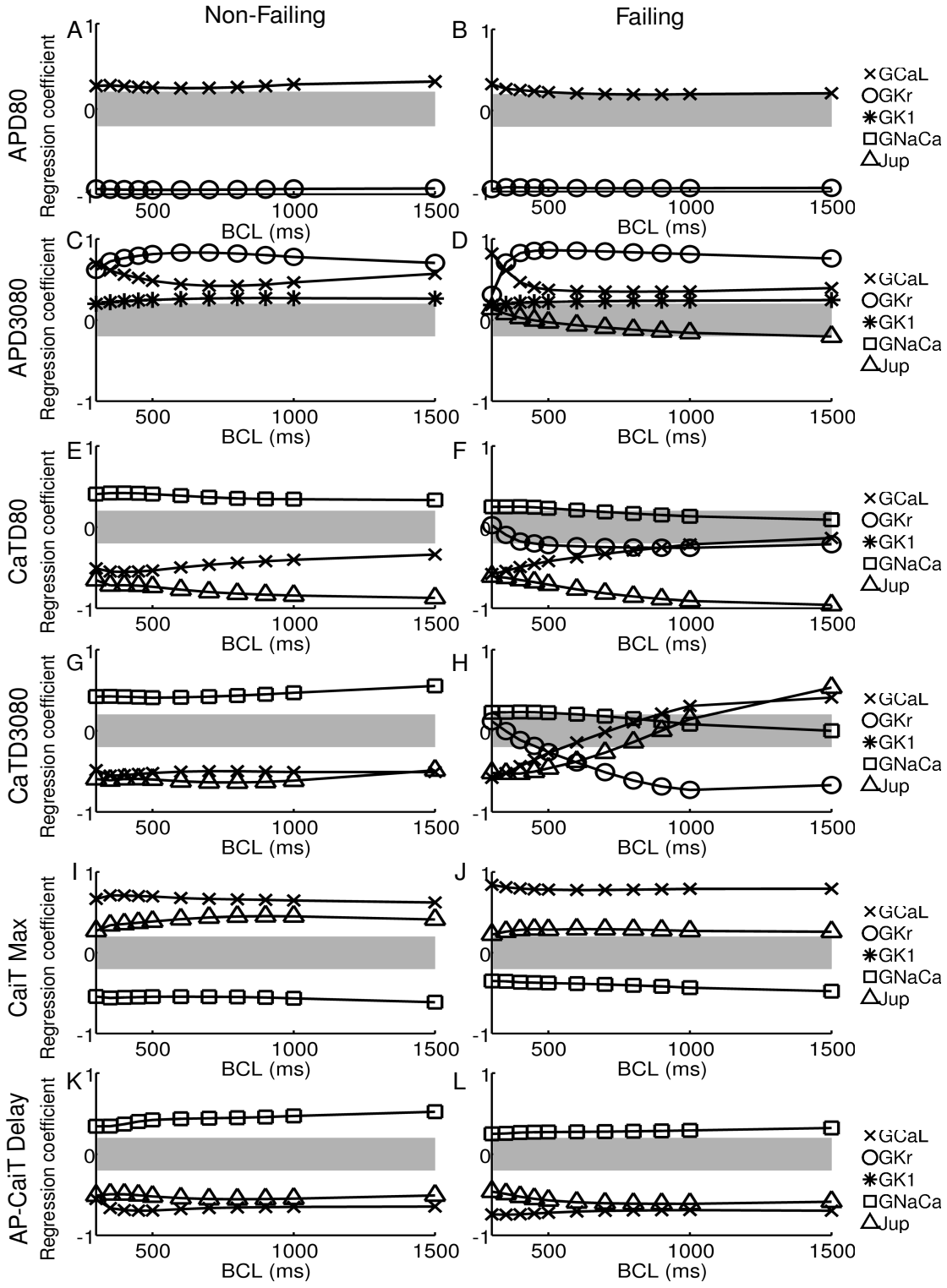

Figure 5.7: **Regression coefficients obtained in the non-failing and failing populations.** Coefficients are plotted at all cycle lengths for A,B) APD_{80}, C,D) APD_{3080}, E,F) $CaTD_{80}$, G,H) $CaTD_{3080}$, I,J) CaT max and K,L) AP-CaT delay. For clarity, only regression coefficients with an absolute value greater than 0.2 are plotted, denoted by the grey band.

unlike APD_{80} also with lowered G_{CaL}, represented by the positive correlation coefficients shown in Fig. 5.7 C,D. Lowered G_{K1} also makes a small contribution to the increase in triangulation. In both populations, the ionic mechanisms determining APD_{3080} are heavily rate dependent, with G_{Kr} being the most important factor at long CLs. At short CLs of 350ms and 300ms AP morphology is driven primarily by G_{CaL}, especially in the failing population.

Calcium transient duration

As illustrated in Fig. 5.7 E,F $CaTD_{80}$ is determined by J_{up}, G_{CaL} in both populations. The magnitude of this effect is rate dependent, with G_{CaL} becoming increasingly important at shorter CLs. G_{NaCa} also has an effect in the non-failing population which is more pronounced than its effect in the failing population. The negative correlation coefficients of J_{up} and G_{CaL} for $CaTD_{80}$ indicate that low J_{up} and G_{CaL} result in prolonged CaTs, with this effect being counteracted in the non-failing population where G_{NaCa} is high. Note that the failing population shows a very different cause for low triangulation at long CLs, with a negative correlation coefficient suggesting that decreased G_{Kr} increases $CaTD_{3080}$ and hence decreases triangulation, the opposite result to that for APD_{3080}.

Calcium transient triangulation

$CaTD_{3080}$ is primarily determined by J_{up}, G_{CaL} in both populations (Fig. 5.7 G,H). As for $CaTD_{80}$, the magnitude of this effect is rate dependent, with G_{CaL} becoming increasingly important at shorter CLs. Again, the effect of G_{NaCa} also has an effect in the non-failing population which is more pronounced than its effect in the failing population. G_{Kr} also affects $CaTD_{3080}$ at longer cycle lengths in the failing population. The negative correlation coefficients of J_{up} and G_{CaL} for $CaTD_{3080}$ suggest that low J_{up} and G_{CaL} result in less triangular CaTs, again counteracted in the non-failing population where G_{NaCa} is high.

Maximum cyctosolic calcium concentration

CaTmax is mainly determined by J_{up}, G_{CaL} and G_{NaCa} in both populations (Fig. 5.7 I,J). Positive correlation coefficients of J_{up} and G_{CaL} for CaTmax suggest that low Ca systolic levels in the failing population are determined by reduced J_{up} and G_{CaL}, with negative correlations for G_{NaCa} suggesting that increased G_{NaCa} contributes to a decrease in systolic Ca. In both populations, the relative importance of G_{CaL} was higher than that of J_{up} and G_{NaCa}.

Action potential-calcium transient delay

Changes in DAPCaT were mainly driven by J_{up}, G_{CaL} and G_{NaCa} in both populations (Fig. 5.7 K,L). Negative correlation coefficients of J_{up} and G_{CaL} for DAPCaT indicate that low J_{up} and G_{CaL} result in increased delay between the upstrokes of voltage and calcium, whereas the positive regression coefficient for G_{NaCa} shows that an increase in G_{NaCa} will lead to an increase in DAPCaT. As before, the relative importance of J_{up} and G_{CaL} is rate dependent.

For each of the calcium biomarkers, the main three parameters driving their changes are the same; J_{up}, G_{CaL} and G_{NaCa}. This is consistent with their sharing the same underlying mechanisms determining these properties, as suggested by the strong correlations shown in Fig. 5.5.

Even when R^2 coefficents are low as in the case in Fig. 5.6 C–D, regression analysis can be useful for identifying markedly non-linear responses in regions of parameter space. The concomitant effects of the parameters J_{up} and G_{CaL} explain both the bimodality shown in the histograms in Fig. 5.4 J–L and the low R^2 values for $CaTD_{3080}$ regression fits. The non-linear relationship between J_{up} and G_{CaL} shown in Fig. 5.8 results in the majority of the parameter space giving either a high or low value for $CaTD_{3080}$, causing the linear model to fail. A relatively small transition region of parameter space separates the high and low $CaTD_{3080}$ regions. This suggests that a large change in either of these parameters individually could produce similar effects in morphology to that resulting from a smaller change in both parameters simultaneously. The regression coefficients still correctly identify the

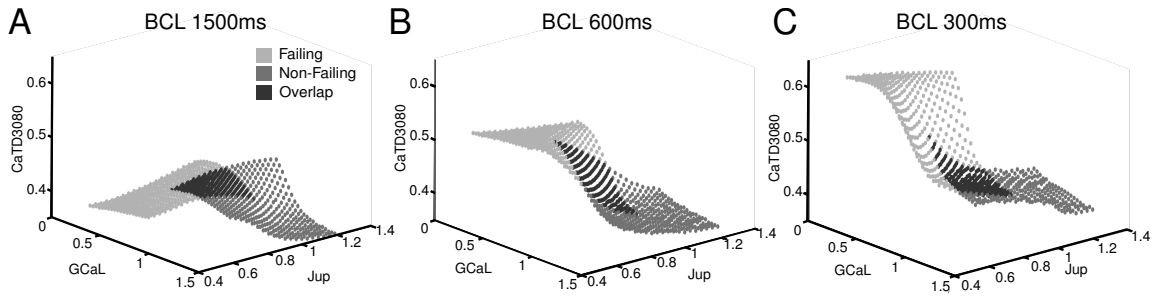

Figure 5.8: **Parameter surfaces for $CaTD_{3080}$ as a function of G_{CaL} and J_{up}.** The parameter surfaces were generated by allowing only G_{CaL} and J_{up}, then plotting both F and NF populations together. Shown are A) CL 1500ms, B) CL 600ms and C) CL 300ms.

parameters that cause the largest changes in this case, and so are included in the analysis above. Note that this need not always be the case for a linear regression study. We do not claim in this case that the linear fit is accurate, but instead that the regression coefficient indicates which parameters demonstrate the largest cause of change in the population. This finding demonstrates that,

1. results of regression analysis must always be checked against actual parameter outputs;

2. linear regression analysis as proposed by Sobie (2009) and Sarkar and Sobie (2010) will not be appropriate for parameterising models in all cases.

5.3.4 Alternans

Fig. 5.9 depicts the number of models displaying alternans in both populations together with a heat map of the parameters used to generate them. In the non-failing population beat-to-beat alternans are observed in the amplitude of the calcium transient and in the APD as CL is decreased. Alternans onset begins in 36 non-failing cells at CL 350ms and is apparent in 2241 of the non-failing cells by CL 300ms. In the standard ORd model, alternans are not observed until CL $\leq$ 300ms. 2:1 block is reported at CL $\leq$ 250ms for the standard ORd model by O'Hara et al. (2011). As can be seen in Fig. 5.9 A,C alternans occur in non-failing cell models with a combination of low J_{up} and high G_{CaL}.

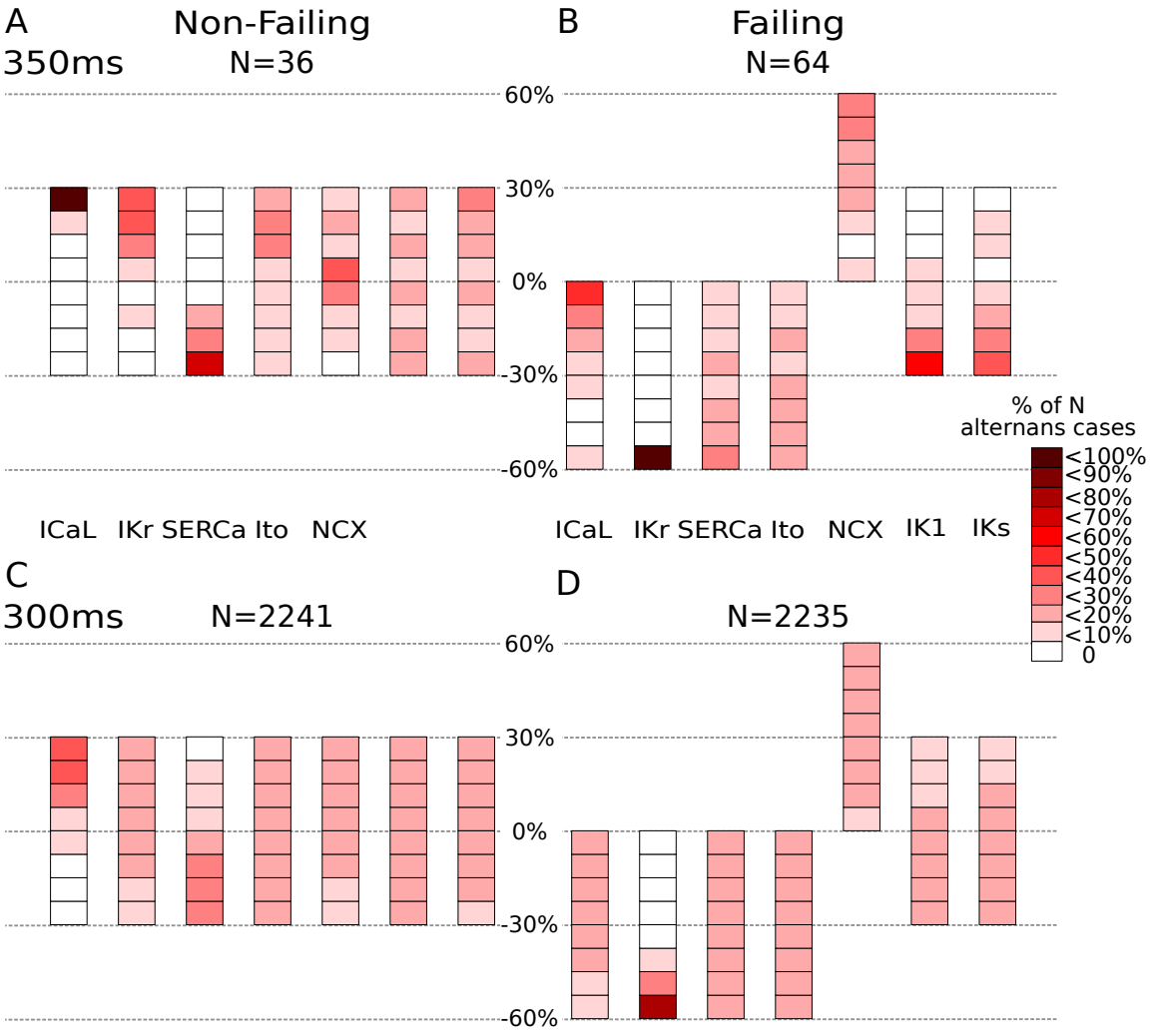

Figure 5.9: **Occurrence of voltage and calcium alternans in the non-failing and failing populations.** Colour scale indicates the proportion of models displaying alternans in APD_{80} and/or $CaTD_{80}$ for each value of each ionic conductance considered. A) There are 36 non-failing alternans cases at 350ms CL. B) There are 64 failing alternans cases at 350ms CL. C) There are 2241 non-failing cells in alternans at 300ms CL. D) There are 2235 failing cell models in alternans at CL 300ms.

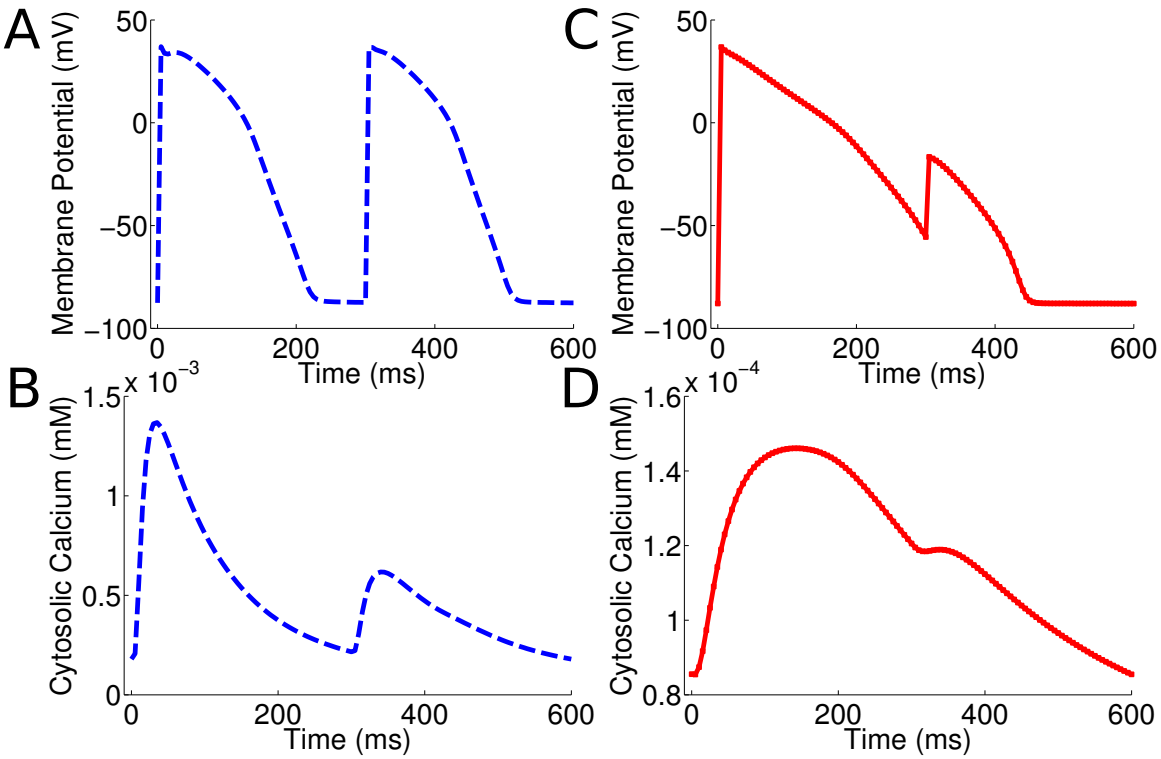

Figure 5.10: **Alternans traces in the non-failing population (blue) and the failing population (red).** Voltage A) and calcium B) traces for a non-failing cell at CL 300ms. Conductivity scales are: G_{CaL} 1.2554, G_{Kr} 1.1231, J_{up} 0.8646, G_{to} 1.0349, G_{NaCa} 1.1225, G_{K1} 0.9713, G_{Ks} 1.0232. Voltage C) and calcium D) traces for a failing cell at CL 300ms. Conductivity scales are: G_{CaL} 0.4025, G_{Kr} 0.4280, J_{up} 0.9912, G_{to} 0.8149, G_{NaCa} 1.5197, G_{K1} 1.0540, G_{Ks} 0.8976.

In the failing population alternans occur in 64 cells at 350ms and in 2235 cells at a CL of 300ms, due to prolonged APD associated with low G_{Kr} (Fig. 5.9 B,D), as demonstrated by the regression analysis. In Fig. 5.10 we show two sample voltage and calcium traces from both the failing and non-failing populations in order to illustrate the form of alternans observed.

5.4 Discussion

5.4.1 Main findings

In this chapter we have developed a population-based approach to investigate the potential of mRNA expression levels measured in failing human hearts to predict electrophysiological

remodelling in AP and CaT, as measured experimentally. Our population-based approach takes into consideration natural variability that may arise from a variety of sources, as well as variability associated with the extent to which mRNA expression affects functional channel conductance at the cell membrane. This is in contrast to the traditional approach of considering unique values of ionic conductances in cardiac models of non-diseased and failing human cardiomyocytes (O'Hara et al., 2011; Priebe and Beuckelmann, 1998; Trenor et al., 2012). Our main findings are:

1. mRNA data associated with G_{CaL}, G_{K1}, G_{Ks}, G_{Kr}, SERCA, G_{to} and G_{NaCa} (as reported by Ambrosi et al. (2013)) predict prolongation and increased triangulation of AP, prolongation and decreased triangulation of Ca transients, decreased maximum systolic Ca, and increased delay between Ca and Vm upstroke in failing versus non-failing human cardiomyocytes, as reported in experimental studies (Table 5.2 and Appendix A Tables 1–7);

2. AP biomarkers (namely APD_{80} and APD_{3080}) are correlated in both non-failing and failing cardiomyocytes, and are primarily determined by G_{Kr}, and secondarily by G_{CaL} and G_{K1};

3. Ca biomarkers (including $CaTD_{80}$, $CaTD_{3080}$ and DAPCaT) are correlated (but only weakly correlated with AP biomarkers) and are primarily determined by J_{up}, G_{CaL} and G_{NaCa};

4. ionic mechanisms underlying the occurrence of alternans are different in the failing population versus the non-failing population: alternans are primarily favoured by low G_{Kr} values in failing human cardiomyocytes and by low SERCA (J_{up}) and high G_{CaL} in non-failing human cardiomyocytes.

5.4.2 Simulated and experimental variability

The non-failing and failing populations of human ventricular cell models are constructed based on the latest human ventricular AP model (O'Hara et al., 2011), which was developed using a consistent and extensive data set of electrophysiological measurements obtained from the left ventricular endocardium of non-diseased human hearts. The non-failing cell model population includes human ventricular cell models sharing the same equations but with ionic conductances varying in $\pm$30% range with respect to control. The overlap in the parameter ranges between the two populations explains some of the overlap in the histograms in Fig. 5.4. Regression analysis demonstrates that some biomarkers are insensitive to changes in certain parameters, increasing the degree of overlap. Variability in ionic conductances lead to variability in biomarker values, with each distribution centered around the original ORd model value. Specifically, APD_{80} ranges from 201ms and 362ms for CL=1500ms and from 158ms and 248ms for CL=300ms, which is in range with the level of variability reported in experimental measurements for non-diseased human cardiomyocytes (Romero et al., 2009; O'Hara et al., 2011). As shown in Table 2 in Appendix A, APD values are very different from one study to another, indicating important sources of variability related to preparations and techniques specific to each study, as well as those discussed in Chapter 2. This may represent an important limitation for the construction of cardiac models built using a variety of data from different laboratories (Quinn et al., 2011).

The failing cell model population is built by including 0–60% downregulation of G_{to}, G_{CaL}, G_{Kr} and SERCA and 0–60% upregulation of I_{NaCa}, based on the data by Ambrosi et al. (2013). Our simulations predict changes in AP and Ca transients, which are in qualitative agreement with experimental recordings summarised in Tables 2–7 in Appendix A. Significant quantitative differences exist between experimental studies and also with our simulation results, which might be due to a range of causes including the type of heart failure (non-ischæmic versus ischæmic), preparation (isolated cells or tissue), recording technique, or variability as discussed in Chapter 2.

5.4.3 Coupling between AP and calcium biomarkers

Changes in AP biomarkers are not strongly correlated with changes in CaT biomarkers, suggesting that different ionic mechanisms cause these biomarker changes. This is explicitly demonstrated through linear regression. In particular different causes determine the duration of AP and CaT in failing cardiac myocytes, namely G_{Kr} for the AP, and SERCA and G_{CaL} for the Ca transient. In the reviewed comparative experimental studies, AP and CaT prolongation occurred concurrently in heart failure. Thus, our findings lead to the prediction that remodelling of both calcium and potassium currents may have occurred in these samples — remodelling of one component alone in our simulations does not lead to the changes seen in these experiments. It is worth noting that Lou et al. (2011) observed no significant prolongation of APD_{80} or $CaTD_{80}$ at the endocardium in the failing population, but did observe other changes in CaT morphology. We suggest that correlation plots may provide a first-pass method to investigate causes of biomarker changes by plotting against biomarkers whose underlying regulatory mechanisms are well known.

5.4.4 Effect of pacing cycle length

Our simulations also show significant rate-dependence in the ionic conductances underlying changes in AP triangulation, $CaTD_{80}$, CaT triangulation and AP-CaT delay in failing and non-failing cardiomyocytes. In particular, the significance of I_{CaL} in affecting the biomarkers under investigation increases at shorter cycle lengths.

5.4.5 Alternans

Our population based approach reveals conditions in which alternans may appear at longer CLs than in the original ORd model. The form of alternans observed in the non-failing population cannot occur in the failing population, as the combination of parameters driving alternans in the non-failing population is outside the parameter range for the failing population. Similarly, the 2:1 block observed in the failing population does not occur in the

non-failing population as G_{Kr} cannot attain sufficiently low values. Thus, the alternans effect is different in each population, arising from different ionic mechanisms. This suggests that alternans observed in failing and non-failing hearts may have different causes, and could require different interventions to correct. This is particularly significant as many experimental studies implicate cytosolic calcium in the generation of APD alternans (Myles et al., 2008).

5.4.6 Modelling Approach

In this study we have only examined one component of the mRNA expression dataset presented by Ambrosi et al. (2013), namely the changes that occur between non-failing and failing human left ventricle. There are several other avenues of investigation still open from this dataset, namely atrial differences and gender specific differences. Whilst Ambrosi et al. (2013) noted no significant difference between male and female left ventricles, other studies have done so (James et al., 2007; Gaborit et al., 2010). This novel population-based approach to modelling disease states is a first step towards clinically relevant modelling of disease states as the methodology is flexible enough to be applied to any data set in order to utilise the information extracted from mRNA data.

5.4.7 Limitations

A limitation of this study is that the non-failing population may contain pathologies or abnormalities and so the range of cardiac ion channel or pump expression may not be physiological (Lou et al., 2011). It is therefore difficult to extrapolate from our non-failing results to healthy human cardiac myocytes. Similarly, the term 'heart failure' describes a range of pathologies as shown in Table 1 in Appendix A, and so our results may not extend to all conditions coming under the description 'heart failure'. For example, Ambrosi et al. (2013) reported a downregulation of NCX1 mRNA transcripts in non-ischæmic but not ischæmic cardiomyopathy as compared to non-failing hearts (see Table 5.1).

There is consistent, though controversial, evidence for spatial heterogeneities in AP behaviour in humans, as discussed in Chapter 2. We do not directly address these heterogeneities in our study, although our population approach does offer some robustness against variability resulting from this by incorporating a degree of variability in conductances affecting the repolarisation phase of the AP. Furthermore, many experimental studies use isolated ventricular myocytes whose original location within the heart is unclear, which may explain some of the large degree of variability in the experimental data shown in Appendix A. The left ventricular wedge studies by Glukhov et al. (2010), Lou et al. (2011) and Glukhov et al. (2012) go some way to addressing this issue, however intercellular coupling may also affect APs in tissue compared to isolated cells.

Finally, it is worth reiterating that our study inherits many of the difficulties in extrapolating from mRNA expression data to functional membrane ion channels as discussed in the introduction and reviewed by Nattel et al. (2010). Furthermore, we explicitly address only changes in conductance, and do not consider other potential consequences of heart failure, such as altered gating dynamics (Schroder et al., 1998). Thus, our conclusions show that the mRNA data are consistent with the remodelling observed in the literature, given the hypothesis that they lead to a degree of change in the conductance of the currents in question. This is not the same as showing that it is the mechanism by which remodelling has occurred, or that other mechanisms could instead be causing this remodelling.

5.4.8 Conclusion

We conclude that, *if* the changes in mRNA expression reported in human heart failure translate into changes in current conductances, *then* they are sufficient to explain experimentally observed remodelling in AP and CaT properties. We have demonstrated that these changes are robust to inter-individual variability, and elucidated which ion currents are driving changes in particular biomarkers. Model construction is guided by mRNA expression data from failing and non-failing human hearts, and we have qualitatively compared the results to a literature review of comparative studies of electrophysiological re-

modelling in failing human hearts.

Chapter 6

Fitting and Extending A Phenomenological Model To Capture Variability

6.1 Introduction

In the previous chapter, we have constructed models displaying inter-individual variability in a biophysically detailed model based on mRNA expression data. In many situations, both from isolated cell and tissue recordings, information on sub-cellular processes causing differences between samples, or sets of samples, will not be available. We have seen in Chapter 3 that parameterisation of cardiac cell models is reliant on subcellular channel information, and that two apparently similar APs may arise from dramatically different underlying parameterisations. Thus, going further than the parameter ranges introduced in Chapter 5 by fitting parameters to a range of experimentally recorded APs may lead to incorrect conclusions.

In this chapter we will show why phenomenological models offer a powerful method for the representation of variability in cardiac electrophysiology when experimental data on subcellular processes are unavailable. Unlike the biophysically detailed models described

in Chapters 3 and 5, phenomenological models make no assumptions about the currents underlying a change in AP morphology for example, and simply provide a representation of the dynamics of interest. Simulating the model in a tissue setting then provides the means to test a hypothesis about the properties of the model.

As we shall see, a major reason for using phenomenological models for studying variability in the behaviour of the AP is their flexibility for capturing different behaviours. In this chapter, we demonstrate the properties of the Bueno-Orovio et al. (2008) (BO08) model. This model is chosen due to its ability to capture AP morphology, unlike the earlier three variable Fenton-Karma model (Fenton and Karma, 1998). Fitting of parameters to models of this form generally involves iteration between fitting different properties (Fenton and Karma, 1998; Oliver and Krassowska, 2005; Bueno-Orovio et al., 2008). We begin by demonstrating how the existing model reproduces maximum velocity of upstroke (Section 6.2.2), conduction velocity (Section 6.2.3), conduction velocity restitution (Section 6.2.4), threshold of excitation (Section 6.2.5) and S1-S2 restitution curves (Section 6.2.6). It is worth doing this systematically, as the only thorough review currently in the literature deals with the Fenton-Karma model (Oliver and Krassowska, 2005).

Having demonstrated the properties of the existing BO08 model, we then fit the AP morphology to experimental data (Section 6.2.7). We finally present a novel modification of the BO08 model in order to reproduce temporal variability (Section 6.2.8). This new phenomenological model is then fitted to reproduce experimentally recorded BVR in patch clamp recordings from four isolated guinea pig ventricular myocytes.

6.2 The Bueno-Orovio (2008) Phenomenological Model

6.2.1 Model structure

The BO08 model consists of four variables, u, v, w and s. u is the non-dimensional membrane potential that is rescaled to a biophysically relevant membrane potential using the

formula $V_m = Vu + R$, where V and R have dimension mV. As u generally takes the value 0 at rest, R is in effect the resting potential of the model. v, w, and s are non-dimensional variables whose decay controls current magnitude. The model equations are as follows:

$$\frac{\partial u}{\partial t} = \nabla \cdot \big(D \nabla u\big) - (J_{fi} + J_{so} + J_{si} - J_{stim}), \tag{6.1}$$

$$\frac{\partial v}{\partial t} = (1 - H(u - \theta_v))(v_\infty - v)/\tau_v^- - H(u - \theta_v)v/\tau_v^+, \tag{6.2}$$

$$\frac{\partial w}{\partial t} = (1 - H(u - \theta_w))(w_\infty - w)/\tau_w^- - H(u - \theta_w)w/\tau_w^+, \tag{6.3}$$

$$\frac{\partial s}{\partial t} = ((1 + \tanh(k_s(u - u_s)))/2 - s)/\tau_s, \tag{6.4}$$

where H is the Heaviside function. The 'currents' J_{fi}, J_{so} and J_{si} are given as follows:

$$J_{fi} = - vH(u - \theta_v)(u - \theta_v)(u_u - u)/\tau_{fi}, \tag{6.5}$$

$$J_{so} = (u - u_o)(1 - H(u - \theta_w))/\tau_o + H(u - \theta_w)/\tau_{so}, \tag{6.6}$$

$$J_{si} = - H(u - \theta_w)ws/\tau_{si}, \tag{6.7}$$

and J_{stim} is the applied stimulus current. Furthermore, some of the time constants themselves depend on the membrane potential as follows:

$$\tau_v^- = (1 - H(u - \theta_v^-))\tau_{v1}^- + H(u - \theta_v^-)\tau_{v2}^-, \tag{6.8}$$

$$\tau_w^- = \tau_{w1}^- + (\tau_{w2}^- - \tau_{w1}^-)(1 + \tanh(k_w^-(u - u_w^-)))/2, \tag{6.9}$$

$$\tau_{so} = \tau_{so1} + (\tau_{so2} - \tau_{so1})(1 + \tanh(k_{so}(u - u_{so})))/2, \tag{6.10}$$

$$\tau_s = (1 - H(u - \theta_w))\tau_{s1} + H(u - \theta_w)\tau_{s2}, \tag{6.11}$$

$$\tau_o = (1 - H(u - \theta_o))\tau_{o1} + H(u - \theta_o)\tau_{o2}. \tag{6.12}$$

The steady state values are given as

$$v_\infty = \begin{cases} 0, & u < \theta_v^- \\ 1, & u \geq \theta_v^-, \end{cases} \tag{6.13}$$

$$w_\infty = (1 - H(u - \theta_o))(1 - u/\tau_{w\infty}) + H(u - \theta_o)w_\infty^*. \tag{6.14}$$

In tissue simulations, the model employs a diffusion term similar to the conductivity in the monodomain equations (see Chapter 3). However, in the course of simulation in the Bueno-Orovio et al. (2008) paper, the diffusion coefficient is taken to be constant at 1.171cm^2 s^{-1}, based on experimental measurements of human ventricular cell dimensions and cytoplasmic resistivity. Thus, the relation in Equation (6.1) becomes the Laplacian in this case, as we can move the constant diffusion coefficient outside of the gradient operator. It should be noted that this model can equally well take into account factors such as fibre orientation by changing the diffusion parameter D to a conductivity tensor.

Most of the parameters have a clear effect on the behaviour of the model, discussed in Sections 6.2.2–6.2.7 below. The 'currents' represent an approximation to groups of currents observed in the cell rather than having any definite biophysical meaning. For example, J_{fi} is designed to have some of the properties of the rapid inward sodium current which is activated during the upstroke of the AP and the Heaviside functions within the currents may be viewed as approximating Hodgkin-Huxley style gating kinetics. The evolution of the potential u, the gating variables v, w and s and the currents J_{fi}, J_{so} and J_{si} over the course of one AP is shown in Fig. 6.1 using the endocardial parameter set from Bueno-Orovio et al. (2008).

Additionally, we suggest a minor modification to the BO08 model that improves its behaviour when fitting restitution properties (see Section 6.2.6), whilst removing sensitive dependence on the membrane potential u in Eqs. (6.9) and (6.14). This sensitivity arises from the fact that the 'voltage' variable u necessarily changes by only a small amount during the diastolic interval. Thus, small parameter changes may have unintended consequences. By

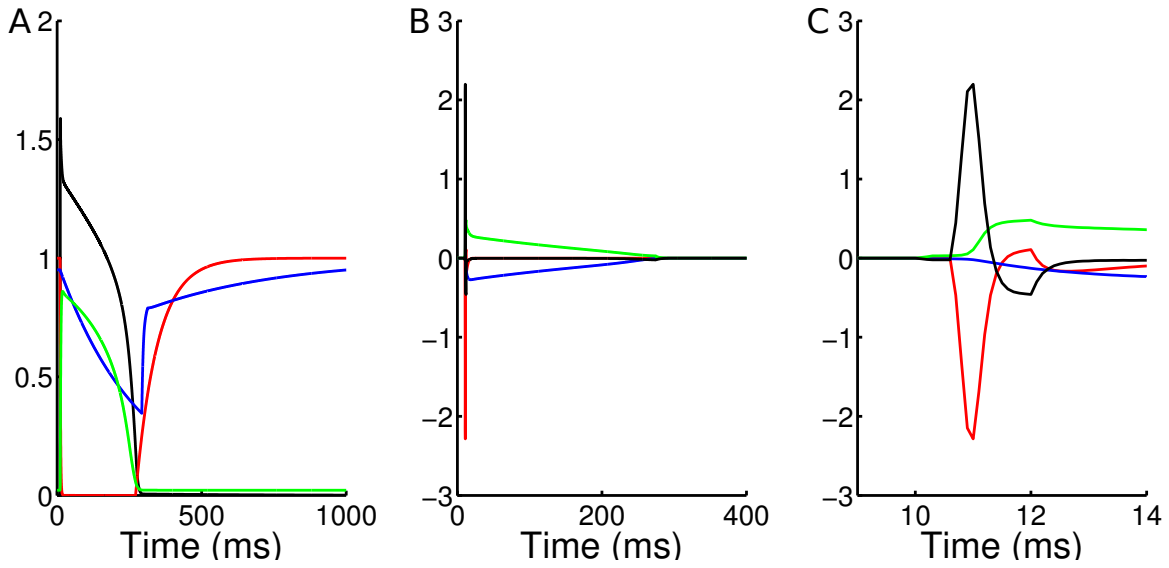

Figure 6.1: **Variables and currents in the BO08 phenomenological model simulated using the published human endocardial cell parameter set.** A) shows the behaviour of the four model variables u (black), v (red), w (blue), and s (green), when paced at a cycle length of 1000ms. B) and C) show the behaviour of the total current (black), and the individual currents J_{fi} (red), J_{si} (blue), and J_{so} (green), when the cell is paced at 1000ms. The time axes in B) and C) have been shortened to better display the current structure, with B) showing the behaviour throughout the AP and C) showing the behaviour during the upstroke of the AP.

instead passing control during this phase to the variable w, more accurate control is gained over the change between different parameter regimes in Eqs. (6.9) and (6.14). This does not affect voltage dependence of excitation, which is controlled by the threshold parameters θ_v, θ_w and u_s. This is because during the diastolic interval of the phenomenological model only very small changes in u but necessarily large changes in w are observed. Using this observation, Equation (6.9) becomes

$$\tau_w^- = \tau_{w1}^- + \left(\tau_{w2}^- - \tau_{w1}^-\right)\left(1 + \tanh\left(k_w^-\left(w - w_w^-\right)\right)\right)/2, \tag{6.15}$$

and Equation (6.14) becomes

$$w_\infty = H\left(w - \theta_{wo}\right)\left(1 - \frac{w}{\tau_{w\infty}}\right) + \left(1 - H\left(w - \theta_{wo}\right)\right) w_\infty^*. \tag{6.16}$$

This requires the addition of an extra parameter θ_{wo} to the model, which controls transition from the exponential phase of recovery to a more linear recovery phase. Setting $\theta_{wo} >$

Table 6.1: **Parameter sets for the modified BO08 model**

Parameter	BO08 Epi	Guinea Pig Apex 1	Guinea Pig Apex 2	Guinea Pig Base 1	Guinea Pig Base 2	Rabbit	Luo-Rudy 1991
θ_v	0.3	0.2985	0.3209	0.2749	0.3005	0.2748	0.4567
θ_w	0.13	0.1299	0.1302	0.1254	0.1202	0.1236	0.0917
θ_v^-	0.2	0.2016	0.1943	0.1908	0.1714	0.2037	-0.0004
θ_o	0.006	0.006	0.0056	0.0058	0.0062	0.0061	-0.0005
u_s	0.9087	0.9502	0.9802	0.9212	0.9391	0.9702	0.9574
w_w^-	0.7	0.77	0.77	0.77	0.77	0.77	0.755
u_{so}	0.65	0.6456	0.6475	0.6645	0.7072	0.6778	0.7668
u_u	1.56	1.546	1.617	1.592	1.575	1.528	1.722
u_o	0	0.0001	-0.0008	0.0004	0.0003	0.0001	-0.001
$\tau_{w\infty}$	0.0273	0.0273	0.041	0.036	0.029	0.0281	0.0941
τ_{o1}	470	462.4	416.8	476.7	456.3	471.1	620.1
τ_{o2}	6	5.951	6.1	5.579	6.042	6.134	8.697
τ_{s1}	2.734	2.689	3.057	2.482	2.813	2.792	4.607
τ_{s2}	2	1.977	2.192	1.764	1.949	2.025	11.08
τ_{so1}	40	39.32	30.91	39.13	28.81	38.18	51.06
τ_{so2}	1.2	1.193	0.2569	1.107	1.287	1.214	1.376
τ_{w1}^-	6	80	80	80	80	80	80
τ_{w2}^-	10	100	100	100	100	100	100
τ_{v1}^-	75	75.39	76.26	72.99	66.59	76.17	77.31
τ_{v2}^-	10	10.03	10.2	9.637	10.03	10.03	992.9
τ_{si}	2.901	2.934	2.727	2.902	2.784	2.959	5.014
τ_v^+	1.451	1.462	1.353	1.525	1.333	1.44	2.755
τ_w^+	280	275.9	276.3	352.8	273.8	274.3	379.4
τ_{fi}	0.13	0.0957	0.1094	0.095	0.0944	0.1012	0.311
w_∞^*	0.825	0.95	1	0.95	0.95	0.95	1.02
k_{so}	2	1.946	2.006	2.023	1.942	1.951	2.005
k_w^-	20	198.2	204	188	207	196.7	62.55
k_s	2.099	2.203	2.293	2.653	2.812	2.168	1.802
θ_{wo}	0.79	1.1	1.1	1.1	1.1	1.1	1.1
V	85.7 mV	94.1 mV	103.8 mV	94.6 mV	90.5 mV	72.5 mV	76.9 mV
R	-84 mV	-73.9 mV	-77.8 mV	-78.1 mV	-76.1 mV	-87 mV	-83.42 mV

w_∞^* gives an exponential only recovery phase. All simulations are performed using the modified model. All parameter sets used in this chapter may be found in Table. 6.1, fitted as discussed in Sections 6.2.6 and 6.2.7.

6.2.2 Upstroke velocity

In the BO08 model, velocity of upstroke, or $\frac{dV_m}{dt}|_{\text{max}}$ is determined by the time constant of decay of the fast inward current J_{fi} (τ_{fi}), and the initial value of the variable v (v_0). Maximum velocity of upstroke is determined as a dimensional quantity as $V \times \frac{dV_m}{dt}|_{\text{max}}$. The parameter

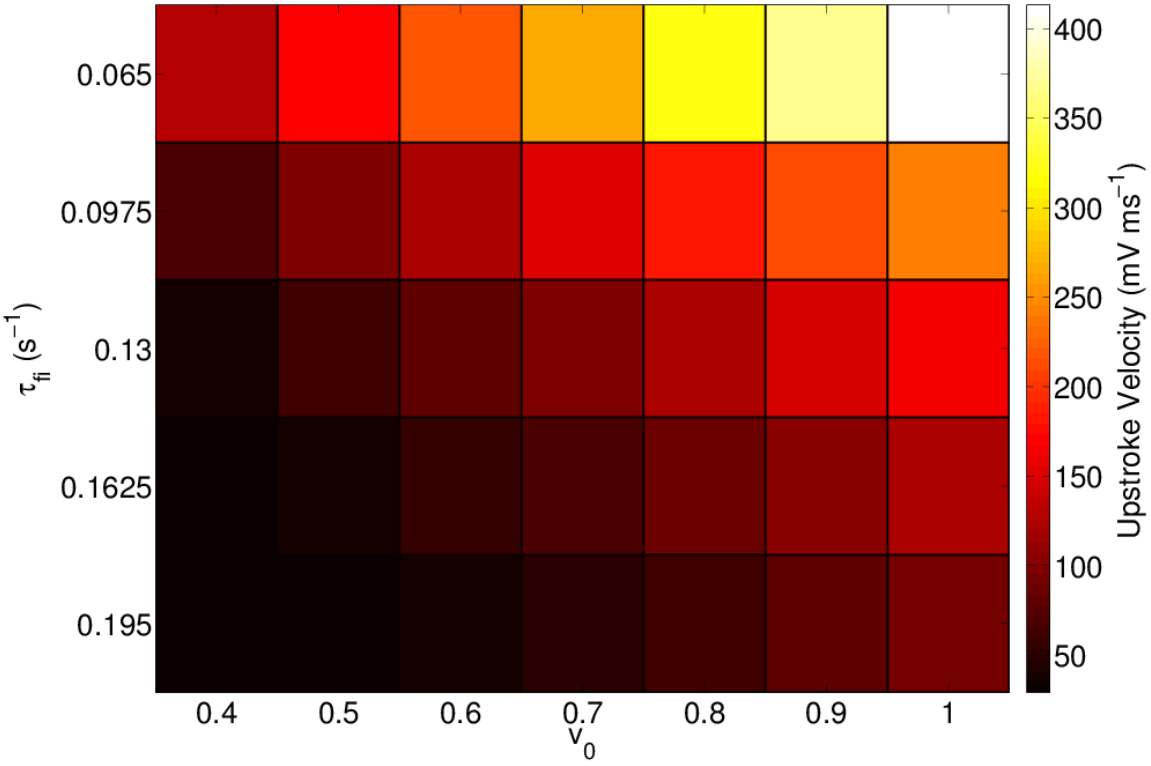

Figure 6.2: **Effect of varying v_0 and τ_{fi} on upstroke velocity in the BO08 model.** The intensity of the heat map shows the value of the upstroke velocity for each pair of parameter values.

heat map in Fig. 6.2 demonstrates the joint effect of varying v_0 and τ_{fi} on the upstroke velocity of the standard BO08 human endocardial model.

6.2.3 Conduction velocity

Conduction velocity of the model may be controlled by two major means, through the parameters affecting the maximum velocity of upstroke in Section 6.2.2, and through the magnitude of the conductivity tensor. The parameter heat map in Fig. 6.3 demonstrates the joint effect of varying the conductivity D in Eq. (6.1), and the time constant of the fast sodium current τ_{fi}, on the conduction velocity of the model in a 2cm fibre. Measurements are taken at 0.25cm and 1.75cm in order to avoid boundary effects (see Cherry and Fenton (2011)).

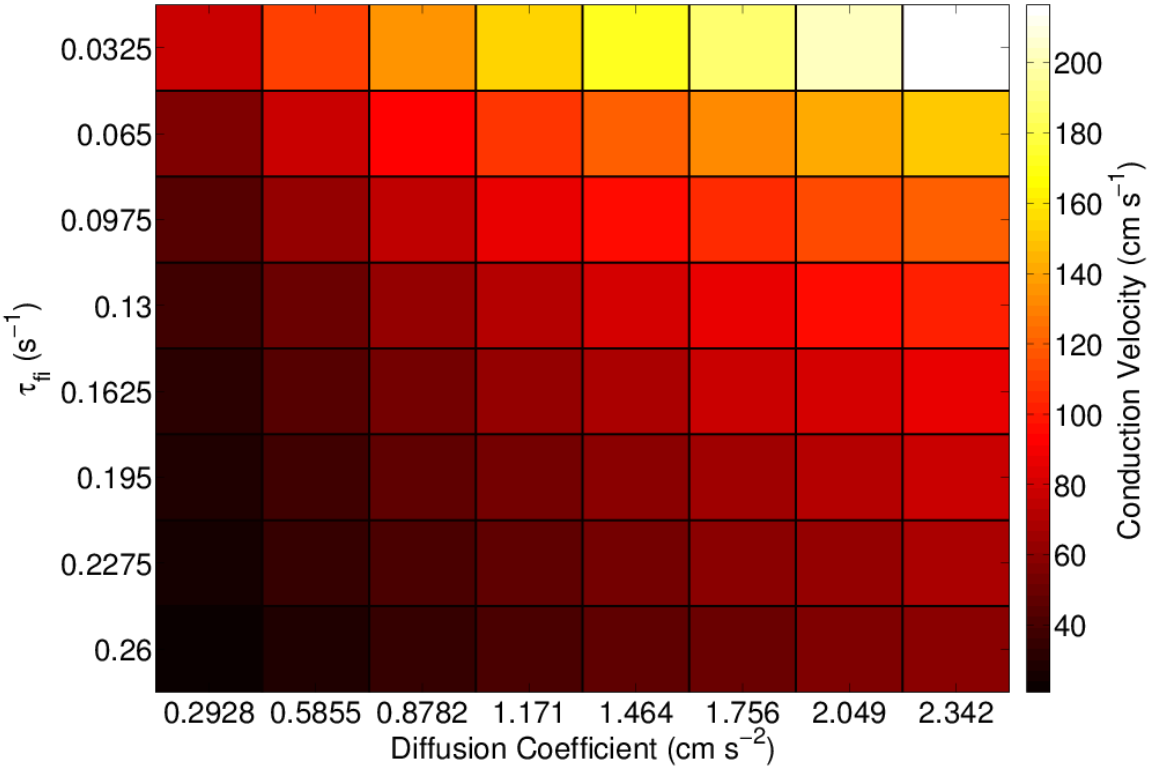

Figure 6.3: **Effect of varying τ_{fi} and D on conduction velocity in the BO08 model.** The heat map shows the value of the conduction velocity for each pair of parameter values.

6.2.4 Conduction velocity restitution

As we have seen in Section 6.2.2, the initial value of the variable v modulates the upstroke of the AP, and hence the conduction velocity in tissue. Thus, the time constant of recovery of this variable will control the degree of excitability of the model. Therefore, an activation sufficiently soon after a previous propagating wave in tissue will have reduced upstroke velocity and hence decreased conduction velocity. This allows the model to reproduce a physiological phenomenon known as conduction velocity restitution, which arises primarily through incomplete recovery of the sodium current in response to a premature stimulus. The effects of varying the main parameter controling this recovery, τ_{v^-} on the conduction velocity restitution curve is shown in Fig. 6.4. Simulations are as described in Section 6.2.3, with an additional stimulus supplied to generate a second propagating wave, whose conduction velocity is plotted in Fig. 6.4.

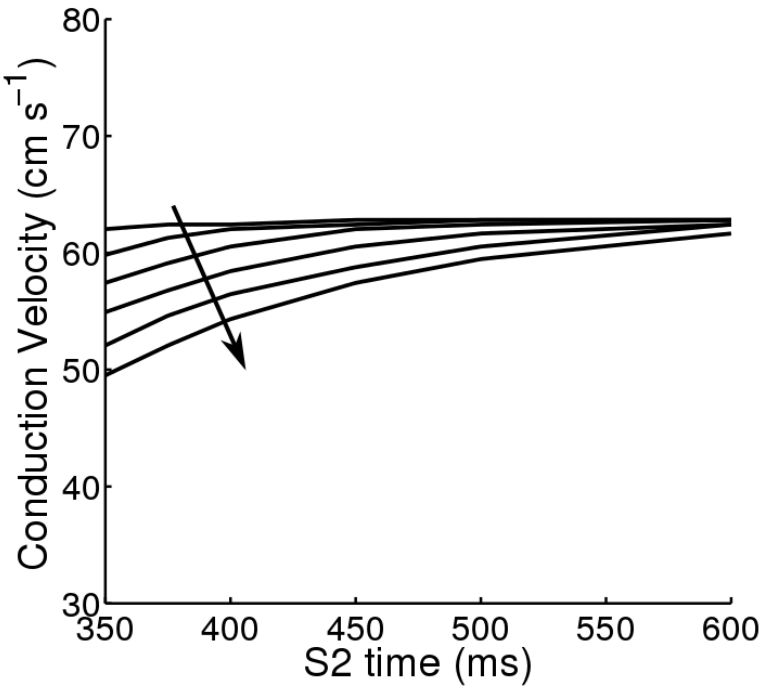

Figure 6.4: **Effect of varying τ_{v^-} on conduction velocity restitution in the BO08 model.** Conduction velocity curves are calculated for a range of values of τ_{v^-} obtained by simultaneously varying both τ_{v1}^- and τ_{v2}^-, and using the standard value of D, 1.171cm/s. The arrow denotes the direction of increasing τ_{v^-} from 0.5$\times$ to 1.75$\times$ its original value.

6.2.5 Threshold of activation

The excitability of the model may be controlled through the value of the parameter θ_v, which then governs the magnitude of the stimulus current required to generate a full AP. Fig. 6.5 shows how the ability of the model to generate an AP varies with stimulus current magnitude and the value of the parameter. The simulations are performed in an isolated cell — tissue simulations require a much larger current to generate an AP due to the effect of electrotonic currents, however the principle remains the same.

6.2.6 S1-S2 restitution

The BO08 model is only able to reproduce one form of restitution in terms of AP duration (APD) — the S1-S2 restitution curve. This is because, as shown in Fig. 6.6 A, the model does not demonstrate the gradual adaption of the APD to a change in cycle length reported

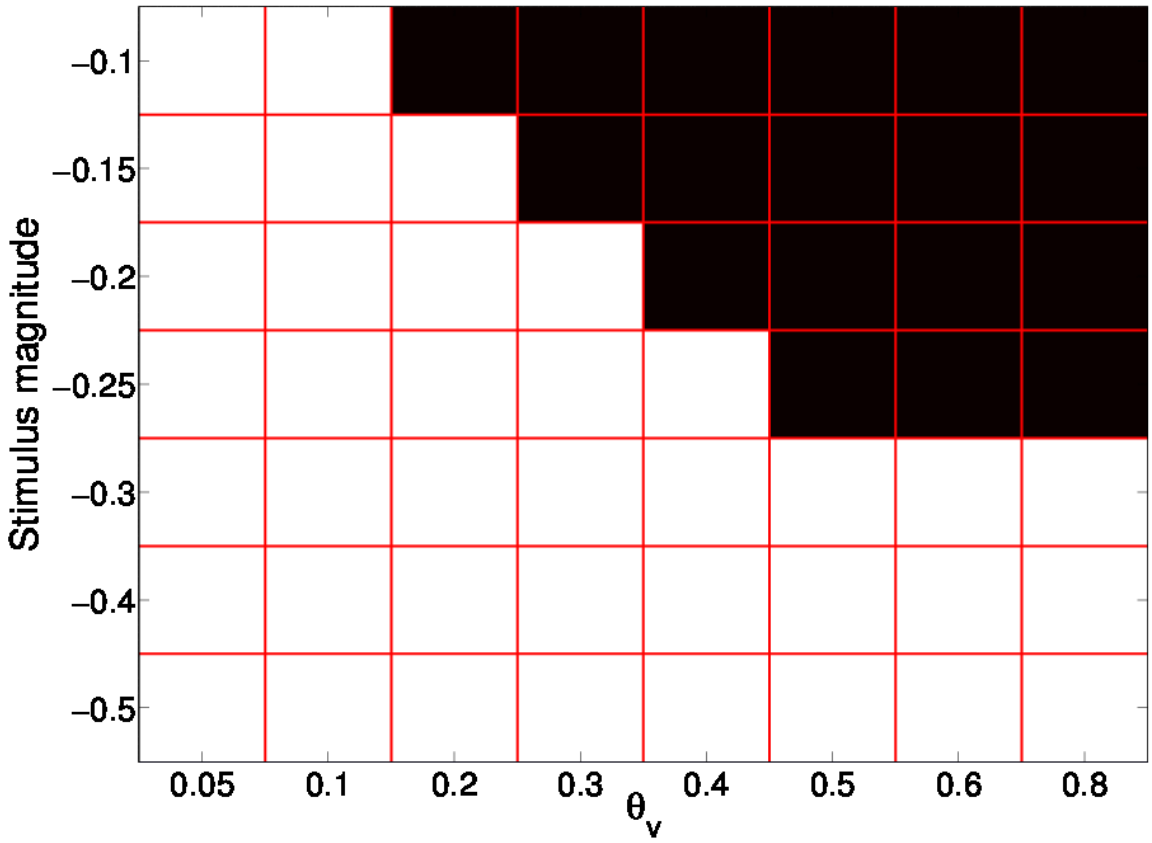

Figure 6.5: **Effect of varying θ_v on the excitability of the BO08 model.** The ability of the model to generate an AP at a range of different currents, with different values of θ_v. A white square denotes a successful AP, and black denotes a failed AP, defined as an APD of $\leq$ 50ms.

in the literature. A recent modification of the BO08 model has enabled the reproduction of this adaptation (Bueno-Orovio et al., 2012). Nevertheless, this one form of restitution still enables the reproduction of a variety of behaviours demonstrated by more complex biophysically detailed models as demonstrated by Bueno-Orovio et al. (2008). Control of APD in the BO08 model is handled by the variable w. With all parameters kept constant, the APD of the BO08 model is a function of the initial value of the variable w at physiological cycle lengths of stimulation as shown in Fig. 6.6 B. Thus, APD restitution properties of the model are governed by w_∞ and τ_w^-, the recovery parameters of the variable w. The recovery of w is shown in Fig. 6.1 A.

We now demonstrate a novel technique for the fitting of the restitution curve of the BO08 model, and other models of its kind. Using the formulation of the parameter controlling the

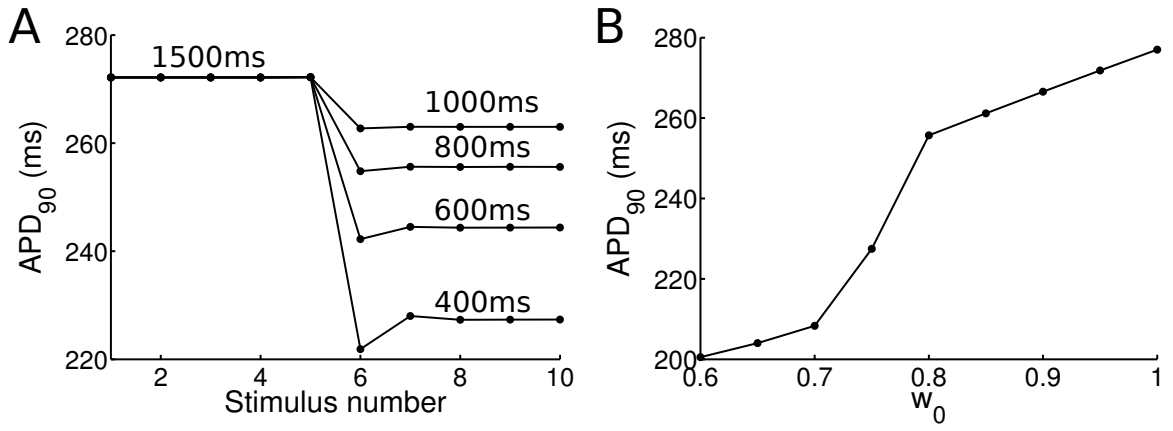

Figure 6.6: **S1-S2 restitution in the BO08 model.** A) shows the lack of adaption in response to a change in pacing cycle length from 1500ms to a pacing cycle length of 1000ms, 800ms, 600ms and 400ms using the epicardial parameter set, as this has a more pronounced CV restitution curve than the endocardial version. B) shows the relationship between APD and the initial value of the variable w before a stimulus is applied.

APD in the model is that we may use its exponential form to derive an 'idealised' set of points at which to measure the model's restitution properties, and thereby fit the restitution curve. There are in total seven parameters associated with this curve, θ_{wo}, $\tau_{w\infty}$, w^*_∞, τ^-_{w1}, τ^-_{w2}, k_{so} and w_{so}. Hence, in principle, seven values from the restitution curve will be necessary to constrain the restitution parameters of the model. Provided $u \leq \theta_w$ we may solve Eq. (6.3) to obtain,

$$w(t) = w_\infty + \left(w\left(t_0\right) - w_\infty\right) \exp \frac{-\left(t - t_0\right)}{\tau^-_w}, \tag{6.17}$$

where t_0 is the time at which u drops below the threshold θ_w.

The function given in (6.17) shows that the phenomenological model implicitly assumes that the initial part of the restitution curve may be approximated by an exponential. The following simplifying assumptions allow the quantification of a minimum number of points to give a good fit to dynamic restitution data. It is assumed that the restitution curve reaches a flat region where increasing cycle length does not increase APD for longer physiological cycle lengths. Thus the parameters θ_{wo} and $\tau_{w\infty}$ that govern drift in APD at longer cycle lengths are not considered. Furthermore, by taking $t \to \infty$ in this model, equivalent to a long but physiologically realistic cycle length, it becomes apparent that w^*_∞ should then be

the value of w required to reproduce the recorded APD at this long cycle length according to the relation between APD and w shown in Fig. 6.6 B. This relation may be used to establish a map between APD and initial value of w.

The minimum recorded point on the dynamic restitution curve must be reached and following the modification in Section 6.2.1 will be reached by an exponential controlled by the parameter τ_{w1}^-. The parameter k_w^- is chosen such that the change between the parameters τ_{w1}^- and τ_{w2}^- is sharp, and then this transition will occur at the value w_w^-. Hence, by setting w_w^- to be the value of w producing the minimum APD of the model. τ_{w1}^- may then be selected to ensure that the model reaches the value τ_{w1}^- at the experimentally recorded minimum cycle length generating a stable APD. It remains to select the value of the parameter τ_{w2}^-, and a time to best discriminate this parameter is now estimated.

The experimentally recorded restitution curve is now modelled by the following exponential equation

$$w(t) = w_\infty + \left(w_w^- - w_\infty\right) \exp\left(\frac{-\left(t - t_w^-\right)}{\tau_{w2}^-}\right), \tag{6.18}$$

where t_w^- is the time at which w reaches the value w_w^-. Thus for any value of τ_{w2}^-, it holds that $w(t_w^-) = w_w^-$ and $w \to w_\infty$ as $t \to \infty$. Thus, as the point at which the absolute difference between any two curves is greatest contains the most information for fitting the parameter, then it is this point at which the data to be recorded would ideally be situated. Given any two parameter values τ_1 and τ_2, the maximum distance between the two exponentials resulting from them occurs at time

$$t = t_w^- + \frac{\tau_1 \tau_2 \ln \frac{\tau_1}{\tau_2}}{\tau_1 - \tau_2}. \tag{6.19}$$

Plotting Eq. (6.19) using a range of values for τ_1 and a prior value for τ_2 (such as one from an existing model) then provides a region containing the maximum difference between the prior value of the time constant and other values. This principle is illustrated in Fig. 6.7. This time may alternatively be derived as the time point maximising the rate of change in

w as a function of τ_{w2}^{-}. Taking the derivative of Eq. (6.18) with respect to τ_{w2}^{-}, we obtain

$$\frac{\partial w\left(t;\tau_{w2}^{-}\right)}{\partial \tau_{w2}^{-}} = \left(w_{w}^{-} - w_{\infty}\right)\left(t - t_{w}^{-}\right)\left(\tau_{w2}^{-}\right)^{-2} \exp\left(\frac{-\left(t - t_{w}^{-}\right)}{\tau_{w2}^{-}}\right). \tag{6.20}$$

To find the time t maximising this rate of change, we differentiate Eq. (6.20) with respect to t to obtain

$$\frac{\partial^2 w\left(t;\tau_{w2}^{-}\right)}{\partial \tau_{w2}^{-} \partial t} = \left(w_{w}^{-} - w_{\infty}\right)\frac{\left(\tau_{w2}^{-} - \left(t - T_{w}^{-}\right)\right)}{\left(\tau_{w2}^{-}\right)^{3}} \exp\left(\frac{-\left(t - t_{w}^{-}\right)}{\tau_{w2}^{-}}\right). \tag{6.21}$$

Hence, the rate of change of w with respect to τ_{w2}^{-} is maximised where $\frac{\partial^2 w\left(t;\tau_{w2}^{-}\right)}{\partial \tau_{w2}^{-} \partial t}(t) = 0$, *i.e.*

$$t = \tau_{w2}^{-} + t_{w}^{-}, \tag{6.22}$$

as shown in Fig. 6.7.

Given this cycle length the appropriate value of w may be found and hence it is possible to solve for τ_{w2}^{-} as

$$\tau_{w2}^{-} = (t_{w}^{-} - T)(\ln \frac{w(T) - w_{\infty}}{w_{w}^{-} - w_{\infty}})^{-1}. \tag{6.23}$$

It has been determined that the key parameters of the model can be fitted with three data points assuming an exponential morphology of the restitution curve. The points are a long cycle length at which the sample has stabilised, a short cycle length that is at or close to the minimum stable cycle length, and one additional data point. A region of maximum deviation from a prior value has then been given that can be used to guide the selection of these points in a simulation study. However, as we shall see, in practice the fitting method described will struggle if the restitution curve is not flat at the longest point in the data set. Thus, it may instead be necessary to fit the parameters τ_{w2}^{-} and w_{∞} simultaneously, using a fitting algorithm.

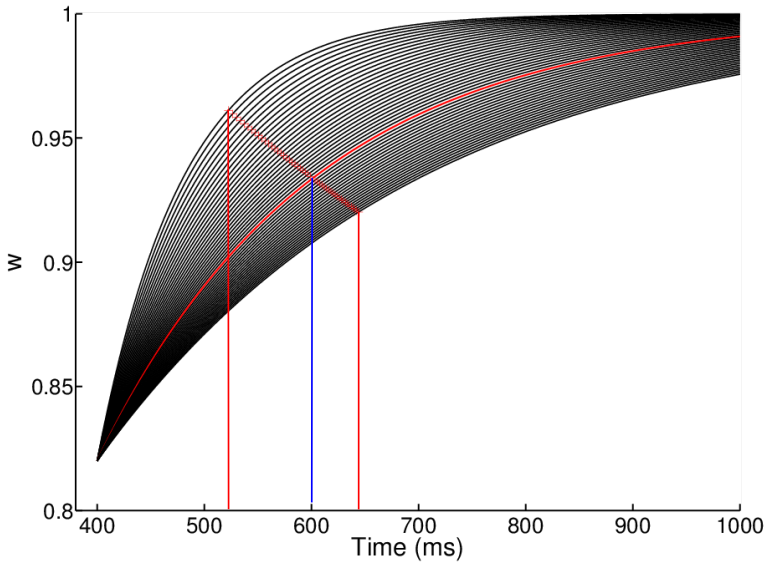

Figure 6.7: **Determining a point of maximum difference from the original restitution curve.** Parameters used are $w_w^- = 0.82$, $t_w^- = 400$ms, and the red line shows $\tau_{w2}^- = 200$. For the black lines, τ_{w2}^- varies between 80ms and 300ms. The red cross denotes the location of the maximum difference between the lines as described in Eq. (6.19), and the blue line denotes the t giving a maximum change in w with respect to τ_{w2}^- as derived in Eq. (6.22).

In order to demonstrate the above method we use a restitution curve recorded from a human left-ventricular wedge preparation published by Lou et al. (2011). Technically, the experimental data show steady-state restitution rather than being generated by an S1-S2 protocol, but they serve the purpose of this example. We consider a restitution curve drawn from one pixel in the middle of the optical mapping field of view.

The basic model used is the guinea-pig apex cell 1 model (see Table 6.1). We set $\theta_{wo} = 1.1 \geq w_\infty^* = 0.949$, ensuring that $w_\infty = w_\infty^*$ in Eq. (6.18). We now consider an AP at a cycle length of 2000ms, and fit its APD using time constant rescaling as in Section 6.2.7 as shown in Fig. 6.8 A. We now construct a map between the APD of the model and the initial value of w as in Fig. 6.6 B), shown in Fig. 6.8 B. Using this map, and the APD80 of the data at a low cycle length of 300ms, we can then determine w_w^-. Given an APD80 of 179ms at 300ms CL, we then get a value of $w_w^- = 0.616$ from our map. We then fit $\tau_{w1}^- = 240\text{ms}^{-1}$ as the time constant required to get from the minimum value of w to w_w^- in the diastolic interval at 300ms cycle length (Fig. 6.8 C. We can then proceed to fit τ_{w2}^-. This could be done using the entire restitution curve, as it is available to us, but instead

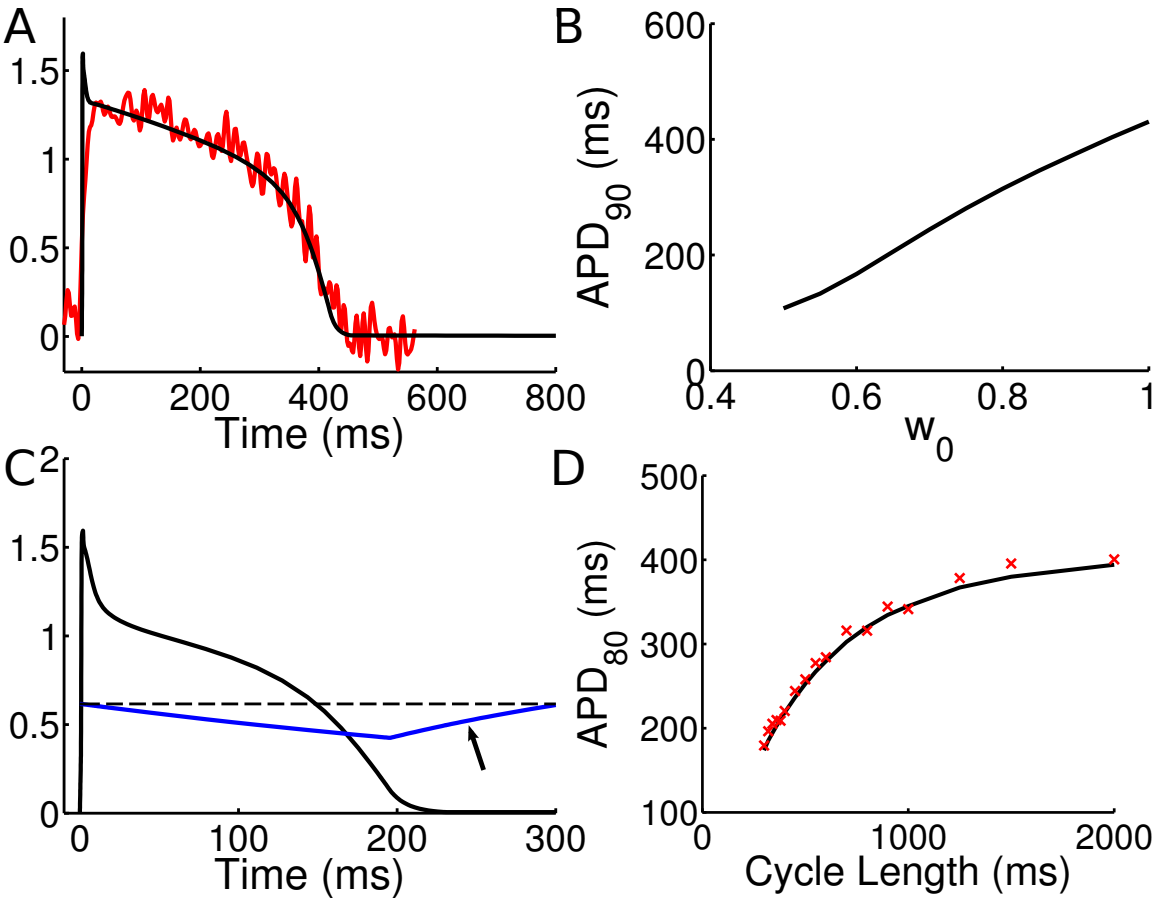

Figure 6.8: **Example of S1-S2 restitution fitting in the BO08 model.** A) The model is fitted to the experimentally recorded action potential at 2000ms cycle length. B) The relationship between APD and initial w for the resulting model. C) Determining τ_{w1}^{-} from the diastolic interval at 300ms cycle length. The arrow denotes the part of the curve controlled by τ_{w1}^{-}, which should recover to the value of w corresponding to the APD at 300ms cycle length (dashed line). D) The resultant model restitution curve (black) compared to experimental data (red crosses).

we demonstrate fitting using the region of interest approach above, using just one cycle length. Using the parameter $\tau_{w2}^{-} = 100$ms from the guinea pig apex cell 1 parameter set as a prior, we choose a cycle length of 300 + 100 = 400ms. This gives a cycle length of 220ms, corresponding to a value of $w = 0.669$. Using Eq. 6.23, we then derive a value of

$$\tau_{w2}^{-} = \frac{300 - 400}{\ln \frac{0.669 - 0.949}{0.616 - 0.949}} = 576\text{ms} \tag{6.24}$$

This parameter fit then produces the restitution curve shown in Fig. 6.8 D.

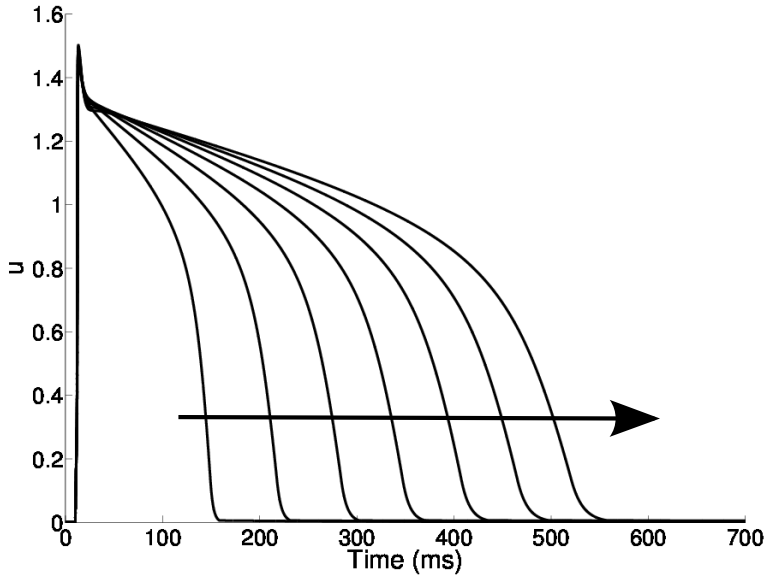

Figure 6.9: **Effect of time constant rescaling on the action potential duration of the BO08 model.** The parameters τ_w^+, τ_s, τ_o, τ_{so} and τ_{si} are all simultaneously rescaled to produce a change in the APD from values between 0.5$\times$ and 2$\times$ their original values. The arrow denotes the direction of increasing parameter value.

6.2.7 Action potential morphology

We have seen in Section 6.2.6 that, given the other parameters of the model are held constant, the initial value of w determines the APD of the BO08 model. However, we can also control the APD by modifying the time constants of the currents active in the repolarisation phase of the APD. An effective way to do this is by simultaneously rescaling the time constants τ_w^+, τ_s, τ_o, τ_{so} and τ_{si}, all active in the repolarisation phase of the model. The effect of this modification is shown in Fig. 6.9. When fitting AP properties in the BO08 model, it is therefore often most effective to select a value of w_∞ using the previous method, then rescale the time constants at a long cycle length to produce an AP with the desired duration. Then by tuning the restitution curve as above, the restitution properties of the entire model are fitted.

Furthermore, as demonstrated by Bueno-Orovio et al. (2008), the model is capable of reproducing the morphology of many different AP morphologies. We now present novel parameter fittings based on experimental data. In Fig. 6.10 we show fits to experimental recordings from A rabbit papillary muscle, B–E isolated guinea pig ventricular myocytes,

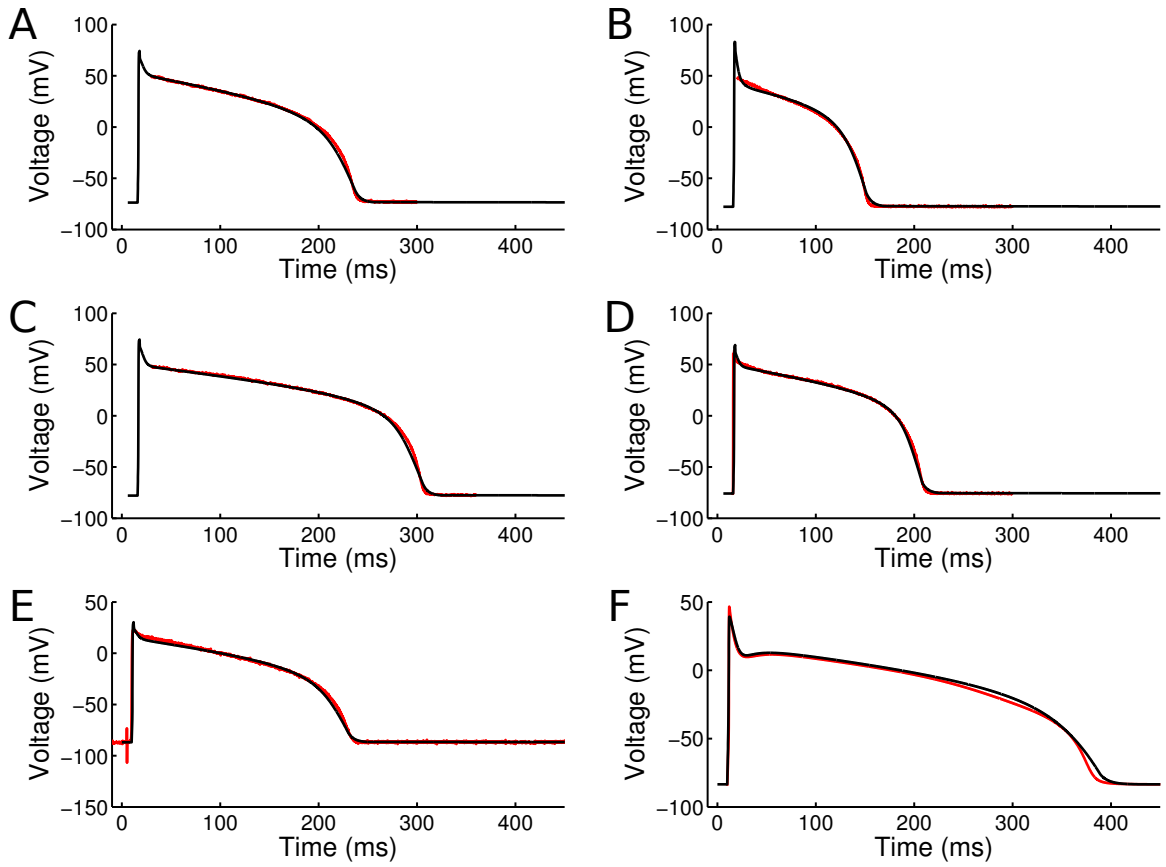

Figure 6.10: **The BO08 model can reproduce a range of experimentally derived action potential morphologies.** Parameter fits (black) are to experimental recordings (red) from A) an apical ventricular myocyte isolated from the endocardium of a guinea pig heart, B) another apical endocardial ventricular myocyte isolated from the same guinea pig heart, C) a basal endocardial ventricular myocyte isolated from a different guinea pig heart, D) another basal endocardial isolated guinea pig ventricular myocyte, E) rabbit papilliary muscle, and F) a simulation of the Luo and Rudy (1991) model.

and F the Luo and Rudy (1991) model. A sensible approach to this problem is to fit the model to key values such as those described in the previous sections, then use optimisation of a sum-of-least-squares objective function to fit to the AP morphology. To generate the final fits to AP morphology in Table 6.1 the Nelder-Mead simplex method is used (Nelder and Mead, 1965). Note that in these cases we have only fitted the morphology of the AP. Restitution properties are set to ensure a flat restitution curve at 1000ms.

6.2.8 Temporal variability

The BO08 model is a deterministic model, not reproducing BVR. We now construct a new version of the model in order to incorporate temporal or beat-to-beat variability into the phenomenological model. We modify equations (6.2), (6.3) and (6.4) by including a Weiner increment in each, forming a stochastic differential equation (SDE) as shown below

$$\partial_t v = (1 - H(u - \theta_v))(v_\infty - v)/\tau_v^- - H(u - \theta_v)v/\tau_v^+ + \sigma_v dW_t^v, \tag{6.25}$$

$$\partial_t w = (1 - H(u - \theta_w))(w_\infty - v)/\tau_w^- - H(u - \theta_w)w/\tau_w^+ + \sigma_w dW_t^w, \tag{6.26}$$

$$\partial_t s = ((1 + \tanh(k_s(u - u_s)))/2 - s)/\tau_s + \sigma_s dW_t^s, \tag{6.27}$$

where σ_v, σ_w and σ_s are taken to be constants changing the magnitude of the Weiner increment. A Weiner process is a stochastic process whose increment dW_t on the interval $[t, t+\Delta t]$ has mean 0 and variance Δt. The superscript is to denote that we have a separate Weiner process for each of the variables v, w and s. We do not include a Weiner increment in the transmembrane potential to reflect the fact that such stochastic fluctuations in APD are hypothesised to be channel level phenomena as mentioned above. The SDE model is integrated using an Euler-Marayama method as described in Chapter 4, with a time step of 0.01ms for all stochastic simulations. A subtlety occurs at 0 and 1 for v, w and s, as stochastic fluctuations may drive the solution outside of the interval $[0\ ,\ 1]$. We therefore integrate the equations with the proviso that any values of v, w and s less than 0 are set to 0 and any greater than 1 are set to 1. This is similar to setting reflective boundary conditions on the SDE at 0 and 1 (Dangerfield et al., 2012).

We aim to fit the mean and variance in APD_{90} to the experimental data, allowing three degrees of freedom in terms of the magnitudes of the noise σ_1, σ_2 and σ_3 as in (6.25), (6.26) and (6.27). We use the parameter sets derived for the guinea pig isolated ventricular myocyte recordings used in Section 6.2.7 as the basis for the stochastic fitting process.

For each of the four cells, the parameter set derived in the deterministic case correspond to an AP with modal APD_{90}. The noise terms for each model, σ_v, σ_w and σ_s are

Table 6.2: **Experimental and simulated variability in APD_{90}**

Parameter	Apex 1	Apex 2	Base 1	Base 2
Mean (exp)	219.5ms	133.7ms	286.5ms	185.8ms
Variance (exp)	37.69	16.80	75.56	21.88
σ_v	0	0	0	0
σ_w	0.0012	0.0015	0.0011	0.0011
σ_s	0.0012	0.002	0.0013	0.0012
Mean (sim)	223.5ms	127.3ms	268.7ms	182.3ms
Variance (sim)	39.22	17.64	77.97	23.73

fitted by simulating chains of 100 APs using the SDE formulation and recording their APDs by searching in a 6×6×6 grid over the interval [0 0.005] for the noise terms. Given the stochastic nature of the model it is not possible to get the same variance on each simulation run, and so we fit the mean variance to the experimentally recorded variance. This has the advantage of being a deterministic property, given a sufficiently large number of simulations. Once appropriate parameter values were found using the grid search, the model was simulated 20 times for the same values to check that the mean of the simulated variance agreed with the variance of the experimental data.

Sample series of APs simulated using the model derived for each of the four cells are shown in Fig. 6.11 E–H. These simulations show good qualitative and quantitative agreement with the experimental results in Fig. 6.11 A–D. There is however no variation in resting potential in Fig. 6.11 E–H. Fitting of the noise terms was successful in matching the mean and variance of the experimental data (Table 6.2). The main effect of increasing σ_v was to increase the mean APD of the model without increasing its variance. We found that $\sigma_v = 0$ provides a good fit for the data. Variance in APD increased with both σ_w and σ_s with mean initially decreasing and then increasing. The fitted noise terms are in Table 6.2.

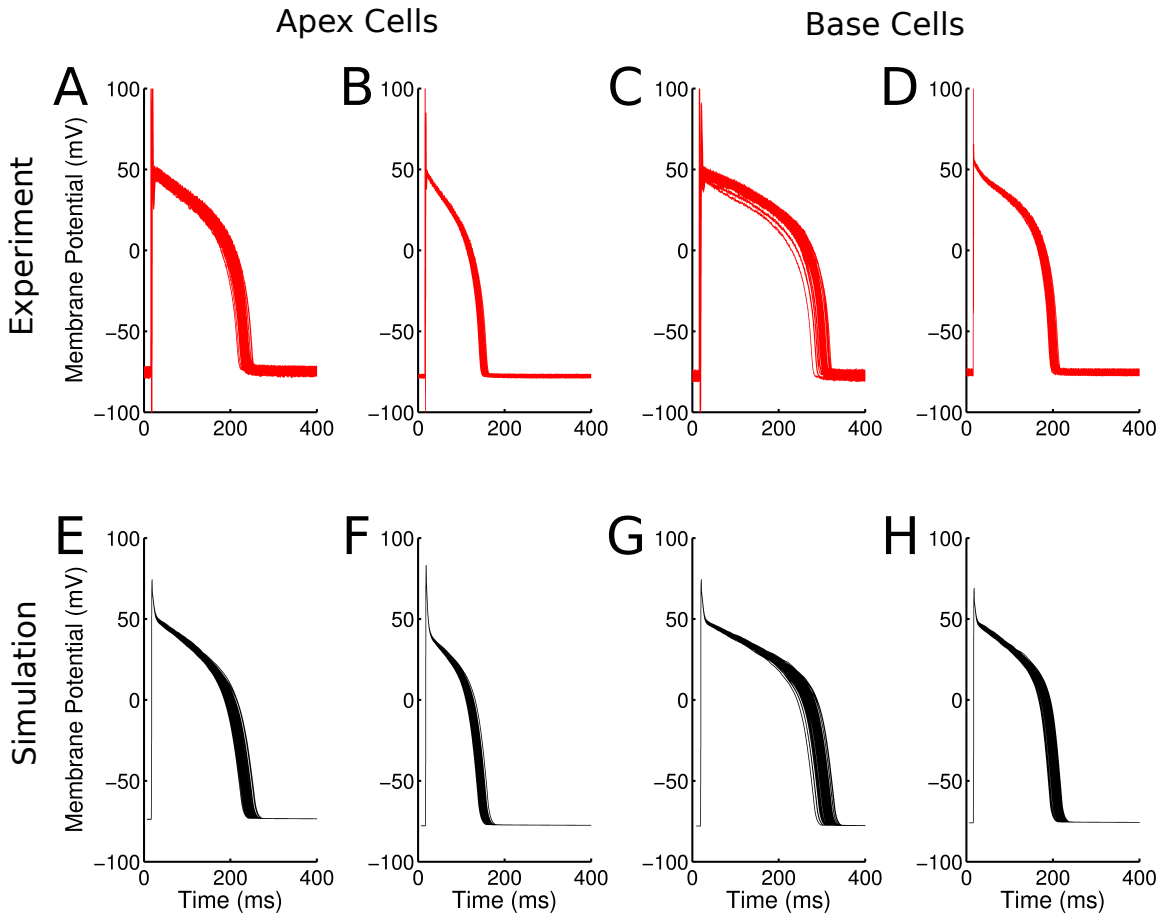

Figure 6.11: **Simulated and experimental temporal variability in repolarisation.** Experimental data showing repeated stimulations of isolated guinea pig ventricular myocytes stimulated at a 1000ms pacing cycle length from A) and B) the apex of the heart and C) and D) the base of the heart. Simulated reproductions of the data using the SDE model are shown in E)–H) respectively. Note that the variability between the cells at apex or base is larger than between apex and base.

6.3 Discussion

In this chapter we have explored the structure of the Bueno-Orovio et al. (2008) cardiac cell model. In particular we have shown that the existing model is able to match a wide range of AP morphologies and properties. Furthermore, we have demonstrated a new improvement to the model that allows the modeller better control over the restitution properties of the model. By focusing on a particular 'region of interest' of the restitution curve we have shown the potential to reduce the amount of points required for fitting and validation of the model. Hence in a joint simulation and experimental study we can reduce the amount of experimental time taken in restitution protocols, therefore giving more opportunity to perform

experiments on other important model aspects. It is also worth noting that as exponential, or double-exponential, fits are commonly used for data analysis of experimentally recorded restitution curves, this concept may have application beyond the realms of computational modelling.

Finally, we have seen that the inclusion of a Weiner process into the model variables v, w and s turns the model into a stochastic model capable of reproducing experimentally recorded temporal variability. This procedure is repeated for sets of patch clamp recordings of the AP exhibiting BVR from four isolated guinea pig myocyte cells. This demonstrates that our method is flexible and suitable for modelling variability between different experimental recordings.

At this stage we have developed a model that reproduces particular properties of the AP. To use this model to gain physiological insight, we must investigate the consequences of the properties of a particular model. A case study investigating the consequences of stochastic variability in tissue reproduced in Section 6.2.8 is presented in Chapter 7.

Chapter 7

Consequences of Sample-Specific Beat-to-Beat Variability in Repolarisation in Tissue

7.1 Introduction

We now move from investigating the *causes* of variability at a cellular scale in Chapter 5, to investigating its *consequences* at a tissue scale. To do so, we will use the four guinea pig ventricular models developed in Chapter 6 from isolated cell data by electrically coupling them in a virtual tissue.

As discussed in Chapter 3, previous simulation studies such as those by Pueyo et al. (2011) and Lemay et al. (2011) have demonstrated that coupling reduces BVR dramatically, but BVR can re-appear as the conductivity of the tissue decreases. In neither of these studies was the temporal variability of repolarisation in the model directly fitted to reproduce that observed in multiple isolated cells. Similarly, studies on inter-cell variability such as that by Lesh et al. (1989) do not include temporal variability. In this chapter, we include this inter-cell variability into monodomain simulations of cardiac tissue in order to investigate whether the experimentally recorded temporal variability from single cells can cause spatial

dispersion of the APD in a tissue setting.

In this chapter, we shall investigate the hypothesis that experimentally observed inter-cell variability in the APD has a larger impact on tissue level dispersion of APD than the experimentally observed temporal variability in the isolated guinea pig myoycyte models constructed in Chapter 6. Furthermore, we will demonstrate that the degree of spatial dispersion in APD will increase as the conductivity of the tissue is reduced.

7.2 Methods

7.2.1 Two-Dimensional Tissue Simulations

We perform all tissue simulations using Chaste, described in Chapter 4. Simulations are performed for both the deterministic and stochastic models in a two-dimensional tissue sheet of dimension 1cm $\times$ 1cm. We use four different values of the diffusion coefficient D to investigate the effects of reduced coupling upon temporal variability of repolarisation. The conductivities are calculated from the basic BO08 model value of D =1.171 cm^2 s^{-1}. This basic conductivity is used to represent physiological conduction, and then simulations are also performed at 0.5 times, 0.1 times, and 0.05 times this basic value, giving values of D equal to 1.171 cm^2 s^{-1}, 0.586 cm^2 s^{-1}, 0.117 cm^2 s^{-1}, and 0.059 ^{2} s^{-1}, respectively. These values of D correspond to conduction velocities of 72 cm s^{-1}, 51 cm s^{-1}, 23 cm s^{-1} and 16 cm s^{-1}, respectively.

To investigate the effect of beat-to-beat variability, a homogeneous sheet is created for both the stochastic and deterministic forms of each cell model in turn. To include the effect of inter-cell variability, a cell model distribution is generated by drawing a uniform random number for each node in the tissue. The four cell models from Chapter 6 are applied to the tissue with equal probability based on this random number. The same distribution is used for both the stochastic and deterministic simulation to enable direct comparison between the two. 50 stimuli are then applied at a pacing cycle length of 1000ms for both

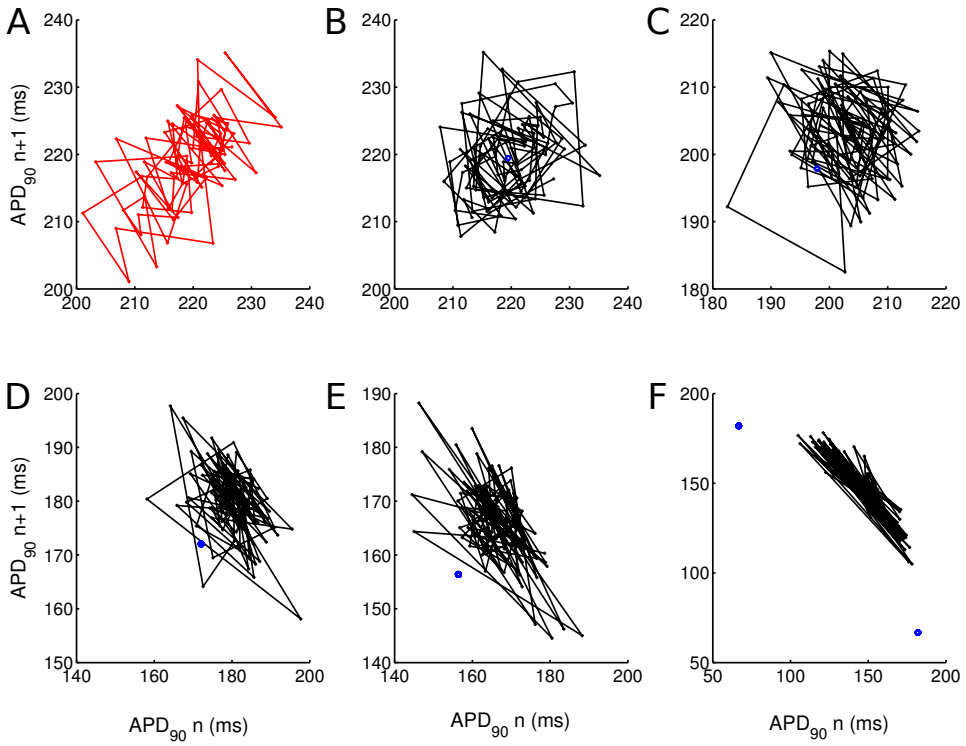

Figure 7.1: **Onset of alternans in a stochastic phenomenological model of an isolated guinea pig ventricular myocyte.** A) A Poincaré plot of the original experimental data (red). Poincaré plots generated from the guinea pig apex cell 1 model developed in chapter 6 are shown at pacing cycle lengths of B) 1000ms C) 400ms D) 300ms E) 260ms and F) 220ms for the stochastic (black) and deterministic (blue) versions of the model.

the deterministic and the stochastic versions of each model.

In the next study we investigate the consequences of the alternans-like behaviour induced in the stochastic model at short cycle lengths shown in Fig. 7.1. To see whether this alternans will affect the magnitude of dispersion of APD measured in the homogeneous case above, a homogeneous apex cell 1 tissue is used. We use only one cell model as the models are not parameterised from data at short cycle lengths. The cycle length is gradually reduced from 230ms CL (where alternans-like behaviour begins to appear in the stochastic cell model) in 2ms intervals every 40 beats until conduction block occurs. Again, simulations are performed for both the deterministic and the stochastic models.

For all simulations, the stimulus is applied at the left hand edge of the tissue (x <0.03 cm). To ensure that the stochastic simulations are comparable, the same pseudo-random number sequence is used for each stochastic simulation.

Simulation results are analysed by recording the upstroke time and APD_{90} after each simulation. We do not perform analysis for $x \leq 0.25$cm or $x \geq 0.75$cm in order to reduce the influence of boundary effects. The maximum dispersion of APD is measured as the maximum difference in APD_{90} across the region 0.25cm $\leq x \leq$ 0.75cm at each node in the mesh. The difference in APD_{90} between the stochastic and deterministic simulation is also computed for every stimulus. Furthermore, when considering the beat-to-beat variability in APD across multiple beats in the tissue, we describe the mean APD_{90} in the tissue in one beat as μ_{APD} for brevity.

7.2.2 Numerical Convergence

In order to ensure numerical convergence in both the stochastic and deterministic models, we examined convergence in the conduction velocity and in the maximum difference in the APD_{90} to determine the numerical parameters used in the simulations.

Simulations are performed for each of the values of D in Section 7.2.1. The spatial discretisations used are 0.1, 0.05, 0.01, 0.005 and 0.0025cm. The PDE time steps used are 0.1, 0.05, 0.025, 0.01, 0.005 and 0.0025ms. Deterministic convergence results are shown in Fig. 7.2. Based upon these convergence plots we determine that a spatial discretisation of 0.01 cm, and a PDE time step of 0.01ms are sufficient for this simulation study.

In order to test convergence we pre-generate a conserved Brownian path for each of the variables w and s for each node in a 0.5cm$\times$ 0.5cm tissue with a spatial discretisation of 0.01cm, as described in Chapter 4. Simulations are performed for a duration of 250ms with the stochastic version of the apex cell 1 model. Simulations are analysed by calculating the difference in APD_{90} at each node between the current simulation and the reference solution obtained at a time step of 0.000625ms (Fig. 7.3). Note that the printing time step had almost no effect on the reported APD_{90}. An absolute difference in APD_{90} of $\leq$ 0.1ms between the reference solution and the 0.00125ms solution is observed in the $D = 0.059$ cm^2 s^{-1} case.

The results of the convergence analysis mean that the simulations described in Section

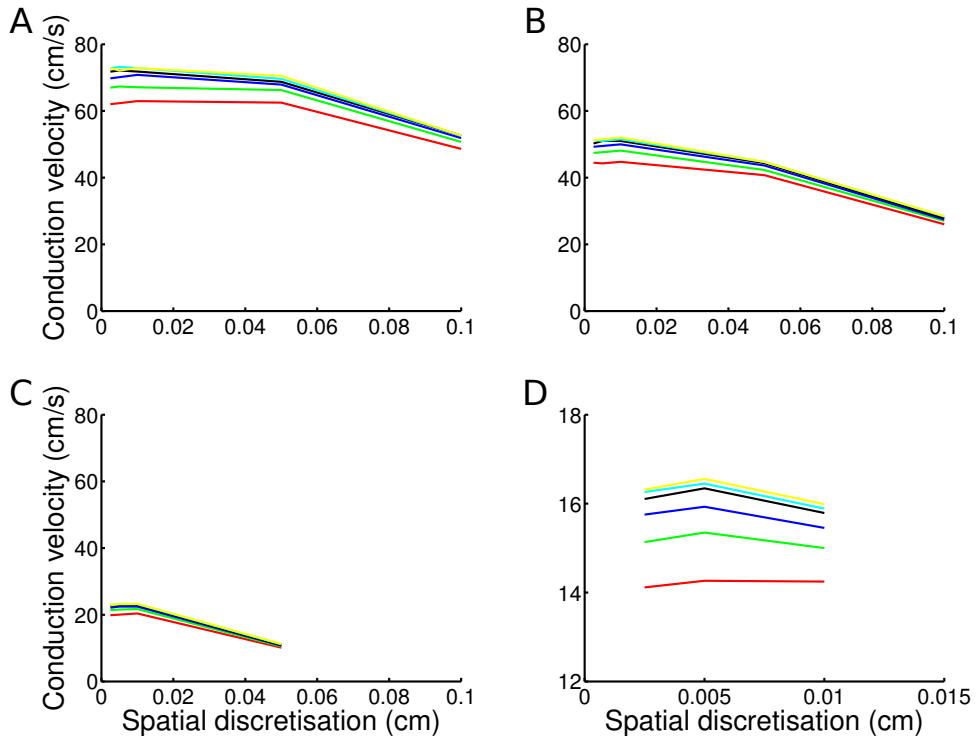

Figure 7.2: **Convergence analysis for the deterministic model investigating the effects of PDE time step and spatial discretisation for each value of $\mathbf{D}$.** Results are plotted for PDE timesteps of 0.1ms (red), 0.05ms (green), 0.025ms (blue), 0.01ms (black), 0.005ms (cyan) and 0.0025ms (yellow). A) shows results with D = 1.171 cm^2 s^{-1}, B) $D = 0.586$ cm^2 s^{-1}, C) $D = 0.117$ cm^2 s^{-1} and D) $D = 0.059$ cm^2 s^{-1}. The axes on plot D) have been rescaled to better display the results. The conduction velocity is not plotted where a propagation failure occurs.

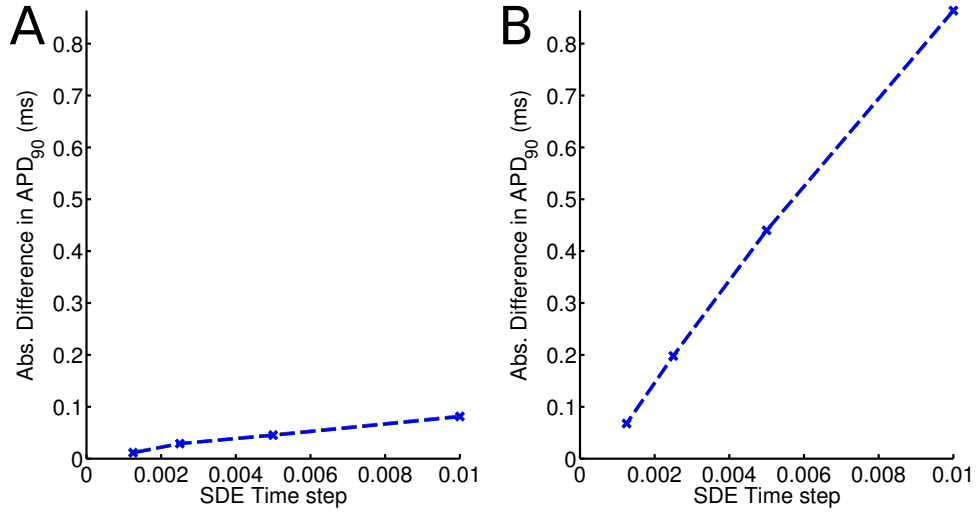

Figure 7.3: **Convergence analysis for the stochastic model.** The absolute difference in APD_{90} is calculated across all nodes between the reference solution (timestep 0.000625ms) and simulations at timesteps of 0.01ms, 0.005ms, 0.0025ms and 0.00125ms. The maximum value of this difference is plotted for each time step with A) $D = 1.171$ cm^2 s^{-1} and B) $D = 0.059$ cm^2 s^{-1}. The printing time steps shown are 1ms (red), 0.1ms (green) and 0.05ms (blue). In most cases, these lie on top of one another.

Table 7.1: **Summary of homogeneous simulations**

Cell Model		D (cm^2 s^{-1})			
		1.171	0.586	0.117	0.059
Apex cell 1	Det. Mean(μ_{APD}) (ms)	219.8	219.8	219.7	219.7
	Det. Var(μ_{APD}) (ms^2)	0	0	0	0
(var. 39.22ms^2)	Stoch. Mean(μ_{APD}) (ms)	219.8	219.8	219.7	219.7
	Stoch. Var(μ_{APD}) (ms^2)	0.020	0.023	0.033	0.037
Apex cell 2	Det. Mean(μ_{APD}) (ms)	134.3	134.3	134.3	134.3
	Det. Var(μ_{APD}) (ms^2)	0	0	0	0
(var. 17.64ms^2)	Stoch. Mean(μ_{APD}) (ms)	134.3	134.3	134.3	134.3
	Stoch. Var(μ_{APD}) (ms^2)	0.012	0.014	0.020	0.021
Base cell 1	Det. Mean(μ_{APD}) (ms)	288.4	288.4	288.3	288.3
	Det. Var(μ_{APD}) (ms^2)	0	0	0	0
(var. 77.97ms^2)	Stoch. Mean(μ_{APD}) (ms)	288.4	288.4	288.4	288.3
	Stoch. Var(μ_{APD}) (ms^2)	0.041	0.047	0.065	0.067
Base cell 2	Det. Mean(μ_{APD}) (ms)	190.8	190.8	190.8	190.8
	Det. Var(μ_{APD}) (ms^2)	0	0	0	0
(var. 23.73ms^2)	Stoch. Mean(μ_{APD}) (ms)	190.8	190.8	190.8	190.8
	Stoch. Var(μ_{APD}) (ms^2)	0.013	0.016	0.022	0.025

7.2.1 are run using a spatial discretisation of 0.01cm, a PDE time step of 0.01ms and an ODE / SDE time step of 0.00125ms.

7.3 Results

7.3.1 Homogeneous cell model distributions

Simulations show a temporal variability in the mean repolarisation in the stochastic simulations for all four cell models, shown in Fig. 7.4. The variability in μ_{APD} increases slightly on a beat-to-beat basis as the diffusion coefficient D is decreased. This is quantified by calculating the variance in μ_{APD} across all 50 beats (see Table 7.1). In all, the distribution of μ_{APD} for the stochastic simulations is centred on the μ_{APD} of the deterministic simulations. The beat-to-beat variance in μ_{APD} also increases with the variance of the underlying cell model (Table 7.1, see brackets after cell model name for isolated cell variance).

The difference between the deterministic and stochastic simulations did not increase with the number of beats for each cell model, as shown in Fig. 7.5, suggesting that stochasticity is not enhanced over time in tissue. The maximum difference between the stochastic

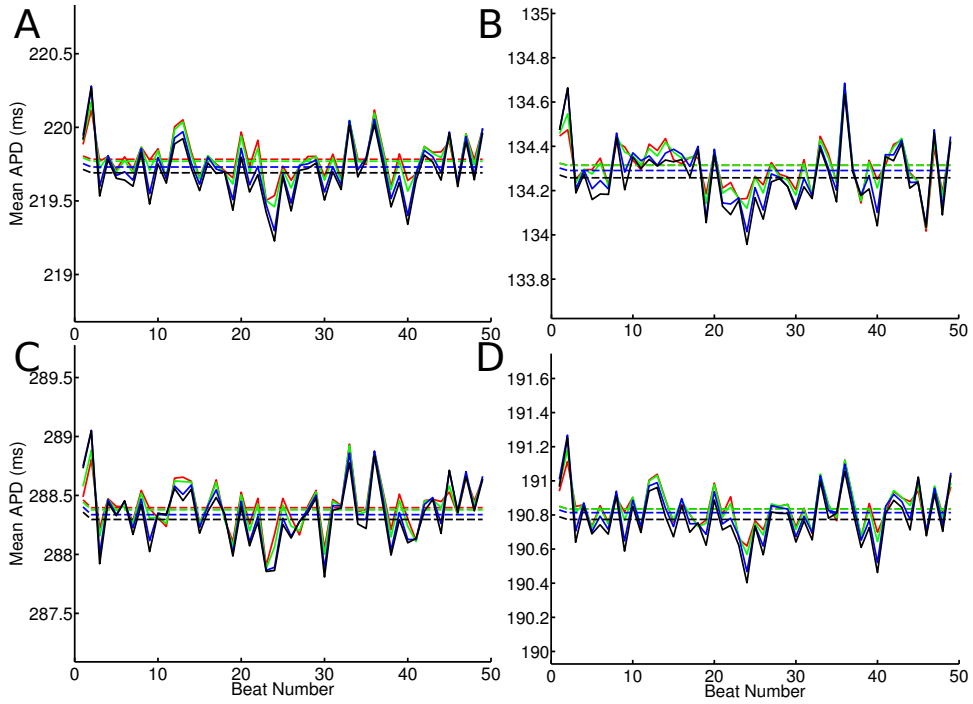

Figure 7.4: **Mean APD_{90} from tissue simulations using homogeneous cell models.** The mean APD_{90} in across all nodes in the central 0.5cm of the tissue is plotted for both the stochastic (solid lines) and deterministic (dashed lines) simulations for each cell model and each value of D. Results are shown for $D =$ 1.171 cm^2 s^{-1} (red), $D =$0.586 cm^2 s^{-1} (green), $D =$ 0.117 cm^2 s^{-1} (blue) and $D =$ 0.059 cm^2 s^{-1} (black). The cell models are A) apex cell 1, B) apex cell 2, C) base cell 1 and D) base cell 2.

and deterministic simulations increased as the conductivity scaling decreased. The largest difference observed was in base cell 1 with $D = 0.059$ cm^2 s^{-1}, with a difference of 2.20ms from the deterministic simulation.

Spatial dispersion in the APD_{90} resulting from stochasticity, as measured by the variance in the difference between the stochastic and deterministic simulation for each beat is shown in Fig. 7.6. Fig. 7.6 shows that the variance increases as D decreases for each cell model, demonstrating an increase in dispersion of APD resulting from the stochastic simulations. Heat maps of the APD in the stochastic case for apex cell 1 are shown in Fig. 7.7 to demonstrate the increase in dispersion in APD resulting from temporal variability in the cell model at low conductivities. A slight dispersion of APD arising from boundary effects (also present in the deterministic simulations) can also be seen at higher conductivities, explained by the dependence of the size of the boundary effect with conductivity as described

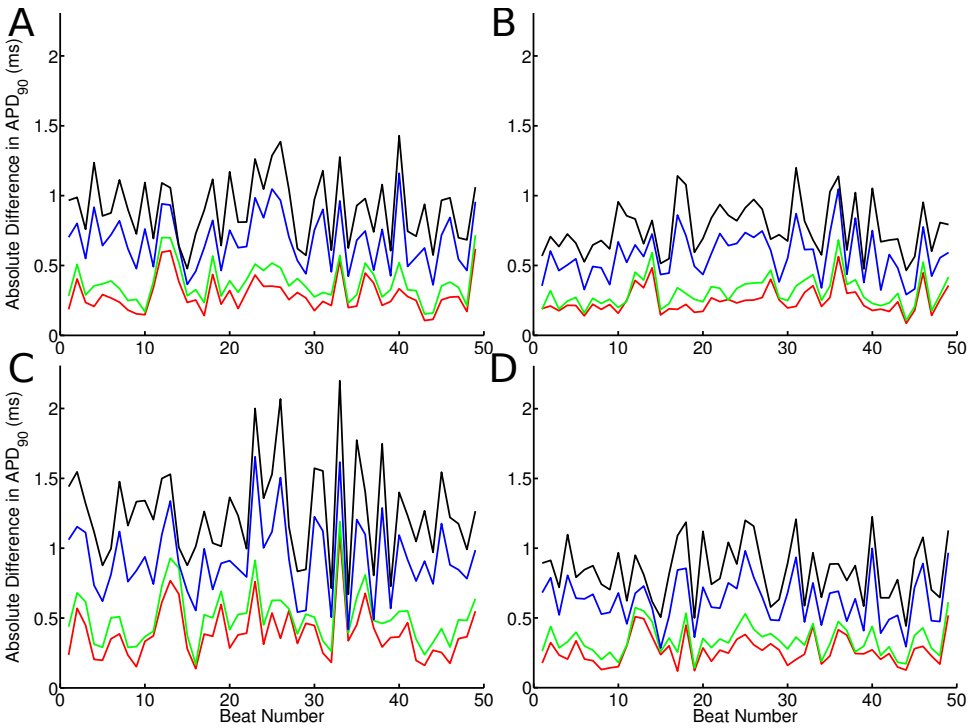

Figure 7.5: **Difference between stochastic and deterministic simulations using homogeneous cell models.** The absolute difference between the deterministic and stochastic simulations is calculated at each node in the central 0.5 cm of the tissue. The maximum of these absolute differences for each beat is then plotted as a function of the number of beats at $D = 1.171$ cm^2 s^{-1} (red), $D = 0.586$ cm^2 s^{-1} (green), $D = 0.117$ cm^2 s^{-1} (blue) and $D = 0.059$ cm^2 s^{-1} (black). Results are shown for A) apex cell 1, B) apex cell 2, C) base cell 1 and D) base cell 2.

by Cherry and Fenton (2011). This dispersion created a variance in both the deterministic and stochastic models at $D = 1.171$ cm^2 s^{-1} of up to 0.18ms^2 in the deterministic case and 0.4ms^2 in the stochastic case (base cell 1).

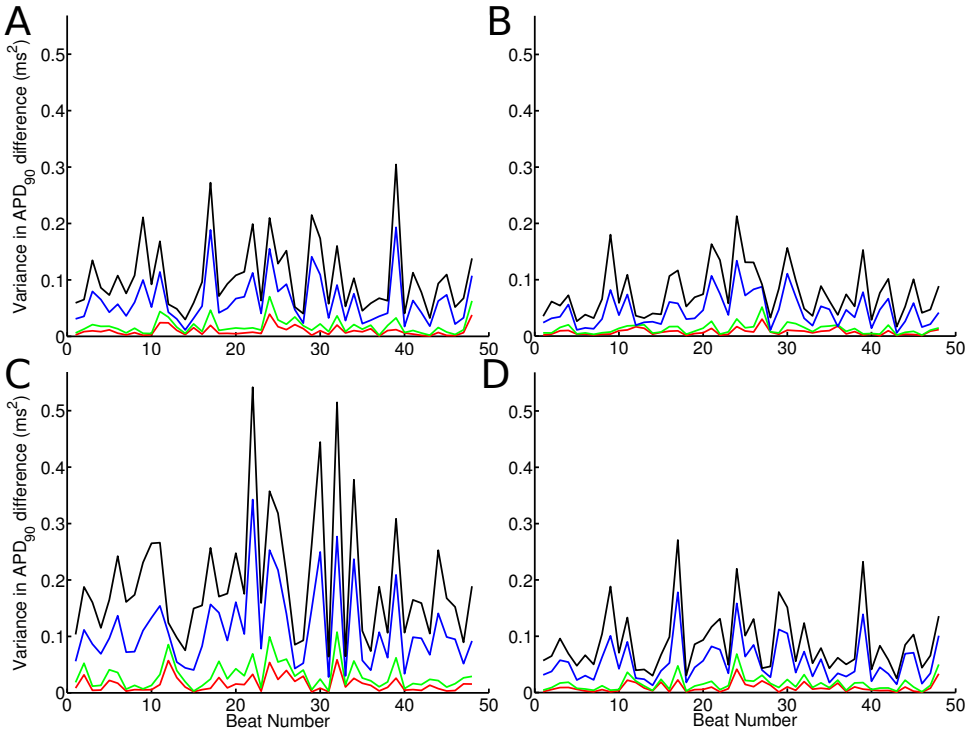

Figure 7.6: **Variance in the difference between stochastic and deterministic APD_{90} values for the homogeneous tissue simulations.** For each beat, the difference between the stochastic and deterministic APD_{90} maps is calculated at each node in the central 0.5cm of the tissue. The variance across these nodes is then calculated for each beat. The variance in the difference between the deterministic and stochastic APD_{90} maps is plotted as a function of the number of beats at $D = 1.171$ cm^2 s^{-1} (red), $D =$0.586 cm^2 s^{-1} (green), $D = 0.117$ cm s^{-2} (blue) and $D = 0.059$ cm^2 s^{-1} (black). Results are shown for A) apex cell 1, B) apex cell 2, C) base cell 1 and D) base cell 2.

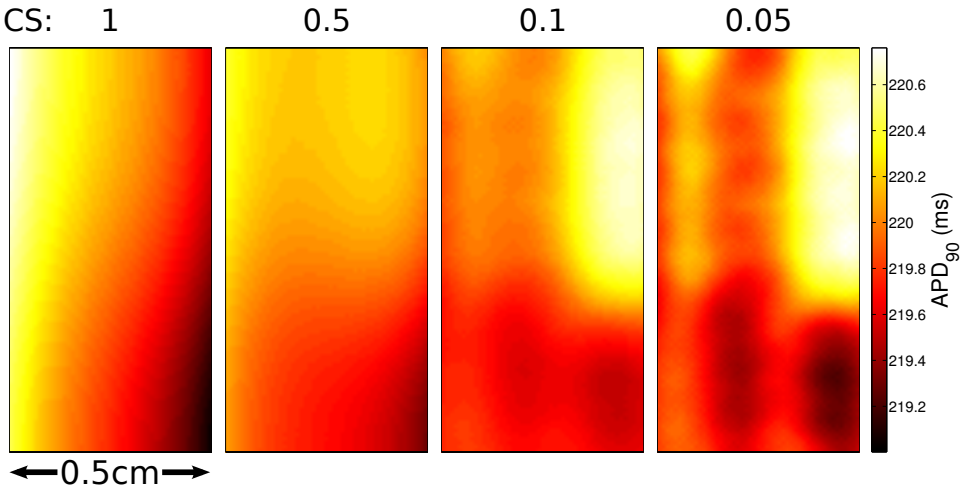

Figure 7.7: **Heat maps of spatial dispersion in APD_{90} for apex cell 1.** APD_{90} maps shown are recorded from base cell 1 with $D =$ A) 1.171 cm^2 s^{-1}, B) 0.586 cm^2 s^{-1}, C) 0.117 cm^2 s^{-1} and D) 0.059 cm^2 s^{-1}. The heat maps shown are generated using the stochastic cell model and are taken from the final beat in the series. APD_{90} maps are plotted from the central 0.5 cm to reduce distortion due to boundary effects.

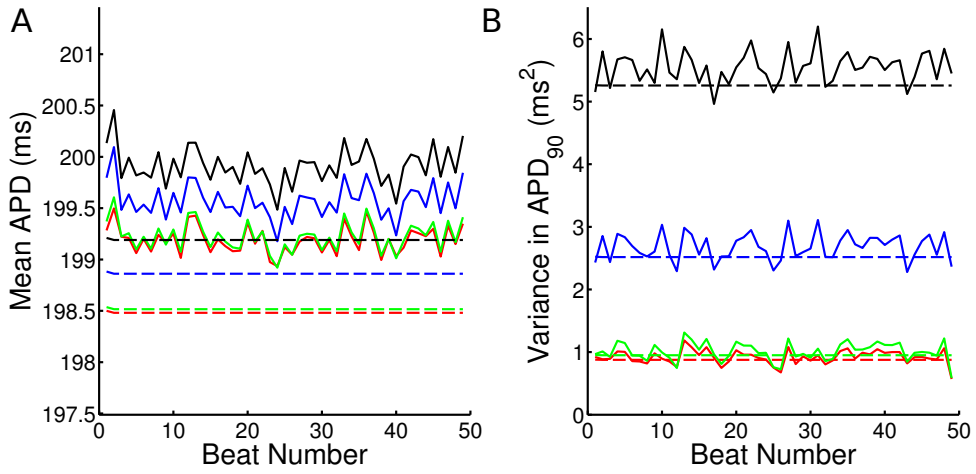

Figure 7.8: **Mean and variance in APD_{90} from tissue simulations using a random cell model distribution.** The mean and variance in the APD_{90} is calculated over all nodes in the central 0.5 cm of the tissue at each beat. The A) mean and B) variance are then plotted for both the stochastic simulations (solid lines) and deterministic simulations (dashed lines) for each beat. Each cell model and each value of D is shown. Values of D are 1.171 cm^2 s^{-1} (red), D =0.586 cm^2 s^{-1} (green), D = 0.117 cm^2 s^{-1} (blue) and D = 0.059 cm^2 s^{-1} (black).

7.3.2 Randomly Generated Cell Model Distributions

As in Section 7.3.1, the μ_{APD} of the deterministic simulations was constant, whereas there was a beat-to-beat variability in μ_{APD} in the stochastic simulations (Fig. 7.8 A). Thus, given a heterogeneous cell population generated from our four cells using a uniform random variable at each node, temporal variability induces beat-to-beat variability in mean APD_{90} behaviour.

The variability in APD_{90} grows as D decreases due to the unmasking of the heterogeneous dispersion of the AP as shown by the increase in cell model variance in Fig. 7.8 B. The variance in the APD_{90}, calculated over the nodes in the central 0.5cm, for the deterministic simulations is slightly lower than that in the stochastic case (Fig. 7.8 B). However, there is still a much larger increase in the variance in the heterogeneous deterministic case than is observed for the homogeneous stochastic cases (Section 7.3.1). At the lowest value of D, the variance reaches a maximum of 6.1ms^2, which remains smaller than the cell models' variance in APD, which ranges between 17.64ms^2 for apex cell 2 and 77.97ms^2 for base cell 1 (Table 7.1). The difference between the deterministic and stochastic simulations

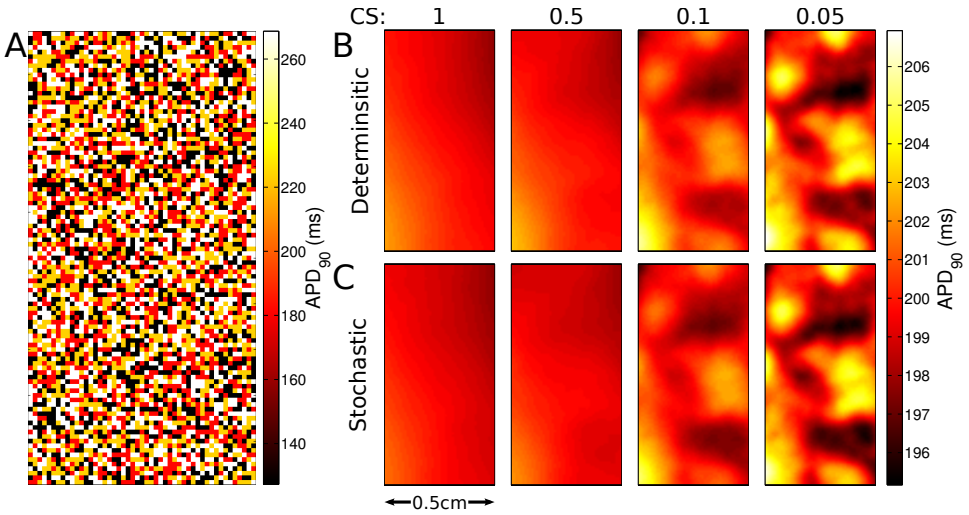

Figure 7.9: **Heat maps of spatial dispersion in APD_{90} using a randomly generated cell distribution.** APD_{90} maps shown are recorded are for A) the underlying cell model distribution, then at $D = 1.171$ cm^2 s^{-1}, 0.586 cm^2 s^{-1}, 0.117 cm^2 s^{-1} and 0.059 cm^2 s^{-1} for the B) deterministic and C) stochastic simulation results respectively. Simulation results shown are for the 50th beat in the series, and from the central 0.5 cm of the tissue only.

remained at similar values to those seen in Section 7.3.1, being bounded between -1ms and $+2$ms at the lowest value of D (0.059 cm^2 s^{-1}). This is again dramatically smaller than the dispersion in the single cell models, which ranged between 22.3ms for apex cell 2 and 47.1ms for base cell 1.

Heat maps of both deterministic and stochastic simulations from the final beat are shown in Fig. 7.9, together with the underlying cell model distribution. This figure demonstrates the increase in dispersion of repolarisation as D is reduced. The maximum dispersion observed is 11ms with $D = 0.059$ cm^2 s^{-1}. Note that as the differences arising from the heterogeneity in the cell model distribution are much larger than those resulting from BVR in the cell models, the heat maps in Fig. 7.9 appear to be almost identical.

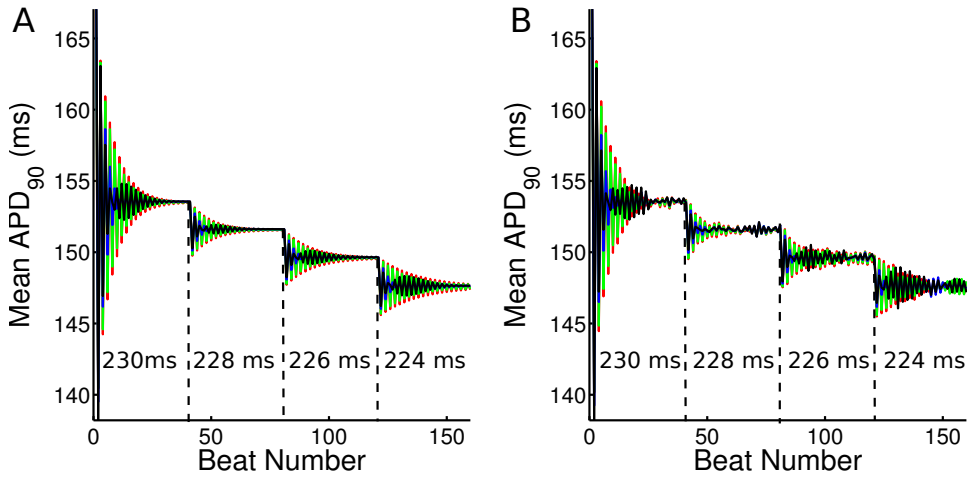

Figure 7.10: **Mean APD in the fast pacing protocol.** The mean APD_{90} (μ_{APD}) is calculated across the nodes in the central 0.5 cm in the tissue for each beat. μ_{APD} is shown as a function of the number of beats for the A) deterministic and B) stochastic model, at $D = 1.171$ cm^2 s^{-1} (red), $D = 0.586$ cm^2 s^{-1} (green), $D = 0.117$ cm^2 s^{-1} (blue) and $D = 0.059$ cm^2 s^{-1} (black). Vertical dashed lines denote a change in pacing cycle length.

7.3.3 Fast Pacing Rates

Action potentials were simulated until a conduction block occurred at a pacing cycle length of 222ms. Conduction block occurred at the same time point in both the deterministic and the stochastic simulations. Fig. 7.10 shows a plot of μ_{APD} recorded at all four values of D over 160 beats. μ_{APD} can be seen to oscillate dramatically in response to a change in cycle length, but these oscillations are damped with the number of beats in both the deterministic and the stochastic cases, leaving a small beat-to-beat alternans in μ_{APD}.

The overall effect of stochasticity on the simulation can be measured by calculating the maximum difference between the stochastic and deterministic simulations, as shown in Fig. 7.11, for all values of D. The difference between the stochastic and deterministic simulations increases as D is reduced. The maximum difference for the lowest value of D (0.059 cm^2 s^{-1}) is bounded by $\pm$ 1.5ms, again smaller than the APD range in the stochastic version of apex cell 1 (31.4ms).

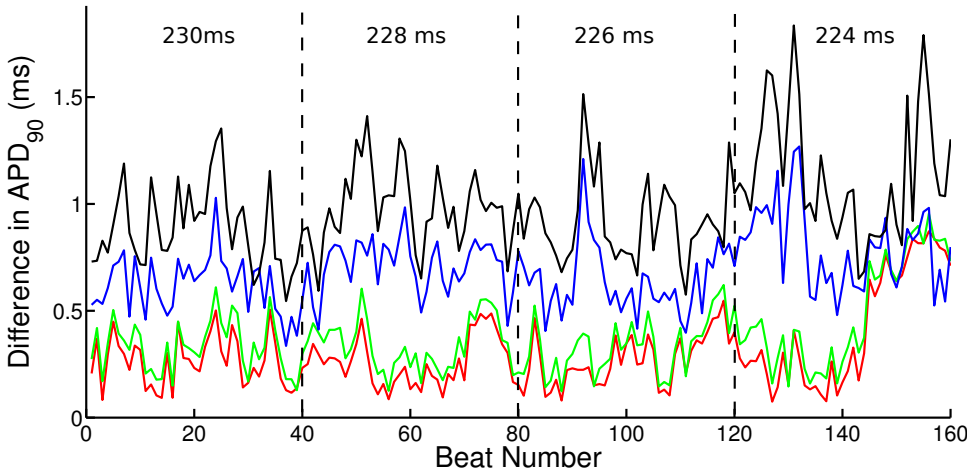

Figure 7.11: **Maximum absolute difference between stochastic and deterministic APD in the fast pacing protocol.** The absolute difference between the APD maps for the deterministic and stochastic simulations is calculated at each node in the central 0.5 cm of the tissue. The maximum of these absolute differences for each beat is then plotted as a function of the number of beats at $D = 1.171$ cm^2 s^{-1} (red), $D = 0.586$ cm^2 s^{-1} (green), $D = 0.117$ cm^2 s^{-1} (blue) and $D = 0.059$ cm^2 s^{-1} (black). Vertical dashed lines denote a change in the pacing cycle length.

In order to evaluate the degree of dispersion in the APD in each beat, we compute the variance within the APD_{90} map at each beat as shown in Fig. 7.12. The dispersion is comparable between the stochastic and deterministic simulations following a change in pacing cycle length. In fact, the stochastic model displayed a reduced change in the mean value in the beats immediately following the change in cycle length as compared to the deterministic model, as is also seen in the single cell model in Fig. 7.1 F. The transient increase in variance was due to the change in cycle length inducing a global alternans in both models which was modulated by boundary effects. To remove this effect, we also examined the mean and variance of the APD once the oscillations have stabilised in the final ten beats of the AP at each cycle length, as shown in Fig. 7.13 and 7.14. For these beats, the mean value of the APD shows a moderately increased variability at low D as compared to the deterministic model. However, there is a dramatic increase in variance in the stochastic model, but not the deterministic model, as the diffusion coefficient of the tissue is reduced, showing that the dispersion of the APD_{90} increases in the stochastic model at low values of D.

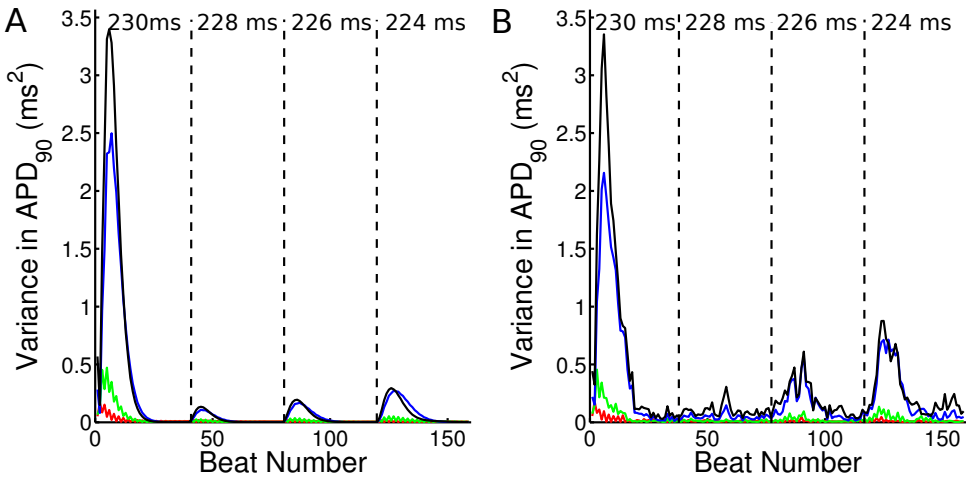

Figure 7.12: **Variance in APD_{90} for the fast pacing protocol.** The variance of the APD is calculated over the nodes in the central 0.5 cm of the tissue for each beat. The variance is plotted as a function of the number of beats for the A) deterministic and B) stochastic models, at $D = 1.171$ cm^2 s^{-1} (red), $D = 0.586$ cm^2 s^{-1} (green), $D = 0.117$ cm^2 s^{-1} (blue) and $D = 0.059$ cm^2 s^{-1} (black). Vertical dashed lines denote a change in pacing cycle length.

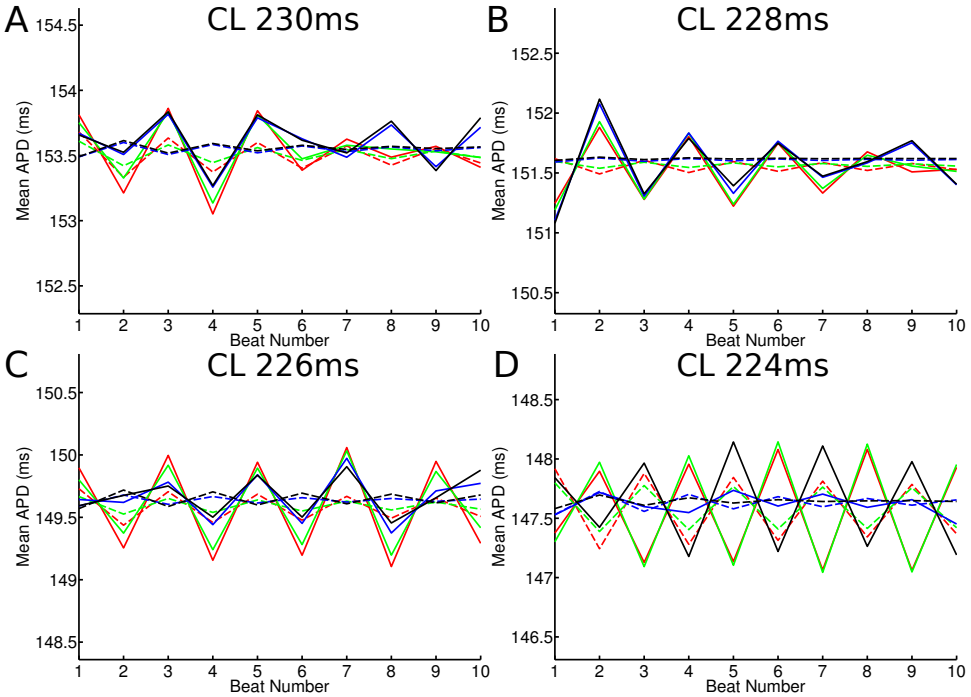

Figure 7.13: **Mean APD_{90} over the last ten beats at each cycle length in the fast pacing protocol.** The mean of the APD_{90} is calculated over the nodes in the central 0.5 cm of the tissue. The mean APD_{90} is plotted for the last 10 beats at each cycle length of A) 230ms, B) 228ms, C) 226ms and D) 224ms for the deterministic (dashed line) and stochastic (solid line) models, for $D = 1.171$ cm^2 s^{-1} (red), $D = 0.586$ cm^2 s^{-1} (green), $D = 0.117$ cm^2 s^{-1} (blue) and $D = 0.059$ cm^2 s^{-1} (black).

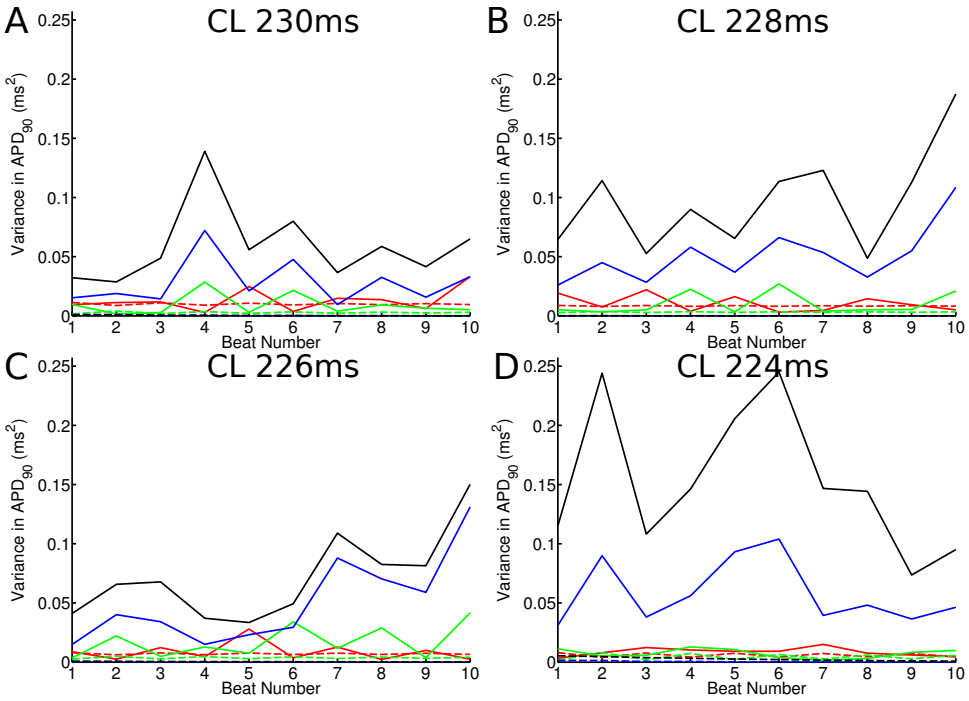

Figure 7.14: **Variance in APD_{90} over the last ten beats at each cycle length.** The variance in the APD_{90} is shown at cycle lengths of A) 230ms, B) 228ms, C) 226ms and D) 224ms for the deterministic (dashed line) and stochastic (solid line) models, for $D = 1.171$ cm^2 s^{-1} (red), $D = 0.586$ cm^2 s^{-1} (green), $D = 0.117$ cm^2 s^{-1} (blue) and $D = 0.059$ cm^2 s^{-1} (black).

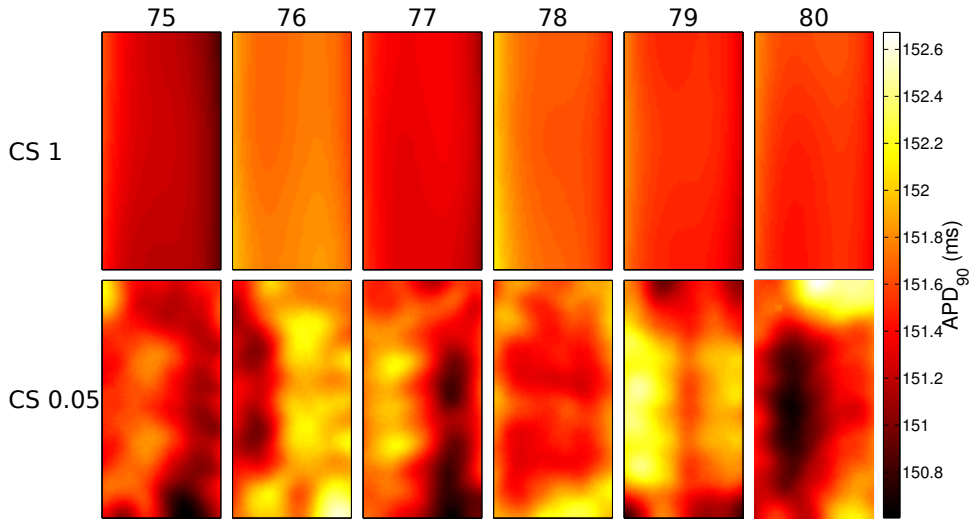

Figure 7.15: **Spatially discordant alternans-like behaviour recorded in the action potential duration at 228ms pacing cycle length in the stochastic model.** The APD_{90} maps shown are simulated at a cyclelength of 228ms (beats 75–80) for the stochastic model for $D = 1.171$ cm s^{-2} and 0.059 cm^2 s^{-1}. APD_{90} maps are plotted from the central 0.5cm only to remove boundary effects.

In the stochastic simulations at the lowest value of D (0.059 cm^2 s^{-1}) we observed phenomena that resembled a spatially discordant beat-to-beat alternans. Fig. 7.15 shows a sequence of six action potential duration maps in the stochastic model from the end of the 228ms pacing cycle length section of the pacing protocol. In the deterministic simulations (Fig. 7.15 A,C), there is almost no spatial heterogeneity in the APD_{90}, and similarly with $D = 1.171$ cm^2 s^{-1} no dispersion is observed in the stochastic model (Fig. 7.15 B). At $D = 0.059$ cm^2 s^{-1}, the stochastic simulations show a modest spatially heterogeneous alternation in the simulated APD_{90} that is not present in either the equivalent deterministic recording at the same value of D, or in either the stochastic or deterministic recording for $D = 1.171$ cm^2 s^{-1}. The maximum amplitude of the oscillations is approximately 2ms.

7.4 Discussion

7.4.1 Main Findings

In this chapter we have demonstrated the use of a phenomenological model representing temporal and inter-cell variability to investigate consequences of this variability. In particular, we have investigated the hypothesis that experimentally observed inter-cell variability in the APD has a larger impact on tissue level dispersion of APD than the experimentally observed temporal variability in isolated guinea pig myocytes, and that spatial dispersion in APD will increase as the conductivity of the tissue is reduced.

In the homogeneous tissue simulations, we observe spatial dispersion of APD resulting from temporal variability for each cell model. The dispersion of APD increases as the diffusion coefficient D is decreased in accordance with previous studies. The dispersion resulting from temporal variability in the APD alone is relatively low. In absolute values, the maximum difference between deterministic and stochastic simulations observed was around 2ms in the case of base cell 1. We observed similar results at fast pacing rates, with the alternans observed in both the stochastic and deterministic models being damped in tissue. Temporal variability in the APD produced a similarly low dispersion in the APD at fast pacing rates.

When the cell model distribution was allowed to vary randomly, we observed a spatial dispersion in APD that was visible even at the highest value of D (1.171 cm^2 s^{-1}). At the lowest value of D (0.059 cm^2 s^{-1}) this dispersion reached a value of 11ms, an order of magnitude larger than that observed in the temporal variability simulations in the homogeneous cell cases. This can also be measured quantitatively by observing the large increase in variance in the random cell model simulations as opposed to that observed in the homogeneous cell model cases. Including temporal variability into the random cell model simulations resulted in a relatively small further increase in the dispersion as measured using variance. We therefore conclude that, when using cell models fitted to experimentally measured cell-to-cell and beat-to-beat variability, the cell-to-cell variability provides a

greater contribution to dispersion of repolarisation than the beat-to-beat variability.

We additionally investigated whether the alternans-like behaviour observed in the stochastic cell model could cause increased dispersion of repolarisation. Some simulations resemble a spatially discordant alternans in APD_{90}, which has been shown in animal models to be arrhythmogenic (Myles et al., 2008). The amplitude of this oscillation is small, however (2ms). The amplitude of both the beat-to-beat and the spatially discordant alternans was dramatically lower than those in the single cell simulations (see Fig. 7.1 F).

It is worth noting that the degree of dispersion resulting from purely beat-to-beat variability is sufficiently small that it is unlikely to be detected even by patch clamp studies. The dispersion observed in the signal when random cell model distributions are used is large enough that it could be detectable using microelectrode arrays given a very clean signal. Given a more spatially organised cell distribution, the dispersion, and hence its detectability, would likely increase as seen in previous studies (Viswanathan et al., 1999).

7.4.2 Limitations

A limitation of this work is that whilst our cell models are fitted as single cell models, the nodes of a finite element mesh do not represent cells as such. Instead, they represent homogenised points in space. Thus the cell model in fact represents averaged behaviour in the area around the node.

The approach presented here for investigating hypothesis two inherits a limitation from the data set used for its parameterisation. Specifically, we only have four cells, and they come from different areas of two different hearts. Without further experiments we cannot say whether this variability arises as a result of abnormal cells, or in some limited way embodies the variability across one heart. Thus, our conclusions are relevant to the coupling together of these four cells in tissue, rather than directly to the hearts in question.

An interesting consequence of using a model fitted directly to data comes in the additional simulations at fast pacing rates. As the model was only fitted at a cycle length of 1000ms, we cannot claim that the alternans behaviour predicted is typical to these cells.

This is why only one cell model was used, rather than all four. Hence, whilst we can conclude that alternans of the type displayed in the simulations in Fig. 7.1 leads to the spatial dispersion observed in tissue, we cannot conclude that they arose as a result of the behaviour observed in the experimental data — they are a product of the model structure.

7.4.3 Conclusions

The work presented in this chapter differs from previous studies on the subject (Lesh et al., 1989; Lemay et al., 2011; Pueyo et al., 2011) in that we use cell models that are directly fitted to the APD and the degree of temporal variability to the recordings of cell membrane potentials. Hence, we have the ability to make a prediction about the consequences of the temporal variability observed in the specific experiments, whereas the previous studies seek to produce a conclusion based on models that have been parameterised from a wide variety of sources, and therefore illustrate a general principle rather than a prediction about a specific experiment.

We conclude that constructing phenomenological models of inter-cell variability, and temporal variability of repolarisation, allows for the investigation of sample-specific hypotheses. Specifically, we conclude that for the guinea pig APs recorded using patch clamp data reported in Chapter 6, the degree of inter-cell variability makes a larger contribution to spatial dispersion in APD_{90} than beat-to-beat variability. However, the choice of a sample specific model may prove restrictive in a way that is not true for biophysically detailed models for investigating subcellular causes that drive this variability. In this chapter, we have assumed that coupling between the cells is uniform throughout the tissue. In the intact myocardium this is unlikely to be the case everywhere, and it is to the level of structural organisation of myocytes that we turn next.

Chapter 8

Sample-Specific Fitting of Conductivity Tensors from Human Optical Mapping Recordings

8.1 Introduction

In the preceding chapters we have investigated the ability of computational models to capture experimentally recorded and population-level variability in the repolarisation phase of the AP. As discussed in Chapter 3, there are many other potential sources of variability in electrophysiological activity within the heart. We now consider how structural features within the heart may affect its conduction by directly comparing experimentally recorded activation times to model prediction.

Inter-individual variability in activation time is frequently observed in humans both *in vivo* (Bueno-Orovio et al., 2012) and *in vitro* (Lou et al., 2011). As discussed in Chapter 2, activation time depends upon the functional coupling of cardiac myocytes through gap junctions and on their arrangement into fibres and sheets. Changes to either will alter the propagation of electrical activity through the myocardium. Pre-existing variability between individuals may be further exacerbated by pathological conditions such as heart failure,

which is associated with changes in conduction and gap junctional remodelling (Glukhov et al., 2012). Furthermore, there is some evidence to suggest that changes in fibre arrangement may occur in heart failure in humans (Eggen et al., 2009).

When performing simulations of the human left ventricle with either the monodomain or bidomain equations a conductivity tensor is used to represent tissue anisotropy (see Eq. (3.32), Eq. (3.33) and Eq. (3.36) in Chapter 3). Personalised conductivity tensors may be derived from histology or diffusion tensor MRI (dt-MRI) (Weiss et al., 2007; Benson et al., 2011; Trayanova, 2011; Zhang et al., 2012). When these are unavailable it is common practice to use a relatively simple rule-based representation of the laminar arrangement of the heart, together with a global estimate of the conductivity tensor. Many rule-based tissue structure descriptions incorporate fibre orientation only, such as those presented by Efimov et al. (1996) and Potse et al. (2006), but some also incorporate sheet orientation (LeGrice et al., 1997). The resulting conductivity tensors provide a physiologically grounded estimate which can be used for simulation studies.

In this chapter, we challenge a commonly used model of transmural fibre orientation (Potse et al., 2006) with activation times recorded experimentally by Lou et al. (2011). We use recordings taken transmurally from explanted human left ventricles using optical mapping. We use three failing and three non-failing samples. We also conduct computer simulations of electrical activation on mesh geometries that capture the shape of each individual wedge. By allowing key model parameters to change, we allow the model to adapt to the inter-sample variability described above. We then compare simulated and experimental activation time maps directly by registering the optical mapping field of view onto the simulation mesh constructed for each sample. Through this process, we have the potential to detect regions of conduction in the experimental recordings that do not correspond to our model of how the ventricles behave, thereby gaining insight into the physiology of conduction in the human left ventricle.

We hypothesize that simulations based on the rule-based method will provide a good estimate for the non-failing human heart activation times, but that the effects of fibre de-

rangement will lead to a poorer match between simulated and experimentally recorded activation (in the failing human hearts).

8.2 Methods

8.2.1 Experimental Data

We use optical mapping recordings of membrane voltage (Vm) from three failing and three non-failing human left ventricular wedge preparations. The experimental data have previously been published by Lou et al. (2011). For full details of the acquisition of human material and experimental procedures, the reader is referred to the papers by Efimov et al. (2010), Glukhov et al. (2010), and Lou et al. (2011). In brief, human hearts are acquired from either end-stage heart failure patients undergoing a heart transplant operation, or from donor hearts which are rejected for transplantation. Left-ventricular wedges perfused by the left marginal artery are excised from the postlateral free wall of the heart. The left marginal artery is cannulated and used for perfusion of the tissue with Tyrode's solution. Tissue is stained with RH237 for Vm mapping. Recordings are taken at 500Hz.

A high-resolution colour photograph is taken from above the wedge and the bright field image of the optical camera's field of view is stored. The optical mapping camera produces 100$\times$ 100 pixel images. Wedges are stimulated using a unipolar electrode at multiple pacing cycle lengths ranging from 1500ms to 300ms at a fixed site on the endocardial surface. Each pacing cycle length is maintained for 100 paces and then the cycle length is reduced. Only the last 3–6 APs are recorded at each cycle length to avoid photobleaching of the membrane voltage and cytosolic calcium dyes.

Vm time series signals are binned and filtered according to the standard provided by Laughner et al. (2012). Specifically, all traces are binned using a 3$\times$3 bin, then a low pass 100Hz finite impulse response filter is applied to the voltage trace for each pixel using Matlab's `fir1` function. A polynomial fit to the data is used to remove drift in the signal where

appropriate and the trace is normalised to take values between 0 and 1. To determine the upstroke time, a window of approximately 200ms is selected around each upstroke in the recording. The upstroke time for each pixel is calculated using a sliding window approach which minimises the difference between the data trace and a Heaviside function. The time point at which the minimal difference appears is taken as the upstroke time. This gives practically identical results to calculating the time of maximum upstroke velocity, and also provides a sensible estimate where the maximum upstroke calculation fails due to noisy data. We then obtain a 100 $\times$100 array containing an upstroke time for most pixels in the field of view.

Summary of modelling assumptions

We now briefly summarise the modelling assumptions we are making in this chapter about conduction in the human left ventricle:

1. The myocardium is an anisotropic medium;
2. A monodomain model adequately captures anisotropic conduction in cardiac tissue;
3. Fibre orientation varies across the wall of the heart based on the findings of Streeter et al. (1969), captured by the cubic formulation of Potse et al. (2006);
4. There is variability in fibre angle that may arise from the wedge orientation;
5. The conductivity is axisymmetric about the fibre direction (*i.e.* a sheet direction is not included);
6. Other than the fibre orientation, there is no spatial variation in the magnitude of the conductivity;
7. Upstroke dynamics are captured by the Bueno-Orovio et al. (2012) electrophysiology model;
8. Optical scattering does not significantly affect the recorded activation times.

These are assumptions that are all commonly made when using a rule-based model of fibre orientation for simulation studies. We challenge them through direct comparison with experimental data.

8.2.2 Mesh Construction

The length scale of the wedge is determined from a ruler placed in the photograph of the wedge. A mapping between the photograph and Cartesian co-ordinates is then established using the scale from the ruler. The optical mapping field of view is then registered onto the wedge photograph as shown in Fig. 8.1 A using features visible in the bright field image. This process is performed using the Matlab functions `cpselect` and `cp2tform` to generate an affine transformation. The resulting maps between the bright-field image and the photograph, and the photograph and the Cartesian co-ordinate system used in the mesh below then allow direct comparison of simulated and experimental data.

Points lying on the boundary of the region to be simulated are selected from the wedge photograph and tagged as epicardial, endocardial and midmyocardial points as shown in Fig. 8.1 B. The electrode location is also recorded. We do not attempt to reproduce features such as trabeculations on the endocardial surface as we do not have sufficient data in the wedge photograph to do so, and the optical mapping data is transmural. The two-dimensional representation of the wedge surface is then given a depth of 0.5cm to produce a three-dimensional tissue region to account for the electrotonic load of the tissue below the cut surface. This is less than the full thickness of the wedge (approximately 1cm) as the full thickness is generally not perfused, and also to reduce computational load. Tetrahedral meshes are then generated from using Tetgen (`http://tetgen.berlios.de/`). A small region outside of the optical mapping field of view is included at the apical and basal ends of the wedge mesh to prevent boundary effects influencing results at the edge of the simulation mesh.

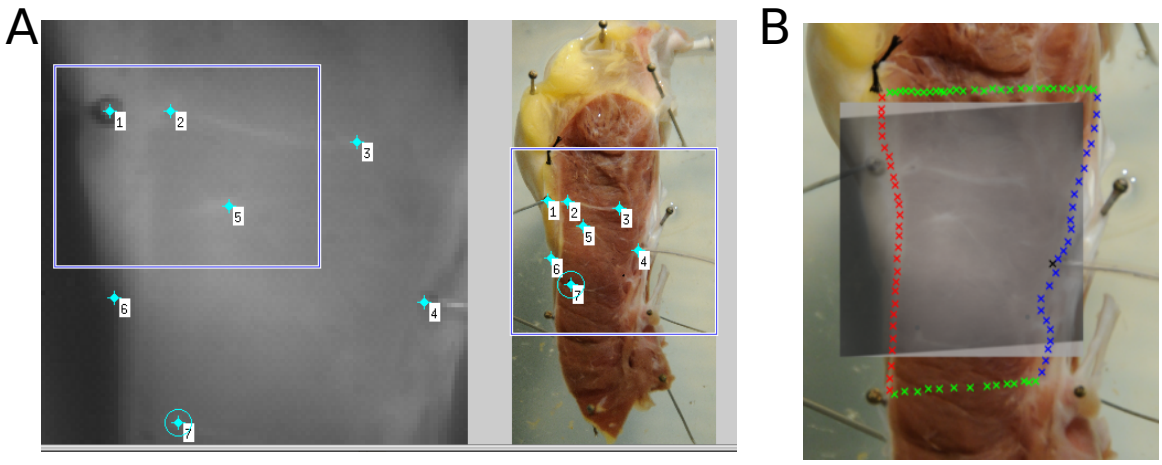

Figure 8.1: **Generation of simulation meshes from wedge photographs.** A) Registration of the optical mapping camera field of view onto the wedge photograph (image has been cropped). B) Selecting boundary points for the construction of the wedge mesh. Red denotes epicardial, green midmyocardial and blue endocardial boundaries of the wedge mesh. The black cross denotes the location of the stimulus.

8.2.3 Electrophysiology Model

The action potential model used as a basis for this work is the Bueno-Orovio et al. (2012) (BO12) phenomenological model, a revised version of the Bueno-Orovio et al. (2008) model described in Chapter 6. The model has six variables and 29 parameters, having been extended to reproduce adaption of APD in response to a change in pacing cycle length. All computational simulations are performed in Chaste. Simulations are performed using a basic ODE timestep of 0.005ms and PDE time step of 0.01ms and saved after every 1ms of simulation for visualisation and postprocessing.

8.2.4 Fibre Orientation Model

Generating fibre orientations

Fibre orientations are generated using the rule-based method described in Potse et al. (2006), as implemented in Chaste (Bernabeu et al., 2008). The method assigns to each tetrahedron in the mesh a fibre orientation based on its relative distance d through the wall

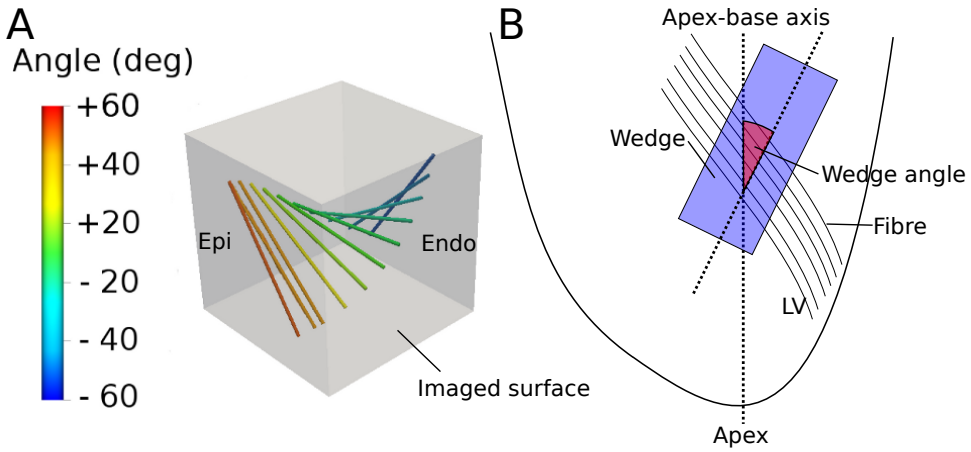

Figure 8.2: **Definition of the fibre parameters under investigation.** A) Physiological meaning of the helix angle (α). α is measured from the normal to the plane of the original wedge photograph when constructing fibre orientations. The relation of the fibre rotation to the optically imaged surface is also shown. This image is modified from Mirams et al. (2013) under the Creative Commons Attribution License. B) Shows the physiological definition of the wedge angle, β is measured from the y axis in the original wedge photograph.

measured from the endocardium,

$$d = \frac{d_{endo}}{d_{endo} + d_{epi}}.$$

The fibre direction is parallel to the epicardial surface and assigned a helix angle, α (shown in Fig. 8.2 A) measured from the apex-base axis. The helix angle α is then allowed to vary as a function of d, so that

$$\alpha = R(1 - 2d)^3, \tag{8.1}$$

where R is the maximum helix angle. Thus, the helix angle varies from R on the endocardial surface to $-R$ on the epicardial surface.

We incorporate variability in both R and the angle from the apex-base axis at which the wedge was cut from the heart (β). β is allowed to vary between -45° and 45° from the apex-base axis. R is allowed to vary between 15° and 75°, reflecting the range of values seen in diffusion tensor MRI and histology. β is shown diagramatically in Fig. 8.2 B). We take five evenly spaced points for each parameter, giving a total of 25 different fibre orientations.

Generating conductivity tensors

We choose the basic diffusion coefficient for the BO12 model as 1.171 cm^2/s, as presented by Bueno-Orovio et al. (2012) to represent human epicardial conduction. To represent tissue anisotropy we consider the conductivity tensor to be axisymmetric (*i.e.* no 'sheet' direction). We consider two anisotropy ratios, 1:$\frac{1}{4}$ in the fibre direction, and 1:$\frac{1}{2}$ in the fibre direction. These are comparable to the experimentally reported values of Caldwell et al. (2009) of 1:$\frac{1}{2}$:$\frac{1}{4}$ for fibre:sheet:normal. The standard diffusion coefficient in the plane normal to the fibre is 0.25$\times$1.171 = 0.293 cm^2/s in the 1:$\frac{1}{4}$ case, and 0.5$\times$1.171 = 0.586 cm^2/s in the 1:$\frac{1}{2}$ case.

For each fibre orientation we then assign a conductivity tensor σ combining the fibre orientation with the fibre and normal conductivities. We perform a grid search over each fibre orientation, scaling the value of the conductivity tensor in twelve evenly spaced steps from 0.5 to 1.6 times the baseline value of the conductivity tensor. Values are chosen to produce conduction velocities in the fibre direction comparable to those observed in human epicardial recordings. Hence we have 25 $\times$ 12 $\times$ 2 = 600 possible conductivity tensors. Simulations are also run in an isotropic tissue for comparison, where the only value to change is the scaling on the basic diffusion coefficient of 1.171cm^2/s. Values in the isotropic case range from 0.125 to 1.6 times the baseline value, *i.e.* the minimum value for the normal direction to the maximal value in the fibre direction in the anisotropic case.

Activation region

For each conductivity tensor we stimulate the tissue by activating a region. This region corresponds to the region active approximately 5ms after stimulation in the optical mapping data, approximated by an ellipse. An example of this activation region is shown in Fig. 8.3. We attempt to make the activated region occupy a similar number of pixels for each wedge as far as possible. Initial conditions are set by imposing 'activated' parameter values of $u = 1.6$ and $v = 0$ in this region. Whilst the location of the stimulus electrode is visible

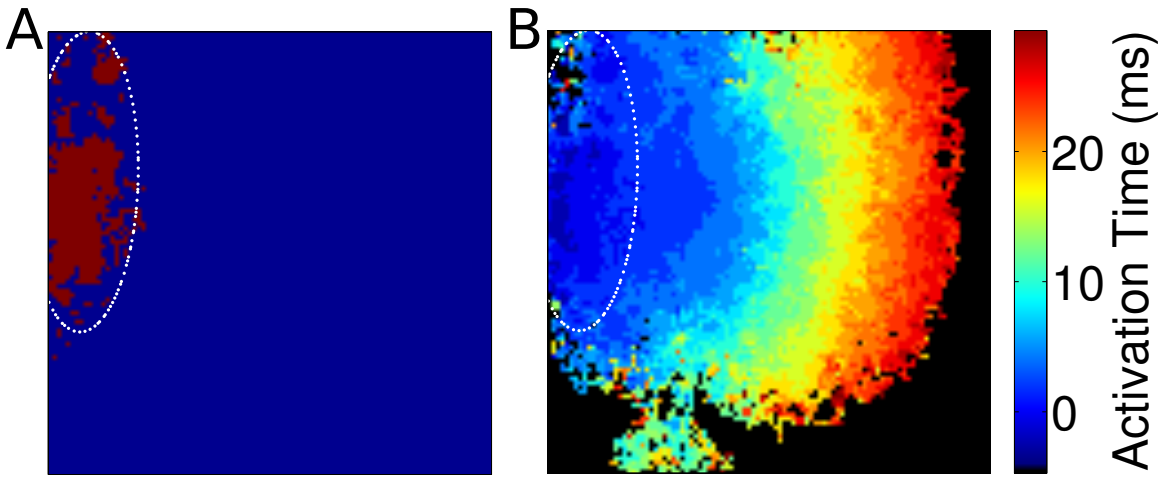

Figure 8.3: **Selecting an elliptical region for activation from experimental data.** An elliptical region for activation is selected for a non-failing wedge by thresholding on the activation time. An ellipse of points is then selected around the thresholded data.

in some images, we do not simply apply a stimulus at this location as it is not visible for all wedges and also the shape of the initially activated region, which we do not know, will heavily influence the future shape of the propagating wave.

Comparison of experimental and simulated data

For each conductivity tensor, simulations run for 100ms to allow the entire computational wedge to activate. Activation time values for each simulation are calculated using Chaste by finding when the non-dimensional membrane voltage u exceeds a threshold value of 0.4. The recorded values are then compared to the experimental data. The experimental activation time map is adjusted so that an activation of approximately 0ms occurs on the boundary between the activated region and the activation data.

Only pixels outside the region stimulated after 5ms activation are considered. At each pixel in the optical mapping data for which an upstroke time is stored, the square difference between the experimental and simulated data for each conductivity tensor is recorded. The total sum across the tissue is then square-rooted to give the root-mean-square difference between simulation and experiment for each simulation performed. To allow comparison between multiple wedges, the sum of squares value is normalised by the number of pixels

in the activation map. The conductivity tensor that minimises the least squares is then accepted. The process is then repeated for all activations of the tissue recorded at 1500ms CL to investigate whether the activation pattern produces a different parameter estimate from beat to beat. For each set of results, we highlight regions of parameter space which differ by $\leq$ 5% from the optimal value in each activation in order to quantitatively demonstrate the uncertainty in our results.

In order to quantify the error that arises due to the 500Hz sampling of the experimental data, we perform a simulation on a 100×100 node mesh with a 0.02cm node spacing. An ellipse on one edge is activated, as for the wedge simulations. Simulations were performed at conductivity scales of 1.6, 1.0, and 0.5 and stored at an output time step of 0.1ms. This recording was then downsampled to 2ms. Upstroke times were then calculated for the 0.1ms and the twenty 2ms recordings. The normalised objective function was then calculated as above. Error due to sampling was in the range 0.0079–0.0082.

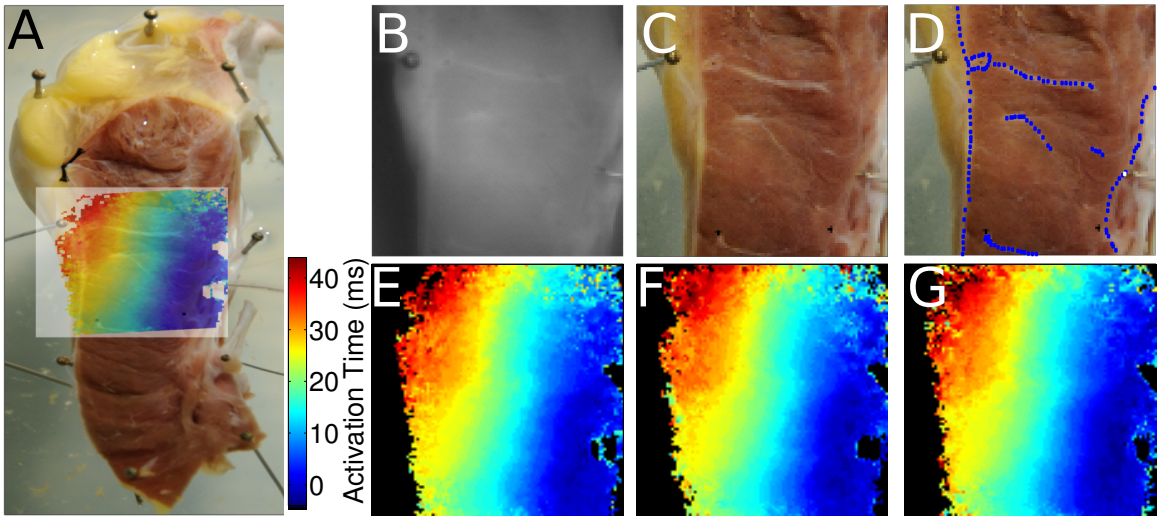

Figure 8.4: **Non-Failing Wedge 1: Experimental data.** A) An activation map registered onto the wedge photograph. B) the optical mapping field of view. C) The region of the wedge photograph registered onto the optical mapping field of view. D) Structural features apparent in the optical mapping field of view are highlighted for comparison with simulated data. E)–G) maps of three subsequent activation times recorded across non-failing wedge 1.

8.3 Results

8.3.1 Non-Failing Wedge 1

The optical mapping field of view is roughly in the middle of the wedge preparation, slightly closer to the base than the apex (Fig. 8.4 A). Three consecutive transmural activations are recorded for this preparation, shown in the activation maps in Fig. 8.4 E–G. The mean conduction velocity across the wedge normal to the wavefront is 43.2cm/s.

Fig. 8.5 describes the effect of conduction parameter variability on the agreement between simulated and experimental activation times for non-failing wedge 1. The degree of agreement is quantified by the value of the normalised sum of square differences objective function. A lower value indicates better agreement between simulation and experiment. The parameter set giving the best agreement for each activation and each anisotropy ratio is indicated by a star, with hatched regions indicating parameter sets with agreement similar to that of the optimal case. The optimal value for each anisotropy ratio is well conserved between each activation of the tissue. For non-failing wedge 1, the optimal parameter set

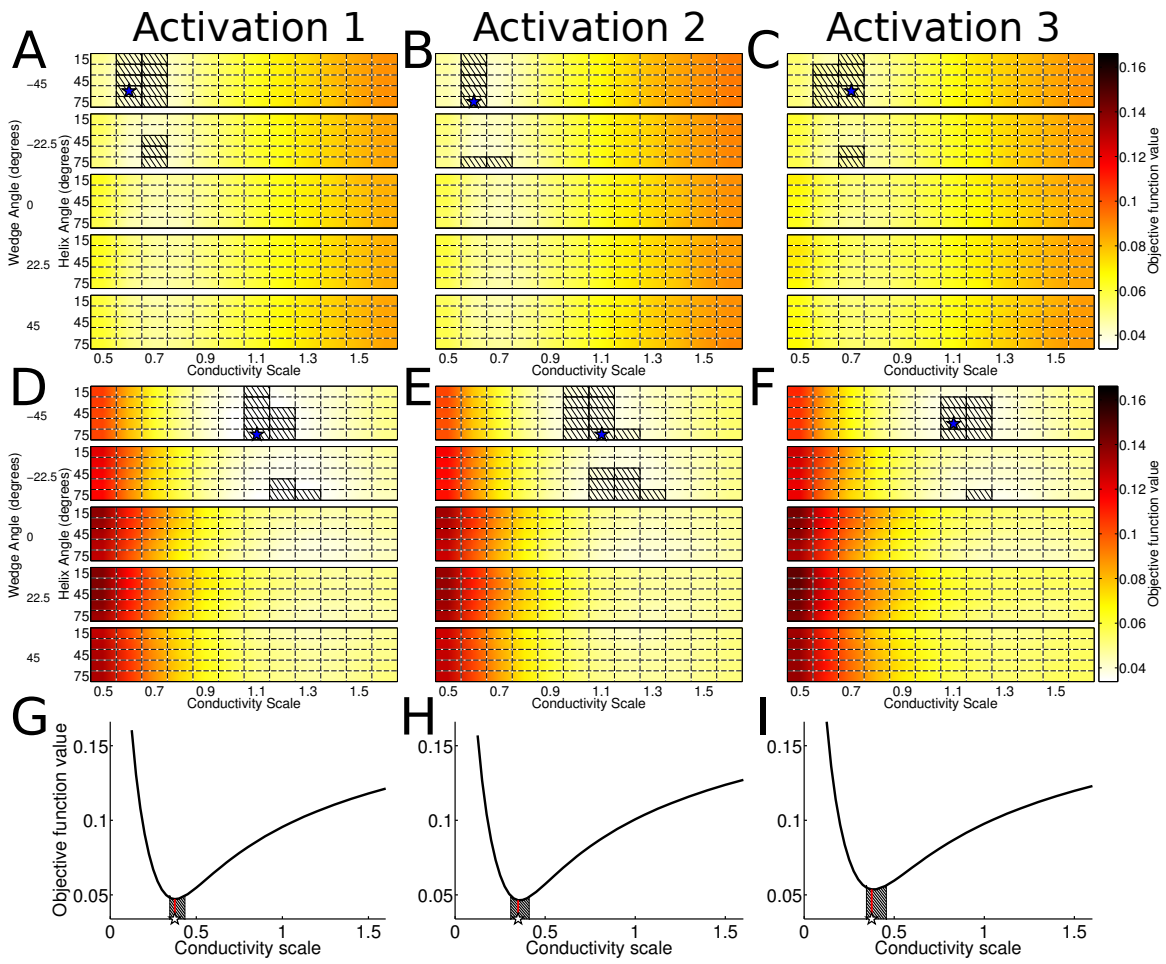

Figure 8.5: **Non-Failing Wedge 1: Assessment of effect of conduction parameter variability on difference between simulation and experiment.** Heat maps show the value of the normalised sum of square differences objective function calculated over the full range of conduction parameter values, for all three recorded activations. Results are shown for anisotropy ratios of A)–C) 1:$\frac{1}{2}$ and D)–F) 1:$\frac{1}{4}$. Each subplot is for a fixed value of the wedge angle. Within each subplot, the helix angle and the conductivity scale vary. G)–I) show the values of the normalised objective function in the isotropic case, where no fibre orientation is applied. For each plot the star denotes the minimal value of the objective function in that plot. The hatched region shows the parameter sets within 5% of the minimal objective function value for that plot.

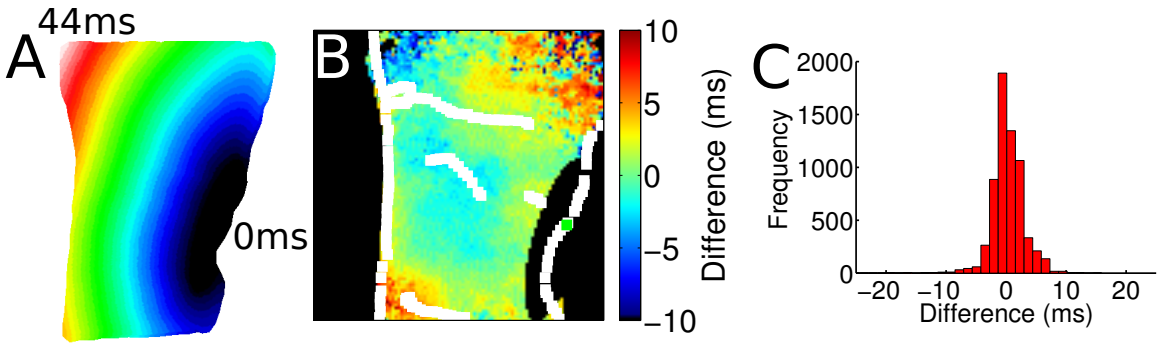

Figure 8.6: **Non-Failing Wedge 1: Difference between simulation and experiment in the optimal case.** A) shows the simulated activation map using optimal parameters for non-failing wedge 1, with a helix angle of 75°, a wedge angle of $-45°$, an anisotropy ratio of 1:$\frac{1}{4}$ and a conductivity scaling of 1.1. B) shows the simulated activation time − experimental activation time at each pixel in the optical mapping field of view. A positive value indicates that the simulation activates later than the experiment, and so is conducting more slowly, and *vice-versa*. Only differences of $\leq$ 10ms are shown. C) Shows a histogram of the difference between simulation and experiment recorded at each pixel.

had a helix angle of 75°, a wedge angle of $-45°$, and a conductivity scaling of 1.1 (Fig. 8.5 D). There are ten parameter sets within 5% of this optimal value, which are clustered at low wedge angle, suggesting a greater sensitivity of results to wedge angle and conductivity scale than to the helix angle.

The activation map giving best agreement between simulation and experiment is shown on the wedge mesh in Fig. 8.6 A. The absolute differences between the experimental activation and optimal simulated activation at each pixel are shown in Fig. 8.6 B. A histogram of the differences is plotted in Fig. 8.6 C. The histogram shows a relatively tight distribution centred on a mean difference of 0.33ms. The inter-quartile range of the error in the simulation is 3.00ms. The difference between simulated and experimental values (Fig. 8.6 B) demonstrates that there is a degree of spatial organisation to the regions where simulation and experiment are in disagreement, rather than simply being a product of noisy data.

There are some structural features visible in the optical mapping field of view (Fig. 8.4 B,C), which are highlighted for comparison with simulations in Fig. 8.4 D. In the middle of the tissue, and at the bottom of the tissue, we see that these coincide with some of the structural features observed in the tissue (Fig. 8.6 B). In the case of the structure in the middle of the tissue this is borne out by a curvature in the wave front at this point in the

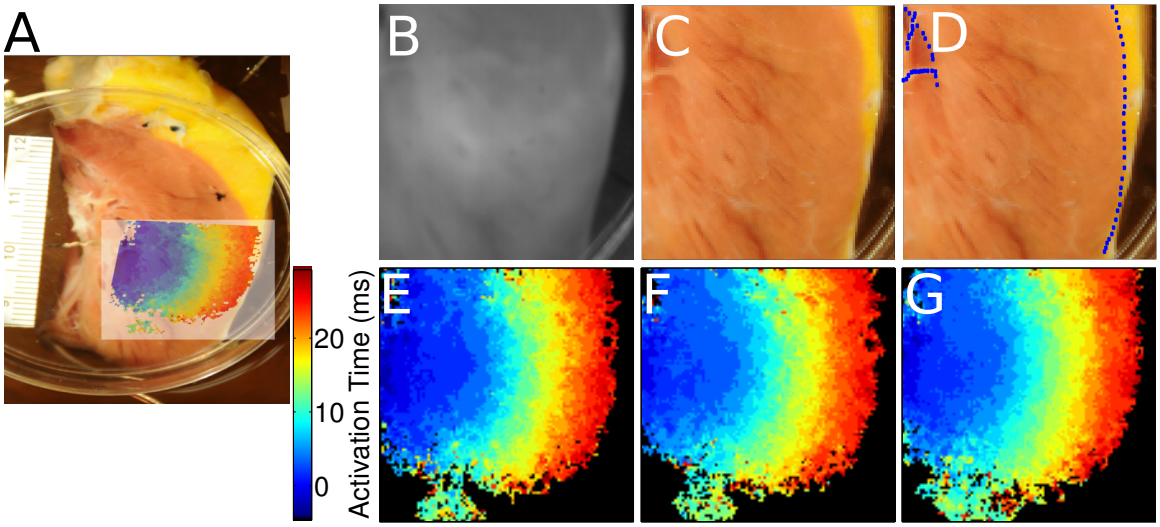

Figure 8.7: **Non-Failing Wedge 2: Experimental data.** A) An activation map registered onto the wedge photograph. B) the optical mapping field of view. C) The region of the wedge photograph registered onto the optical mapping field of view. D) Structural features apparent in the optical mapping field of view are highlighted for comparison with simulated data. E)–G) experimentally recorded activation times across non-failing wedge 2.

experimental data (Fig. 8.4 A).

8.3.2 Non-Failing Wedge 2

The optical mapping field of view is again roughly in the middle of the wedge preparation, closer to the apex end of the wedge (Fig. 8.7 A). As a large portion of the apex has been removed in this case, it is probable that the imaged region is again somewhere in the middle of the apex-base axis. Three activation maps were recorded for this preparation, shown in Fig. 8.7 E–G. The mean conduction velocity across the wedge normal to the wavefront is 63.0cm/s.

Fig. 8.8 describes the effect of conduction parameter variability on the agreement between simulated and experimental activation times for non-failing wedge 2. The degree of agreement is quantified by the value of the normalised sum of square differences objective function. A lower value indicates better agreement between simulation and experiment. The parameter set giving the best agreement for each activation and each anisotropy ratio is indicated by a star, with hatched regions indicating parameter sets with agreement simi-

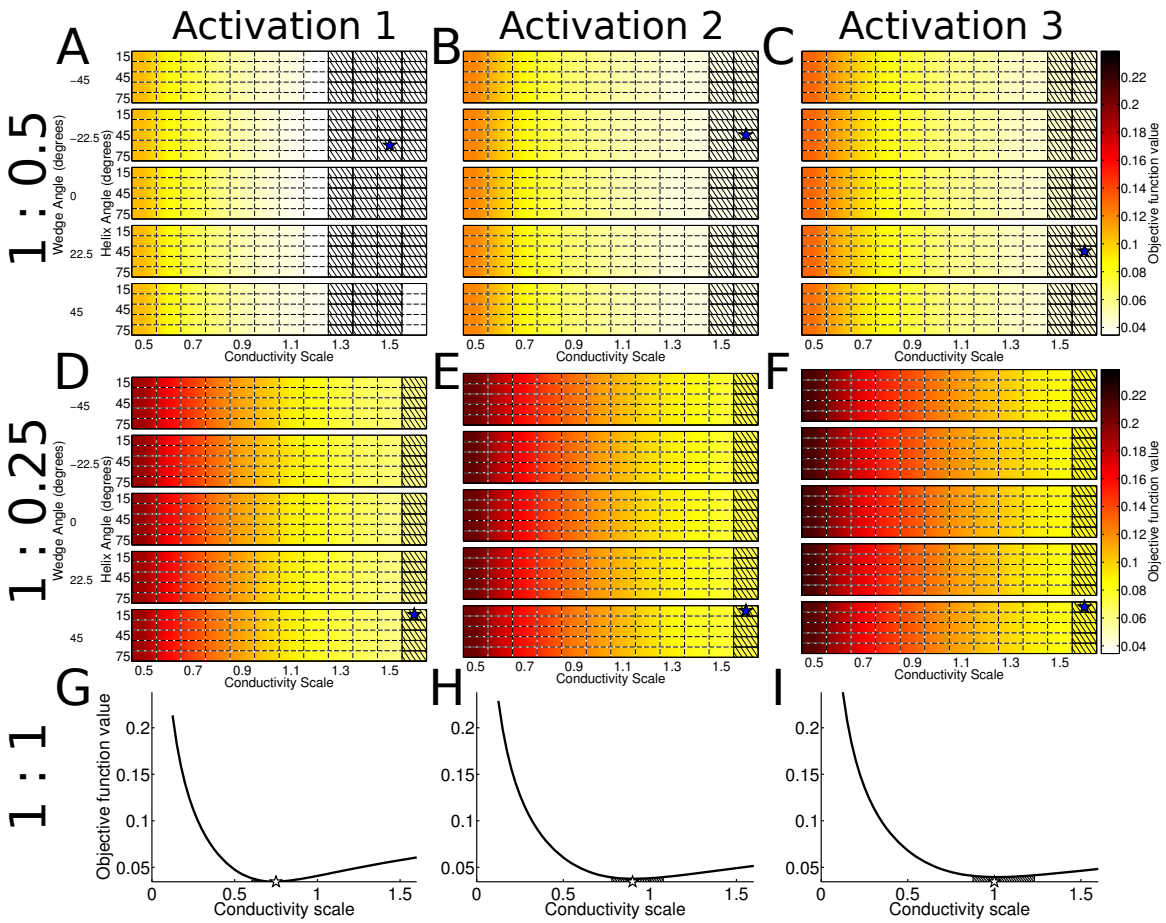

Figure 8.8: **Non-Failing Wedge 2: Assessment of effect of conduction parameter variability on difference between simulation and experiment.** Heat maps show the value of the normalised sum of square differences objective function calculated over the full range of conduction parameter values, for all three recorded activations. Results are shown for anisotropy ratios of A)–C) 1:$\frac{1}{2}$ and D)–F) 1:$\frac{1}{4}$. Each subplot is for a fixed value of the wedge angle. Within each subplot, the helix angle and the conductivity scale vary. G)–I) show the values of the normalised objective function in the isotropic case, where no fibre orientation is applied. For each plot the star denotes the minimal value of the objective function in that plot. The hatched region shows the parameter sets within 5% of the minimal objective function value for that plot.

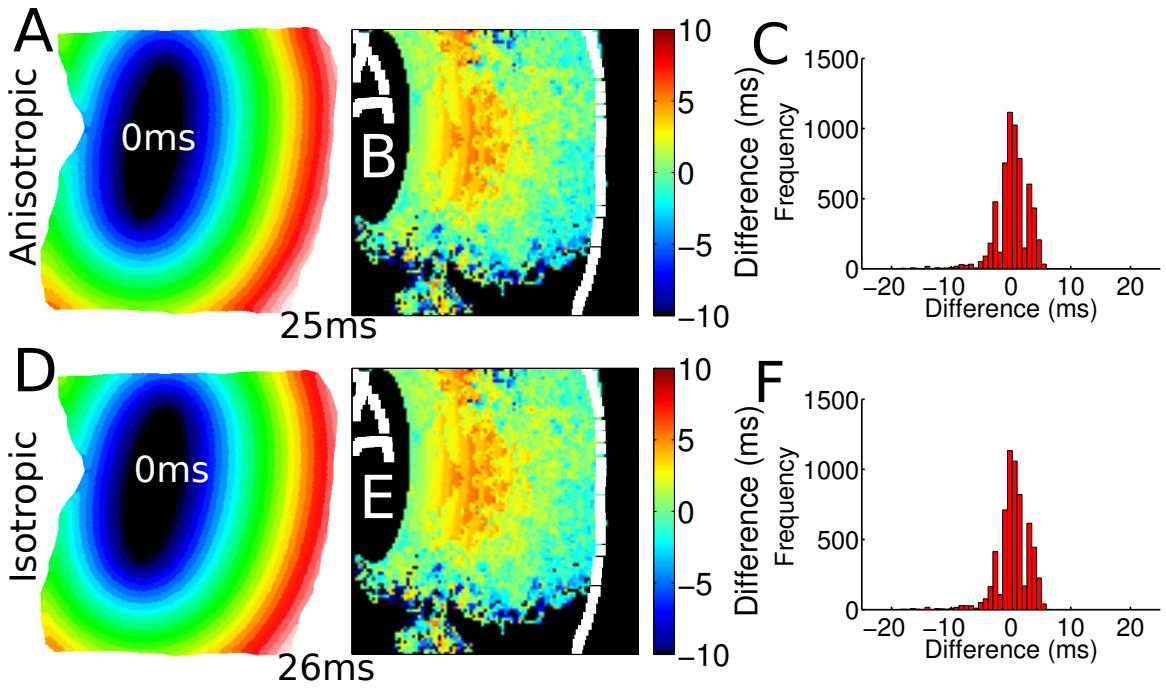

Figure 8.9: **Non-Failing Wedge 2: Difference between simulation and experiment in the optimal cases.** A)and D) show the simulated activation maps using optimal parameters for non-failing wedge 2 in the anisotropic and isotropic cases respectively. In the anisotropic case a helix angle of 60°, a wedge angle of $-45°$, an anisotropy ratio of 1:$\frac{1}{2}$ and a conductivity scaling of 1.1 are used. In the isotropic case a conductivity scaling of 0.75 is used. B) and E) show the simulated activation time − experimental activation time at each pixel in the optical mapping field of view for the anisotropic and isotropic cases respectively. A positive value indicates that the simulation activates later than the experiment, and so is conducting more slowly, and *vice-versa*. Only differences of $\leq$ 10ms are shown. C) and F) show histograms of the difference between simulation and experiment recorded at each pixel in the anisotropic and isotropic cases, respectively.

lar to that of the optimal case. The region of parameter space in which the optimal values lie is much flatter than for non-failing wedge 1, indicated by a far larger range of parameter values within 5% of the minimum. For non-failing wedge 2, two optimal fits are achieved with the same objective function value (Fig. 8.8 A,G). One of the fits was achieved with an anisotropy ratio of 1:$\frac{1}{2}$, a conductivity scaling of 1.5, a wedge angle of $-45°$ and a helix angle of 60°. The same objective function value is achieved using isotropic tissue with a conductivity scaling of 0.75. The equally good fits in the isotropic and anisotropic cases suggest that the results are relatively insensitive to the wedge and helix angle.

The activation maps giving best agreement between simulation and experiment is shown on the wedge mesh in Fig. 8.9 A (anisotropic) and D (isotropic). The absolute differences

between the experimental activation and optimal simulated activation at each pixel are shown in Fig. 8.9 B and E. Histograms of these differences are plotted in Fig. 8.6 C and F for the anisotropic and isotropic case, respectively. The histograms in Fig. 8.9 C and F are similar with a distribution centred on a mean difference of 0.20ms in the anisotropic case and 0.30ms in the isotropic case. The inter-quartile range of the distribution is 3ms in the anisotropic case and 2.96ms in the isotropic case. In both cases, the largest region of difference is positive and located transmurally, suggesting that the simulation moves too slowly through the endocardial and midmyocardial regions.

This wedge shows none of the structural features observed for non-failing wedge 1 in the optical mapping field of view (Fig. 8.7 B,C). The boundary of the fatty epicardial region and a small visible structural feature probably associated with trabecular muscle is highlighted in Fig. 8.7 D). Hence, we conclude that the disagreement between simulation and experiment is not due to visible structures in this case.

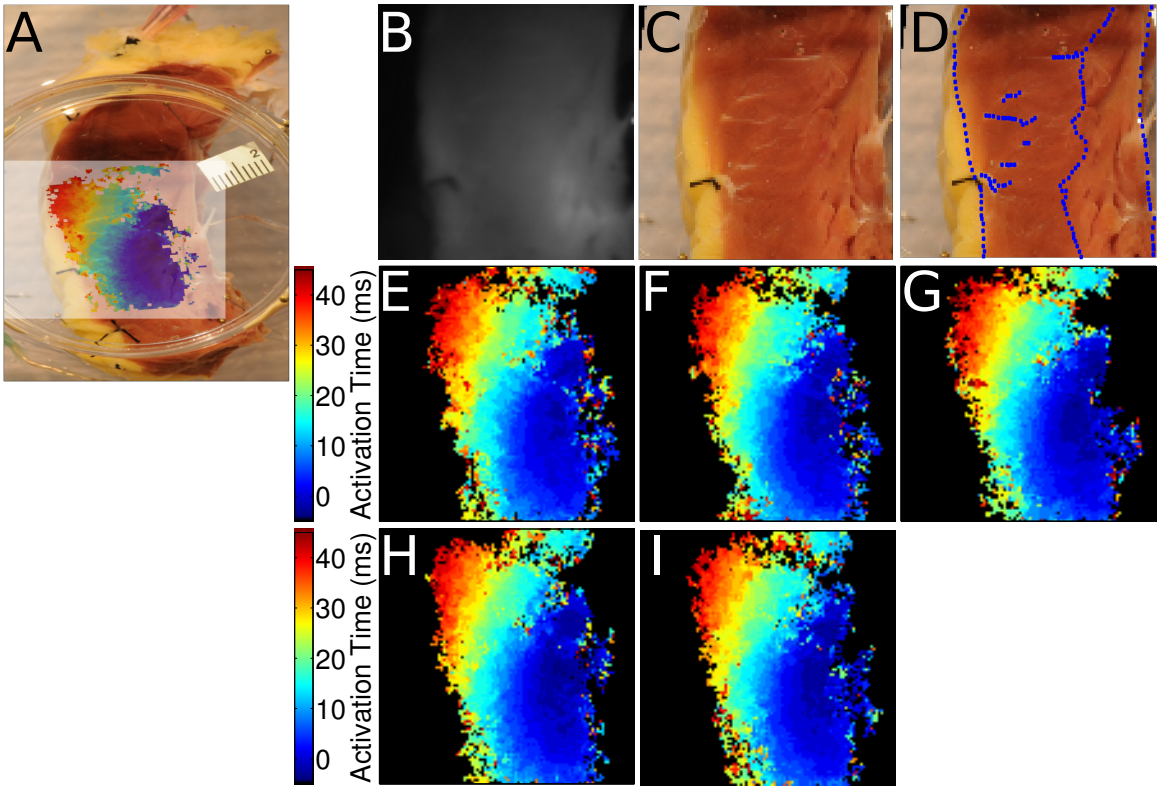

Figure 8.10: **Non-Failing Wedge 3: Experimental data.** A) An activation map registered onto the wedge photograph. B) the optical mapping field of view. C) The region of the wedge photograph registered onto the optical mapping field of view. D) Structural features apparent in the optical mapping field of view are highlighted for comparison with simulated data. E)–I)) Five experimentally recorded activation times across non-failing wedge 3.

8.3.3 Non-Failing Wedge 3

The optical mapping field of view is in the middle of the wedge preparation, closer to the apex end of the wedge (Fig. 8.10 A). Five activation maps were recorded for this preparation, shown in Fig. 8.10 E–I. The mean conduction velocity across the wedge normal to the wavefront is 38.5cm/s.

Fig. 8.11 describes the effect of conduction parameter variability on the agreement between simulated and experimental activation times for non-failing wedge 3. The degree of agreement is quantified by the value of the normalised sum of square differences objective function. A lower value indicates better agreement between simulation and experiment. The parameter set giving the best agreement for each activation and each anisotropy ra-

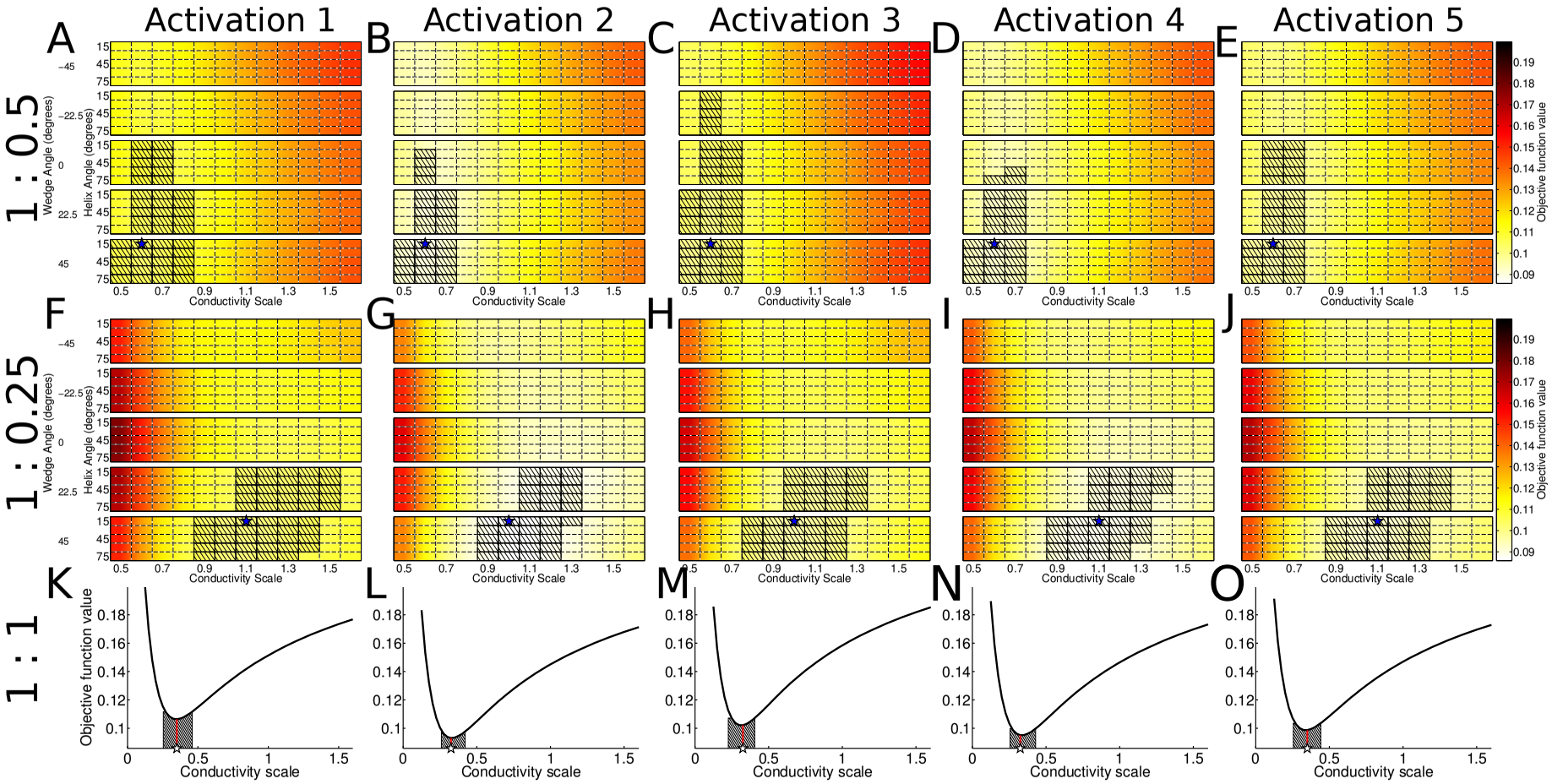

Figure 8.11: **Non-Failing Wedge 3: Assessment of effect of conduction parameter variability on difference between simulation and experiment.** Heat maps show the value of the normalised sum of square differences objective function calculated over the full range of conduction parameter values, for all three recorded activations. Results are shown for anisotropy ratios of A)–C) 1:$\frac{1}{2}$ and D)–F) 1:$\frac{1}{4}$. Each subplot is for a fixed value of the wedge angle. Within each subplot, the helix angle and the conductivity scale vary. G)–I) show the values of the normalised objective function in the isotropic case, where no fibre orientation is applied. For each plot the star denotes the minimal value of the objective function in that plot. The hatched region shows the parameter sets within 5% of the minimal objective function value for that plot.

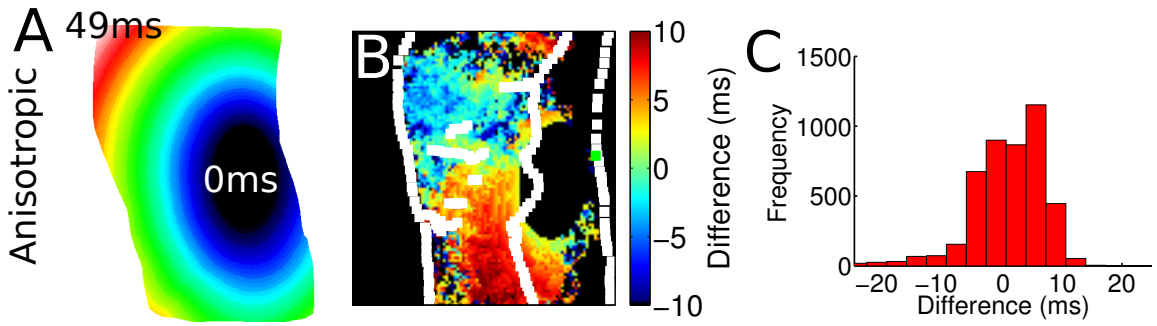

Figure 8.12: **Non-Failing Wedge 3: Difference between simulation and experiment in the optimal cases.** A) shows the simulated activation maps using optimal parameters for non-failing wedge 3. A helix angle of 15°, a wedge angle of 45°, an anisotropy ratio of 1:$\frac{1}{4}$ and a conductivity scaling of 1 are used. B) shows the simulated activation time − experimental activation time at each pixel in the optical mapping field of view for the anisotropic and isotropic cases respectively. Only differences of $\leq$ 10ms are shown. C) shows a histogram of the difference between simulation and experiment in the anisotropic and isotropic cases respectively.

tio is indicated by a star. Hatched regions indicate parameter sets with agreement similar to that of the optimal case. The optimal value for each anisotropy ratio is well conserved between each activation. The best fit is achieved with an anisotropy ratio of 1:$\frac{1}{4}$, a wedge angle of 45°, a helix angle of 15°, and a conductivity scale of 1.0.

The simulated activation time map in the optimal case is shown in Fig. 8.12 A. The absolute differences between the experimental activation and optimal simulated activation at each pixel are shown in Fig. 8.12 B. As indicated by the higher value of the normalised objective function and the spread of the histogram in Fig. 8.12 C, the fit to the experimental data is poor for non-failing wedge 3. Some structural features are apparent in the myocardium, as well as a relatively large region of trabecular muscle. (Fig. 8.10 B,C). These features are marked for comparison in Fig. 8.10 D, as shown in Fig. 8.12 B. One potential explanation for the poor agreement between simulation and experiment can be seen in the tissue region towards the apex region of the wedge (Fig. 8.10 C,D). This region consists of a relatively large amount of trabecular muscle compared to the region closer to the base. This bottom region activates more quickly than the region closer to the base, possibly suggesting a role for faster conduction through trabecular muscle, that is not captured by our model. Other differences in conduction between simulation and experiment do not appear

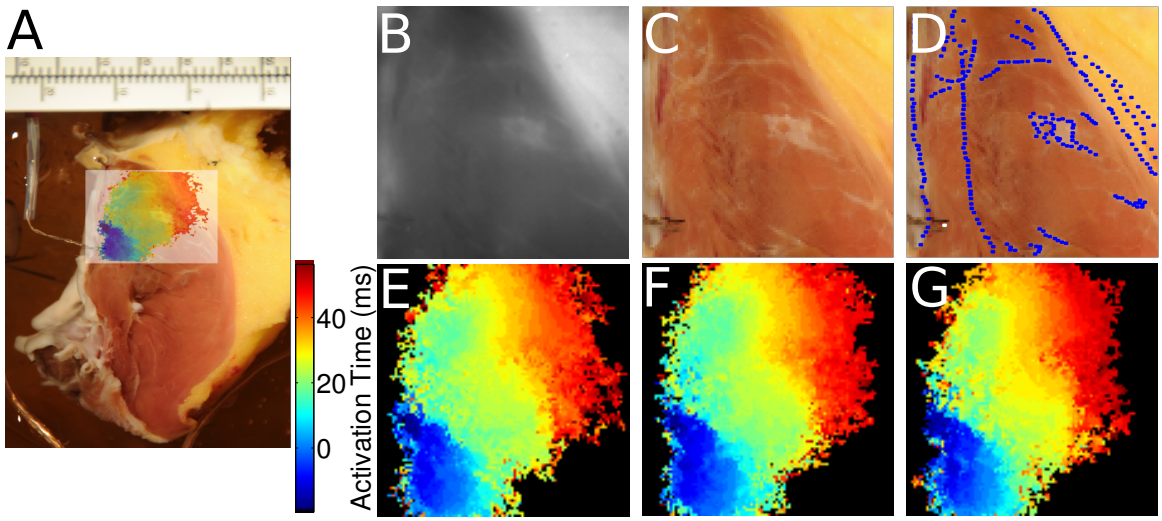

Figure 8.13: **Failing Wedge 1: Experimental data.** A) An activation map registered onto the wedge photograph. B) the optical mapping field of view. C) The region of the wedge photograph registered onto the optical mapping field of view. D) Structural features apparent in the optical mapping field of view are highlighted for comparison with simulated data. E)–G)) Three experimentally recorded activation times across failing wedge 1.

to be associated with other structures highlighted in the wedge (Fig. 8.10 D).

8.3.4 Failing Wedge 1

The optical mapping field of view in failing wedge 1 is very close to the base end of the wedge (Fig. 8.13 A). Three activations maps are recorded for this wedge, shown in Fig. 8.13 E–G. The mean conduction velocity across the wedge normal to the wavefront is 35.8cm/s.

Fig. 8.14 describes the effect of conduction parameter variability on the agreement between simulated and experimental activation times for failing wedge 1. The degree of agreement is quantified by the value of the normalised sum of square differences objective function. A lower value indicates better agreement between simulation and experiment. The parameter set giving the best agreement for each activation and each anisotropy ratio is indicated by a star, with hatched regions indicating parameter sets with agreement similar to that of the optimal case. For failing wedge 1, the best fit is achieved with an anisotropy ratio of 1:$\frac{1}{4}$, a wedge angle of -45°, a helix angle of 75°, and a conductivity scale of 1.4. The fibre orientation is conserved across activations, but one activation obtains a different

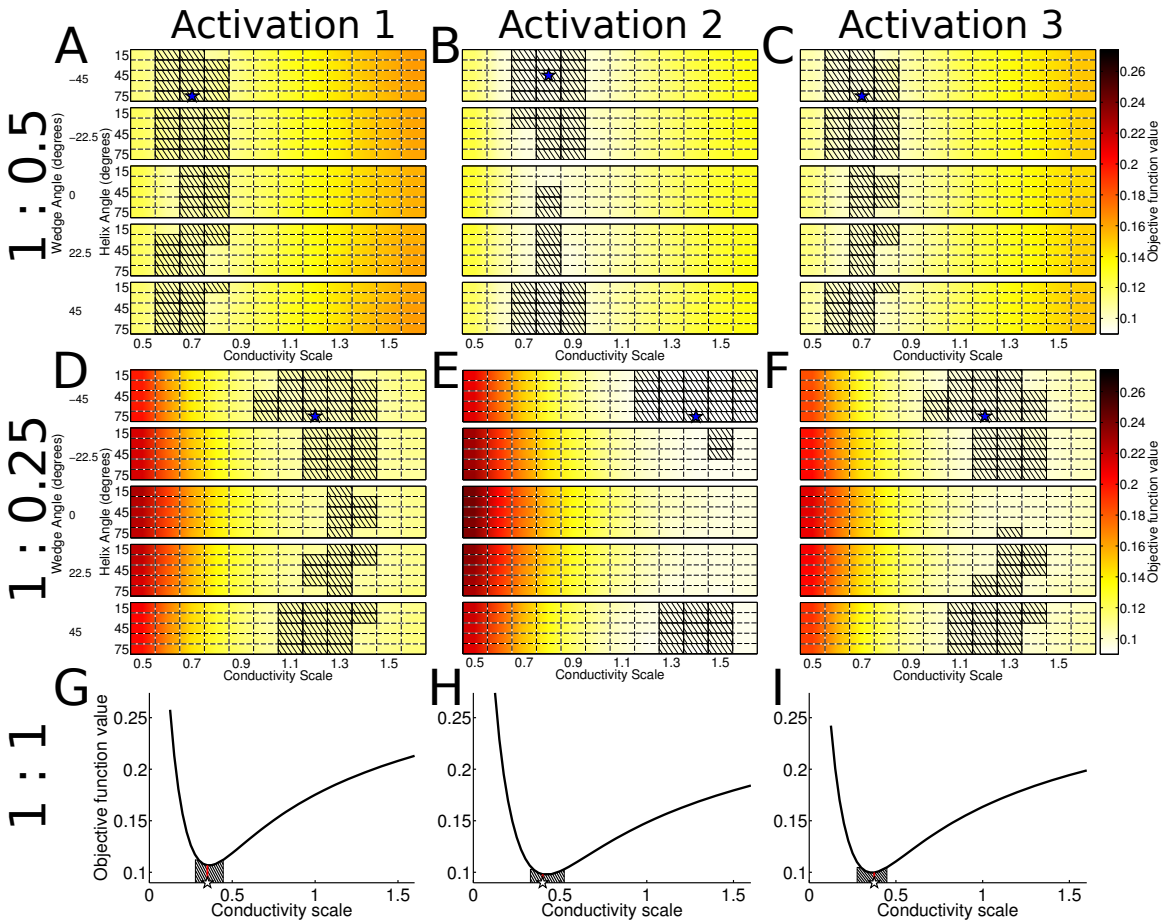

Figure 8.14: **Failing Wedge 1: Assessment of effect of conduction parameter variability on difference between simulation and experiment.** Heat maps show the value of the normalised sum of square differences objective function calculated over the full range of conduction parameter values, for all three recorded activations. Results are shown for anisotropy ratios of A)–C) 1:$\frac{1}{2}$ and D)–F) 1:$\frac{1}{4}$. Each subplot is for a fixed value of the wedge angle. Within each subplot, the helix angle and the conductivity scale vary. G)–I) show the values of the normalised objective function in the isotropic case, where no fibre orientation is applied. For each plot the star denotes the minimal value of the objective function in that plot. The hatched region shows the parameter sets within 5% of the minimal objective function value for that plot.

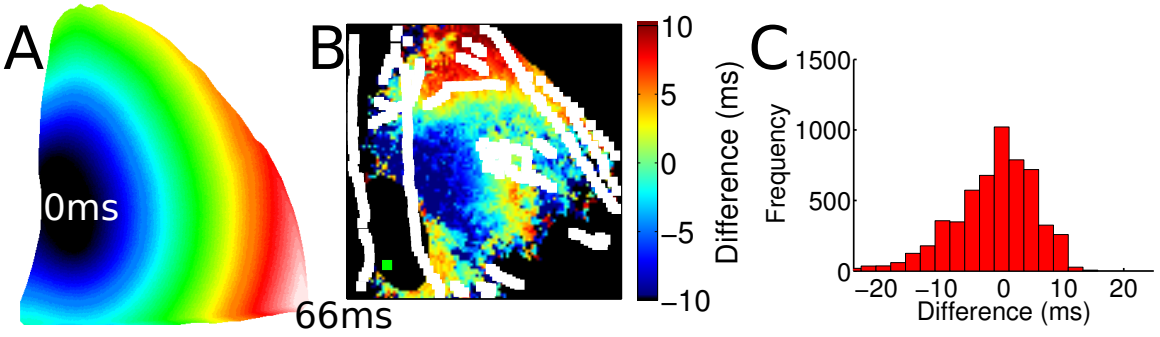

Figure 8.15: **Failing Wedge 1: Difference between simulation and experiment in the optimal cases.** A) shows the simulated activation maps using optimal parameters for failing wedge 1. A helix angle of 75°, a wedge angle of $-45°$, an anisotropy ratio of 1:$\frac{1}{4}$ and a conductivity scaling of 1.4 are used. B) shows the simulated activation time $-$ experimental activation time at each pixel in the optical mapping field of view for the anisotropic and isotropic cases respectively. Only differences of $\leq$ 10ms are shown. C) shows a histogram of the difference between simulation and experiment recorded at each pixel.

conductivity scaling of 1.2.

The activation maps giving best agreement between simulation and experiment is shown on the wedge mesh in Fig. 8.15 A. The absolute differences between the experimental activation and optimal simulated activation at each pixel are shown in Fig. 8.15 B. As indicated by the relatively high value of the normalised optimisation function and the spread of the histogram in Fig. 8.15 C, the fit to the experimental data is poor. A large difference in activation time (≈ -10ms) is observed directly next to the stimulated region, indicating that the model conducts far too quickly here, and a region close to the epicardial region with a difference close to $+10$ms indicates that the simulation is arriving in this region too late.

This wedge features a large number of structural features apparent in the myocardium, as well as a region contiguous with the trabecular muscles inside the heart (apparent from Fig. 8.13 A, showing a recording in context). Both have been marked up on the wedge photograph in Fig. 8.13 D. When compared to the structures apparent in the wedge no clear pattern emerges. One potential explanation would be that there is slowed conduction from the trabecular region (where the wedge is stimulated) into the myocardium, explaining the sharp difference in activation times apparent in the experimental recordings.

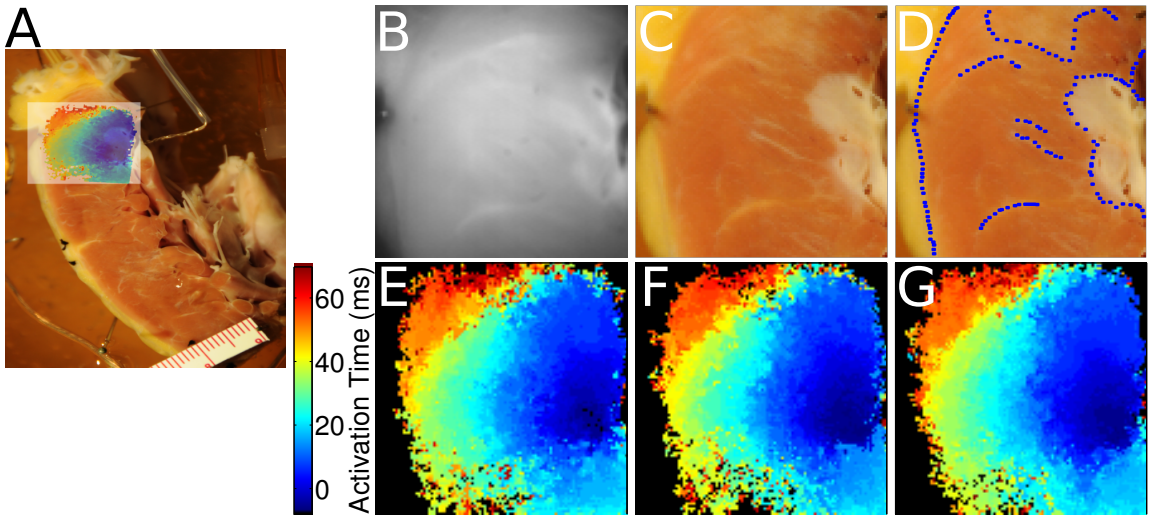

Figure 8.16: **Failing Wedge 2: Experimental data.** A) An activation map registered onto the wedge photograph. B) The optical mapping field of view. C) The region of the wedge photograph registered onto the optical mapping field of view. D) Structural features apparent in the optical mapping field of view are highlighted for comparison with simulated data. E)–G)) Three experimentally recorded activation times across failing wedge 2.

8.3.5 Failing Wedge 2

The field of view for failing wedge 2 is recorded close to the base end of the wedge (Fig. 8.16 A). Three activations were recorded for this wedge, shown in Fig. 8.16 E–G. The mean conduction velocity across the wedge normal to the wavefront is 29.0cm/s.

Fig. 8.17 describes the effect of conduction parameter variability on the agreement between simulated and experimental activation times for failing wedge 2. The degree of agreement is quantified by the value of the normalised sum of square differences objective function. A lower value indicates better agreement between simulation and experiment. The parameter set giving the best agreement for each activation and each anisotropy ratio is indicated by a star, with hatched regions indicating parameter sets with agreement similar to that of the optimal case. For failing wedge 2, the best fit is achieved with an isotropic conductivity tensor and conductivity scaling of 0.125 and a normalised objective function value of 0.1056, as shown in Fig. 8.17.

The optimal simulated activation map for failing wedge 2 is shown in Fig. 8.18 A. The difference between simulation and experiment are shown for each pixel in Fig. 8.18 B, and

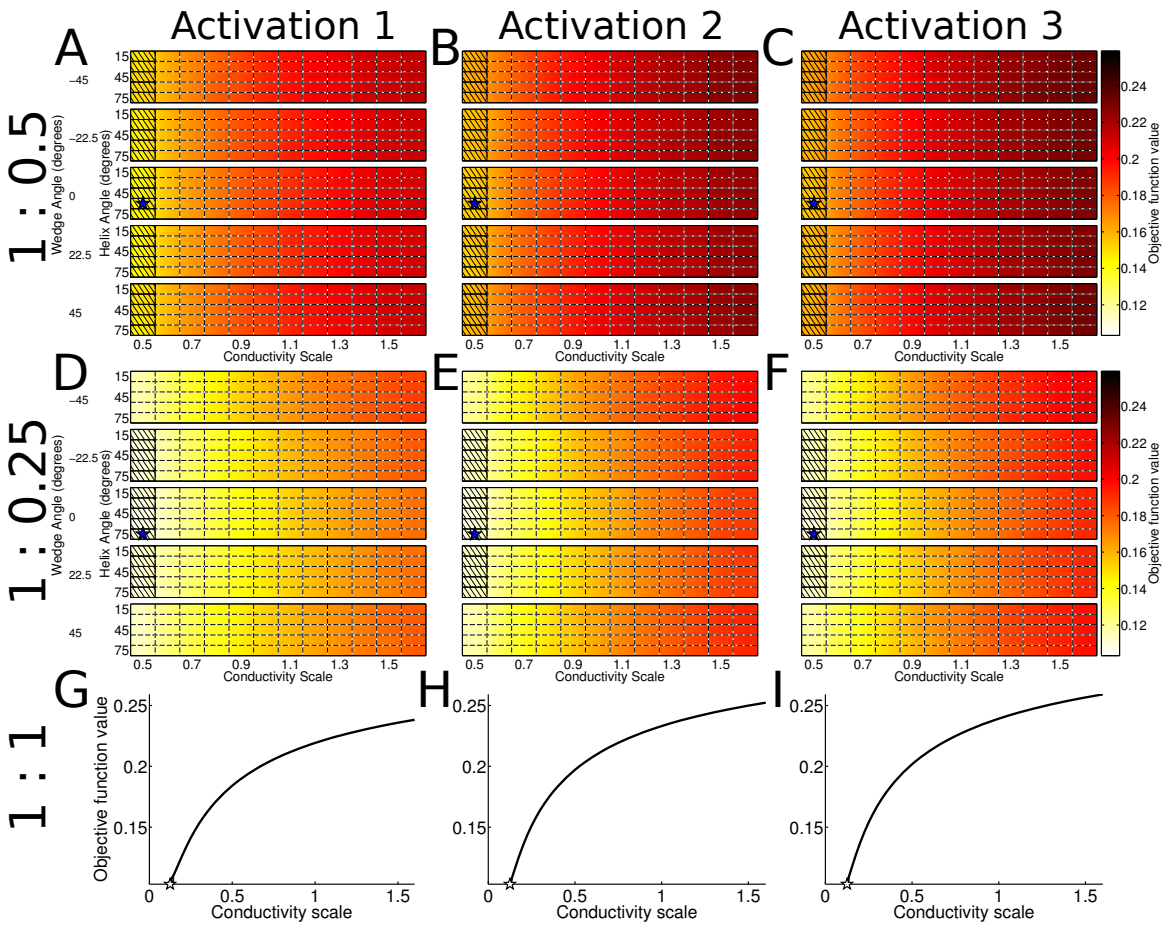

Figure 8.17: **Failing Wedge 2: Normalised objective function values.** Heat maps are shown of normalised objective function values for all three recorded activations. Results are shown for anisotropy ratios of A)–C) 1:$\frac{1}{2}$and D)–F) 1:$\frac{1}{4}$. Each subplot is for a fixed value of the wedge angle. Within each subplot, the helix angle and the conductivity scale vary. G)–I) show the values of the normalised objective function in the isotropic case, where no fibre orientation is applied. For each plot the star denotes the minimal value of the objective function in that plot. The hatched region shows the region within 5% of the minimal objective function value for that plot.

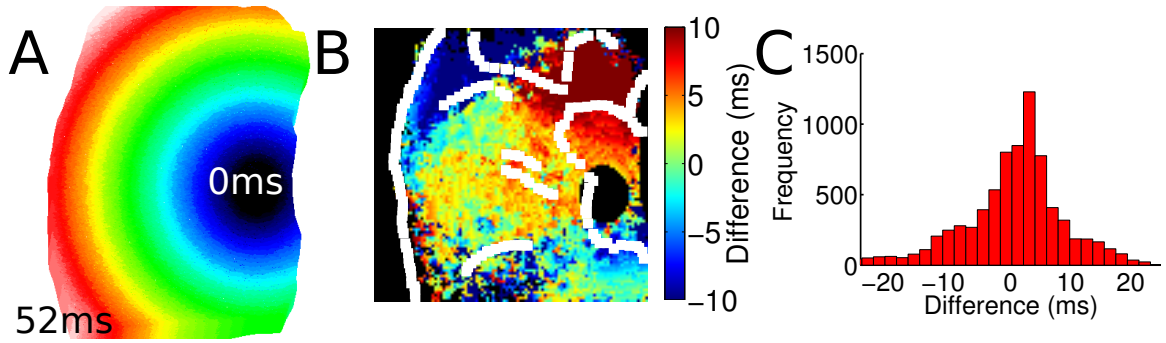

Figure 8.18: **Failing Wedge 2: Difference between simulation and experiment in the optimal cases.** A) shows the simulated activation maps using optimal parameters for failing wedge 1. An isotropic conductivity tensor with a conductivity scaling of 0.125 is used. B) shows the simulated activation time − experimental activation time at each pixel in the optical mapping field of view. Only differences of $\leq$ 10ms are shown. C) shows a histogram of the difference between simulation and experiment.

achieved using the lowest conductivity scaling and a 1:$\frac{1}{4}$ anisotropy ratio.

For failing wedge 2, propagation emerges from a trabeculation, which is clearly visible in Fig. 8.16 B and C. This may explain the poor fit to between simulation and experiment (Fig. 8.18 B), with abnormal conduction occurring along the endocardium due to uneven conduction around the edge of the trabeculation. A number of structural features are visible in the myocardium including a larger grey tinged region which may be fibrotic (Fig. 8.16 D). These may also contribute to the poor fit.

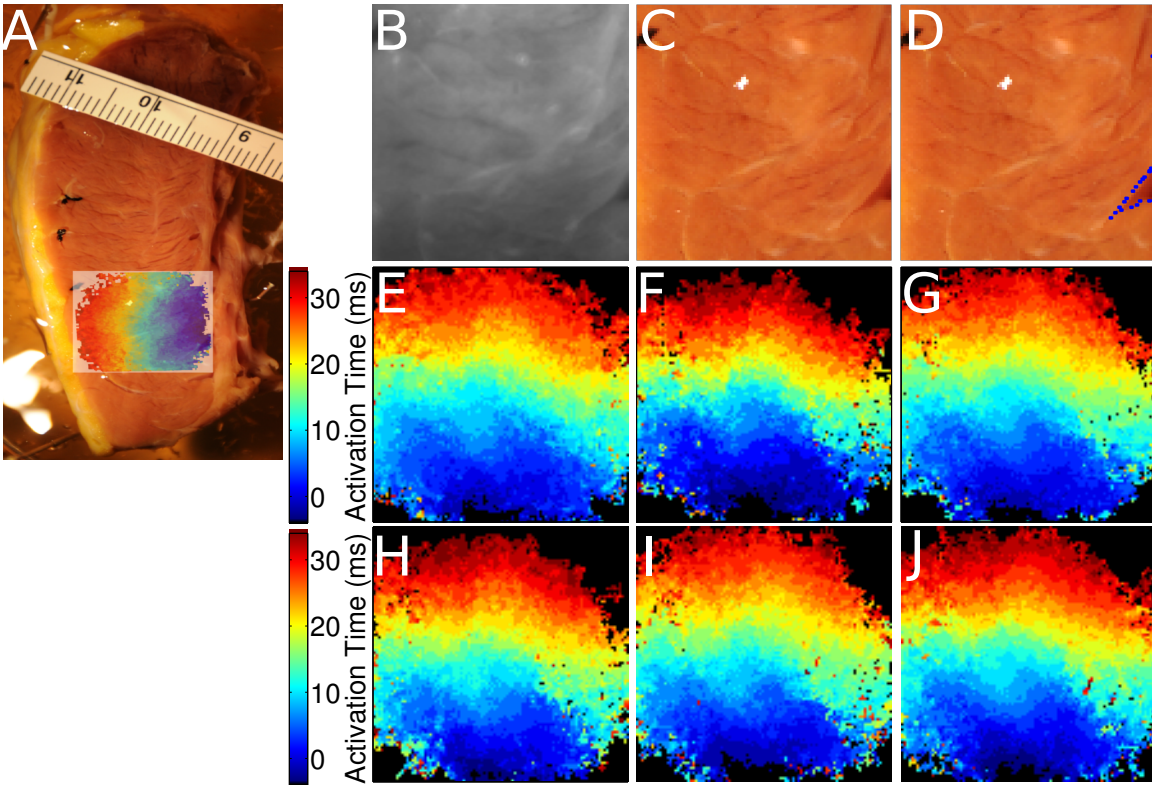

Figure 8.19: **Failing Wedge 3: Experimental data.** A) An activation map registered onto the wedge photograph. B) The optical mapping field of view. C) The region of the wedge photograph registered onto the optical mapping field of view. D) Structural features apparent in the optical mapping field of view are highlighted for comparison with simulated data. E)–J) Six experimentally recorded activation times across failing wedge 3.

8.3.6 Failing Wedge 3

The field of view in failing wedge three is taken towards the apex end of the wedge as shown in Fig. 8.19 A. Six activations were recorded for this wedge, as shown in Fig. 8.19 E–J. The mean conduction velocity across the wedge normal to the wavefront is 40.5cm/s.

Fig. 8.20 describes the effect of conduction parameter variability on the agreement between simulated and experimental activation times for failing wedge 3. The degree of agreement is quantified by the value of the normalised sum of square differences objective function. A lower value indicates better agreement between simulation and experiment. The parameter set giving the best agreement for each activation and each anisotropy ratio is indicated by a star, with hatched regions indicating parameter sets with agreement similar

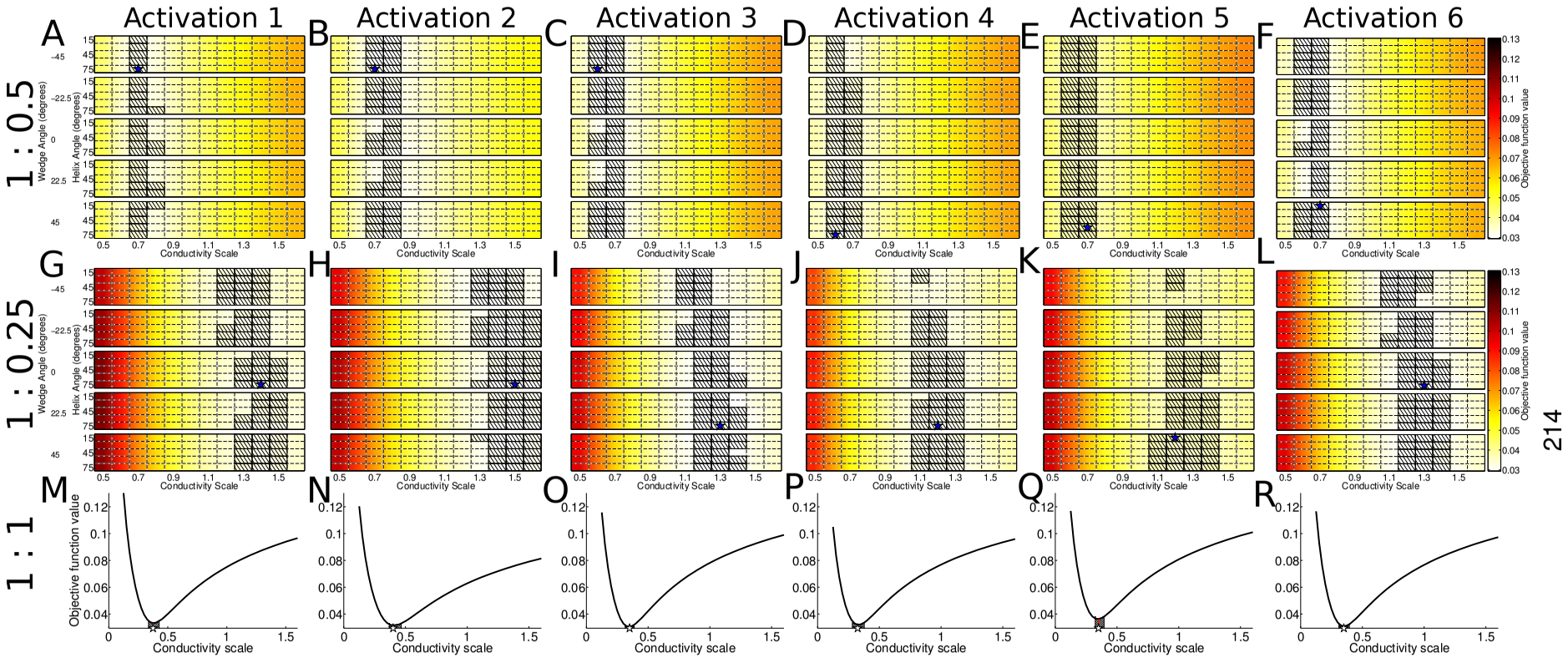

Figure 8.20: **Failing Wedge 3: Normalised objective function values.** Heat maps are shown of normalised objective function values for all six recorded activations. Results are shown for anisotropy ratios of A)–F) 1:$\frac{1}{2}$ and G)–L) 1:$\frac{1}{4}$. Each subplot is for a fixed value of the wedge angle. Within each subplot, the helix angle and the conductivity scale vary. M)–R) show the values of the normalised objective function in the isotropic case, where no fibre orientation is applied. For each plot the star denotes the minimal value of the objective function in that plot. The hatched region shows the region within 5% of the minimal objective function value for that plot.

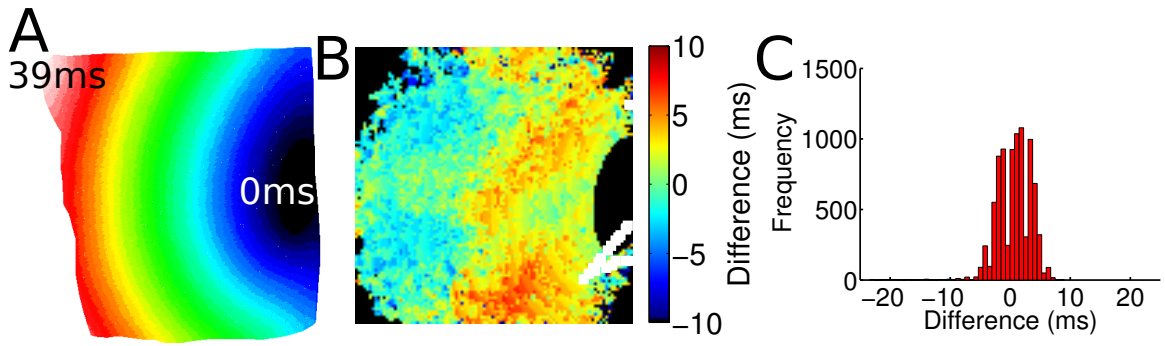

Figure 8.21: **Failing Wedge 3: Difference between simulation and experiment in the optimal cases.** A) shows the simulated activation maps using optimal parameters for failing wedge 1. A helix angle of 75°, a wedge angle of 22.5°, an anisotropy ratio of 1:$\frac{1}{4}$ and a conductivity scaling of 1.3 are used. B) shows the simulated activation time − experimental activation time at each pixel in the optical mapping field of view. Only differences of $\leq$ 10ms are shown. C) shows a histogram of the difference between simulation and experiment at each pixel.

to that of the optimal case. The best fit to the recorded activation map for failing wedge 3 was achieved using an ansotropy ratio of 1:$\frac{1}{4}$, a conductivity scaling of 1.3, a helix angle of 75° and a wedge angle of 22.5° (Fig. 8.20 G). There is a large degree of variability between the results for different activations in the helix angle, suggesting that the fibre orientation does not have a large effect on the fit to the data. This is backed up by a large number of parameter sets within 5% of the minimum objective function value, suggesting a relatively flat parameter space. Conductivity scaling was generally well conserved between activations.

Fig. 8.21 A shows the simulated activation time map on the mesh for failing wedge 3. The difference between simulation and experiment at each pixel is shown in Fig. 8.21 B. A histogram of these differences over all pixels is shown in Fig. 8.21 C. As can be seen by the relatively low value of the normalised objective function and the low inter-quartile range of the distribution of errors in the data, there was a good match between simulated and experimental activation maps for failing wedge 3.

Very few of the structural features seen in some of the other wedges are visible in the field of view for failing wedge three (Fig. 8.19 C,D). Differences were not associated with the structural features visible in the wedge, as can be seen in Fig. 8.21 B, suggesting that

Table 8.1: **Simulation Comparison Summary**

Wedge	Exp. CV	Location	OFV	IQR	Longitudinal Scale	Transverse Scale	Helix Angle	Wedge Angle
Non-Failing 1	43.2cm/s	Middle	0.0339	3.00ms	1.1	0.275	75°	−45°
Non-Failing 2	63.0cm/s	Middle	0.0345 0.0345	3.00ms 2.96ms	1.5 0.75	0.75 0.75	60° –	−45° –
Non-Failing 3	38.5cm/s	Middle-Apex	0.0858	7.43ms	1.0	0.25	15°	45°
Failing 1	35.8cm/s	Base	0.0899	8.49ms	1.2	0.3	75°	−45°
Failing 2	29.0cm/s	Base	0.1056	8.46ms	0.125	0.125	–	–
Failing 3	40.5cm/s	Apex	0.0294	3.97ms	1.3	0.325	75°	22.5°

OFV: Optimal normalised objective function value.
IQR: Inter-quartile range of results histogram.

discrepancies between simulation and experiment are not associated with visible structural features.

8.3.7 Summary

Summary statistics for the optimal fit to each of the six left-ventricular wedges under investigation are shown in Table 8.3.7. The quality of fit to the experimental data is shown by both the minimum value of the normalised objective function. We also show the inter-quartile range of the distribution of differences between the simulation and the experiment in the optimal case to quantify the difference between simulation and experiment in this case. Both measures agree on the wedges that have the best fits — non-failing wedges 1 and 2, and failing wedge 3. Similarly, worse fits are obtained for either measure by non-failing wedge 3, and failing wedges 1 and 2. This agreement validates the normalisation of the objective function for inter-wedge comparison. The resulting conductivity tensors are described here by their transverse and longitudinal scalings to facilitate comparison of the magnitude of the components in each case.

8.4 Discussion

8.4.1 Main Findings

In this chapter we have investigated the effectiveness of a commonly-used model of fibre orientation in capturing experimentally observed activation times across the wall of the heart. We used activation times recorded using optical mapping from three failing and three non-failing human hearts.

We hypothesised that the uniform conductance fibre rotation model would perform well for the non-failing hearts, but would perform less well for the failing hearts. Having allowed the parameters of the model determining the conductivity tensor to change to incorporate inter-sample variability, we obtained a good fit for two non-failing hearts and one failing heart, as quantified by normalised objective function values of 0.0339, 0.0345 and 0.0294 and inter-quartile ranges of 3.0ms, 2.96ms and 3.97ms in the optimal cases, respectively. More data would be required to statistically test this hypothesis. It is however interesting to note that there was a non-failing heart for which the model did not capture the activation sequence correctly, contradicting our hypothesis and the expectation of uniform conduction in the non-failing case.

We also note the advantage of using image registration to interpret optical mapping results, even in the absence of simulation, as this allows the detection of features associated with abnormal wave-front curvature, such as the midmyocardial feature in non-failing wedge 1.

In the cases where the activation map is well approximated by the simulated activation time, we additionally gain a parameter set which could be used for wedge-specific simulation. In general, the fibre orientation had a smaller effect on the optimal parameter set chosen than the conductivity scaling.

8.4.2 Explanation of Findings

Where good fits to the experimental data were obtained, there were still regions of disagreement between the simulation and the experiment. This may suggest changes in conductivity across the wall of the heart, or it may result from the fact that the model under investigation does not include a sheet orientation which could accelerate conduction across the wall of the heart.

Two factors seem to separate the wedges for which the activation maps did and did not agree with experiment. The first is the presence of structural features, which could be fatty deposits, blood vessels, or fibrosis within the myocardium. Very few of these were apparent in non-failing wedge 2 or failing wedge 3, and those that were in non-failing wedge 1 were associated with regions which proved more difficult to fit. Non-failing wedge 3 and failing wedges 1 and 2 had a large number of these structural features visible within the myocardium. There was limited association between these points and other regions of poor fit in these cases, however. The other factor separating the two groups was the large amount of tissue that appeared to be associated with the trabeculae lining the interior walls of the heart that was visible in these recordings. We suggest that differences in connectivity and conduction between the trabeculae and the myocardium may account for the failure of the model to reproduce the recorded activation time maps.

An important role for the trabeculae in explaining model failure is consistent with the model assumptions we were challenging. The commonly reported rotation in fibre angle is generally restricted to the myocardium, and does not extend to the trabeculae, or presumably also to related structures which are conjoined with the myocardium. Many simulation meshes do not include these structures, and when they are included, such as by Bishop et al. (2010), they are generally treated as an extension of the myocardium. Our analysis suggests that this may be an oversimplification that leads to poor agreement between simulation and experiment.

We also note that the point of stimulation for many of the wedges was on the trabeculae, rather than inside the myocardium, which leads to the trabeculae being the earliest excited

regions of tissue. Thus conduction through them will play a large role of the results of this study. This may change given other pacing protocols such as apical stimulation.

8.4.3 Characterising Variability in Structure

We have presented parameterisations of a model of fibre orientation to determine whether these assumptions can agree with measured optical mapping activation times. Using diffusion tensor magnetic resonance imaging, it is possible to resolve cell orientations within cardiac tissue, obtaining both fibre and sheet orientations (Benson et al., 2011; Trayanova, 2011; Zhang et al., 2012). In order to gain confidence in the predictive ability of the proposed parameter fitting regime for further studies, one option is to compare simulation results to established techniques for capturing fibre orientation, as proposed by Weiss et al. (2007), who compared simulation results from a rule-based method for wedge fibre orientation to one derived from dt-MRI. Several other studies have also proposed the fitting of parameters in a rule-based method using dt-MRI. Our method would enhance this by also offering direct comparison to experimental activation times, as well as between the two simulated sets of activation times.

Capturing the structural features bound to the endocardium is not in general practice. However, high resolution meshes for rabbit (Vadakkumpadan et al., 2009; Bishop et al., 2010) offer a method to evaluate the potential effect of these structures. (Bishop et al., 2010) report early epicardial breakthroughs when comparing the results of the high resolution mesh against a downsampled version not featuring many of the endocardial features. Their rule-based fibre orientation did treat endocardial structures differently but did not allow them to extend into the heart wall as we have sometimes observed above.

In the specific case of the wedge preparation used in this study two options exist: dt-MRI and histology. Both have advantages and disadvantages. Using dt-MRI retains the tissue for further analysis, but can suffer from edge effects, which would not capture the endocardial behaviour we describe. Histology slicing has a higher resolution and is more likely to preserve fibre orientation near the boundaries of the tissue. This would be necessary

at points where endocardially bound structures join the myocardium. However, histology samples can become dessicated and deformed relative to their original shape, and are two dimensional rather than three dimensional. The resulting fibre behaviour could be interpolated onto the mesh and compared to the fibre structure generated by our method. Either of these is in principle possible for the wedges used in this study, which at the time of writing are preserved in a freezer in Washington University in St. Louis.

Another complimentary strategy, possible for future wedge experiments, would be to stimulate at multiple pacing sites within the optical mapping field of view. This would give a set of data unused in the fitting process with which to challenge our model. Simulations could be performed on the same mesh using the same framework as above, but only using the optimal parameter set, or perhaps those within a set objective function value.

8.4.4 Limitations

The filtering method used with the experimental data can certainly affect the upstroke times recorded. We use the standardised method for filtering optical mapping recordings provided by Laughner et al. (2012), and use a sliding window approach to determine upstroke time.

As is inevitable with (most) optical mapping studies, information is only recorded from near the cut surface being imaged. There is the potential for subsurface waves to affect the recorded activation times — this possibility is not accounted for in our fitting method. Similarly, optical scattering will affect experimentally recorded upstroke times. This could be incorporated into future work given a suitably parallelised implementation of the optical scattering simulations of Bishop et al. (2006), for example. This was not included in this study primarily due to the relatively low temporal resolution of the experimental data. It is also worth noting that Walton et al. (2012) have shown that the time of maximum upstroke is consistent between simulations with and without optical scattering, even if the width of the upstroke is changed. Our samples also suffer from a relatively low temporal resolution of the upstroke (2ms sample rate) due to dual mapping of voltage and calcium, which

will introduce a degree of error into the calculation of the upstroke time, which we have quantified.

8.4.5 Conclusions

We conclude that a commonly used model of fibre orientation is capable of reproducing sample-specific activation times from human left-ventricular wedges. We note that, across the three wedges where a good fit was obtained, there was a considerable degree of variability in the fitted parameters, particularly the transverse component of the conductivity.

The model does not always provide a good match to experimental data, even when allowed to adapt for inter-sample variability. The primary cause of this disagreement appears to be structural features visible within the wedge, notably trabeculae. These are not included in many geometries used in cardiac simulation, and determining how far they extend into the myocardium is challenging. Our findings suggest that they impact conduction near the endocardial surface. Hence, trabeculae should where possible be included in simulation meshes, as in the high-resolution meshes demonstrated by Vadakkumpadan et al. (2009) and Bishop et al. (2010).

Chapter 9

Conclusions and Future Directions

9.1 Conclusions

We have investigated the following thesis:

> Given an appropriate underlying model of electrophysiological behaviour in cardiac tissue, it is possible to construct sample-specific models of cardiac electrophysiology at both a cell and tissue level. These models provide insight into the consequences of variability in activation and repolarisation of the cardiac action potential. Where only information on activation, or action potential morphology, is available then a phenomenological model that reproduces these properties without reconstructing membrane currents suffices. If subcellular phenomena are being investigated then a biophysically detailed model of the cardiac action potential is required. Whether or not direct comparison to experimental data is possible depends on both the simulation results generated and the experimental data available.

We have done so by using mRNA expression data to construct populations of biophysically detailed models; by demonstrating the properties of phenomenological models; constructing phenomenological models representing cell-cell and beat-to-beat variability from

experimental recordings; and by estimating sample specific conductivity tensors from optical mapping recordings taken from optical mapping recordings. Raw experimental data are used both quantitatively and qualitatively for the construction of models, and the comparison of results to experimental data. We have also used qualitative results from a literature review of comparitive studies to compare to modelling results for non-failing and failing states.

Taken in a broader context, we have presented the first population-based simulation study comparing disease and non-diseased states, building on the work of Sobie (2009), Romero et al. (2009), and Sarkar and Sobie (2011). Previous population based studies in cardiac electrophysiology have typically focussed on generating only one population rather than comparing two. We suggest that this method is more robust to inter-individual variability and parameter uncertainty than the more traditional approach of changing selected parameters by a fixed amount.

Our stochastic model is both the first phenomenological model of temporal variability in the ventricles, and the first whose morphology and BVR has been fitted directly to AP recordings from individual myocytes. We have found similar results in terms of reduction in BVR in tissue to the simulation study of Pueyo et al. (2011). However, we extended their results and those of Lesh et al. (1989) by considering the interaction between BVR and inter-cell variability, concluding that inter-cell variability in APD makes a greater contribution to dispersion of repolarisation under reduced electrical coupling than BVR in each myocyte.

Finally, we have demonstrated an extensible method for directly comparing simulation results to experimental data recorded from wedge preparations. We directly compared activation from the monodomain model to activation maps recorded in tissue using sample-specific geometries. This offers a method to extend the work of Weiss et al. (2007), whose comparison between simulations of human left ventricle with both a rule based and dt-MRI derived fibre orientations did not incorporate any way to compare the results to experimental data. Our findings indicate a role for endocardial structures and midmyocardial structural features in disrupting the otherwise relatively uniform conduction through the myocardium.

Whilst previous studies such as Bishop et al. (2010) have included detailed endocardial and epicardial geometry, our work suggests that the role of transmural structural features in modulating conduction should also be considered.

In conclusion, the study of inter-sample variability is becoming increasingly feasible through computational simulations. This type of simulation requires more direct comparison to the full range of experimental data than 'traditional' approaches. Whilst we have shown that this can be challenging due to the ranges sometimes present in (particularly human) experimental data, we have also shown that it is possible in a meaningful way. The nature of the comparison can and should be different depending on the data available — we use direct comparison in Chapters 6 and 8, and through a more qualitative approach where the available mRNA expression data is not directly comparable to electrophysiological recordings. Both approaches have their advantages and disadvantages, but in each of Chapters 5, 7, and 8, we show that they may lead to physiologically relevant conclusions drawn resulting from inter-sample variability.

9.2 Future Directions

9.2.1 Populations of biophysically detailed models

The issue of population level variability is receiving increasing amounts of attention in the computational literature. It is worth considering how a model, or models, of this variability ought to be parameterised. Models of population-level variability have been based on introducing a probability distribution for each parameter considered in the study, as described in Chapter 5 and Sarkar et al. (2012). Thus, we can consider these studies as consisting of one model, with parameter distributions instead of values. The resulting sets of parameters are realisations of this one model.

Recently, Britton et al. (2013) have challenged this concept by presenting a population of biophysically detailed models which was calibrated against an experimental data set.

In this case, models outside the range of experimental data as determined by a set of biomarkers are rejected. Hence we now have a true 'population of models' — there is no underlying distribution. Given a suitable data set is available, this approach should be considered for future studies. Validation of the constructed population is essential in this case given the ill-posed nature of fitting to the AP morphology, discussed in Chapter 3.

The investigation in Chapter 5 raises several more immediate issues. What are suitable ranges for the parameters we do choose to investigate? Whilst our numbers are guided by both values in the literature as described by Romero et al. (2009) and also by the mRNA expression data provided by Ambrosi et al. (2013), it must be said that they are somewhat arbitrary. It is incumbent upon mathematical modellers to make a convincing case, through modelling, that variability in measured parameters is very much relevant to cardiac electrophysiology. As discussed in Chapter 2, this certainly could explain variable responses to pharmaceutical agents within a population. Gaining information on the range of conductances in cardiac myocytes, where possible, is crucial. It is worth noting a data representation issue here — experimental studies frequently present observed values as a mean $\pm$ standard deviation, with the implicit assumption that the data is normally distributed. It is not clear that this is the case. Particularly where relatively small sample numbers occur, it is better to record individual values from experiments.

Another issue is the co-variance of different model parameters. Even if distributions for individual parameters could be reliably obtained, their co-variance will be critical. We have already alluded to this issue in the work presented in Chapter 5, through our regression analysis. For example, we have shown that a decrease in I_{CaL} should increase the calcium transient duration in a human ventricular myocyte, whereas an increase in I_{NaCa} would be expected to decrease the duration of the calcium transient. Thus, if these two channels were co-regulated, then this could serve to either exacerbate or protect against a change in one or the other.

In both cardiac electrophysiology and neuroscience literature, the issue of correlated channel regulation is only beginning to be understood, and will be crucial to understand-

ing inter-individual variability in the future (Marder and Taylor, 2011; Sarkar et al., 2012). Some experimental studies have begun to explore co-regulation of channels. Xiao et al. (2008) demonstrated that isolated canine ventricular myocytes had increased I_{Ks} density in response to chronic block of I_{Kr} by dofetilide. Densities of other repolarisation currents remained unchanged. Interestingly, mRNA expression levels of transcripts encoding I_{Ks} subunits remained unchanged despite an increase in protein levels, suggesting post-translational modification as the mechanism by which upregulation occurs. Li et al. (2012) report increases in I_{CaL} and I_{NaCa} in SERCA knock-out mice. Modelling work demonstrated that both could be explained as a response to depressed calcium transients and diastolic calcium concentrations resulting from SERCA downregulation. The increase in I_{NaCa} also then lead to an increase in intracellular sodium concentration. Pott et al. (2007) have also shown that mice increase expression of I_{to} and decrease expression of I_{CaL} in response to I_{NaCa} knockout to maintain calcium homeostasis with reduced calcium efflux. This is achieved by reducing calcium influx through I_{CaL} and shortening the action potential through Ito to trigger SERCA early. Particularly in the last two cases, the mechanism of regulation appears to be ionic concentration. This should be considered as a factor in future modelling studies.

9.2.2 Temporal and cell-cell variability

The current state of modelling, as shown in this dissertation and other publications, suggests that stochastic fluctuations in the membrane potential have only modest effects when cells are coupled together into cardiac tissue. Nevertheless, early after-depolarisations are reported in tissue experiments, perhaps due to accumulation of calcium in local regions of the tissue, or calcium sparking events. This certainly merits further investigation. It may be worth considering whether some aspects of this reduction in temporal variability in a monodomain setting is due to the strength of electrotonic coupling in this modelling framework. This is not the only modelling framework in use for stochastic models, and discrete models such as those used by Lemay et al. (2011) or Bub and Shrier (2002) may well be more

appropriate for investigating the tissue level consequences of variability in repolarisation.

As discussed in Chapter 3, increases in BVR in isolated myocytes are associated with increased arrhythmic risk of pharmaceutical agents (Johnson et al., 2010). This is a process that cannot be represented by mainstream deterministic models. If BVR as a biomarker lives up to its early promise could be important for recently developed high-throughput simulation based screening programs such as Mirams et al. (2011). The incorporation of variability into biophysically detailed models for this could be accomplished using frameworks such as those proposed by Pueyo et al. (2011) and Dangerfield et al. (2012). They may need extension to incorporate spontaneous diastolic calcium release as reported by Johnson et al. (2013).

9.2.3 Constructing sample-specific models of human ventricular wedges

Our study presented in Chapter 8 is intended as the first part in a larger framework for the parameterisation of the properties of individual optical mapping samples. The estimated value of the conductivity tensor can be used to inform the magnitude of the electrotonic load in the heterogeneously repolarising tissue. A diagrammatic description of this framework proposed can be found in Fig. 9.1. Greyed sections form part of the framework that were not addressed in this dissertation, but ought to be addressed in future work.

The intention is that by fitting the repolarisation phase of the action potential using a phenomenological model, it may be tractable to perform parameter estimation in tissue, rather than at a single cell level. This is primarily due to the attractive properties of phenomenological models as outlined in Chapter 6. This wider context informed our choice of a monodomain framework rather than more computationally efficient modelling frameworks for activation such as Eikonal or graph-based methods. A validation approach for such a method would be the fact that in the process of recording electrophysiological data from the wedges, the ECG is recorded. Significantly, the location of the electrode used to record the ECG is also recorded in the photographs of the wedges.

Two potential schemes for the parameterisation of a phenomenological model in tissue

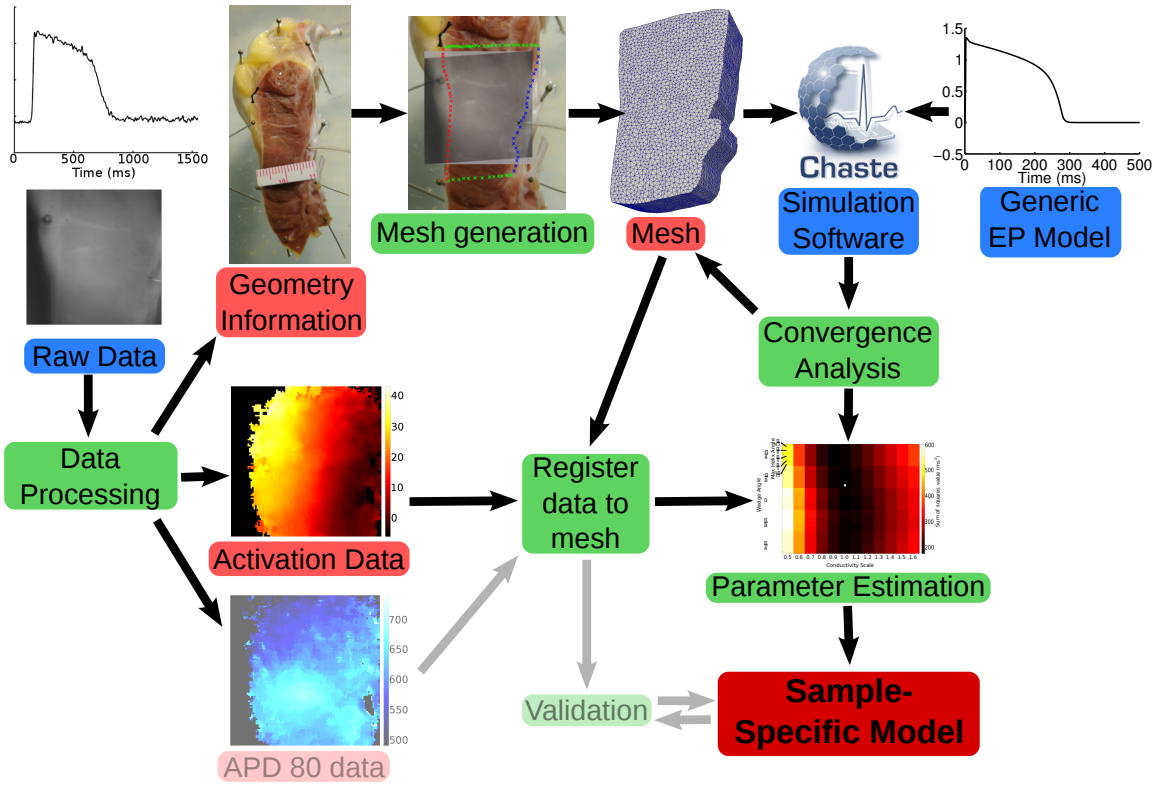

Figure 9.1: **A conceptual framework for the production of sample-specific models of human ventricular electrophysiology.** Greyed features are not addressed in this dissertation but form part of a broader vision for future progress using this or similar data sets.

are apparent. The first would be a straightforward, but computationally intensive, minimisation procedure using the monotonic relationship between APD and time constant rescaling in Bueno-Orovio models as demonstrated in Chapter 6. Since we are interested in repolarisation time, not activation time, a coarser resolution mesh could be used to speed up simulations without affecting results. A second method could be to derive from the recordings and the fitted conductivity tensor an estimate of the electrotonic current for each pixel. This current acting at each pixel would then be used to fit an electrotonically loaded cell model at each pixel. Using the data-mesh map from Chapter 8, a cell model could then be assigned to each node in the mesh, perhaps using a mean value where data is missing.

Given the data available in this thesis we would argue against the use of a biophysically detailed model for this estimation. Leaving aside the important issue of the time taken for

the simulations in question, we suggest that there is a danger in the necessary modelling assumptions. In altering a phenomenological model we do not make assumptions about the physiological change which has driven the prolongation of the AP compared to the original model. In a biophysically detailed model such an assumption is necessary in order to match experiment to data. At present, we have little information on what has changed *in the specific sample under investigation* and so this could lead to false conclusions about the role of a particular current, particularly if some sort of simulated pharmaceutical intervention was applied to the model. However, if such information were available, a viable strategy could be to fit a phenomenological model to the tissue as discussed above, then apply biophysically detailed models matching the APD (for example) of this model from a population of models such as the one described in Chapter 5. This would treat the population as a form of 'model database' — an idea originally proposed by Prinz et al. (2003) in the neuroscience literature.

Another application of having constructed maps between a simulation mesh and the recorded data is that an entirely different modelling method could be used within the framework we have constructed. Partcular examples would be Eikonal or graph based methods coupled to simplified electrophysiology models as proposed by Relan et al. (2011) or Wallman et al. (2012). Again, the recorded ECG shows promise as a validation method in this case. Similarly, both the methodology and the simulation, registration and postprocessing code created during this project is extensible to a wide range of data sets. One exciting possibility would be the parameterisation of sample-specific models of electrophysiology recordings from pseudo-2D preparations such as rabbit myocardial slices (Lee et al., 2012b). This would avoid some of the disadvantages present in surface optical mapping recordings which do not account for electrical activity that is not close to the surface of the preparation. Cell orientation could be determined using histology to establish a conductivity tensor.

9.3 Final Thought

In this thesis, and other recent modelling studies, a picture is building up showing that the inter-sample variability, so often averaged out in experimental reports, may have important physiological and pathological effects. If the integrated vision presented in reviews such as Carusi et al. (2012) and Quinn and Kohl (2013) is to be realised, it is now incumbent upon computational modellers to make this case to the wider electrophysiology community. This could have major implications for both our understanding of physiology, and also for the way experimental results are reported.

Appendix A

Experimental Data Tables for Human Heart Failure

Table A.1: **Experimental Data: Population Details**

Publication	Preparation	Recording Method	Cohort	Gender	Age
Gwathmey et al. (1987)	RV muscle strips	Aequorin	8 NF	3 f, 5 m	7-56
			9 F (3 Id, 4 Is, 1 MD, 1 NDBVH)	2 f, 5 m	14-54
Beuckelmann et al. (1992)	isolated LV myocyte	Fura-2, patch clamp	3 NF	not given	not given
			14 F (9 D, 5 Is)	3 f, 11 m	51.8+/-11.6
1993 Beuckelmann et al. (1993)	isolated LV myocyte	patch clamp	6 NF	not given	not given
			16 F (10 D, 6 Is)	2 f, 14 m	46.6+/-3.6
Vahl et al. (1994)	LV muscle strips	Fura-2	3 NF	not given	not given
			7 F (7 D)	not given	not given
Sipido et al. (1998)	isolated LV myocyte	Fluo 3 (+Fura red),	5 F (Is)	5 male	48-67
		patch clamp	6 F (D)	3 f, 3 m	21-60
Kubo et al. (2001)	isolated LV myocyte	Fluo 3+voltage clamp	10 NF	not given	56.3+/-4.4
			20 F (10 IsD, 10 NIsD)	not given	IsD 56.4+/-3.7, NIsD 48.6+/-4.4
Piacentino III et al. (2003)	isolated LV myocyte	Fluo 3+ AP clamp,	7 NF	2 f, 5 m	66+/-3
		patch clamp	11 F (5 Is, 6 IdD/NIsD)	2 f, 9 m	49+/-4
Li et al. (2004)	isolated RV myocyte	patch clamp	5 NF	not given	30-65
			6 F	not given	34-58
Glukhov et al. (2010)	transmural LV wedge	di-4-ANEPPS	5 NF	2 f, 3 m	19-68
			5 F (1 Id, 1 Is, 1 R, 1 NIs, 1 D)	1 f, 4 m	28-64
Lou et al. (2011)	transmural LV wedge	RH237. Rhod-2 AM	6 NF	2 f, 3 m	47-59
			5 F (2 Is, 3 Id)	3 f, 2 m	49-65
Glukhov et al. (2012)	transmural LV wedge	di-4-ANEPPS	10 NF	5 f, 5 m	19-76
			10 F (4 Id, 3 D, 2 NIs, 1 H)	6 f, 4 m	28-66

Abreviations used: F = failing, NF = non-failing, D = dilated cardiomyopathy, Is = ischaemic cardiomyopathy, MD = myocardial deterioration post-surgery, NDBVH = non-dilated biventricular hypertrophy, IsD = Ischaemic dilated cardiomyopathy, NIsD = non-ischaemic dilated cardiomyopathy, IdD = idiopathic dilated cardiomyopathy, NIs = non-ischaemic cardiomyopathy, R = restrictive cardiomyopathy, H = hypertrophic cardiomyopathy, f = female, m = male. Ages are displayed as either mean +/- standard deviation or min-max.

Table A.2: **Experimental Data: Action potential biomarkers**

Publication	BCL	Cohort	APD90(ms)	APD80(ms)				APD50 (ms)
				endo	mid	epi	max	
Beuckelmann et al. (1992)	2000ms	NF	649+/-101					
		F	1038+/223					
Beuckelmann et al. (1993)	2000ms	NF	650+/-100					
		F	1090+/-90					
Sipido et al. (1998)	4000ms	F (Is)	537+/133					433+/-31
		F (D)	516+/-49					408+/-45
	2000ms	F (Is)	496+/-27					389+/-29
		F (D)	474+/-41					369+/-40
	1000ms	F (Is)	451+/-19					343+/-7
		F (D)	417+/-31					311+/-29
	500ms	F (Is)	352+/-19					255+/-17
		F (D)	341+/-20					250+/-23
Piacentino III et al. (2003)	2000ms	NF						511+/-49
		F						663+/-29
Li et al. (2004)	2000ms	NF	364+/-23					241+/-22
		F	545+/-51					397+/-42
	1000ms	NF	305+/-17					234+/-16
		F	438+/-38					305+/-28
	500	NF	281+/-16					213+/-12
		F	324+/-19					234+/-19
Glukhov et al. (2010)	4000ms	NF		510+/-22	471+/-21	408+/-21	615+/-45	
		F		516+/-39	507+/-32	482+/-25	521+/-30	
	2000ms	NF		494+/-22	455+/-20	383+/-21	537+/-40	
		F		506+/-35	495+/-25	477+/-22	495+/-30	
	1000ms	NF		437+/-18	405+/-16	350+/-16	466+/-25	
		F		450+/-35	437+/-31	415+/-18	455+/-34	
	750ms	NF		383+/-21	362+/-20	316+/-16	410+/-16	
		F		373+/-21	367+/-19	357+/-13	379+/-20	
	500ms	NF		316+/-15	297+/-12	263+/-12	330+/-12	
		F		305+/-17	299+/-13	292+/-9	313+/-11	
	300ms	NF		226+/-9	216+/-8	196+/-8	228+/-3	
		F		207+/-1	206+/-6	196+/-5	215+/-8	
Lou et al. (2011)	1500ms	NF		451+/-85	420+/-81	394+/-81		
		F		426+/-70	408+/-64	400+/-66		
	1000ms	NF		398+/-62	380+/-61	361+/-47		
		F		394+/-65	375+/-50	364+/-50		
	800ms	NF		359+/-60	348+/-53	330+/-56		
		F		353+/-43	338+/-44	329+/-46		
	600ms	NF		315+/-43	303+/-37	294+/-44		
		F		308+/-43	291+/-38	295+/-43		
Glukhov et al. (2012)	4000ms	NF		492+/-18	453+/-17	387+/-19		
		F		561+/-35	538+/-26	512+/-29		
	2000ms	NF		481+/-17	441+/-16	371+/-16		
		F		525+/-35	481+/-31	468+/-27		
	1000ms	NF		429+/-14	398+/-13	342+/-13		
		F		439+/-15	413+/-13	386+/-15		
	750ms	NF		374+/-16	351+/-16	305+/-13		
		F		372+/-14	352+/-13	328+/-16		
	500ms	NF		311+/-11	292+/-9	256+/-9		
		F		319+/-18	304+/-10	280+/-10		
	300ms	NF		226+/-6	212+/-5	192+/-6		
		F		21+/-9	202+/-7	194+/-11		

Abreviations used: F = failing, NF = non-failing, Is = ischaemic cardiomyopathy, D = dilated cardiomyopathy. Max denotes the maximum APD value in the tissue. All values given as mean +/- standard deviation.

Table A.3: **Experimental Data: Calcium transient durations**

Publication	BCL	Cohort	CaTD80 (ms)				CaTD50 (ms)
			-	endo	mid	epi	
Gwathmey et al. (1987)	3000ms	NF	246+/-37				
		F	546+/-48				
Beuckelmann et al. (1992)	2000ms	NF					320+/-68
		F					692+/-166
Kubo et al. (2001)	500ms	NF					555+/-20
		F					664+/-42
Lou et al. (2011)	1500ms	NF		530+/-80	486+/-69	446+/-73	
		F		538+/-88	493+/-71	465+/-75	
	1000ms	NF		475+/-58	441+/-56	414+/-60	
		F		489+/-81	449+/-64	436+/-64	
	800ms	NF		441+/-43	410+/-46	376+/-49	
		F		435+/-59	412+/-48	395+/-45	
	600ms	NF		393+/-21	366+/-26	333+/-30	
		F		384+/-48	364+/-31	358+/-46	

Abreviations used: F = failing, NF = non-failing, - denotes no transmural spatial location given. All values given as mean +/- standard deviation.

Table A.4: **Experimental Data: Calcium transient decay time constants**

Publication	BCL	Cohort	CaT τ (ms)			
			-	endo	mid	epi
Kubo et al. (2001)	500ms	NF	269+/-75			
		F	372+/-71			
Piacentino III et al. (2003)	1000ms	NF	209+/-31			
		F	306+/-27			
Lou et al. (2011)	1500ms	NF		152+/-12	137+/-11	128+/-7
		F		168+/-22	154+/-21	142+/-13

Abreviations used: F = failing, NF = non-failing, τ = time constant of decay for the calcium transient, - denotes no transmural spatial location given.All values given as mean +/- standard deviation.

Table A.5: **Experimental Data: Calcium transient magnitude**

Publication	BCL	Cohort	Diastolic Cai (nM)	Systolic Cai (nM)	Δ Cai (nM)
Beuckelmann et al. (1992)	2000ms	NF	96+/-47	746+/-249	
		F	165+/-61	367+/-109	
Vahl et al. (1994)	-	NF	195+/-80	1435+/-230	
		F	234+/-75	1562+/-172	
Kubo et al. (2001)	500ms	NF	125+/12	506+/-25	
		F	150+/-16	407+/-16	
Piacentino III et al. (2003)	1000ms	NF	153+/-20		804+/-197
		F	147+/-14		398+/-58

Abreviations used: F = failing, NF = non-failing, Δ denotes change throughout CaT. All values given as mean +/- standard deviation.

Table A.6: **Experimental Data: Calcium transient triangulation**

Publication	BCL	Cohort	CaTD30/CaTD80		
			endo	mid	epi
Lou et al. (2011)	1500ms	NF	0.53+/-0.03	0.50+/-0.03	0.45+/-0.05
		F	0.58+/-0.04	0.57+/-0.02	0.52+/-0.05

Abreviations used: F = failing, NF = non-failing. All values given as mean +/- standard deviation.

Table A.7: **Experimental Data: Calcium transient upstroke**

Publication	BCL	Cohort	Time to peak(ms)*				AP-CaT delay (ms)		
			-	endo	mid	epi	endo	mid	epi
Gwathmey et al. (1987)	3000ms	NF	33+/-6						
		F	53+/-5						
Lou et al. (2011)	1500ms	NF		30+/-3	25+/-3	35+/-3	8.8+/-0.5	8.3+/-0.5	8.1+/-0.7
		F		38+/-16	27+/-4	27+/-6	9.7+/-0.5	9.0+/-0.2	8.0+/-0.4

Abreviations used: F = failing, NF = non-failing, - denotes no transmural spatial location given. All values given as mean +/- standard deviation. *Time to peak is given as the time from 10% to 90% rise time for the CaT in Lou et al. (2011).

Appendix B

Regression Coefficients and R^2 Values

Table B.1: **Regression coefficients: nonfailing, APD80**

Parameter	BCL (ms)										
	1500	1000	900	800	700	600	500	450	400	350	300
GCaL	0.322	0.289	0.269	0.256	0.247	0.244	0.250	0.256	0.267	0.278	0.270
GKr	-0.932	-0.937	-0.942	-0.945	-0.947	-0.948	-0.948	-0.948	-0.946	-0.943	-0.938
GKs	-0.078	-0.092	-0.093	-0.096	-0.099	-0.102	-0.106	-0.107	-0.108	-0.108	-0.106
GK1	-0.051	-0.054	-0.056	-0.058	-0.060	-0.062	-0.064	-0.065	-0.067	-0.071	-0.078
GNaCa	0.088	0.112	0.120	0.125	0.127	0.124	0.114	0.107	0.098	0.087	0.073
Gto	0.015	0.009	0.007	0.005	0.004	0.003	0.004	0.004	0.005	0.006	0.008
Jup	0.042	0.044	0.038	0.033	0.027	0.022	0.016	0.012	0.007	0.003	-0.003

Regression coefficients for the fit to APD80 in the non-failing population at each BCL.

Table B.2: **Regression coefficients: nonfailing, APD3080**

Parameter	BCL (ms)										
	1500	1000	900	800	700	600	500	450	400	350	300
GCaL	0.570	0.465	0.437	0.422	0.422	0.441	0.483	0.519	0.558	0.610	0.692
GKr	0.705	0.778	0.801	0.820	0.832	0.832	0.814	0.792	0.764	0.724	0.618
GKs	-0.049	-0.057	-0.055	-0.052	-0.049	-0.045	-0.042	-0.039	-0.038	-0.042	-0.060
GK1	0.265	0.269	0.271	0.270	0.267	0.260	0.249	0.241	0.232	0.220	0.201
GNaCa	0.098	0.125	0.116	0.093	0.056	0.006	-0.053	-0.087	-0.115	-0.138	-0.152
Gto	0.176	0.158	0.150	0.142	0.132	0.121	0.111	0.104	0.099	0.098	0.102
Jup	0.063	0.024	0.009	0.007	0.017	0.041	0.076	0.096	0.115	0.132	0.140

Regression coefficients for the fit to APD3080 in the non-failing population at each BCL.

Table B.3: **Regression coefficients: nonfailing, CaTD80**

Parameter	BCL (ms)										
	1500	1000	900	800	700	600	500	450	400	350	300
GCaL	-0.338	-0.403	-0.421	-0.440	-0.465	-0.497	-0.535	-0.547	-0.552	-0.548	-0.509
GKr	-0.029	0.002	0.017	0.031	0.045	0.056	0.060	0.058	0.048	0.032	0.030
GKs	-0.001	0.003	0.004	0.006	0.008	0.010	0.012	0.012	0.011	0.009	0.007
GK1	-0.003	-0.004	-0.004	-0.004	-0.004	-0.004	-0.004	-0.004	-0.004	-0.001	0.010
GNaCa	0.334	0.344	0.346	0.354	0.368	0.388	0.407	0.417	0.420	0.420	0.407
Gto	-0.036	-0.037	-0.036	-0.036	-0.036	-0.037	-0.038	-0.039	-0.039	-0.040	-0.038
Jup	-0.873	-0.843	-0.833	-0.820	-0.800	-0.771	-0.736	-0.721	-0.716	-0.718	-0.654

Regression coefficients for the fit to CaT80 in the non-failing population at each BCL.

Table B.4: **Regression coefficients: nonfailing, CaTD3080**

Parameter	BCL (ms)										
	1500	1000	900	800	700	600	500	450	400	350	300
GCaL	-0.509	-0.508	-0.503	-0.498	-0.497	-0.504	-0.520	-0.532	-0.547	-0.553	-0.485
GKr	0.045	0.104	0.123	0.141	0.158	0.175	0.186	0.189	0.184	0.173	0.165
GKs	0.011	0.017	0.019	0.022	0.024	0.026	0.027	0.028	0.028	0.028	0.026
GK1	-0.005	-0.007	-0.006	-0.005	-0.004	-0.002	-0.001	-0.001	-0.002	-0.000	0.006
GNaCa	0.553	0.469	0.450	0.434	0.421	0.413	0.408	0.415	0.420	0.424	0.422
Gto	-0.051	-0.044	-0.040	-0.037	-0.035	-0.033	-0.033	-0.034	-0.035	-0.037	-0.036
Jup	-0.487	-0.615	-0.630	-0.637	-0.635	-0.622	-0.600	-0.593	-0.595	-0.610	-0.595

Regression coefficients for the fit to CaTD3080 in the non-failing population at each BCL.

Table B.5: **Regression coefficients: nonfailing, CaTmax**

Parameter	BCL (ms)										
	1500	1000	900	800	700	600	500	450	400	350	300
GCaL	0.622	0.647	0.654	0.660	0.666	0.677	0.697	0.701	0.709	0.710	0.665
GKr	-0.117	-0.136	-0.146	-0.153	-0.155	-0.151	-0.135	-0.119	-0.095	-0.069	-0.051
GKs	-0.014	-0.019	-0.020	-0.022	-0.023	-0.024	-0.023	-0.021	-0.018	-0.015	-0.010
GK1	0.002	0.003	0.003	0.003	0.003	0.003	0.003	0.004	0.003	-0.000	-0.014
GNaCa	-0.612	-0.565	-0.554	-0.548	-0.545	-0.544	-0.544	-0.550	-0.554	-0.560	-0.542
Gto	0.056	0.053	0.052	0.051	0.050	0.050	0.050	0.050	0.051	0.053	0.050
Jup	0.412	0.450	0.453	0.449	0.437	0.416	0.386	0.372	0.356	0.341	0.271

Regression coefficients for the fit to CaTmax in the non-failing population at each BCL.

Table B.6: **Regression coefficients: nonfailing, AP-CaT delay**

Parameter	BCL (ms)										
	1500	1000	900	800	700	600	500	450	400	350	300
GCaL	-0.645	-0.650	-0.653	-0.657	-0.664	-0.677	-0.695	-0.696	-0.689	-0.665	-0.553
GKr	0.110	0.114	0.119	0.123	0.125	0.122	0.107	0.091	0.069	0.062	0.090
GKs	0.012	0.015	0.016	0.016	0.018	0.018	0.018	0.016	0.015	0.013	0.019
GK1	-0.003	-0.003	-0.003	-0.003	-0.004	-0.004	-0.006	-0.009	-0.014	-0.005	0.008
GNaCa	0.524	0.472	0.458	0.449	0.443	0.437	0.423	0.403	0.371	0.346	0.344
Gto	-0.036	-0.036	-0.036	-0.036	-0.036	-0.036	-0.035	-0.034	-0.032	-0.029	-0.028
Jup	-0.508	-0.547	-0.553	-0.555	-0.552	-0.541	-0.521	-0.506	-0.494	-0.493	-0.510

Regression coefficients for the fit to AP-CaT delay in the non-failing population at each BCL.

Table B.7: **Regression coefficients: failing, APD80**

Parameter	BCL (ms)										
	1500	1000	900	800	700	600	500	450	400	350	300
GCaL	0.212	0.201	0.197	0.197	0.201	0.210	0.225	0.238	0.252	0.267	0.324
GKr	-0.955	-0.957	-0.959	-0.959	-0.958	-0.957	-0.954	-0.952	-0.948	-0.947	-0.970
GKs	-0.086	-0.097	-0.098	-0.100	-0.101	-0.103	-0.103	-0.103	-0.102	-0.101	-0.102
GK1	-0.054	-0.057	-0.058	-0.060	-0.061	-0.062	-0.064	-0.066	-0.069	-0.075	-0.085
GNaCa	0.105	0.094	0.090	0.085	0.081	0.076	0.071	0.067	0.063	0.059	0.058
Gto	0.010	0.007	0.006	0.005	0.005	0.004	0.004	0.004	0.004	0.005	0.007
Jup	-0.054	-0.041	-0.034	-0.027	-0.020	-0.014	-0.009	-0.005	-0.005	-0.009	-0.013

Regression coefficients for the fit to APD80 in the non-failing population at each BCL.

Table B.8: **Regression coefficients: failing, APD3080**

Parameter	BCL (ms)										
	1500	1000	900	800	700	600	500	450	400	350	300
GCaL	0.394	0.354	0.352	0.351	0.352	0.356	0.373	0.403	0.467	0.611	0.820
GKr	0.760	0.813	0.824	0.835	0.846	0.856	0.861	0.853	0.826	0.709	0.311
GKs	-0.042	-0.045	-0.042	-0.039	-0.036	-0.031	-0.027	-0.027	-0.036	-0.069	-0.103
GK1	0.247	0.239	0.238	0.236	0.233	0.229	0.223	0.220	0.214	0.201	0.185
GNaCa	0.166	0.117	0.099	0.081	0.062	0.042	0.019	0.005	-0.009	-0.023	-0.054
Gto	0.173	0.152	0.145	0.137	0.127	0.116	0.105	0.101	0.101	0.109	0.117
Jup	-0.203	-0.158	-0.139	-0.118	-0.093	-0.063	-0.027	-0.003	0.028	0.077	0.138

Regression coefficients for the fit to APD3080 in the non-failing population at each BCL.

Table B.9: **Regression coefficients: failing, CaTD80**

Parameter	BCL (ms)										
	1500	1000	900	800	700	600	500	450	400	350	300
GCaL	-0.134	-0.213	-0.251	-0.289	-0.329	-0.373	-0.420	-0.457	-0.492	-0.541	-0.578
GKr	-0.211	-0.255	-0.254	-0.252	-0.246	-0.235	-0.222	-0.201	-0.177	-0.096	0.023
GKs	-0.022	-0.030	-0.030	-0.030	-0.030	-0.029	-0.027	-0.023	-0.018	-0.003	0.002
GK1	-0.001	-0.001	-0.002	-0.001	-0.001	-0.001	0.001	0.002	0.008	0.029	0.039
GNaCa	0.090	0.134	0.149	0.168	0.188	0.210	0.232	0.244	0.252	0.250	0.250
Gto	-0.018	-0.025	-0.027	-0.028	-0.029	-0.030	-0.031	-0.030	-0.030	-0.028	-0.023
Jup	-0.959	-0.910	-0.885	-0.855	-0.816	-0.767	-0.709	-0.678	-0.651	-0.624	-0.607

Regression coefficients for the fit to CaTD80 in the non-failing population at each BCL.

Table B.10: **Regression coefficients: failing, CaTD3080**

Parameter	BCL (ms)										
	1500	1000	900	800	700	600	500	450	400	350	300
GCaL	0.410	0.306	0.212	0.103	-0.017	-0.144	-0.273	-0.358	-0.436	-0.522	-0.580
GKr	-0.670	-0.729	-0.687	-0.613	-0.511	-0.390	-0.263	-0.186	-0.115	-0.004	0.117
GKs	-0.073	-0.091	-0.085	-0.076	-0.063	-0.047	-0.029	-0.017	-0.005	0.015	0.016
GK1	0.000	0.002	0.002	0.003	0.003	0.003	0.004	0.005	0.011	0.029	0.036
GNaCa	0.000	0.081	0.116	0.150	0.180	0.204	0.222	0.230	0.232	0.228	0.228
Gto	0.028	0.013	0.005	-0.002	-0.008	-0.014	-0.019	-0.020	-0.021	-0.019	-0.020
Jup	0.534	0.144	0.003	-0.139	-0.270	-0.380	-0.463	-0.503	-0.527	-0.527	-0.518

Regression coefficients for the fit to CaTD3080 in the non-failing population at each BCL.

Table B.11: **Regression coefficients: failing, CaTmax**

Parameter	BCL (ms)										
	1500	1000	900	800	700	600	500	450	400	350	300
GCaL	0.792	0.790	0.785	0.780	0.777	0.776	0.781	0.784	0.795	0.810	0.840
GKr	-0.098	-0.092	-0.089	-0.087	-0.083	-0.074	-0.056	-0.044	-0.037	-0.082	-0.155
GKs	-0.014	-0.015	-0.015	-0.015	-0.015	-0.014	-0.012	-0.011	-0.011	-0.020	-0.019
GK1	0.002	0.002	0.002	0.002	0.003	0.003	0.002	0.001	-0.005	-0.028	-0.040
GNaCa	-0.476	-0.433	-0.417	-0.404	-0.392	-0.382	-0.375	-0.370	-0.366	-0.354	-0.350
Gto	0.065	0.058	0.055	0.051	0.048	0.045	0.043	0.041	0.039	0.037	0.033
Jup	0.260	0.270	0.280	0.287	0.291	0.292	0.285	0.290	0.284	0.261	0.225

Regression coefficients for the fit to CaTmax in the non-failing population at each BCL.

Table B.12: **Regression coefficients: failing, AP-CaT delay**

Parameter	BCL (ms)										
	1500	1000	900	800	700	600	500	450	400	350	300
GCaL	-0.696	-0.688	-0.691	-0.693	-0.698	-0.707	-0.722	-0.731	-0.741	-0.745	-0.743
GKr	0.116	0.098	0.093	0.089	0.083	0.076	0.067	0.064	0.071	0.115	0.180
GKs	0.013	0.013	0.013	0.013	0.012	0.012	0.011	0.011	0.012	0.018	0.018
GK1	-0.006	-0.006	-0.006	-0.006	-0.007	-0.007	-0.006	-0.005	-0.001	0.013	0.026
GNaCa	0.324	0.294	0.287	0.282	0.278	0.276	0.273	0.271	0.267	0.256	0.251
Gto	-0.025	-0.027	-0.027	-0.027	-0.027	-0.027	-0.027	-0.027	-0.027	-0.025	-0.025
Jup	-0.586	-0.611	-0.611	-0.609	-0.604	-0.593	-0.569	-0.549	-0.524	-0.489	-0.461

Regression coefficients for the fit to AP-CaT delay in the non-failing population at each BCL.

R^2 coefficients

Table B.13: **Non-failing R^2 values**

Biomarker	BCL (ms)										
	1500	1000	900	800	700	600	500	450	400	350	300
APD80	0.988	0.985	0.985	0.985	0.985	0.986	0.988	0.989	0.990	0.990	0.989
APD3080	0.940	0.942	0.949	0.957	0.966	0.973	0.979	0.982	0.984	0.987	0.985
CaTD80	0.983	0.987	0.987	0.988	0.989	0.990	0.991	0.992	0.992	0.992	0.993
CaTD3080	0.803	0.864	0.865	0.860	0.852	0.840	0.831	0.842	0.861	0.890	0.920
CaTmax	0.943	0.957	0.960	0.959	0.955	0.949	0.948	0.945	0.944	0.939	0.926
AP-CaT delay	0.957	0.953	0.953	0.953	0.954	0.953	0.940	0.908	0.857	0.808	0.814

R^2 values for each fit to the non-failing population.

Table B.14: **Failing R^2 values**

Biomarker	BCL (ms)										
	1500	1000	900	800	700	600	500	450	400	350	300
APD80	0.981	0.981	0.981	0.981	0.981	0.981	0.982	0.983	0.983	0.981	0.979
APD3080	0.901	0.914	0.918	0.923	0.929	0.937	0.947	0.954	0.961	0.946	0.885
CaTD80	0.988	0.954	0.932	0.903	0.868	0.825	0.780	0.766	0.759	0.753	0.761
CaTD3080	0.909	0.663	0.539	0.435	0.371	0.361	0.407	0.468	0.532	0.601	0.658
CaTmax	0.933	0.894	0.877	0.861	0.848	0.838	0.834	0.836	0.847	0.858	0.880
AP-CaT delay	0.943	0.940	0.938	0.936	0.933	0.928	0.919	0.910	0.897	0.872	0.835

R^2 values for each fit to the failing population.

Bibliography

F.G. Akar and D.S. Rosenbaum. Transmural electrophysiological heterogeneities underlying arrhythmogenesis in heart failure. *Circ. Res.*, 93:638–645, 2003.

F.G. Akar, G.X. Yan, C. Antzelevitch, and D.S. Rosenbaum. Unique topographical distribution of M cells underlies reentrant mechanism of torsade de pointes in the Long-QT syndrome. *Circulation*, 105:1247–1253, 2002.

C.M. Ambrosi, K.A. Yamada, J.M. Nerbonne, and I.R. Efimov. Gender differences in electrophysiological gene expression in failing and nonfailing human hearts. *PLoS ONE*, 8 (1):e54635, 2013.

C. Antzelevitch, S. Sicouri, S.H. Litovsky, A. Lukas, S.C. Krishnan, J.M. Di Diego, G.A. Gintant, and D.W. Liu. Heterogeneity within the ventricular wall. Electrophysiology and pharmacology of epicardial, endocardial, and M cells. *Circ. Res.*, 69:1427–1449, 1991.

P Archard and E De Schutter. Complex parameter landscape for a complex neuron model. *PLOS Comput. Biol.*, 2:794–804, 2006.

C.J. Arthurs, M.J. Bishop, and D. Kay. Efficient simulation of cardiac electrical propagation using high order finite elements. *J. Comput. Phys.*, 231(10):3946–3962, 2012.

J.R. Balser, D.M. Roden, and P.B. Bennett. Global parameter optimization for cardiac potassium channel gating models. *Biophys. J.*, 57:433–444, 1990.

R.J. Bauer, B.F. Bowman, and J.L. Kenyon. Theory of the kinetic analysis of patch-clamp data. *Biophys. J.*, 52:961–978, 1987.

H.C. Bazett. An analysis of the time-relations of electrocardiograms. *Heart*, 7:353–370, 1920.

J. Beaumont, F.A. Roberge, and D.R. Lemieux. Estimation of the steady-state characteristics of the Hodgkin-Huxley model from voltage-clamp data. *Math. Biosci.*, 115:145–186, 1993a.

J. Beaumont, F.A. Roberge, and L.J. Leon. On the interpretation of voltage-clamp data using the Hodgkin-Huxley model. *Math. Biosci.*, 115:65–101, 1993b.

G.W. Beeler and H. Reuter. Reconstruction of the action potential of ventricular myocardial fibres. *J. Physiol.*, 268:177–210, 1977.

A.P. Benson, O. Bernus, H. Dierckx, S.H. Gilbert, J.P. Greenwood, A.V. Holden, K. Mohee, S. Plein, A. Radjenovic, M.E. Ries, G.L. Smith, S. Sourbron, and R.D. Walton. Construction and validation of anisotropic and orthotropic ventricular geometries for quantitative predictive cardiac electrophysiology. *Interface Focus*, 1:101–116, 2011.

M.O. Bernabeu, M.J. Bishop, J. Pitt-Francis, D.J. Gavaghan, V. Grau, and B. Rodríguez. High performance computer simulations for the study of biological function in 3D heart models incorporating fibre orientation and realistic geometry at para-cellular resolution. In *Proc. Comp. Cardiol.*, volume 35, pages 721–724, 2008.

M.O. Bernabeu, J. Southern, N. Wilson, P. Strazdins, J. Cooper, and J.M. Pitt-Francis. Chaste: a case study of parallelisation of an open source finite-element solver with applications to computational cardiac electrophysiology simulation. *Int. J. High. Perform. C.*, 2013.

O. Bernus, R. Wilders, C.W. Zemlin, H. Verschelde, and A.V. Panfilov. A computationally efficient electrophysiological model of human ventricular cells. *Am. J. Physiol. Heart Circ. Physiol.*, 282:H2296–H2308, 2002.

D.J. Beuckelmann, M. Nabauer, and E. Erdmann. Intracellular calcium handling in isolated ventricular myocytes from patients with terminal heart failure. *Circulation*, 85:1046–1055, 1992.

D.J. Beuckelmann, M. Nabauer, and E. Erdmann. Alterations of K+ currents in isolated human ventricular myocytes from patients with terminal heart failure. *Circ. Res.*, 73: 379–385, 1993.

U.S. Bhalla and J.M. Bower. Exploring parameter space in detailed single neuron models: Simulations of the mitral and granule cells of the olfactory bulb. *J. Neurophysiol.*, 69(6): 1948–1965, 1993.

M.J. Bishop and G. Plank. Representing cardiac bidomain bath-Loading effects by an augmented monodomain approach: Application to complex ventricular models. *IEEE Trans. Biomed. Eng.*, 58(4):1066–1075, 2011.

M.J. Bishop, B. Rodríguez, J. Eason, J.P. Whiteley, N. Trayanova, and D.J. Gavaghan. Synthesis of voltage-sensitive optical signals: Application to panoramic optical mapping. *Biophys. J.*, 90:2938–2945, 2006.

M.J. Bishop, G. Plank, R.A.B. Burton, J.E. Schneider, D.J. Gavaghan, V. Grau, and P. Kohl. Development of an anatomically-detailed MRI-derived rabbit ventricular model and assessment of its impact on simulation of electrophysiological function. *Am. J. Physiol. Heart Circ. Physiol.*, 298:H699–H718, 2010.

M.J. Bishop, E. Vigmond, and G. Plank. Cardiac bidomain bath-loading effects during arrhyhmias: interaction with anatomical heterogeneity. *Biophys. J.*, 101:2871–2881, 2011.

V.E. Bondarenko, G.P. Szigeti, G.C. Bett, S.J. Kim, and R.L. Rasmusson. Computer model of action potential of mouse ventricular myocytes. *Am. J. Physiol. Heart Circ. Physiol.*, 287:H1378–H1403, 2004.

R. Bordas, K. Gillow, Q. Lou, I.R. Efimov, D.J. Gavaghan, P. Kohl, V. Grau, and B. Rodríguez. Rabbit-specific ventricular model of cardiac electrophysiological function including specialized conduction system. *Prog. Biophys. Mol. Biol.*, 107:90–100, 2011.

M.S. Bray, C.A. Shaw, M.W. Moore, R.A. Garcia, M.M. Zanquetta, D.J. Durgan, W.J. Jeong, J.Y. Tsai, H. Bugger, D. Zhang, A. Rohrwasser, J.H. Rennison, J.R. Dyck, S.E Litwin, P.E. Hardin, C.W. Chow, M.P. Chandler, E.D. Abel, and M.E. Young. Disruption of the circadian clock within the cardiomyocyte influences myocardial contractile function, metabolism, and gene expression. *Am. J. Physiol. Heart Circ. Physiol.*, 294:H1036–H1047, 2008.

M. Brennan, M. Palaniswami, and P. Kamen. Do existing measures of Poincare plot geometry reflect nonlinear features of heart rate variability? *IEEE Trans. Biomed. Eng.*, 48 (11):1342–1347, 2001.

T. Brennan, M. Fink, and B. Rodríguez. Multiscale modelling of drug-induced effects on cardiac electrophysiological activity. *Eur. J. Pharm. Sci.*, 36:62–77, 2009.

O. Britton, A. Bueno-Orovio, K. van Ammel, H.R. Lu, R. Towart, D.J. Gallacher, and B. Rodríguez. Experimentally-calibrated population of models predicts and explains inter-subject variability in cardiac cellular electrophysiology. *P. Natl. Acad. Sci. USA*, 110(23): E2098–E2105, 2013.

M. Brunner, X. Peng, G.X. Liu, X-Q. Ren, O. Ziv, B-R. Choi, R. Mathur, M. Hajjiri, K.E. Odening, E. Steinberg, E.J. Folco, E. Pringa, J. Centracchio, R.R. Macharzina, T. Donahay, L. Schofield, N. Rana, M. Kirk, G.F. Mitchell, A. Poppas, M. Zehender, and G. Koren. Mechanisms of cardiac arrythmias and sudden death in transgenic rabbits with long QT syndrome. *J. Clin. Invest.*, 118(6):2246–2259, 2008.

G. Bub and A. Shrier. Propagation through heterogeneous substrates in simple excitable media models. *Chaos*, 12(3):747–753, 2002.

A. Bueno-Orovio, E.M. Cherry, and F.H. Fenton. Minimal model for human action potentials in tissue. *J. Theor. Biol.*, 253:544–560, 2008.

A. Bueno-Orovio, B.M. Hanson, J.S. Gill, P. Taggart, and B. Rodríguez. Left-to-right ventricular differences in rate adaptation transiently increase pro-arrhythmic risk following rate acceleration. *PLoS ONE*, 7(12):e52234, 2012.

R.A.B. Burton, G. Plank, J.E. Schneider, V. Grau, H. Ahammer, S.L. Keeling, J. Lee, N.P. Smith, D. Gavaghan, N. Trayanova, and P. Kohl. Three-dimensional models of individual cardiac histoanatomy: tools and challenges. *Ann. N. Y. Acad. Sci.*, 1080:301–319, 2006.

R.A.B. Burton, T.A. Quinn, and P. Kohl. Rediscovering the third coronary artery. *Eur. Heart J.*, 32:1435–1437, 2011.

C. Cabo and P.A. Boyden. Electrical remodeling of the epicardial border zone in the canine infarcted heart: a computational analysis. *Am. J. Physiol. Heart Circ. Physiol.*, 284: H1378–H1403, 2003.

J.W. Cain and D.G. Schaeffer. Shortening of cardiac action potential duration near an insulating boundary. *Math. Med. Biol.*, 25:21–36, 2008.

B.J. Caldwell, M.L. Trew, G.B. Sands, D.A. Hooks, I.J. LeGrice, and B.H. Smaill. Three distinct directions of intramural activation reveal nonuniform side-to-side electrical coupling of ventricular myocytes. *Circ. Arrhythmia Electrophysiol.*, 2:433–440, 2009.

A.J. Camm. Cardiac arrhythmias - trials and tribulations. *Lancet*, 380:1448–1450, 2012.

D.L. Campbell, R.L. Rasmusson, Y. Qu, and H.C. Strauss. The calcium-independent transient outward potassium current in isolated ferret right ventricular myocytes. I. Basic characterization and kinetic analysis. *J. Gen. Physiol.*, 101:571–601, 1993.

I.R. Cantalapiedra, A. Penaranda, B. Echebarria, and J. Bragard. Phase-2 reentry in cardiac tissue: Role of the slow calcium pulse. *Phys. Rev. E*, 82:1–13, 2010.

E. Carmeliet and J. Vereecke. *Cardiac Cellular Electrophysiology*. Springer, 2002.

J. Carro, J.F. Rodríguez, P. Laguna, and E. Pueyo. A human ventricular cell model for investigation of cardiac arrhythmias under hyperkalaemic conditions. *Phil. Trans. R. Soc. Lond. A*, 369(1954):4205–4232, 2011.

A. Carusi, K. Burrage, and B. Rodríguez. Bridging experiments, models and simulations: An integrative approach to validation in computational cardiac electrophysiology. *Am. J. Physiol. Heart Circ. Physiol.*, 303(2):H144–H155, 2012.

V.S. Chauhan, E. Downar, K. Nanthakumar, J.D. Parker, H.J. Ross, W. Chan, and P. Picton. Increased ventricular repolarization heterogeneity in patients with ventricular arrhythmia vulnerability and cardiomyopathy: a human in vivo study. *Am. J. Physiol. Heart Circ. Physiol.*, 290:H79–H86, 2006.

J. Cheng, K. Kamiya, W. Liu, Y. Tsuki, J. Toyama, and I. Kodama. Heterogeneous distribution of the two components of delayed rectifier K+ current: a potential mechanism of the proarrhythmic effects of methanesulfonanilide class III agents. *Cardiovasc. Res.*, 43: 135–147, 1999.

E.M. Cherry and F.H. Fenton. Suppression of alternans and conduction blocks despite steep APD restitution: Electrotonic, memory and conduction velocity restitution effects. *Am. J. Physiol. Heart Circ. Physiol.*, 286:H2332–2341, 2004.

E.M. Cherry and F.H. Fenton. A tale of two dogs: Analyzing two models of canine ventricuar electrophysiology. *Am. J. Physiol. Heart Circ. Physiol.*, 292:H43–H55, 2007.

E.M. Cherry and F.H. Fenton. Effects of boundaries and geometry on the spatial distribution of action potential duration in cardiac tissue. *J. Theor. Biol.*, 285:164–176, 2011.

E.M. Cherry, F. Xie, Z. Feliciano, and A. Garfinkel. Computer modeling of atrial fibrillation. *Cardiac Electrophysiol. Rev.*, 5:271–276, 2001.

B-R. Choi and G. Salama. Simultaneous maps of optical action potentials and calcium transients in guinea-pig hearts: Mechanisms underlying concordant alternans. *J. Physiol.*, 529:171–188, 2000.

C.E. Clancy, Z.I. Zhu, and Y. Rudy. Pharmacogenetics and anti-arrhythmic drug therapy: a theoretical investigation. *Am. J. Physiol. Heart Circ. Physiol.*, 292:H66–H75, 2007.

J.R. Clay and L.J. DeFelice. Relationship between membrane excitability and single channel open-close kinetics. *Biophys. J.*, 28:377–390, 1983.

J.R. Clay, D. Paydarfar, and D.B. Forger. A simple modification of the Hodgkin and Huxley equations explains type 3 excitability in squid giant axons. *J. R. Soc. Interface*, 5:1421–1428, 2008.

R.H. Clayton and A.V. Holden. Propagation of normal beats and re-entry in a computational model of ventricular cardiac tissue with regional differences in action potential shape and duration. *Prog. Biophys. Mol. Biol.*, 85:473–499, 2004.

S.D. Cohen and A.C. Hindmarsh. CVODE, A stiff/nonstiff ODE solver in C. *Comp. Phys.*, 10(2):138–143, 1996.

P. Colli Franzone, L. Guerri, and S. Rovida. Wavefront propagation in an activation model of the anisotropic caridac tissue: asymptotic analysis and numerical simulations. *J. Math. Biol.*, 28:121–176, 1990.

P. Colli Franzone, L.F. Pavarino, and B. Taccardi. Simulating patterns of excitation, repolarization and action potential duration with cardiac Bidomain and Monodomain models. *Math. Biosci.*, 197:35–66, 2005.

P. Colli Franzone, L.F. Pavarino, S. Scacchi, and B. Taccardi. Modeling ventricular repolarization: Effects of transmural and apex-to-base heterogeneities in action potential durations. *Math. Biosci.*, 214:140–152, 2008.

D. Colquhoun and A.G. Hawkes. On the stochastic properties of single ion channels. *Proc. R. Soc. Lond. B*, 211:205–235, 1981.

C.E. Conrath, R. Wilders, R. Coronel, J.M.T. de Bakker, P. Taggart, J.R. de Groot, and T. Opthof. Intercellular coupling through gap junctions masks M cells in the human heart. *Cardiovasc. Res.*, 62:407–414, 2004.

J. Cooper. *Automatic Validation and Optimisation of Biological Models*. PhD thesis, University of Oxford, 2009.

J. Cooper, A. Corrias, D.J. Gavaghan, and D. Noble. Considerations for the use of cellular electrophysiology models within cardiac tissue simulations. *Prog. Biophys. Mol. Biol.*, 107(1):74–80, 2011a.

J. Cooper, G.R. Mirams, and S.A. Niederer. High-throughput functional curation of cellular electrophysiology models. *Prog. Biophys. Mol. Biol.*, 107(1):11–20, 2011b.

A. Corrias, W. Giles, and B. Rodríguez. Ionic mechanisms of electrophysiological properties and repolarization abnormalities in rabbit Purkinje fibers. *Am. J. Physiol. Heart Circ. Physiol.*, 300(5):H1806–H1813, 2011.

A. Corrias, P. Pathmanathan, D.J Gavaghan, and M.L. Buist. Modelling tissue electrophysiology with multiple cell types: applications of the extended bidomain framework. *Integr. Biol.*, 4:192–201, 2012.

S. Cortassa, M.A. Aon, B O'Rourke, H.J. Tseng, E. Marbán, and R.L. Winslow. A computational model integrating electrophysiology, contraction, and mitochondrial bioenergetics in the ventricular myocyte. *Biophys. J.*, 91(4):1564–1589, 2006.

M. Courtemanche, J.R. Rafael, and S. Nattel. Ionic mechanisms underlying human atrial action potential properties: insights from a mathematical model. *Am. J. Physiol. Heart Circ. Physiol.*, 44:H301–H321, 1998.

M.J. Cutler, D. Jeyaraj, and D.S Rosenbaum. Cardiac electrical remodeling in health and disease. *Trends Pharmacol. Sci.*, 32(3):174–180, 2011.

C.E. Dangerfield, D. Kay, and K. Burrage. Modeling ion channel dynamics through reflected stochastic differential equations. *Phys. Rev. E*, 85(5):051907, 2012.

K.F. Decker, J. Heijman, J.R. Silva, T.J. Hund, and Y. Rudy. Properties and ionic mechanisms of action potential adaptation, restitution, and accommodation in canine epicardium. *Am. J. Physiol. Heart Circ. Physiol.*, 296:H1017–H1026, 2009.

D. DiFrancsesco and D. Noble. A model of cardiac electrical activity incorporating ionic pumps and concentration changes. *Phil. Trans. R. Soc. Lond. B*, 307:353–398, 1985.

S. Dokos and N.H. Lovell. Parameter estimation in cardiac ionic models. *Prog. Biophys. Mol. Biol.*, 85:407–431, 2004.

K. Doya and A.I. Selverston. A learning algorithm for Hodgkin-Huxley type neuron models. In *Proc. IJCNN*, 1993.

E. Drouin, F. Charpentier, C. Gauthier, K. Laurent, and H. Le Marec. Electrophysiologic characteristics of cells spanning the left ventricular wall of human heart: Evidence for presence of M cells. *J. Am. Coll. Cardiol.*, 26:185–192, 1995.

Y.E. Earm and D. Noble. A model of the single atrial cell: relation between calcium current and calcium release. *Proc. R. Soc. Lond. B*, 240:83–96, 1990.

I.R. Efimov, B. Ermentrout, D.T. Huang, and G. Salama. Activation and repolarization patterns are governed by different structural characteristics of ventricular myocardium: Experimental study with voltage-sensitive dyes and numerical simulations. *J. Cardiovasc. Electrophysiol.*, 7:512–530, 1996.

I.R. Efimov, F. Aguel, Y. Cheng, B. Wollenzier, and N. Trayanova. Virtual electrode polarization in the far field: implications for external defibrillation. *Am. J. Physiol. Heart Circ. Physiol.*, 279:H1055–H1070, 2000.

I.R. Efimov, V.V. Fedorov, A.V. Glukhov, Q. Lou, C.M. Ambrosi, D. Janks, W.J. Hucker, T. Kurian, R.B. Scheussler, and N. Moazami. Multiscale imaging of the human heart: Building the foundation for human systems physiology and translational medicine. In *Conf. Proc. IEEE Eng. Med. Biol. Soc.*, pages 5177–5180, 2010.

M.D. Eggen, C.M. Swingen, and P.A. Iaizzo. Analysis of fiber orientation in normal and failing human hearts using diffusion tensor MRI. In *Biomedical Imaging: From Nano to Macro, 2009. ISBI '09. IEEE International Symposium on*, pages 642–645, 2009.

Z.J. Engelman, M.L. Trew, and B.H. Smaill. Structural heterogeneity alone is a sufficient substrate for dynamic instability and altered restitution. *Circ. Arrhythmia Electrophysiol.*, 3:195–203, 2010.

G.M. Faber, J. Silva, L. Livshitz, and Y. Rudy. Kinetic properties of the cardiac L-type Ca2+ channel and its role in myocyte electrophysiology: a theoretical investigation. *Biophys. J.*, 92:3835–3847, 2007.

V.V. Fedorov, I.T. Lozinsky, E.A. Sosunov, E.P. Anyukhovsky, M.R. Rosen, C.W. Balke, and I.R. Efimov. Application of blebbistatin as an excitation–contraction uncoupler for electrophysiologic study of rat and rabbit hearts. *Heart Rhythm*, 4:619–626, 2007.

F. Fenton and A. Karma. Vortex dynamics in three-dimensional continuous myocardium with fiber rotation: Filament instability and fibrillation. *Chaos*, 8(1):20–46, 1998.

F. Fenton, S. Evans, and H. Hastings. Memory in an excitable medium; A mechanism for spiral wave breakup in the low-excitability limit. *Phys. Rev. Lett.*, 83:3964–3967, 1999.

F.H. Fenton, E.M. Cherry, H.M. Hastings, and S.J. Evans. Multiple mechanisms of spiral wave breakup in a model of cardiac electrical activity. *Chaos*, 5:271–276, 2002.

M. Fink and D. Noble. Markov models for ion channels: versatility versus identifiability and speed. *Phil. Trans. R. Soc. Lond. A*, 367:2161–2179, 2009.

M. Fink, S.A. Niederer, E.M. Cherry, F.H. Fenton, J.T. Koivumäki, G. Seemann, R. Thul, H. Zhang, F.B. Sachse, D. Beard, E.J. Crampin, and N.P. Smith. Cardiac cell modelling: Observations from the heart of the cardiac physiome project. *Prog. Biophys. Mol. Biol.*, 104:2–21, 2011.

R. FitzHugh. Mathematical models of threshold phenomena in the nerve membrane. *Bull. Math. Biophysics*, 17:257–278, 1955.

R. FitzHugh. Impulses and physiological states in theoretical models of nerve membrane. *Biophys. J.*, 1:445–466, 1961.

M. Forbes and N. Sperelakis. *Physiology and Pathophysiology of the Heart*, chapter Ultrastructure of mammalian cardiac muscle, pages 3–41. Kluwer Academic, 1989.

W.R. Foster, L.H. Ungar, and J.S. Schwaber. Significance of conductances in Hodgkin-Huxley models. *J. Neurophysiol.*, 70(6):2502–2518, 1993.

P. Fotiadis and D.B. Forger. Modeling the effects of the circadian clock on cardiac electrophysiology. *J. Biol. Rhythm.*, 28(1):69–78, 2013.

J.J. Fox, J.L. McHarg, and R.F. Gilmour. Ionic mechanism of electrical alternans. *Am. J. Physiol. Heart Circ. Physiol.*, 282:H516–H530, 2002.

R.F. Fox and Y.N. Lu. Emergent collective behavior in large numbers of globally coupled independently stochastic ion channels. *Phys. Rev. E*, 49:3421–3431, 1994.

N. Gaborit, A. Varró, S. Le Boulter, V. Szuts, D. Escande, S. Nattel, and S. Demolombe. Gender-related differences in ion-channel and transporter subunit expression in non-diseased human hearts. *J. Mol. Cell. Cardiol.*, 49:639–646, 2010.

J.G. Gaines and T.J. Lyons. Variable step size control in the numerical solution of stochastic differential equations. *SIAM J. Appl. Math.*, 57(5):1455–1484, 1997.

P.M. Gemmell, K. Burrage, B. Rodríguez, and T.A. Quinn. Exploring the parameter space of a rabbit ventricular action potential model to investigate the effect of variation on action potential and calcium transients. In *Conf. Proc. IEEE Eng. Med. Biol. Soc.*, pages 2662–2665, 2010.

P.M. Gemmell, K. Burrage, B. Rodríguez, and T.A. Quinn. Quantifying importance of repolarization currents underlying physiological variability in rabbit cellular electrophysiology. *Biophys. J.*, 102(3):540a, 2012.

K. Gima and Y. Rudy. Ionic current basis of electrocardiographic waveforms: A model study. *Circ. Res.*, 90:889–896, 2002.

A.V. Glukhov, V.V. Fedorov, Q. Lou, V.K. Ravikumar, P.W. Kalish, R.B. Schuessler, N. Moazami, and I.R. Efimov. Transmural dispersion of repolarization in failing and non-failing human ventricle. *Circ. Res.*, 106:1–11, 2010.

A.V. Glukhov, V.V. Fedorov, Q. Lou, D. Janks, V.K. Ravikumar, P.W. Kalish, R.B. Scheussler, N. Moazami, and I.R. Efimov. Conduction remodeling in human end-stage nonischemic left ventricular cardiomyopathy. *Circulation*, 125:1835–1847, 2012.

M. Goernig, J. Haueisen, M. Liehr, M. Schlosser, H.R. Figulla, and U. Leder. Detection of U wave activity in healthy volunteers by high-resolution magnetocardiography. *J. Electrocardiol.*, 43:43–47, 2010.

A.A. Grace and D.M. Roden. Systems biology and cardiac arrhythmias. *Lancet*, 380: 1498–1508, 2012.

E. Grandi, F.S. Pasqualini, and D.M. Bers. A novel computational model of the human ventricular action potential and Ca transient. *J. Mol. Cell. Cardiol.*, 48(1):112–121, 2010.

R.A. Greenbaum, S.Y. Ho, D.G. Gibson, A.E. Becker, and R.H. Anderson. Left ventricular fibre architecture in man. *Br. Heart J.*, 45:248–263, 1981.

M.R. Guevara and T.J. Lewis. A minimal single-channel model for the regularity of beating in the sinoatrial node. *Chaos*, 5(1):174–183, 1995.

T. Guo, A. Al Abed, N.H. Lovell, and S. Dokos. A generic ionic model of cardiac action potentials. In *Conf. Proc. IEEE Eng. Med. Biol. Soc.*, pages 1465–1468, 2010.

M. Gurkiewicz and A. Korngreen. A numerical approach to ion channel modelling using whole-cell voltage-clamp recordings and a genetic algorithm. *PLOS Comput. Biol.*, 3: 1633–1647, 2007.

G.K. Gwathmey, L. Copelas, R. MacKinnon, F.J. Schoen, M.D. Feldman, W. Grossman, and J.P. Morgan. Abnormal intracellular calcium handling in myocardium from patients with end-stage heart failure. *Circ. Res.*, 61:70–76, 1987.

D. Hafner, U. Borchard, O. Richter, and M. Neugebauer. Parameter estimation in Hodgkin-Huxley-type equations for membrane action potentials in nerve and heart muscle. *J. Theor. Biol.*, 91:321–345, 1981.

O.P. Hamill, A. Marty, E. Neher, B. Sakmann, and S.J. Sigworth. Improved patch-clamp techniques for high-resolution current recording from cells and cell-free membrane patches. *Pflugers Arch.*, 391(2):85–100, 1981.

T.J. Herron, P. Lee, and J. Jalife. Optical imaging of voltage and calcium in cardiac cells & tissues. *Circ. Res.*, 110:609–623, 2012.

M. Hestenes and E. Stiefel. Methods of conjugate gradients for solving linear systems. *J. Res. Natl. Bureau Standards*, 49(6):409–436, 1952.

D.W. Hilgemann and D. Noble. Exitation-contraction coupling and extracellular calcium transients in rabbit atrium: reconstruction of basic cellular mechanisms. *Proc. R. Soc. Lond. B*, 230(1259):163–205, 1987.

A.C. Hindmarsh, P.N. Brown, K.E. Grant, S.L. Lee, R. Serban, D.E. Shumaker, and C.S. Woodward. SUNDIALS: Suite of nonlinear and differential/algebraic equation solvers. *ACM Trans. Math. Softw.*, 31(3):363–396, 2005.

M. Hinterseer, B.M. Beckmann, M. Thomsen, A. Pfeufer, M. Ulbrich, M.F. Sinner, S. Perz, H.E. Wichmann, C. Lengyel, R. Schimpf, S. Maier, A. Varró, M.A. Vos, G. Steinbeck, and S. Kääb. Usefulness of short-term variability of QT intervals as a predictor for electrical remodeling and proarrhythmia in patients with nonischemic heart failure. *Am. J. Cardiol.*, 106(2):216–20, 2010.

A.L. Hodgkin and A.F. Huxley. Currents carried by sodium and potassium ions through the membrane of the giant axon of Loligo. *J. Physiol.*, 116:449–472, 1952a.

A.L. Hodgkin and A.F. Huxley. The components of membrane conductance in the giant axon of Loligo. *J. Physiol.*, 116:473–496, 1952b.

A.L. Hodgkin and A.F. Huxley. The dual effect of membrane potential on sodium conductance in the giant axon of Loligo. *J. Physiol.*, 116:497–506, 1952c.

A.L. Hodgkin and A.F. Huxley. A quantitative description of membrane current and its application to conduction and excitation in nerve. *J. Physiol.*, 117:500–544, 1952d.

A.L. Hodgkin, A.F. Huxley, and B. Katz. Measurement of current-voltage relations in the membrane of the giant axon of Loligo. *J. Physiol.*, 116:424–448, 1952.

R. Hoefen, M. Reumann, I. Goldenberg, A.J. Moss, J. O-Uchi, Y. Gu, S. McNitt, W. Zareba, C. Jons, J.C. Kanters, P.G. Platonov, W. Shimizu, A.A.M. Wilde, J.J. Rice, and C.M. Lopes. In silico cardiac risk assessment in patients with long QT syndrome: type 1: Clinical predictability of cardiac models. *J. Am. Coll. Cardiol.*, 60(21):2182–2191, 2012.

K.M. Holzem and I.R. Efimov. Arrhythmogenic remodelling of activation and repolarization in the failing human heart. *Europace*, 14(5):v50–v57, 2012.

L.M. Hondeghem, L. Carlsson, and G. Duker. Instability and triangulation of the action potential predict serious proarrhythmia, but action potential duration prolongation is antiarrhythmic. *Circulation*, 103(15):2004–2013, 2001.

D.A. Hooks, K.A. Tomlinson, S.G. Masrsden, I.J. LeGrice, B.H. Smaill, A.J. Pullan, and P.J. Hunter. Cardiac microstructure: implications for electrical propagation and defibrillation in the heart. *Circ. Res.*, 91:331–338, 2002.

D.A. Hooks, M.L. Trew, B.J. Caldwell, G.B. Sands, I.J. LeGrice, and B.H. Smaill. Laminar arrangement of ventricular myocytes influences electrical behavior of the heart. *Circ. Res.*, 101:e103–e112, 2007.

B.C.B. Hui, S. Dokos, and N.H. Lovell. Parameter identifiability of cardiac ionic models using a novel CellML least squares optimization tool. In *Proceedings of the 29th Annual International Conference of the IEEE EMBS*, 2007.

T.J. Hund and Y. Rudy. Rate dependence and regulation of action potential and calcium transient in a canine cardiac ventricular cell model. *Circulation*, 110:3168–3178, 2004.

T.J. Hund, J.P. Kucera, N.F. Otani, and Y. Rudy. Ionic charge conservation and long-term steady state in the Luo-Rudy dynamic cell model. *Biophys. J.*, 81:3324–3331, 2001.

C.J. Hyatt, S.F. Mironov, F.J. Vetter, C.W. Zemlin, and A.M. Pertsov. Optical action potential upstroke morphology reveals near-surface transmural propagation direction. *Circ. Res.*, 97:277–284, 2005.

Y. Iwasa, S. Doi, and S. Kumagai. Parameter estimation for a pancreatic beta-cell model gradient descent learning with line search. In *The IEEE EMBS Asian Pacific Conference on BME*, 2003.

V. Iyer, R. Mazhari, and R.L. Winslow. A computational model of the human left-ventricular epicardial myocyte. *Biophys. J.*, 87:1507–1525, 2004.

M.S. Jafri, J.J. Rice, and R.L. Winslow. Cardiac Ca2+ dynamics: the roles of ryanodine receptor adaptation and sarcoplasmic reticulum load. *Biophys. J.*, 74:1149–1168, 1998.

A.F. James, S.C. Choisy, and J.C. Hancox. Recent advances in understanding sex differences in cardiac repolarization. *Prog. Biophys. Mol. Biol.*, 94(3):265–319, 2007.

D. Jeyaraj, S.M. Haldar, X. Wan, M.D. McCauley, J.A. Ripperger, K. Hu, Y. Lu, B.L. Eapen, N. Sharma, E. Ficker, M.J. Cutler, J. Gulick, A. Sanbe, J. Robbins, S. Demolombe, R.V. Kondratov, S.A. Shea, U. Albrecht, X.H. Wehrens, D.S. Rosenbaum, and M.K. Jain. Circadian rhythms govern cardiac repolarization and arrhythmogenesis. *Nature*, 483:96–99, 2012.

R.M. John, U.B. Tedrow, B.A. Koplan, C.M. Albert, L.M. Epstein, M.O. Sweeney, A.L. Miller, G.F. Michaud, and W.G. Stevenson. Ventricular arrhythmias and sudden cardiac death. *Lancet*, 380:1520–1529, 2012.

D.M. Johnson, J. Heijman, C.E. Pollard, J.P. Valentin, H.J.G.M. Crijns, N. Abi-Gerges, and P.G.A. Volders. IKs restricts excessive beat-to-beat variability of repolarization during beta-adrenergic receptor stimulation. *J. Mol. Cell. Cardiol.*, 48:122–130, 2010.

D.M. Johnson, J. Heijman, E.F. Bode, D.J. Greensmith, H. Van der Linde, N. Abi-Gerges, D.A. Eisner, A.W. Trafford, and P.G.A. Volders. Diastolic spontaneous calcium release from the sarcoplasmic reticulum increases beat-to-beat variability of repolarization in canine ventricular myocytes after β-adrenergic stimulation. *Circ. Res.*, 112:246–256, 2013.

S. Kääb, M. Hinterseer, M. Näbauer, and G. Steinbeck. Sotalol testing unmasks altered repolarization in patients with suspected acquired long-QT-syndrome–a case-control pilot study using i.v. sotalol. *Eur. Heart J.*, 24(7):649–657, 2003.

A. Kanai and G. Salama. Optical mapping reveals that repolarization spreads anisotropically and is guided by fiber orientation in guinea pig hearts. *Circ. Res.*, 77:784–802, 1995.

A. Karma. Spiral breakup in model equations of action potential propagation in tissue. *Phys. Rev. Lett.*, 71:1103–1106, 1993.

A.M. Katz. *Physiology of the heart*. Lippincott, Williams & Wilkins, 2006.

A.M. Katz and P.B. Katz. Homogeneity out of heterogeneity. *Circulation*, 79(3):712–717, 1989.

D.U.J. Keller, D.L. Weiss, O. Dössel, and G. Seemann. Influence of IKs heterogeneities on the genesis of the T-wave: A computational evaluation. *IEEE Trans. Biomed. Eng.*, 59 (2):311–322, 2012.

P.E. Kloeden and E. Platen. *Numerical Solution of Stochastic Differential Equations (Stochastic Modelling and Applied Probability), corrected edition*. Springer, 2010.

P. Kohl and F. Sachs. Mechanoelectric feedback in cardiac cells. *Phil. Trans. R. Soc. Lond. A*, 359:1173–1185, 2001.

T. Krogh-Madsen, L. Glass, E.J. Doedel, and M.R. Guevara. Apparent discontinuities in the phase-resetting response of cardiac pacemakers. *J. Theor. Biol.*, 230:499–519, 2004.

H. Kubo, K.B. Marguiles, V. Piacentino III, J.P. Gaughan, and S.R. Houser. Patients with end-stage congestive heart failure treated with β-adrenergic receptor antagonists have improved ventricular myocyte calcium regulatory protein abundance. *Circulation*, 104: 1012–1018, 2001.

S. Land, S.A. Niederer, J.M. Aronsen, E.K.S. Espe, L. Zhang, W.E. Louch, I. Sjaastad, O.M. Sejersted, and N.P. Smith. An analysis of deformation-dependent electromechanical coupling in the mouse heart. *J. Physiol.*, 590(18):4553–4569, 2012.

J.I. Laughner, F.S. Ng, M.S. Sulkin, M.A. Arthur, and I.R. Efimov. Processing and analysis of cardiac optical mapping data obtained with potentiometric dyes. *Am. J. Physiol. Heart Circ. Physiol.*, 303(7):H753–H765, 2012.

J. Lee, B. Smaill, and N.P. Smith. Hodgkin-Huxley type ion channel characterization: An improved method of voltage clamp experiment parameter estimation. *J. Theor. Biol.*, 242:123–134, 2006.

P. Lee, C. Bollensdorff, T.A. Quinn, J.P. Wuskell, L.M. Loew, and P. Kohl. Single-sensor system for spatially-resolved, continuous and multi-parametric optical mapping of cardiac tissue. *Heart Rhythm*, 8:1482–1491, 2011.

P. Lee, F. Taghavi, P. Yan, P. Ewart, E.A. Ashley, L.M. Loew, P. Kohl, and C. Bollensdorff. *In situ* optical mapping of voltage and calcium in the heart. *PLoS ONE*, 7(8):e42562, 2012a.

P. Lee, K. Wang, C.E. Woods, P. Yan, P. Kohl, P. Ewart, L.M. Loew, D.A. Terrar, and C. Bollensdorff. Cardiac electrophysiological imaging systems scalable for high-throughput drug testing. *Pflugers Arch.*, 464(6):645–656, 2012b.

I.J. LeGrice, P.J. Hunter, and B.H. Smaill. Laminar structure of the heart: a mathematical model. *Am. J. Physiol. Heart Circ. Physiol.*, 272:H2466–H2476, 1997.

M. Lemay, E. De Lange, and J.P. Kucera. Effects of stochastic channel gating and distribution on the cardiac action potential. *J. Theor. Biol.*, 281:84–96, 2011.

C. Lerma, T. Krogh-Madsen, M.R. Guevara, and L. Glass. Stochastic aspects of cardiac arrhythmias. *J. Stat. Phys.*, 128:347–374, 2007.

M.D. Lesh, M. Pring, and J.F. Spear. Cellular uncoupling can unmask dispersion of action potential duration in ventricular myocardium: A computer modeling study. *Circ. Res.*, 65: 1426–1440, 1989.

G-R. Li, C-P. Lau, T-L. Leung, and S. Nattel. Ionic current abnormalities associated with prolonged action potentials in cardiomyocytes from diseased human right ventricles. *Heart Rhythm*, 4:460–468, 2004.

G.R. Li, J. Feng, L. Yue, and M. Carrier. Transmural heterogeneity of action potentials and Ito1 in myocytes isolated from the human right ventricle. *Am. J. Physiol. Heart Circ. Physiol.*, 275:H369–H377, 1998.

L. Li, S.A. Niederer, W. Idigo, Y.H. Zhang, P. Swietach, B. Casadei, and N.P. Smith. A mathematical model of the murine ventricular myocyte: a data-driven biophysically based approach applied to mice overexpressing the canine NCX isoform. *Am. J. Physiol. Heart Circ. Physiol.*, 299(4):H1045–H1063, 2010.

L. Li, W.E. Louch, S.A. Niederer, J.M. Aronsen, G. Christensen, O.M. Sejersted, and N.P. Smith. Sodium accumulation in SERCA knockout-induced heart failure. *Biophys. J.*, 102 (9):2039–2048, 2012.

G.T. Lines, M.L. Buist, P. Grottum, A.J. Pullan, J. Sundnes, and A. Tveito. Mathematical models and numerical methods for the forward problem in cardiac electrophysiology. *Comput. Visual. Sci.*, 5:215–239, 2003.

L. Livshitz and Y. Rudy. Uniqueness and stability of action potential models during rest, pacing, and conduction using problem-solving environment. *Biophys. J.*, 97(5):1265–1276, 2009.

C.M. Lloyd, J.L. Lawson, P. Hunter, and P.F. Nielsen. The CellML model repository. *Bioinformatics*, 24(18):2122–2123, 2008.

Q. Lou, V.V. Fedorov, A.V. Glukhov, N. Moazami, V.G. Fast, and I.R. Efimov. Transmural heterogeneity and remodeling of ventricular excitation-contraction coupling in human heart failure. *Circulation*, 123:1881–1890, 2011.

Q. Lou, W. Li, and I.R. Efimov. The role of dynamic instability and wavelength in arrhythmia maintenance as revealed by panoramic imaging with blebbistatin vs. 2,3-butanedione monoxime. *Am. J. Physiol. Heart Circ. Physiol.*, 302(1):H262–H269, 2012.

C.H. Luo and Y. Rudy. A model of the ventricular cardiac action potential. Depolarization, repolarization, and their interaction. *Circ. Res.*, 68:1501–1526, 1991.

C.H. Luo and Y. Rudy. A dynamic model of the cardiac ventricular action potential. I. Simulations of ionic currents and concentration changes. *Circ. Res.*, 74:1071–1096, 1994a.

C.H. Luo and Y. Rudy. A dynamic model of the cardiac ventricular action potential. II. Afterdepolarizations, triggered activity and potentiation. *Circ. Res.*, 74:1097–1113, 1994b.

J.L. Madden, Z.B. Miled, R.C.Y. Chin, and J. Schild. On parameter estimation for neuron models. In *IEEE International Symposium on Bio-Informatics and Biomedical Engineering*, 2000.

A. Mahajan, Y. Shiferaw, D. Sato, A. Baher, R. Olcese, L-H. Xie, M-J. Yang, P-S. Chen, J.G. Restrepo, A. Karma, A. Garfinkel, Z. Qu, and J.N. Weiss. A rabbit ventricular action potential model replicating cardiac dynamics at rapid heart rates. *Biophys. J.*, 94:392–410, 2008.

E. Marder and A.L. Taylor. Multiple models to capture the variability in biological neurons and networks. *Nat. Neurosci.*, 14(2):133–138, 2011.

G. Maruyama. Continuous Markov processes and stochastic equations. *Rend. Circ. Mat. Palermo*, 4(1):48–90, 1955.

R.R. McAllister, D. Noble, and R.W. Tsien. Reconstruction of the electrical activity of cardiac Purkinje fibres. *J. Physiol.*, 251:1–59, 1975.

L.S. Milescu, G. Akk, and F. Sachs. Maximum likelihood estimation of ion channel kinetics from macroscopic currents. *Biophys. J.*, 88:2494–2515, 2005.

W.T. Miller and D.B. Geselowitz. Simulation studies of the electrocardiogram. I. The normal heart. *Circ. Res.*, 43(2):301–315, 1978.

G.R. Mirams, Y. Cui, A. Sher, M. Fink, B.M. Heath, N.C. McMahon, D.J. Gavaghan, and D. Noble. Simulation of multiple ion channel block provides improved early prediction of compounds' clinical torsadogenic risk. *Cardiovasc. Res.*, 91(1):53–61, 2011.

G.R. Mirams, C.J. Arthurs, M.O. Bernabeu, R. Bordas, J. Cooper, A. Corrias, Y. Davitt, S-J. Dunn, A.G. Fletcher, D.G. Harvey, M.E. Marsh, J.M. Osborne, P. Pathmanathan, J. Pitt-Francis, J. Southern, N. Zemzemi, and D.J. Gavaghan. Chaste: an open source C++ library for computational physiology and biology. *PLOS Comput. Biol.*, 9(3):e1002970, 2013.

K.T. Murray, T. Anno, P.B. Bennett, and L.M. Hondeghem. Voltage clamp of the cardiac sodium current at 37°C in physiologic solutions. *Biophys. J.*, 57:607–613, 1990.

R.C. Myles, F.L. Burton, S.M. Cobbe, and G.L. Smith. The link between repolarisation alternans and ventricular arrhythmia: Does the cellular phenomenon extend to the clinical problem? *J. Mol. Cell. Cardiol.*, 45:1–10, 2008.

R.C. Myles, O. Bernus, F.L. Burton, S.M. Cobbe, and G.L. Smith. Effect of activation sequence on transmural patterns of repolarization and action potential duration in rabbit ventricular myocardium. *Am. J. Physiol. Heart Circ. Physiol.*, 299:H1812–H1822, 2010.

J. Nagumo, S. Arimoto, and S. Yoshizawa. An active pulse transmission line simulating nerve axon. *Proc. IRE*, 50:2061–2070, 1962.

K. Nanthakumar, J. Jalife, S. Masse, E. Downar, M. Pop, J. Asta, H. Ross, V. Rao, S. Mironov, E. Sevaptsidis, J. Rogers, G. Wright, and R. Dhopeshwarkar. Optical mapping of Langendorff-perfused human hearts: Establishing a model for the study of ventricular fibrillation in humans . *Am. J. Physiol. Heart Circ. Physiol.*, 293:H875–H880, 2007.

M.P. Nash, C.P. Bradley, P.M. Sutton, R.H. Clayton, P. Kallis, M.P. Hayward, D.J. Paterson, and P. Taggart. Whole heart action potential duration restitution properties in cardiac patients: a combined clinical and modelling study. *Exp. Physiol.*, 91:339–354, 2006.

S. Nattel, A. Maguy, S. Le Boulter, and Y-H. Yeh. Arrhythmogenic ion-channel remodeling in the heart: heart failure, myocardial infarction, and atrial fibrillation. *Physiol. Rev.*, 87: 425–456, 2007.

S. Nattel, Y. Frelin, N. Gaborit, C. Loualt, and S. Demolombe. Ion-channel mRNA-expression profiling: Insights into cardiac remodeling and arrhythmic substrates. *J. Mol. Cell. Cardiol.*, 48(1):96–105, 2010.

S. Nattel, C. Antzelevitch, and D. Noble. Resolving the M-cell debate: Why and how. *Heart Rhythm*, 8(8):1293–1295, 2011.

J.A. Nelder and R. Mead. A simplex method for function minimization. *Comput. J.*, 7(4): 308–313, 1965.

S.A. Niederer, M. Fink, D. Noble, and N.P. Smith. A meta-analysis of cardiac electrophysiology computational models. *Exp. Physiol.*, 94(5):486–495, 2009.

S.A. Niederer, E. Kerfoot, A.P. Benson, M.O. Bernabeu, O. Bernus, C. Bradley, E.M. Cherry, R. Clayton, F.H. Fenton, A. Garny, E. Heidenrich, S. Land, M. Maleckar, P. Pathmanathan, G. Plank, J.F. Rodríguez, I. Roy, F.B. Sachse, G. Seemann, O. Skavhaug, and N.P. Smith. Verification of cardiac tissue electrophysiology simulators using an N-version benchmark. *Phil. Trans. R. Soc. Lond. A*, 369:4331–4351, 2011.

D. Noble. Cardiac action and pacemaker potentials based on the Hodgkin-Huxley equations. *Nature*, 188:495–497, 1960.

D. Noble. A modification of the Hodgkin-Huxley equations applicable to Purkinje fibre action and pacemaker potentials. *J. Physiol.*, 160:317 352, 1962.

D. Noble. Successes and failures in modeling heart cell electrophysiology. *Heart Rhythm*, 8(11):1798–1803, 2011.

D. Noble and Y. Rudy. Models of cardiac ventricular action potentials: Iterative interaction between experiment and simulation. *Phil. Trans. R. Soc. Lond. A*, 359:1127–1142, 2001.

D. Noble, S.J. Noble, G.C.L. Bett, Y.E. Earm, W.K. Ho, and I.S. So. The role of sodium-calcium exchange during the cardiac action potential. *Ann. N Y Acad. Sci.*, 639:334–353, 1991.

D. Noble, A. Varghese, P. Kohl, and P.J. Noble. Improved guinea-pig ventricular cell model incorporating a diadic space, IKr & IKs, and length- & tension-dependent processes. *Can. J. Cardiol.*, 14:123–134, 1998.

D. Noble, A. Garny, and P.J. Noble. How the Hodgkin-Huxley equations inspired the Cardiac Physiome Project. *J. Physiol.*, 590(11):2613–2628, 2012.

P.J. Noble and D. Noble. Remodelling of calcium dynamics in guinea-pig ventricular cells. *J. Physiol.*, 533:41P, 2001.

A. Nygren, L. Fiset, J.W. Clark, D.S. Lindbald, R.B. Clark, and W.R. Giles. Mathematical model of an adult human atrial cell - the role of K+ currents in repolarisation. *Circ. Res.*, 82:63–81, 1998.

A. Nygren, L.J. Leon, and W.R. Giles. Simulations of the human atrial action potential. *Phil. Trans. R. Soc. Lond. A*, 359:1111–1125, 2001.

T. O'Hara, L. Virág, A. Varró, and Y. Rudy. Simulation of the undiseased human cardiac ventricular action potential: Model formulation and experimental validation. *PLOS Comput. Biol.*, 7(75):e1002061, 2011.

R.A. Oliver and W. Krassowska. Reproducing cardiac restitution properties using the Fenton - Karma membrane model. *Ann. Biomed. Eng.*, 33:907–911, 2005.

S.V. Pandit, R.B. Clark, W.R. Giles, and S.S. Demir. A mathematical model of action potential heterogeneity in adult rat left ventricular myocytes. *Biophys. J.*, 81:3029–3051, 2001.

P. Pathmanathan, M.O. Bernabeu, R. Bordas, J. Cooper, A. Garny, J.M. Pitt-Francis, J.P. Whiteley, and D.J. Gavaghan. A numerical guide to the solution of the bidomain equations of cardiac electrophysiology. *Prog. Biophys. Mol. Biol.*, 102:136–155, 2010.

P. Pathmanathan, G.R. Mirams, J.A. Southern, and J.P. Whiteley. The significant effect of the choice of ionic current integration method in cardiac electrophysiological simulations. *Int J. Numer. Meth. Biomed. Engng.*, 27:1751–1770, 2011.

V. Piacentino III, C.W. Weber, X. Chen, J. Weisser-Thomas, K.B. Marguiles, D.M. Bers, and S.R. Houser. Cellular basis of abnormal calcium transients of failing human ventricular myocytes. *Circ. Res.*, 92:651–658, 2003.

J. Pitt-Francis, P. Pathmanathan, M.O. Bernabeu, R. Bordas, J. Cooper, A.G. Fletcher, G.R. Mirams, P. Murray, J.M. Osborne, A. Walter, S.J. Chapman, A. Garny, I.M.M. Van Leeuwene, P.K. Maini, B. Rodríguez, S.L. Waters, J.P. Whiteley, H.M. Byrne, and D.J. Gavaghan. Chaste: A test-driven approach to software development for biological modelling. *Comp. Phys. Commun.*, 180:2452–2471, 2009.

R. Plonsey and R.C. Barr. *Bioelectricity: A Quantitative Approach*. Kluwer Academic, second edition, 2000.

S. Poelzing, F.G. Akar, E. Baron, and D.S. Rosenbaum. Heterogeneous connexin43 expression produces electrophysiological heterogeneities across ventricular wall. *Am. J. Physiol. Heart Circ. Physiol.*, 286:H2001–H2009, 2004.

J.G.C. Ponard, A.A. Kondratyev, and J.P. Kucera. Mechanisms of intrinsic beating variability in cardiac cell cultures and model pacemaker networks. *Biophys. J.*, 92:3734–3752, 2007.

A.J. Pope, G.B. Sands, B.H. Smaill, and I.J. LeGrice. Three-dimensional transmural organization of perimysial collagen in the heart. *Am. J. Physiol. Heart Circ. Physiol.*, 295: H1243–H1252, 2008.

M. Potse, B. Dubé, J. Richer, A. Vinet, and R.M. Gulrajani. A comparison of monodomain and bidomain reaction-diffusion models for action potential propagation in the human heart. *IEEE Trans. Biomed. Eng.*, 53(12):2425–2435, 2006.

C. Pott, X. Ren, D.X. Tran, M-J. Yang, S. Henderson, M.C. Jordan, K.P. Roos, A. Garfinkel, K.D. Philipson, and J.I. Goldhaber. Mechanism of shortened action potential duration in Na+-Ca2+ exchanger knockout mice. *Am. J. Physiol. Cell Physiol.*, 292:C968–C973, 2007.

L. Priebe and D.J. Beuckelmann. Simulation study of cellular electric properties in heart failure. *Circ. Res.*, 82:1206–1223, 1998.

A.A. Prinz, C.P. Billimoria, and E. Marder. Alternative to hand tuning conductance-based models: construction and analysis of databases of model neurons. *J. Neurophysiol.*, 90: 3998–4015, 2003.

E. Pueyo, A. Corrias, L. Virág, N. Jost, T. Szél, A. Varró, N. Szentandrássy, P.P. Nánási, K. Burrage, and B. Rodríguez. A multi-scale investigation of repolarization variability and its role in cardiac arrhythmogenesis. *Biophys. J.*, 101(12):2892–2902, 2011.

J.L. Puglisi and D.M. Bers. LabHEART: an interactive computer model of rabbit ventricular myocytes ion channels and Ca transport. *Am. J. Physiol. Heart Circ. Physiol.*, 281: C2049–C2060, 2001.

T.A. Quinn and P. Kohl. Combining wet and dry research: experience with model development for cardiac mechano-electric structure-function studies. *Cardiovasc. Res.*, 97: 601–611, 2013.

T.A. Quinn, S. Granite, M.A. Allessie, C. Antzelevitch, C. Bollensdorff, G. Bub, R.A. Burton, E. Cerbai, P.S. Chen, M. Delmar, D. Difrancesco, Y.E. Earm, I.R. Efimov, M. Egger, E. Entcheva, M. Fink, R. Fischmeister, M.R. Franz, A. Garny, W.R. Giles, T. Hannes, S.E. Harding, P.J. Hunter, G. Iribe, J. Jalife, C.R. Johnson, R.S. Kass, I. Kodama, G. Koren, P. Lord, V.S. Markhasin, S. Matsuoka, A.D. McCulloch, G.R. Mirams, G.E. Morley, S. Nattel, D. Noble, S.P. Olesen, A.V. Panfilov, N.A. Trayanova, U. Ravens, S. Richard, D.S. Rosenbaum, Y. Rudy, F. Sachs, F.B. Sachse, D.A. Saint, U. Schotten, O. Solovyova, P. Taggart, L. Tung, A. Varró, P.G. Volders, K. Wang, J.N. Weiss, E. Wettwer, E. White, R. Wilders, R.L. Winslow, and P. Kohl. Minimum Information about a Cardiac Electrophysiology Experiment (MICEE): standardised reporting for model reproducibility, interoperability, and data sharing. *Prog. Biophys. Mol. Biol.*, 10(7):4–10, 2011.

R.L. Rasmusson, J.W. Clark, W.R. Giles, K. Robinson, R.B. Clark, E.F. Shibata, and D.L. Campbell. A mathematical model of electrophysiological activity in a bullfrog atrial cell. *Am. J. Physiol. Heart Circ. Physiol.*, 259(2):H370–H389, 1990.

M.S. Reid, E.A. Brown, and S.P. DeWeerth. A parameter-space search algorithm tested on a Hodgkin-Huxley model. *Biol. Cybern.*, 96:625–634, 2007.

J. Relan, P. Chinchapatnam, M. Sermesant, K. Rhode, M. Ginks, H. Delingette, C.A. Rinaldi, R. Ravazi, and N. Ayache. Coupled personalization of cardiac electrophysiology models for prediction of ischaemic ventricular tachycardia. *Interface Focus*, 1:396–407, 2011.

D.M. Roden. Taking the "Idio" out of "Idiosyncratic": Predicting torsades de pointes. *PACE*, 211(5):1029–1034, 1998.

D.M. Roden and R.L. Abraham. Refining repolarization reserve. *Heart Rhythm*, 8(11): 1756–7, 2011.

B. Rodríguez, L. Li, J.C. Eason, I.R. Efimov, and N.A. Trayanova. Differences between left and right ventricular chamber geometry affect cardiac vulnerability to electric shocks. *Circ. Res.*, 97(2):168–175, 2005.

J.F. Rodríguez, J. Carro Fernandez, E. Pueyo, K. Burrage, and B. Rodríguez. Impact of multiple ionic changes in arrhythmic risk biomarkers in human ventricular electrophysiology. *Biophys. J.*, 102(3):543a, 2012.

S. Rohr. Role of gap junctions in the propagation of the cardiac action potential. *Cardiovasc. Res.*, 62(5):309–322, 2004.

L. Romero, E. Pueyo, M. Fink, and B. Rodríguez. Impact of ionic current variability on human ventricular cellular electrophysiology. *Am. J. Physiol. Heart Circ. Physiol.*, 297: H1436–H1445, 2009.

L. Romero, B. Carbonell, B. Trenor, B. Rodríguez, J. Saiz, and J.M. Ferrero. Systematic characterization of the ionic basis of rabbit cellular electrophysiology using two ventricular models. *Prog. Biophys. Mol. Biol.*, 107:60–73, 2011.

D.S. Rosenbaum, D.T. Kaplan, A. Kanai, L. Jackson, H. Garan, and G. Salama. Repolarization inhomogeneities in ventricular myocardium change dynamically with abrupt cycle length shortening. *Circulation*, 84(3):1333–1345, 1991.

B.J. Roth. Electrical conductivity values used with the bidomain model of cardiac tissue. *IEEE Trans. Biomed. Eng.*, 44:987–999, 1997.

Y Rudy and J.R. Silva. Computational biology in the study of cardiac ion channels and cell electrophysiology. *Q. Rev. Biophys.*, 39(1):57–116, 2006.

Y. Saad and M.H. Schultz. GMRES: a generalized minimal residual algorithm for solving nonsymmetric linear systems. *SIAM J. Sci. Comput.*, 7:856–869, 1986.

K.J. Sampson, V. Iyer, A.R. Marks, and R.S. Kass. A computational model of Purkinje fibre single cell electrophsyiology: implications for the long QT syndrome. *J. Physiol.*, 588: 2643–2655, 2010.

A.X. Sarkar and E.A. Sobie. Regression analysis for constraining free parameters in electrophysiological models of cardiac cells. *PLOS Comput. Biol.*, 6(9):e1000914, 2010.

A.X. Sarkar and E.A. Sobie. Quantification of repolarization reserve to understand interpatient variability in the response to proarrhythmic drugs: A computational analysis. *Heart Rhythm*, 8:1749–1755, 2011.

A.X. Sarkar, D.J. Christini, and E.A. Sobie. Exploiting mathematical models to illuminate electrophysiological variability between individuals. *J. Physiol.*, 590(11):2555–2567, 2012.

J.J. Saucerman, L.L. Brunton, A.P. Michailova, and A.D. McCulloch. Modeling beta-adrenergic control of cardiac myocyte contractility in silico. *J. Biol. Chem.*, 278(48): 47997–48003, 2003.

F. Schroder, R. Handrock, D.J. Beuckelmann, S. Hirt, R. Hullin, L. Priebe, R.H.G. Schwinger, J. Weil, and S. Herzig. Increased availability and open probability of single L-type calcium channels from failing compared with nonfailing human ventricle. *Circulation*, 98:969–976, 1998.

R. Sebastian, V. Zimmerman, D. Romero, D. Sanchez-Quintana, and A.F. Frangi. Characterization and modeling of the peripheral cardiac conduction system. *IEEE Trans. Med. Imaging*, 32(1):45–55, 2013.

G. Seemann, F.B. Sachse, M. Karl, D.L. Weiss, V. Heuveline, and O. Dössel. Framework for modular, flexible and efficient solving of the bidomain equations using PETSc. In *Progress in Industrial Mathematics at ECMI 2008*, volume 15, pages 363–369, 2010.

T.R. Shannon, F. Wang, J. Puglisi, C. Weber, and D.M. Bers. A mathematical treatment of integrated Ca dynamics in the ventricular myocyte. *Biophys. J.*, 87:3351–3371, 2004.

R.M. Shaw and Y. Rudy. Ionic mechanisms of propagation in cardiac tissue: Roles of the sodium and L-type calcium currents during reduced excitability and decreased gap junction coupling. *Circ. Res.*, 81:727–741, 1997.

A.A. Sher, K. Wang, A. Wathen, P.J. Maybank, G.R. Mirams, D. Abramson, D. Noble, and D.J. Gavaghan. A local sensitivity analysis method for developing biological models with identifiable parameters: Application to cardiac ionic channel modelling. *Future Gener. Comp. Sy.*, 29(2):591–598, 2013.

S. Sicouri and C. Antzelevitch. A subpopulation of cells with unique electrophysiological properties in the deep subepicardium of the canine ventricle. The M cell. *Circ. Res.*, 68: 1729–1741, 1991.

J.R. Silva, H. Pan, D. Wu, A. Nekouzadeh, K.F. Decker, J. Cui, N.A. Baker, D. Sept, and Y. Rudy. A multiscale model linking ion-channel molecular dynamics and electrostatics to the cardiac action potential. *P. Natl. Acad. Sci. USA*, 106(27):11102–11106, 2009.

K.R. Sipido, T. Stankovica, W. Flameng, J. Vanhaecke, and F. Verdonck. Frequency dependence of Ca2+ release from the sarcoplasmic reticulum in human ventricular myocytes from end-stage heart failure. *Cardiovasc. Res.*, 37:478–488, 1998.

E.A. Sobie. Parameter sensitivity analysis in electrophysiological models using multivariable regression. *Biophys. J.*, 96(4):1264–1274, 2009.

E. Soltysinska, S.P. Olesen, T. Christ, E. Wettwer, A. Varró, M. Grunnet, and T. Jespersen. Transmural expression of ion channels and transporters in human nondiseased and end-stage failing hearts. *Pflugers Arch.*, 459:11–23, 2009.

D.D. Streeter, H.M. Spotnitz, D.P. Patel, Ross J., and E.H. Sonnenblick. Fiber orientation in the canine left ventricle during diastole and systole. *Circ. Res.*, 24(3):339–347, 1969.

J. Sundnes, G.J. Lines, X. Cai, B.F. Nielsen, K-A. Mardal, and A. Tveito. *Computing the electrical activity in the heart*. Springer, 2006.

Z. Syed, E. Vigmond, S. Nattel, and L.J. Leon. Atrial cell action potential parameter fitting using genetic algorithms. *Med. Biol. Eng. Comput.*, 43:561–571, 2005.

N. Szentandrássy, T. Banyasz, T. Biro, G. Szabo, B.I. Toth, J. Magyar, J. Lazar, A. Varró, L. Kovacs, and P.P. Nanasi. Apico-basal inhomogeneity in distribution of ion channels in canine and human ventricular myocardium. *Cardiovasc. Res.*, 65:851–860, 2005.

P. Taggart, P.M.I. Sutton, T. Opthof, R. Coronel, R. Trimlett, W. Pugsley, and P. Kallis. Transmural repolarisation in the left ventricle in humans during normoxia and ischaemia. *Cardiovasc. Res.*, 50:454–462, 2001.

N. Takahashi, S. Doi, and S. Kumagai. Parameter estimation of ventricular myocardial cell model using an on-line learning algorithm. In *SICE-ICAS International Joint Conference*, 2006.

K.H.W.J. Ten Tusscher and A.V. Panfilov. Alternans and spiral breakup in a human ventricular tissue model. *Am. J. Physiol. Heart Circ. Physiol.*, 291:H1088–H1100, 2006.

K.H.W.J. Ten Tusscher, D. Noble, P.J. Noble, and A.V. Panfilov. A model for human ventricular tissue. *Am. J. Physiol. Heart Circ. Physiol.*, 286:H1573–H1589, 2004.

M.B. Thomsen, S.C. Verduyn, M. Stengl, J.D.M. Beekman, G. De Pater, J. Van Opstal, P.G.A. Volders, and M.A. Vos. Increased short-term variability of repolarization predicts d-sotalol-induced torsades de pointes in dogs. *Circulation*, 110(16):2453–9, 2004.

M.B. Thomsen, C. Wang, N. Ozgen, H-G. Wang, M.R. Rosen, and G.S. Pitt. Accessory subunit KChIP2 modulates the cardiac L-type calcium current. *Circ. Res.*, 104:1382–389, 2009.

G.F. Tomaselli and E. Márban. Electrophysiological remodeling in hypertrophy and heart failure. *Cardiovasc. Res.*, 42:270–283, 1999.

G.F. Tomaselli and D.P. Zipes. What causes sudden death in heart failure? *Circ. Res.*, 95: 754–763, 2004.

T.I. Tóth and V. Crunelli. A numerical procedure to estimate kinetic and steady-state characteristics of inactivating ionic currents. *J. Neurosci. Methods*, 63:1–12, 1995.

N.A. Trayanova. Whole-heart modeling: Applications to cardiac electrophysiology and electromechanics. *Circ. Res.*, 108:113–128, 2011.

B. Trenor, K. Cardona, J.F. Gomez, S. Rajamani, J.M. Ferrero Jr., L. Belardinelli, and J. Saiz. Simulation and mechanistic investigation of the arrhythmogenic role of the late sodium current in human heart failure. *PLoS ONE*, 7(3):e32659, 2012.

J.K. Triedman, M. Jolley, J. Stinstra, D.H. Brooks, and R. MacLeod. Predictive modeling of defibrillation utilizing hexahedral and tetrahedral finite element models: Recent advances. *J. Electrocardiol.*, 41(6):482–486, 2008.

L. Tung. *A bi-domain model for describing ischemic myocardial D-C potentials*. PhD thesis, Massachusetts Institute of Technology, 1978.

F. Vadakkumpadan, L.J. Rantner, B. Tice, P. Boyle, A.J. Prassl, E. Vigmond, G. Plank, and N. Trayanova. Image-based models of cardiac structure with applications in arrhythmia and defibrillation studies. *J. Electrocardiol.*, 42:157.e1–157.e10, 2009.

C.F. Vahl, A. Bonz, T. Timek, and S. Hagl. Intracellular calcium transient of working human myocardium of seven patients transplanted for congestive heart failure. *Circ. Res.*, 74: 952–958, 1994.

A. Varghese and G.R. Sell. A conservation principle and its effect on the formulation of Na-Ca exchanger current in cardiac cells. *J. Theor. Biol.*, 189:33–40, 1997.

F.J. Vetter, S.B. Simons, S.F. Mironov, C.J. Hyatt, and A.M. Pertsov. Epicardial fiber organization in swine right ventricle and its impact on propagation. *Circ. Res.*, 96:244–251, 2005.

E.J. Vigmond, R. Weber dos Santos, A.J. Prassl, M. Deo, and G. Plank. Solvers of the cardiac bidomain equations. *Prog. Biophys. Mol. Biol.*, 96:3–18, 2008.

P.C. Viswanathan, R.M. Shaw, and Y. Rudy. Effects of IKr and IKs heterogeneity on action potential duration and its rate. *Circulation*, 99:2466–2474, 1999.

F. Voss, T. Opthof, J. Marker, A. Bauer, H.A. Katus, and R. Becker. There is no transmural heterogeneity in an index of action potential duration in the canine left ventricle. *Heart Rhythm*, 6:1028–1034, 2009.

M. Wallman, N.P. Smith, and B. Rodríguez. A comparative study of graph-based, eikonal and monodomain simulations for the estimation of cardiac activation times. *IEEE Trans. Biomed. Eng.*, 59(6):1739–1748, 2012.

R.D. Walton, R.M. Smith, B.G. Mitrea, E. White, O. Bernus, and A.M. Pertsov. Extracting surface activation time from the optically recorded action potential in three-dimensional myocardium. *Biophys. J.*, 102:30–38, 2012.

G.J. Wang and J. Beaumont. Parameter estimation of the Hodgkin-Huxley gating model: an inversion procedure. *SIAM J. Appl. Math.*, 64:1249–1267, 2004.

L. Wang and E. Sobie. Mathematical model of the neonatal mouse ventricular action potential. *Am. J. Physiol. Heart Circ. Physiol.*, 294:H2565–H2575, 2008.

D.L. Weiss, D.U.J. Keller, G. Seemann, and O. Dössel. The influence of fibre orientation, extracted from different segments of the human left ventricle, on the activation and repolarization sequence: a simulation study. *Europace*, 9:96–104, 2007.

R. Wilders and H.J. Jongsma. Beating irregularity of single pacemaker cells isolated from the rabbit sinoatrial node. *Biophys. J.*, 65:2601–2613, 1993.

A.R. Willms. NEUROFIT: software for fitting Hodgkin-Huxley models to voltage-clamp data. *J. Neurosci. Methods*, 121:139–150, 2002.

A.R. Willms, D.J. Baro, R.M. Harris-Warrick, and J. Guckenheimer. An improved parameter estimation method for Hodgkin-Huxley models. *J. Comput. Neurosci.*, 6:145–168, 1999.

R.L. Winslow, J.J. Rice, S. Jafri, E. Marban, and B. O'Rourke. Mechanisms of altered excitation-contraction coupling in canine tachycardia-induced heart failure. II. Model studies. *Circ. Res.*, 84:571–586, 1999.

L. Xiao, J. Xiao, X. Luo, H. Lin, Z. Wang, and S. Nattel. Feedback remodeling of cardiac potassium current expression: a novel potential mechanism for control of repolarization reserve. *Circulation*, 118(10):983–992, 2008.

P.C. Yang and C.E. Clancy. *In silico* prediction of sex-based differences in human susceptibility to cardiac ventricular tachyarrhythmias. *Front. Physiol.*, 3:360, 2012.

L. Yue, J. Feng, G.R. Li, and S. Nattel. Transient outward and delayed rectifier currents in canine atrium: properties and role of isolation methods. *Am. J. Physiol. Heart Circ. Physiol.*, 270(6):H2157–68, 1996.

M. Zaniboni, A.E. Pollard, L. Yang, and K.W. Spitzer. Beat-to-beat repolarization variability in ventricular myocytes and its suppression by electrical coupling. *Am. J. Physiol. Heart Circ. Physiol.*, 278:H677–H687, 2000.

M. Zaniboni, I. Riva, F. Cacciani, and M. Groppi. How different two almost identical action potentials can be: A model study on cardiac repolarization. *Math. Biosci.*, 228:56–70, 2010.

N. Zemzemi, M.O. Bernabeu, J. Saiz, J. Cooper, P. Pathmanathan, G.R. Mirams, J. Pitt-Francis, and B. Rodríguez. Computational assessment of drug-induced effects on the electrocardiogram: from ion channel to body surface potentials. *Br. J. Pharmacol.*, 168 (3):718–733, 2012.

J. Zeng, K.R. Laurita, D.S. Rosenbaum, and Y. Rudy. Two components of the delayed rectifier K+ current in centricular myocytes of the guinea pig type: theoretical formulation and their role in repolarization. *Circ. Res.*, 77:1–13, 1995.

Y. Zhang, X. Liang, J. Ma, Y. Jing, M.J. Gonzales, C. Villongco, A. Krishnamurthy, L.R. Frank, V. Nigam, P. Stark, S.M. Narayan, and A.D. McCulloch. An atlas-based geometry pipeline for cardiac Hermite model construction and diffusion tensor reorientation. *Med. Image Anal.*, 16:1130–1141, 2012.